

**POST-TRANSLATIONAL REGULATION OF 4-1BB, AN EMERGING
TARGET FOR CANCER IMMUNOTHERAPY**

by

Ruoxuan Sun

A Dissertation

Submitted to the Faculty of Purdue University

In Partial Fulfillment of the Requirements for the degree of

Doctor of Philosophy



Department of Medicinal Chemistry and Molecular Pharmacology

West Lafayette, Indiana

May 2022

THE PURDUE UNIVERSITY GRADUATE SCHOOL
STATEMENT OF COMMITTEE APPROVAL

Dr. Seung-Oe Lim, Chair

Department of Medicinal Chemistry and Molecular Pharmacology

Dr. Qing Deng

Department of Biological Sciences

Dr. Michael K Wendt

Department of Medicinal Chemistry and Molecular Pharmacology

Dr. Zhong-Yin Zhang

Department of Medicinal Chemistry and Molecular Pharmacology

Approved by:

Dr. Andy Hudmon

This dissertation is dedicated to those who supported me through the toughest times

ACKNOWLEDGMENTS

I would like to thank my advisor Dr. Seung-Oe Lim for serving as my thesis supervisor in the last five years. Dr. Lim helped me improve my experimental skills, logical thinking, and scientific writing. He encouraged me to pursue my research interest and created an ideal environment that allowed most of my proposed research take place in the lab. My Ph.D. study would not be conducted so quickly and smoothly without the platform established by Dr. Lim.

I would also like to thank all my thesis committee what is composed by Dr. Michael K. Wendt, Dr. Zhong-Yin Zhang (both from our department) and Dr. Qing Deng (from the Department of Biological Sciences), for continuously providing thoughtful and constructive suggestions during my Ph.D. study. They, together with my advisor Dr. Seung-Oe Lim, assured my study to be performed at high quality. Additionally, Dr. Val J Watts, Dr. Chiwook Park and Dr. Richard M van Rijn as members of my original proposal committee provided critical suggestions that I benefitted largely from.

My graduate research could not be accomplished without the generous support out of lab. Dr. Chau-Wen Chou, the co-director of The Proteomics and Mass Spectrometry Facility at University of Georgia, provided significant assistance on the identification of protein modification and proximity labeling assay. I would also give special appreciation to Chuang Li and Yan Liu, two graduate students in Dr. Zhaoqing Luo's laboratory in the Department of Biology. Chuang shared his experience in proximity labeling which is the key approach utilized in my study (the first part). Yan and I had a lot of constructive discussions about the fundamental strategies investigating protein modification, which greatly fulfilled my knowledge gap in this field.

Finally, I would like to share my achievement and pleasure with my family who supported me unconditionally during the last few years. I particularly thank my girlfriend Qin Yang, who is not only an intellectual and selfless person, but an extraordinary junior scientist, for being the indispensable support of mine.

TABLE OF CONTENTS

LIST OF TABLES	8
LIST OF FIGURES	9
ABSTRACT	14
CHAPTER 1. INTRODUCTION	16
1.1 Cancer immunotherapy	16
1.1.1 Overview of immuno-oncology	16
1.1.2 Clinical immunotherapy: From benchside to bedside	20
1.1.3 Regulation of natural and drug-induced anti-tumor immunity	22
1.2 4-1BB, a potent accelerator of anti-tumor immunity	30
1.2.1 Molecular foundation of 4-1BB as a stimulatory immune signaling receptor	30
1.2.2 The biological significance of 4-1BB in cancers and non-cancer diseases	32
1.2.3 4-1BB in clinical cancer immunotherapy	34
1.3 Protein ubiquitination	36
1.3.1 The process and functions of protein ubiquitination	36
1.3.2 Impact of ubiquitination in anti-tumor immunity	38
1.3.3 Protein ubiquitination as a target for cancer immunotherapy	39
1.4 Protein <i>N</i> -glycosylation	41
1.4.1 Overview of <i>N</i> -linked glycosylation	41
1.4.2 The biosynthesis of <i>N</i> -glycoproteins	41
1.4.3 Targeting protein <i>N</i> -glycosylation for cancer immunotherapy	44
CHAPTER 2. IDENTIFICATION OF FBXL20 AS AN E3 UBIQUITIN LIGASE THAT FACILITATES THE PROTOSOMAL DEGRADATION OF 4-1BB	46
2.1 Summary	46
2.2 Results	46
2.2.1 Tumoral 4-1BB expression is associated with optimal antitumor immunity	46
2.2.2 4-1BB has four acceptor sites for polyubiquitination	49
2.2.3 4-1BB is degraded through UPS	51
2.2.4 Ubiquitination-mediated proteolysis of 4-1BB depends on its <i>N</i> -glycosylation status	56

2.2.5	Profiling the interacting partners of 4-1BB by PL coupled with proteomics analysis	59
2.2.6	Identification and validation of FBXL20 acts as the E3 ligase promoting 4-1BB ubiquitination and degradation	62
2.3	Discussion.....	64
CHAPTER 3. THE FUNCTIONAL CHARACTERIZATION OF N-GLYCOSYLATION IN THE REGULATION OF 4-1BB		67
3.1	Summary.....	67
3.2	Results	67
3.2.1	Identification of <i>N</i> -glycosylation sites on human 4-1BB.....	67
3.2.2	<i>N</i> -glycosylation of human 4-1BB has minimal contribution to its engagement with 4-1BBL	68
3.2.3	<i>N</i> -glycosylation contributes to 4-1BB transportation towards cell membrane	69
3.2.4	4-1BB is destabilized by <i>N</i> -glycosylation.....	70
3.2.5	<i>N</i> -glycosylation-deficient 4-1BB is more intensively multimerized.....	72
3.2.6	A modified form of 4-1BB 2NQ is membrane-localized and sensitive to UPS-degradation	76
3.3	Discussion.....	76
CHAPTER 4. CONCLUSIONS AND FUTURE DIRECTIONS		79
4.1	Conclusions	79
4.2	Questions to be answered	80
4.3	Future directions	81
CHAPTER 5. MATERIALS AND METHODS		85
5.1	Instruments and materials	85
5.1.1	Instruments	85
5.1.2	Cell lines.....	86
5.1.3	Chemical reagents	86
5.1.4	Biological reagents	88
5.1.5	Kits	91
5.1.6	Buffer preparation	91
5.1.7	Oligonucleotides.....	92

5.1.8	Software	94
5.2	Experimental procedures	95
5.2.1	Cell culture	95
5.2.2	Molecular cloning	95
5.2.3	Transfection.....	99
5.2.4	Lentivirus packaging & Stabling cell line establishment.....	100
5.2.5	Immunoblotting assay	100
5.2.6	Coomassie blue staining.....	102
5.2.7	Immunoprecipitation	103
5.2.8	<i>In vivo</i> ubiquitination assay	103
5.2.9	Cycloheximide (CHX) chase assay	104
5.2.10	PNGase F digestion	104
5.2.11	Membrane protein labeling and enrichment.....	104
5.2.12	RNA extraction and qRT-PCR.....	105
5.2.13	Determination of 4-1BB/4-1BBL binding affinity.....	105
5.2.14	Detection of cell surface 4-1BB	105
5.2.15	Mass spectrometry.....	106
5.2.16	Glycomics.....	107
5.2.17	<i>In-silico</i> analysis.....	107
5.2.18	Statistics	108
APPENDIX A. SUPPLEMENTARY FIGURES		109
APPENDIX B. SUPPLEMENTARY TABLES.....		117
REFERENCES		144
VITA		177
PUBLICATIONS.....		178

LIST OF TABLES

Table 1.1. The summary of clinical trials involving Urelumab in combination with other regimens.	35
Table 1.2. The summary of clinical trials involving Utomilumab in combination with other regimens.	35
Table 4.1. Some representative studies aiming to overcome 4-1BB-related liver toxicity.	82
Table 5.1. The list of equipment (parental and self-established) used in this study.	85
Table 5.2. The list of cell lines (parental and self-established) used in this study.	86
Table 5.3. The list of chemical reagents used in this study.	87
Table 5.4. The list of biological reagents used in this study.	89
Table 5.5. The list of kits used in this study.	91
Table 5.6. The list of DNA oligoes used in this study.	92
Table 5.7. The list of software used in this study.	94
Table 5.8. The list of plasmids used in this study.	98
Table 5.9. The summary of all tools used for <i>in-silico</i> analysis in this study.	107

LIST OF FIGURES

Figure 1.1. Several milestones in the history of immuno-oncology.	16
Figure 1.2. The entire process of T cell-based immune attack against cancer (cancer immune cycle) ³	18
Figure 1.3. Elimination, equilibrium, and escape represent three states that function either independently or in sequence in which a different relation between transformed cells and the immune system is established. The entire process is called “cancer immunoediting” (adapted from Purroy <i>et al.</i> ⁹).	19
Figure 1.4. The structure comparison of natural TCR (left) and CAR from the first to the third generation (adapted from Singh <i>et al.</i> ³²).	22
Figure 1.5. MHC Class I-dependent tumor antigen presentation machinery (adapted from Jhunjhunwala <i>et al.</i> ⁸⁴).	25
Figure 1.6. Innate immune signaling for DNA and RNA virus detection (adapted from Zhou <i>et al.</i> ¹⁵⁵).	29
Figure 1.7. The molecular insights into the 4-1BB signalosome assembly. (A) the side view of 4-1BB downstream signal components in the presence of 4-1BBL engagement. (B) The top view of 4-1BB signal network after 4-1BBL-mediated receptor crosslinking (modified from Zapata <i>et al.</i> ¹⁹⁰).	31
Figure 1.8. The conjugation process of protein ubiquitination (adapted from Jiang <i>et al.</i> ²⁶⁰).	37
Figure 1.9. A simplified pictorial summary of mammalian protein <i>N</i> -glycosylation process. The figure was adapted from Reily <i>et al.</i> ³¹⁷ . The four steps mentioned above are outlined and marked.	42
Figure 2.1. The correlation between the <i>TNFRSF</i> transcription and OS (A) or RFS (B) of high-TMB TCGA cancers. The figure was generated by GEPIA2. Bold outline, $p < 0.05$ (Log-rank analysis); HR, hazards ratio. A lower HR indicates positive correlation of gene expression and patients’ survival.	47
Figure 2.2. The Kaplan-Meier survival plots showing the correlation between <i>TNFRSF9</i> expression and ICB outcomes of melanoma patients (A, dataset PRJEB23709 ³⁴⁸ , $n = 41$; B, dataset phs000452.v3.p1 ³⁴⁹ , $n = 74$). The figures were acquired from TIDE. The p values were calculated by Log-rank analysis.	47
Figure 2.3. High level of <i>TNFRSF9</i> transcript is associated with an inflamed cancer immune microenvironment. (A-F) The correlation between <i>TNFRSF9</i> expression with the infiltration level of CD8 ⁺ T cell (A), CD4 ⁺ T cell (B), NK cells (C), MDSC (D), T _{reg} cells (E) and M2 macrophages (F) in TCGA-SKCM dataset ($n = 471$) unveiled by TIMER2.0. The x and y axis represents infiltration level and relative <i>TNFRSF9</i> expression, respectively. The p values were calculated by Spearman’s correlation analysis.	48

Figure 2.4. The tandem mass spectrum of a human 4-1BB fragment with ubiquitinated K214, K218, K219 and K225 locus. The recognized y and b ions were highlighted in red. 50

Figure 2.5. human 4-1BB is polyubiquitinated on four Lys residues. (A) Amino acid sequence alignment of mammalian 4-1BB on its ubiquitinated region located in the intracellular domain. (B) *In vivo* ubiquitination assay comparing the ubiquitination of 4-1BB WT and 4KR. The indicated plasmids were co-transfected to HEK293T cells followed by *in vivo* ubiquitination assay. SP, signal peptide; ECD, extracellular domain; TM, transmembrane domain; ICD, intracellular domain; IP, immunoprecipitant; WCL, whole cell lysate..... 51

Figure 2.6. The comparison of turnover between 4-1BB WT and 4KR. (A) Representative immunoblotting (IB) results of CHX-chase assay comparing degradation of 4-1BB WT and 4KR. (B) The quantitative results of the remaining 4-1BB at each time point. 50% degradation was indicated by the dashed line. Monoexponential decay curve was used for data exhibition. Results represent mean \pm SD. * $p < 0.05$; ** $p < 0.01$ (two-tailed student's *t*-test). 52

Figure 2.7. The membrane expression of 4-1BB WT and 4KR. (A) IB analysis of 4-1BB expression on parental and lentivirus-transduced Jurkat cells. (B) Flow cytometry analysis comparing membrane level of 4-1BB WT and 4KR. Jurkat cells were transduced with lentivirus encoding 4-1BB WT or 4KR followed by flow cytometry detection. (C) Quantification of membrane 4-1BB WT and 4KR level in (A) ($n = 4$). Results represent mean \pm SD. ** $p < 0.01$ (two-tailed student's *t*-test); MFI, mean fluorescence intensity. 53

Figure 2.8. The protein level of 4-1BB upon the treatment with MG-132. (A - D) Proteasome inhibition by MG-132 treatment led to 4-1BB protein accumulation by not mRNA upregulation in HDLM-2 (A, B) and H1975 (C, D). (E, F) Proteasome inhibition by MG-132 treatment led to upregulation of ectopically expressed 4-1BB ectopically in HEK293T (E) and Jurkat cells (F). Results represent mean \pm SD. *N.S.* $p > 0.05$; ** $p < 0.01$ (two-tailed student's *t*-test). 54

Figure 2.9. The turn-over of 4-1BB is determined by ubiquitination. (A) CHX-chase assay comparing the degradation of 4-1BB with or without proteasome inhibition. HEK293T/4-1BB cells were pre-treated with DMSO or 10 μ M MG-132 for 2 h, then incubated with CHX (100 μ M) for indicated periods of time. (B) The quantification of IB results in (A) ($n = 3$). 50% degradation was indicated by the dashed line. Monoexponential decay curve was used for data exhibition. Results represent mean \pm SD. ** $p < 0.01$ (two-tailed student's *t*-test). 55

Figure 2.10. Luciferase assay comparing the amplification of NF- κ B activity by 4-1BB WT and 4KR. Plasmids were transfected to HEK293T/NF- κ B reporter cell line and harvested to analyze the NF- κ B reporter activity by measuring bioluminescence ($n = 4$). Data acquired from the same set of experiment were paired. * $p < 0.05$ (two-tailed, paired student's *t*-test); RLU, relative light unit. 56

Figure 2.11. Highly-glycosylated 4-1BB is more susceptible to ubiquitination-mediated degradation. (A) IB analysis of 4-1BB WT, 4KR and 2NQ from Jurkat cells transduced with indicating lentivirus. (B) IB analysis of PNGase F digestion of lysate from Jurkat cells stably expressing 4-1BB WT and 2NQ mutant. The 4-1BB mutants were lentivirally expressed on Jurkat cells. (C) Amino acid sequence alignment of mammalian 4-1BB on its *N*-glycosylation region at extracellular domain. EV, empty vector; Triangle, high-MW band (mature form) of 4-1BB; Square, medium-MW band (immature form) of 4-1BB; Circle, low-MW band (*N*-glycan-abolished form)

of 4-1BB. SP, signal peptide; ECD, extracellular domain; CRD, cysteine-rich domain; TM, transmembrane domain; ICD, intracellular domain..... 57

Figure 2.12. Highly-glycosylated 4-1BB represents the membrane-localized form. (A) Impact of BFA treatment to 4-1BB WT on HEK293T/4-1BB cells analyzed by IB (B) FACS assessment of membrane 4-1BB level of HEK293T/4-1BB cells following 1 μ M BFA treatment identical to (A). (C) Jurkat cells were transduced with lentivirus encoding 4-1BB WT or 4KR, then incubated with 1 μ M BFA for the indicated time before IB analysis. (D) Enrichment of membrane-associated 4-1BB by sulfo-NHS-SS-biotin labeling strategy. The membrane proteome of Jurkat/4-1BB cells was labeled, enriched, and analyzed by IB. WCL, whole cell lysate; FT, flow-through. 58

Figure 2.13. The assay setup of 4-1BB PL. (A) The estimated structure of 4-1BB-BioID2 fusion protein. The structure of human 4-1BB is predicted by Alpha-fold, while BioID2 was taken from PDB# 2EAY. (B) The flow diagram of the cellular biotin labeling process. (C) Validation of target biotinylation in BioID cell lines by streptavidin blotting. Lysates of biotin-treated cells were subjected to IB and visualized with dye-conjugated streptavidin. ECD, extracellular domain; TM, transmembrane domain; ICD, intracellular domain; N, N-terminus; C, C-terminus; EV, empty vector..... 60

Figure 2.14. The sample preparation for PL assay and label-free quantification of MS results. (A) The streptavidin blotting result of the triplicated pull-down samples. (B) Venn plot showing the reproducibility of BioID pull-down and mass spectrometry profiling. (C) Volcano plot illustrating the differentially enriched biotinylated proteins in BioID2 group versus 4-1BB-BioID2 group. Three replicated sets of samples were included for LFQ. Significant hits ($FC > 2$, $p < 0.01$) were highlighted (BioID2 group by blue dots, and 4-1BB-BioID2 group by red dots)..... 61

Figure 2.15. FBXL20 promotes the polyubiquitination and degradation of 4-1BB. (A) Co-IP confirmation of 4-1BB-FBXL20 interaction. HEK293T cells were co-transfected with 4-1BB-Flag and Myc-FBXL20 plasmids followed by anti-Flag immunoprecipitation. (B) IB results of 4-1BB protein level change on HEK293T/4-1BB cell line upon transfection of empty vector or Myc-FBXL20 plasmid. (C) IB result showing 4-1BB protein level change on HEK293T/4-1BB cell line upon the transfection of non-targeting or FBXL20-targeting siRNA. (D) Validation of FBXL20 knockdown by measuring mRNA level through qRT-PCR ($n = 4$). Results represent mean \pm SD. (E) Assessment of FBXL20-promoted polyubiquitination of 4-1BB. Myc-FBXL20 and HA-Ub plasmids were co-transfected to HEK293T/4-1BB cell line followed by *in vivo* ubiquitination assay. *** $p < 0.001$ (two-tailed student's *t*-test); EV, empty vector; siNC, non-targeting siRNA; IP, immunoprecipitant; WCL, whole cell lysate..... 63

Figure 2.16. Impact of FBXL20 in cancer development and ICB treatment outcome. (A, B) Kaplan-Meier survival curves showing the inverse correlation of FBXL20 transcripts with the disease-free survival of patients in TCGA-STAD (A) and TCGA-OV (B) datasets. (C, D) Kaplan-Meier survival curves showing the inverse correlation of FBXL20 transcripts and ICB outcomes in two cohorts of melanoma patients (C, dataset phs000452.v2.p1³⁶⁸, $n = 42$; D, dataset PRJEB23709³⁴⁸, $n = 32$). The figures were acquired on GEPIA2 and TIDE. Significance values were calculated by log-rank analysis. 64

Figure 3.1. The impact of *N*-glycosylation to 4-1BB/4-1BBL interaction. (A) The validation of PNGase F-mediated 4-1BB deglycosylation. (B) The relative level of bound 4-1BBL to PNGase F-treated and untreated 4-1BB protein ($n = 3$). (C) Octet analysis calculating the binding affinity

of glycosylated (black) and deglycosylated 4-1BB (red) to 4-1BBL along with the K_D values. *N.S.*, $p > 0.05$ (two-tailed student's *t*-test); Black dot, PNGase F band. 69

Figure 3.2. The cell surface level of 4-1BB is determined by *N*-glycosylation. (A) Jurkat cells were transduced with lentivirus encoding 4-1BB WT and glycosylation-deficient mutant including N138Q, N149Q and 2NQ, respectively. The membrane levels of 4-1BB in each group were compared by flow cytometry. The percentages of positive events were included in the plots. (B) The quantitative results of membrane 4-1BB level in each group in (A) ($n = 3$). (C) The IB analysis of total 4-1BB from cells in (A). Results represent mean \pm SD. One-way analysis of variance (ANOVA) was applied for statistical analysis in (B). *N.S.*, $p > 0.05$; ***, $p < 0.001$; MFI, mean fluorescence intensity..... 70

Figure 3.3. *N*-glycans stabilize 4-1BB. Indicated 4-1BB plasmids were transfected to HEK293T for CHX-chase assay (0-8 h)..... 71

Figure 3.4. The increased stability of 4-1BB 2NQ was accompanied by decreased polyubiquitination and proteasomal degradation. (A) IB analysis of MG-132 effect on 4-1BB WT and 2NQ. HEK293T/4-1BB WT and HEK293T/4-1BB 2NQ cells were treated by 10 μ M MG-132 for 0, 4 and 8 h followed by IB assay. (B) Comparison of polyubiquitination level between WT and 2NQ 4-1BB. 4-1BB-Flag and HA-Ub plasmids were co-transfected to HEK293T cells followed by *in vivo* ubiquitination assay 48 h after transfection. IP, immunoprecipitant. WCL, whole cell lysate..... 72

Figure 3.5. Unglycosylated 4-1BB form covalent multimer through C121 residue. (A) Plasmids were transfected to HEK293T cells before sample harvesting. Non-reducing SDS-PAGE uncovered the formation of dimerized, trimerized and oligomerized 4-1BB 2NQ. The major bands exist in the presence of DTT (lane 4 and 5) were considered monomers. The white circle, triangle, square and star represent monomerized, dimerized, trimerized and oligomerized form of 4-1BB 2NQ. (B) 4-1BB 2NQ failed to form multimer when lacking the key cysteine residue C121 (lane 3 v.s. 4). Sample preparation process was identical to (A)..... 73

Figure 3.6. Topological analysis showing the relative position and orientation of C121 residue N138-linked carbohydrate of human 4-1BB. The protein structure was obtained from PDB #7D4B and modified using PyMOL 2.5. Blue, 4-1BB ectodomain; Magentas, N138-linked glycan; Orange, N149-linked glycan; Red, C121 residue. 74

Figure 3.7. Oligomerization is coupled with augmented stability of non-*N*-glycosylated 4-1BB. (A) HEK293T cells were transfected with Flag-tagged 4-1BB WT, C121A, 2NQ and 2NQ/C121A followed by CHX-chase assay to compare their stability. (B) The quantification of the remaining 4-1BB at each time points ($n = 3$). The percentage values of band intensity were normalized to time 0 h. 50% degradation was indicated by the dashed line. Results represent mean \pm SD. One-way ANOVA was performed to compare the percentage values on 8 h point. Monoexponential decay curve was used for data exhibition. *N.S.*, $p > 0.05$; ***, $p < 0.001$ 74

Figure 3.8. C121-mediated multimerization governs the localization of non-*N*-glycosylated 4-1BB. (A) Jurkat cells were transduced with lentivirus encoding 4-1BB WT, C121A, 2NQ and 2NQ/C121A, respectively. The membrane levels of 4-1BB in each group were compared by FACS. The percentages of positive events were included in the plots. (B) The quantitative results of membrane 4-1BB level in each group in (A) ($n = 3$). (C) The IB analysis of total 4-1BB from each

group of cells in (A). Results represent mean \pm SD. *N.S.*, $p > 0.05$; ***, $p < 0.001$ (one-way ANOVA); MFI, mean fluorescence intensity. 75

Figure 3.9. A subset of 4-1BB 2NQ is membrane-bound and proteasomally degraded. (A) Enrichment of membrane-associated 4-1BB 2NQ by sulfo-NHS-SS-biotin labeling strategy. The membrane proteome of Jurkat/4-1BB cells was labeled, enriched, and analyzed by IB. (B) The IB result of 4-1BB from HEK293T/4-1BB 2NQ cells treated with 50 μ M CQ or 10 μ M MG-132 for 8 h. WCL, whole cell lysate. FT, flow-through. 76

Figure 4.1. A graphic summary of the observations in this study. The figure was created on BioRender. 79

ABSTRACT

Cancer is well known as a disease involving genetic disorders, which make them distinguishable from normal tissue by the altered molecular signatures. Theoretically, malignant cells can be recognized and attacked by innate and adaptive immune system as “non-self” species, and the idea to take advantage of host immunity to treat cancer has been discussed for over a century. Through the multi-disciplinary research efforts from immunology, cancer biology, cell engineering *etc.*, cancer immunotherapy has been successfully translated from benchside to bedside. While the clinical application of immunotherapeutic regimens has achieved extraordinary success including the unprecedented long-term survival of metastatic melanoma patients, we must take it seriously that only a small proportion (about 20% on average) of patients benefit from immunotherapy, and many develop secondary progression after the initial response. Advancements have been made in biomarker development to identify the group the patients who may benefit from immunotherapy, yet the accuracy and adaptability remain to be improved. In general, the performance of immunotherapy is hardly satisfactory as the current situation.

The effect out of T cell-mediated immune response is mediated by plenty pairs of receptor-ligand interactions in the immune synapse between T cells and target cells. Despite the T cell receptor-mediated first signal and CD28-mediated second signal, a huge collection of co-signals molecules serves unneglectable roles to keep the T-cell immune response fine-tuned under appropriate threshold. Inadequate co-signaling transduction result in with immune deficiency or autoimmunity depending on the type of signal (stimulatory or inhibitory). 4-1BB is a significant co-receptor which is mainly expressed on T cells and delivers activation signal to drive T cell proliferation and cytotoxicity. 4-1BB is targetable for cancer treatment and can be used as a tumor-reactive T cell marker as well. Hence, it is of substantial importance to understand how co-signaling molecules, such as 4-1BB, are regulated under specific physiological or pathological conditions.

Proteins are regulated at multiple levels, including transcription, translation, localization, and interaction with other biomolecules (covalently or non-covalently). Post-translational modification (PTM) constitutes a critical type of mechanism that elicit multidimensional effects to the biophysical properties of target proteins. Herein, I sought to elaborate how 4-1BB, an TNFRSF family co-stimulatory receptor, is possessed and regulated by PTMs, particularly ubiquitination

and *N*-glycosylation. In the first part of this study, I confirmed that 4-1BB is degraded through ubiquitination-proteasome pathway and identified FBXL20 to be the E3 ligase subunit mediating 4-1BB polyubiquitination. While conducting the first section, I noticed that 4-1BB is heavily *N*-glycosylated and thereby dissected the biological significance of this modification which made up the second part of this study. I experimentally characterized that 4-1BB necessitates its *N*-glycans to be efficaciously transported to cell membrane through the secretory pathway. Plus, the glycosylated 4-1BB has short half-life. Without the spatial hindrance established by *N*-linked carbohydrate moieties, the exposed C121 residue of 4-1BB can be used to forms stable multimer which intracellular retention and stabilization of 4-1BB.

This study uncovered the post-translational mechanisms of action of 4-1BB regulation for the first time. More fundamentally, we provided a blueprint to study the post-translational regulation network of immune receptors which may be applied for future investigations in other targets. Our ultimate hope is to be able to grasp the dynamic of key immune regulators in the context of microenvironment and based on which pair the right therapeutics with the correct populations.

CHAPTER 1. INTRODUCTION

1.1 Cancer immunotherapy

1.1.1 Overview of immuno-oncology

Cancer is a disease with genetic alteration under physiological or pathological stress. Mutations including substitutions, insertions, or deletions of small or large fragments of DNA are accumulated and give rise to uncontrolled cell growth and eventually carcinoma. Both innate and adaptive immunity are deployed by the host to limit tumor development.

The utilization of host immunity against cancer has a history of over 130 years (Fig 1.1). Dr. William B. Coley, who is generally known as the father of immunotherapy, noticed the spontaneous remission of inoperable cancer from some patients who also experienced *Streptococcus pyogenes* infection. He reasoned that the self-cure of cancer patients was related to the invigorated host immunity triggered by bacterial infection, and thereby harness this strategy by treating cancer patients with a mixture of bacteria products (also termed “Coley toxin”) in wish to reprogram the anti-tumor immunity in 1891¹. This was considered the first application of clinical immunotherapy.

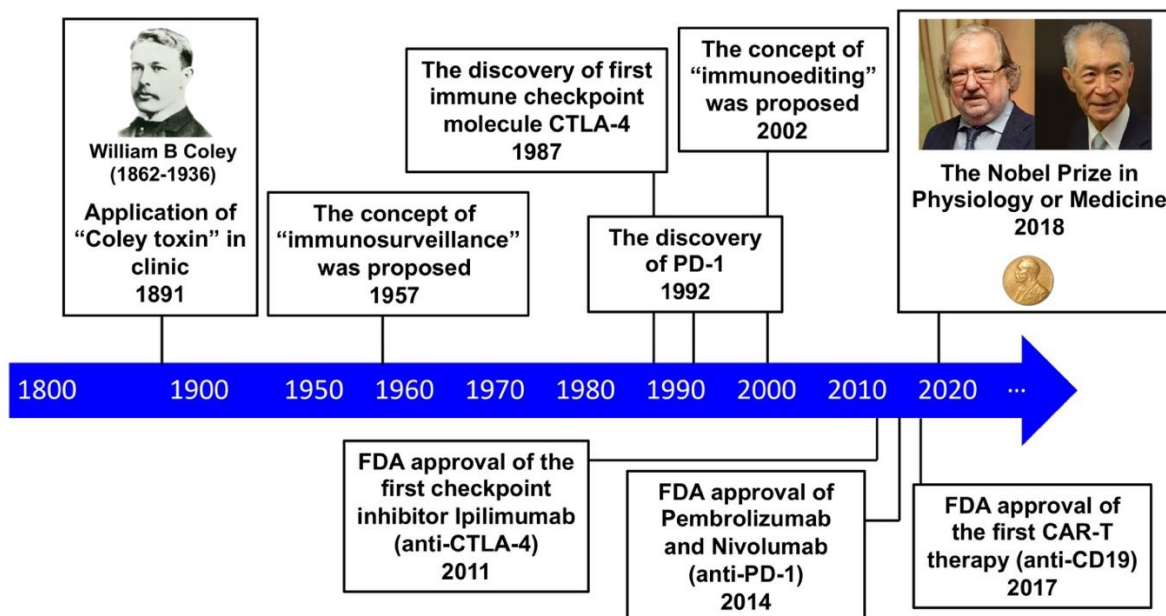


Figure 1.1. Several milestones in the history of immuno-oncology.

Many fundamental and historical achievements in both the basic research and clinical practice of immunology took place in the 20th century. In 1957, Thomas and Burnet first proposed the theory of cancer immunosurveillance ². They suggested that lymphocytes play the roles as guards to distinguish the malignant cells which harbor genetic mutations. The cancer immunosurveillance acts as an extrinsic tumor suppressor that protects the host from the development of neoplasia. This concept was validated by a great number of studies showing that mice that lacked innate or adaptive immunity were more prone to tumor development. While the idea of immunosurveillance was broadly accepted for decades. The immune system-mediated cancer clearance is typically achieved through seven core steps, which are also known as the cancer-immune cycle (Fig 1.2) ³. First of all, neoantigens (also termed tumor-associated antigens or TAA) constantly released by tumor tissues can be uptake by antigen presenting cells (APCs) such as dendritic cells (DCs) for processing and presentation (step 1). Next, neoantigen-derived peptides can be presented by major histocompatibility complex (MHC) complexes on their surfaces (step 2), allowing the priming, activation and clonal expansion of effector T cell responses against the cancer-specific antigens in tumor-draining lymph nodes (TDLNs, step 3). At this point, the tumor-specific T cells (both CD4 and CD8) have gained the potential to attack tumor cells which present specific antigens. The nature of the immune response is determined at this stage, with a critical balance between T effector cells versus T regulatory cells being essential to determine the immune outcome. Finally, the activated effector T cells traffic through blood vessels to (step 4) and infiltrate the tumor microenvironment (TME, step 5), specifically recognizing and binding to cancer cells through the interaction between its T cell receptor (TCR) and its cognate antigen bound to MHC-I (step 6). With the sufficient second activation signal activated, the effector CD8⁺ T cells can elicit the cancer-killing effect (step 7).

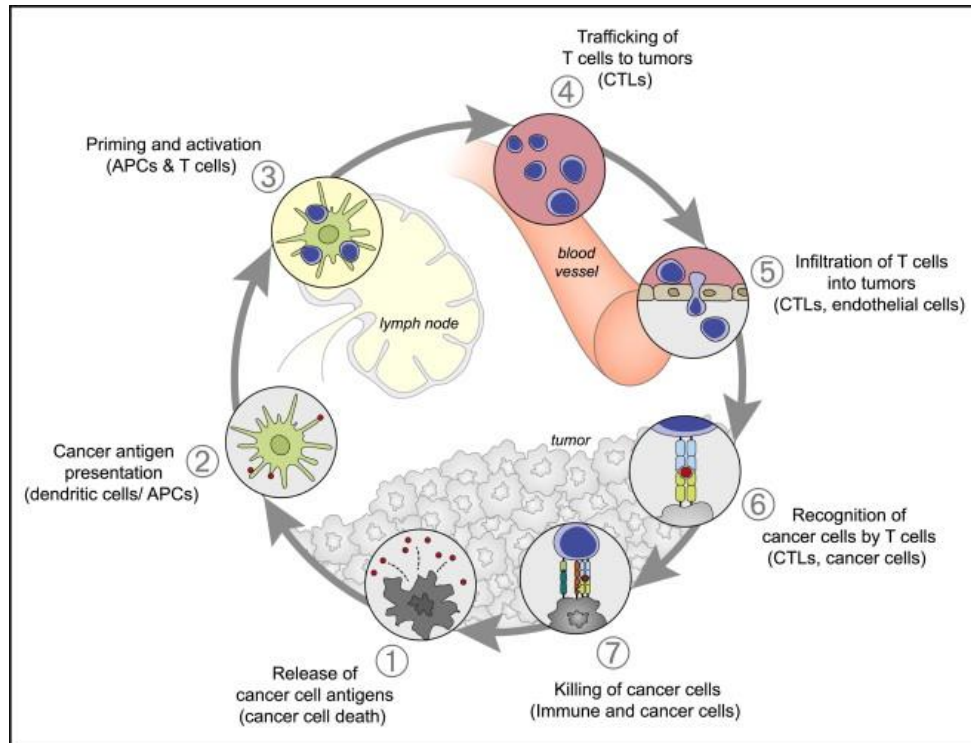


Figure 1.2. The entire process of T cell-based immune attack against cancer (cancer immune cycle)³.

Decades later, however, people started to realize that host-tumor interaction is rather a complicated long-term process which could not be described simply by the concept of immunosurveillance. A hallmark study in 2011 by Shankaran *et al.* demonstrated that tumors form on immunocompetent mice was less immunogenic than the identical-originated tumors grew on immune-deficient mice⁴, suggesting that tumor cells underwent clonal selection by host immunity. The dynamic interaction between cancer and the immune system was later named “immunoediting” in the study of Ikeda *et al.* in 2002 and gradually replaced “immunosurveillance”⁵. The whole process of tumor immunoediting can be divided into three stages: Elimination, Equilibrium, and Escape⁶. The elimination stage matches the immunosurveillance hypothesis which occurs at the onset of cancer before it becomes clinically apparent. During this phase, innate and adaptive immunity cooperatively detect and eradicate the antigenic neoplasm. However, a certain subset of cancer cells (usually the low-immunogenic population) may survive the elimination stage and coexist with the immune system, in other words, entering equilibrium stage. The equilibrium stage is a state of immune-mediated dormancy when malignant cells can neither grow rapidly nor be eradicated. Heterogeneity and genomic instability are the foundations that allow those tumor cells

to survive and adapt to the anti-tumor immunity, therefore, gaining the potential to evade the host immune attack. The tumor cells passing the equilibrium stage are highly resistant to anti-tumor immunity and continue to grow eventually leading to observable malignancies, which is the escape stage. The dysfunctional anti-tumor immunity is usually observed when tumors enter this phase. The neoantigen-directed selection pressure by immune environment can also be observed during the early-stage of tumors in clinic⁷. A recently published study by Martin *et al.* underlines the enriched loss of tumor suppressor genes was largely driven by the challenge of adaptive immunity, which represented another aspect of pro-tumor immune function⁸. Unlike immunosurveillance which primarily focuses on the early stage where the anti-tumor immune system remains active, immunoediting better reflects complicated interaction between cancer and immunity spanning a longer time course.

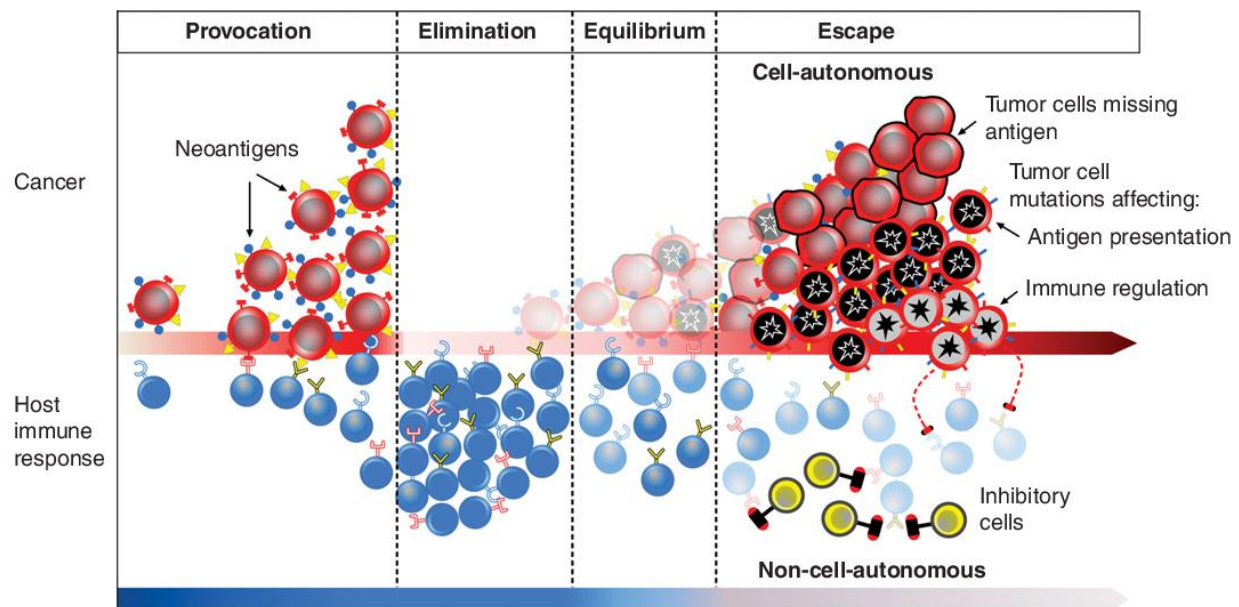


Figure 1.3. Elimination, equilibrium, and escape represent three states that function either independently or in sequence in which a different relation between transformed cells and the immune system is established. The entire process is called “cancer immunoediting” (adapted from Purroy *et al.* ⁹).

An adequate anti-tumor immunity necessitates all steps in the tumor-immune cycle (Fig 1.2) to be properly executed; however, mechanisms of numerous diversities may intercept one or several steps to disallow the immune response, giving rise to the concept to restore the immune response by correcting the mis-conducted steps. In the next paragraphs, I will introduce the clinical

applications of cancer immunotherapies and some critical factors that may affect natural and drug-induced anti-tumor response.

1.1.2 Clinical immunotherapy: From benchside to bedside

Immune modulators have been applied in clinic against carcinoma for over a century since the early experimental therapy with Coley toxin as mentioned in Fig 1.1. In this section, we will specifically introduce modern immunotherapies including immune checkpoint blockade (ICB) antibodies and adoptive cell therapies (ACT).

Cytotoxic T-lymphocyte-associated protein 4 (CTLA-4) was the first cloned in 1987 by Brunet *et al.* from a mouse T cell cDNA library¹⁰. The work published on 1995 first showed CTLA-4 outcompete CD28 to be engaged with B7 which intervenes the second activation signal¹¹. Simultaneously, antibody-mediated blockade of CTLA-4 was found to exert remarkable *in vivo* effects on syngeneic mouse cancer model¹². Later studies unveiled more complicated immune-inhibitory mechanisms of CTLA-4 which involves the trans-endocytosis of B7 molecules presented on APCs¹³. Large-scale clinical trials proved the efficacy of CTLA-4 blockade in previously untreated or treated melanoma patients^{14,15}. Eventually, the anti-CTLA-4 antibody Ipilimumab was approved by U.S. Food and Drug Administration (FDA) in 2011 as the standard treatment for unresectable or metastatic melanoma. Later, a pooled, long-term study including about 1900 metastatic melanoma patients showed the durable tumor control by Ipilimumab on about 20% of patients for over four years¹⁶.

Programmed cell death protein 1 (PD-1) was initially identified and speculated as a cell death inducer (which explained how it was named) protein by the team of Honjo in 1992¹⁷. The immune inhibitory axis of PD-1- Programmed death-ligand 1 (PD-L1) and PD-1-PD-L2 were individually identified by Freeman *et al.*¹⁸ and Latchman *et al.*¹⁹, respectively. In 2002, the first proof-of-concept animal study was published in which the PD-L1 blockade antibody showed *in vivo* anti-tumor effect²⁰. Promising results from two large-scale clinical studies were reported in 2012^{21,22}. PD-1/PD-L1 antibodies, as mono or combinational treatment, have been approved for a broad spectrum of solid tumors (<https://www.cancerresearch.org/immunotherapy/timeline-of-progress>). Co-blockade of CTLA-4 and PD-1 axis was first approved in 2015²³. In 2017, Pembrolizumab was approved for treating solid tumor patients with microsatellite instability-high (MSI-H) or mismatch repair deficiency (dMMR), becoming the first-in-history “pan-cancer”

treatment which is biomarker- instead of disease location-guided. Now PD-1/PD-L1 is being used for clinical management of 20 types of cancers (by FDA) and there remain over 5,600 clinical trials involving PD-1/PD-L1 blockade antibodies worldwide by the end of 2021²⁴. It should be noted that anti-CTLA-4 and anti-PD-1 elicit different cellular mechanisms to *in vivo*²⁵, although both are known as “T cell brake”. Their combination also reprograms the immune cell population in a manner distinct from monotherapy²⁶.

Another clinically applied immune target is lymphocyte activation gene-3 (LAG-3) which was identified in 1990 by Triebel *et al.*²⁷. When engaged with peptide-loaded MHC-II, LAG-3 elicits inhibitory signal to limit T cell activation, albeit the controversy which one between MHC-II and fibrinogen-like protein 1 (FGL1) serves as the main functional ligand^{28,29}. According to Phase II/III RELATIVITY-047 trial (NCT 03470922), Relatlimab (anti-LAG-3) in combination with Nivolumab showed optimal effect over Nivolumab alone for melanoma therapy³⁰, paving the way for the approval by FDA in 2022.

ACT refers to another type of therapy by extending the tumor-killing effect of autologous T cells. The therapeutic T cells can either be naturally existing or *ex vivo* engineered. Here we will focus our discussion on chimeric antigen receptor (CAR)-T therapy which is the only FDA-approved cell therapy for cancer. CAR is a synthetic receptor comprising extracellular antigen binding domain and intracellular signaling domain. The extensive modularity makes CAR-T an adaptable approach for various cancers. The first CAR structure was reported on 1995 by fusing the single-chain Fv domain (scFv) of anti-2,4,6-trinitrophenyl (TNP) antibody with ζ chain of TCR³¹. Afterwards, CAR frameworks have been upgraded by incorporating one or two co-stimulatory domains which will further enhance the magnitude of CAR-T function (Fig 1.4). Thus far, optimization of CAR construct design remains a critical research focus in the field.

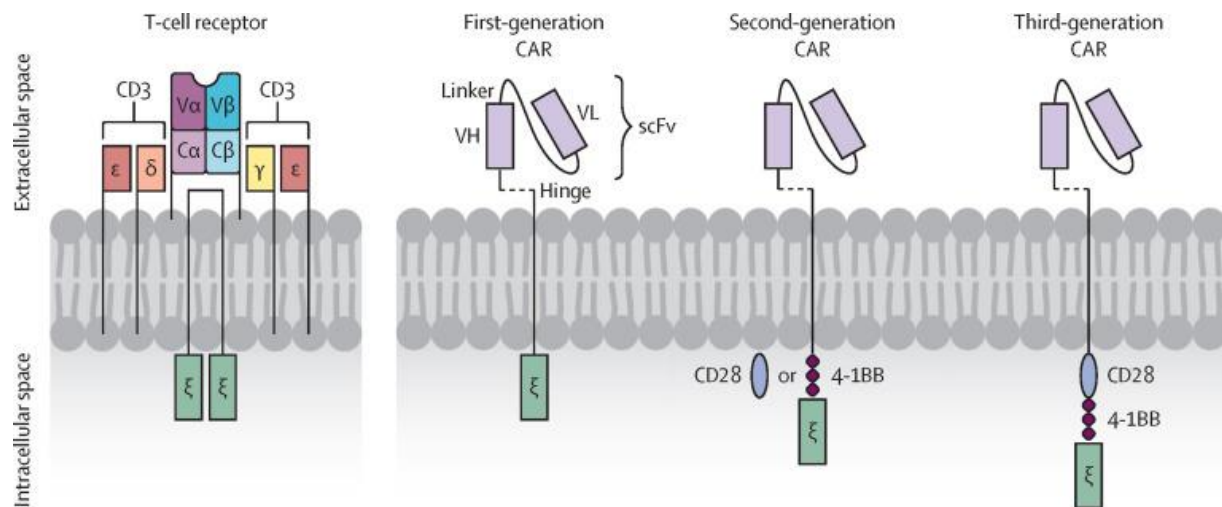


Figure 1.4. The structure comparison of natural TCR (left) and CAR from the first to the third generation (adapted from Singh *et al.*³²).

To date, six CAR-T products have been approved by FDA (four against CD19⁺ B cell malignancies and two for BCMA⁺ multiple myeloma) based on clinical reports with respect to safety and efficacy^{33–39}. Recently, the team of Carl June published the decade-long followed up study on CD19 CAR-treated B cell leukemia patients. They observed a group of CD4⁺ CAR-T cells showing high activity and duration after infusion for over 10 years⁴⁰. Despite the feasibility of cell transfer therapy in hematological malignancies, the solid tumor remains a “forbidden zone” for CAR-T application and the reasons for it largely overlap with the resistance mechanism underscoring ICB^{41,42}.

1.1.3 Regulation of natural and drug-induced anti-tumor immunity

The immune-suppressive microenvironment is established through immunoediting. Immunotherapy which aims to refine the dysfunctional anti-tumor immunity is considered the third revolutionary cancer treatment strategy after chemotherapy and targeted therapy. While immunotherapeutic agents are used broadly in clinic (as discussed in section 1.1.2), Yet, the vast majority (approximately 80%) of patients across many prevalent cancer types are nonresponsive towards immunotherapies⁴³. Introduction of tumor antigenicity-based biomarkers such as MSI-H and dMMR may increase the objective response rate (ORR) up to 40% but still not satisfactory enough^{44,45}, let alone the dilemma how to intervene the cases with low antigenicity or low immune

infiltration (cold tumor). In the past years, mounting evidence has attribute key factors such as tumor antigenicity, immune infiltration, immunometabolism and innate immunity that affects tumor immune response fundamentally. In this section, I will introduce the regulation of anti-tumor immunity by these factors, and how pharmacological interference of these resistance may help optimize the therapeutic outcome. Apart from so, it is hard to ignore the fundamental breakthroughs in some arising perspectives such as gut microbiota^{46,47}, ferroptotic cell death⁴⁸, B lymphocytes function^{49,50} regarding their impact on anti-tumor immunity. They are not included here since the lack of clinical manifestation.

Tumor antigenicity. Tumors express neoantigens that can trigger adaptive immunity to eradicate them. Inadequate antigen presentation by cancer cells accounts for tumor immune suppression and unsatisfactory ICB response⁵¹. Pharmaceutically enhancing TAA presentation by inducing immunogenic cell death or administrating neoantigens-derived peptide vaccine synergizes with checkpoint blockade⁵²⁻⁵⁴. The MHC-I-mediated antigen presentation (exist on all nucleated cells) is achieved by the molecular machinery demonstrated in Fig 1.5, and many of the components involved control anti-tumor immune reaction. For example, high expression of proteasome subunit beta type-8 (PSMB8) and PSMB9, two major components of the immunoproteasome but not regular proteasome, is predictive of more beneficial clinical outcome of ICB to melanoma patients⁵⁵. As shown by Venida *et al.*, the inhibition of autophagy-triggered MHC-I degradation rescued immunogenicity of pancreatic ductal adenocarcinoma (PDAC) which is resistant to ICB⁵⁶. Downregulation of peptide transporter TAP1/2 accounts for the immune evasion of cancer cells by restraining the antigen processing^{57,58}. Similarly, genetic loss of β -2-microglobulin (B2M), a key component of MHC-I complex, is frequently found in non-responders among ICB-treated cancer patients⁵⁹. Indeed, many antigen presentation factors belong to interferon (IFN)-stimulated genes (ISGs) which are transcriptionally activated by IFN γ signaling cascade. IFN γ is produced by many immune cell types and elicit pleiotropic functions by binding to IFN- γ receptor (IFNGR) which is expressed on all nucleated cells^{60,61}. Genetic profile of IFN γ pathway was associated with clinical response of ICB⁶²⁻⁶⁶. Many IFN γ pathway regulators genes were then experimentally proved to be regulators of immunotherapy as well. Patel *et al.* found that the G protein coupled receptor (GPCR) APLNR was required for JAK/STAT-dependent expression of B2M⁶⁷. Protein tyrosine phosphatase non-receptor type 2 (PTPN2) mitigates the IFN γ effect by dephosphorylating many signaling components. Loss of tumor intrinsic PTPN2

potentiates ICB on melanoma and colorectal cancer models by upregulating antigen presentation^{68,69}. The process of antigen presentation is also regulated epigenetically. Activation of histone acetyltransferases p300/CBP together with NF- κ B epigenetically induce the many antigen presentation genes (*e.g.*, *Ifngr2*, *Psmb9*, *etc.*) and potentiate cancer chemoimmunotherapy⁷⁰. Function loss of a histone H3K4 methyltransferase KMT2D enhances the susceptibility of tumor to ICB through inducing chromatin remodeling and antigen presentation⁷¹. Ablation of polycomb repressive complex 2 (PRC2) amplified the IFN γ -mediated MHC-I expression and cancer immunogenicity⁷². Pharmacological antagonism of enhancer of zeste homolog 2 (EZH2), another key factor in PRC2, upregulates the antigen presentation by MHC-I and circumvents the failure of PD-1 blockade in head and neck cancer⁷³. Plus, non-coding RNA transcript can also affect anti-tumor immunity by regulating MHC-I expression⁷⁴. DNA damage response (DDR) defects promote genome instability and tumor antigenicity. A considerable number of ongoing clinical trials involve the combination of ICB and antagonism of DDR-related genes such as poly (ADP-ribose) polymerase (PARP), ataxia-telangiectasia mutated (ATM), ataxia-telangiectasia mutated and Rad3-related (ATR) kinases (comprehensively reviewed by Chabanon *et al.*⁷⁵). Breast cancer-associated gene (BRCA)1/2 mutant tumors were found to be more prone to immunotherapy as well^{75,76}. Besides, alterations occur on mRNA level such as dysregulated RNA editing and splicing also make profound contributions to tumor immunogenicity^{77–79}. Oncolytic virus represents an innovative type of cancer therapy regimen which works in part by enforcing TAA release through lytic cell death⁸⁰. The high prevalence of human endogenous retroviruses (hERVs) signatures represents another source of tumor antigen signal and may predict ICB response especially in kidney carcinoma⁸¹. Despite the predominant research interest focused on MHC-I-mediated antigen presentation which triggers CD8⁺ T cell response, it has been realized that MHC-II loaded neoantigen is also dispensable for effective anti-tumor immunity⁸². As the importance of cytotoxic CD4⁺ T cell has been increasingly recognized (reviewed elsewhere⁸³), the regulation of tumoral antigens presentation by MHC-II molecule need to be profoundly interrogated.

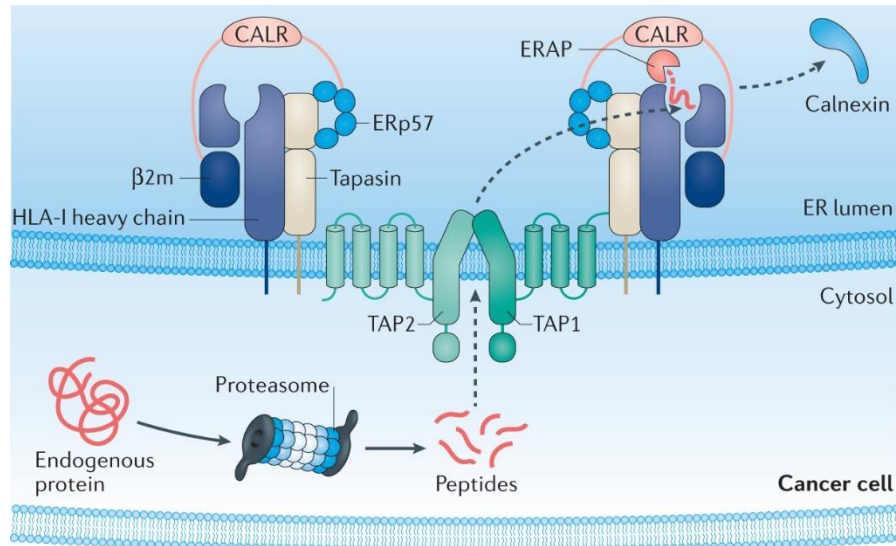


Figure 1.5. MHC Class I-dependent tumor antigen presentation machinery (adapted from Jhunjhunwala *et al.*⁸⁴).

Immune infiltration. The recruitment of anti-tumor immune cells into the TME is another determinant of immune attack to malignancies. The infiltration of immune cells is largely dictated by the binding of chemokines and their corresponding receptors^{85,86}. Migration of cytotoxic CD8⁺ T cells (CTLs) towards TME follows the gradient of TH1-type chemokines such as CXC-chemokine ligand 9 (CXCL9) and CXCL10⁸⁵. Epigenetic silencing of TH1-type chemokines prohibited the CTL signature in TME, which could be reversed by EZH2 or DNA methyltransferase 1 (DNMT1) inhibition^{87,88}. CXC-chemokine receptor 3 (CXCR3), the receptor of CXCL9/10, facilitates intravascular adhesion and extravasation of CTLs in tumor. Instead, CXCR3^{-/-} CTLs were not equally enriched intratumorally⁸⁹. The significance of CXCR3 was also proved by a study showing PD-1 blockade failed to restrict the growth of xenograft tumor on CXCR3^{-/-} mice⁹⁰. House *et al.* showed that the efficacy of anti-PD-1+anti-CTLA-4 on both murine models and patients was dependent on macrophage-derived CXCL9/10. Blockade of CXCR3 inhibited the migration and activity of tumor-reactive CD8⁺ T cells⁹¹. Inhibition of dipeptidylpeptidase 4 (DPP4), an enzyme that degrades CXCL10, enhanced immunotherapy by refining immune infiltration⁹². By examining the solid tumor tissue and The Cancer Genome Atlas (TCGA) database, Dangaj *et al.* reported that co-expression of CCL5 and CXCL9 dictates immunoreactive tumors that are highly infiltrated⁹³. Chemokine receptors are GPCRs which are functionally inhibited by regulator of G protein signaling (RGS) family proteins⁹⁴. Huang *et al.*

performed a proof-of-concept study showing that targeting RGS1 augmented chemokine receptor signaling, giving rise to another therapeutic strategy to optimize the CTL infiltration in TME⁹⁵. Immune-suppressive myeloid cells such as myeloid-derived suppressive cells (MDSCs) and tumor-associated macrophages (TAMs) can be recruited by CCR2/CCL2 axis in TME⁹⁶. Flores-Toro *et al.* showed that administration of CCR2 antagonist sensitizes the glioblastoma response to PD-1 blockade by excluding the tumor-infiltrating MDSCs⁹⁷. A recent work showed that CCL2, which can be degraded by DPP4, can be protected by glutaminy-peptide cyclotransferase-like (QPCTL)-mediated N-terminus modification. Plus, treatment of QPCTL inhibitor reduced the frequency of TAMs and augmented natural and ICB-induced anti-tumor immunity⁹⁸. Chemoattraction of MDSCs is also mediated by CXCR2-CXCLs (CXCL1-3 and CXCL5-8). Co-blockade of CXCR2 synergize with anti-PD-1 therapy in sarcoma model⁹⁹. CCR4-CCL17/22 axis promotes the tumoral infiltration of regulatory T (T_{reg}) cells. Antibody-mediated blockade of CCR4 led to reduced frequency of T_{reg} and resulted in increased antitumor activity¹⁰⁰. It is crucial but usually overlooked that aberrant and dysfunctional vessel organization becomes a physical barrier prohibiting immune cell infiltration into tumor stroma. While high dose antiangiogenic agents such as antibodies against Vascular endothelial growth factor (VEGF) or Angiopoietin-2 (ANGPT2) have been utilized for cancer treatment for years, many studies have shown that relatively low dose treatment normalizes the tumor vasculature, facilitates extravasation of effector cells and reverses the suppressive tumor immune microenvironment (TIME)^{26,101–104}. The increment of effector cells in TME was observed in those studies as the favorable outcome of blood vessel reconstruction. Besides, other mechanisms such as Notch or CD93 signaling control tumor vesicular architecture and determine the CTL infiltration in tumors^{105,106}. High endothelial venules (HEVs), which are known as specialized post-capillary venules immune cells use for homing into lymph nodes. Intriguingly, a subset of blood vessels in human primary cancer tissues were found to display HEV-like features and their density correlate with favorable cancer prognosis¹⁰⁷. A recent work by the same team demonstrated that these tumor-associated HEVs (TA-HEVs) are the main location where CTL entered TME during PD-1/CTLA-4 co-treatment, and the abundance of TA-HEVs predicted the therapeutic outcome in melanoma patients¹⁰⁸. Breaking down of collagen fiber alignment in tumor extracellular matrix (ECM) makes another direction to restore immune infiltration and it has been proved in some studies^{109,110}.

Immunometabolism. Reprogrammed metabolic network is one of the hallmarks in TIME. Here we focus on the how the abnormal metabolism of glucose, amino acids and lipid, three main types of nutrients, determines immune cells function in TIME. Increased glucose consumption and aerobic glycolysis lead to lactate accumulation in TME¹¹¹. Tumor-derived lactate hinders anti-tumor through a plethora of distinct mechanisms involving CTLs^{112,113}, natural killer (NK) cells¹¹³, T_{reg} cells^{114,115}, *etc.* Genetically or pharmacologically abolishing tumor lactate production rebuilt the metabolic homeostasis of anti-tumor immune cells and synergizes with ICB or cytokine therapy *in vivo*^{116–120}. Gu *et al.* showed that NF-κB-inducing kinase (NIK) maintained T cell glycolysis and anti-tumor potential by preventing the autophagic degradation of hexokinase 2 (HK2)¹²¹. Dysfunctional mitochondria were abundantly observed in CD8⁺ TILs. Administration of nicotinamide riboside enhanced T cell mitochondrial fitness and synergized with anti-PD-1 treatment as reported in Yu *et al.*¹²². Some specific amino acids play considerable roles in tumoral immune metabolic milieu. Tryptophan, once converted into kynurenine by indoleamine 2, 3-dioxygenase (IDO), elicit pleiotropic immune-suppressive effects through many effector and suppressive cell types such as CTLs, T_{reg}, TAMs¹²³. Accordingly, a handful number of IDO inhibitors are being tested as immune booster in patients suffering from different cancers¹²⁴. Additionally, Leone *et al.* found that glutamine (Glu, Q) antagonism not only blocks the oxidative phosphorylation (OXPHOS) in tumor cells but promoted the T cells metabolic reprogramming¹²⁵. Tumor cells can also outcompete T cells for methionine to impair T cell function¹²⁶. Ye *et al.* reported the augmentation of CD8⁺ T cell proline metabolism by proline dehydrogenase (PRODH2) strengthened CAR-T therapy *in vivo*¹²⁷. Lipid metabolism has divergent effects on various immune cells. Genetic perturbation of sterol regulatory-element binding proteins (SREBP)-mediated lipid metabolism in T_{reg} cells reduced the immunosuppression effect and unleashed the anti-tumor immune response¹²⁸. Improving fatty acid (FA) metabolism of CTLs reinvigorated their potential in tumor rejection^{129,130}. Hampering cholesterol esterification in T cells by genetic depletion or pharmacological blockade of acetyl-CoA acetyltransferase 1 (ACAT1) largely potentiates their tumor-killing capacity¹³¹. A later work by Ma *et al.* reported that cholesterol depletion reverses the exhaustion phenotype on CD8⁺ T cells by ameliorating ER stress¹³².

Innate immune signaling. Of note, the innate immune system is essential to maintenance the adaptive immune function in the whole cancer-immunity cycle. Rameshbabu *et al.* summarized the landscape of current clinical trials involving innate immune stimulators for cancer treatment¹³³.

Upon microbe invasion, the type I IFN (IFN- α and IFN- β) response is rapidly induced through many innate immune components including nucleic acid sensing and pattern recognition receptors (PRRs) pathways (Fig 1.6)¹³⁴. Cyclic GMP-AMP synthase (cGAS)-Stimulator of interferon genes (STING) pathway induces strong type I IFN response upon the detection of virus-derived double strand DNA (dsDNA) species¹³⁵. cGAS-STING response is continuously triggered by dsDNA derived from dead cells in TME. Mice genetically lacking cGAS or STING showed increased susceptibility to tumor development along with the impaired response to immune checkpoint therapy^{136,137}. Several studies showed that systematic activation of STING by neocleotide/nonnucleotide agonists elicit robust *in vivo* anti-tumor immune response^{136,138–142}. Retinoic acid-inducible gene I (RIG-I)-like receptors (RLRs)-mitochondrial antiviral-signaling protein (MAVS) pathway is responsible for detecting dsRNA virus infection¹⁴³. Co-activation of RLR-MAVS pathway by synthetic RNA mimic 3pRNA sensitizes tumors to ICB and ACT by triggering anti-viral IFN cascade^{144,145}. Other strategies such as targeting RNA splicing machinery or epigenetic regulators can cause cytosolic dsRNA accumulation which consequently activated anti-viral immune signaling^{78,146,147}. Toll-like receptors (TLRs) are a class of PRRs that recognize a variety of microbe-derived pathogen-associated molecular patterns (PAMPs) and turn on the expression of pro-inflammatory cytokines¹⁴⁸. It has become an attractive method to restore the compromised anti-tumor immunity by co-stimulating TLR pathways. TLR4 agonism by monophosphoryl lipid A (MPLA), an LPS derivative, repolarizes tumor-associated macrophages to be tumoricidal in metastatic cancer models¹⁴⁹. TLR9 detects the unmethylated CpG-rich dsDNA derived from bacteria and viruses. Intratumorally delivery of TLR9 agonist reversed the resistance to immunotherapeutic agents^{65,150,151}. Activation of endosomal ssRNA detector TLR7/8 by R848 reduced tumor burden and altered immune microenvironment¹⁵². In principle, many chemotherapies and radiotherapies, which are routinely applied in combination with ICB, were found to sensitize anti-tumor immunity through promoting the innate immune response^{75,153,154}.

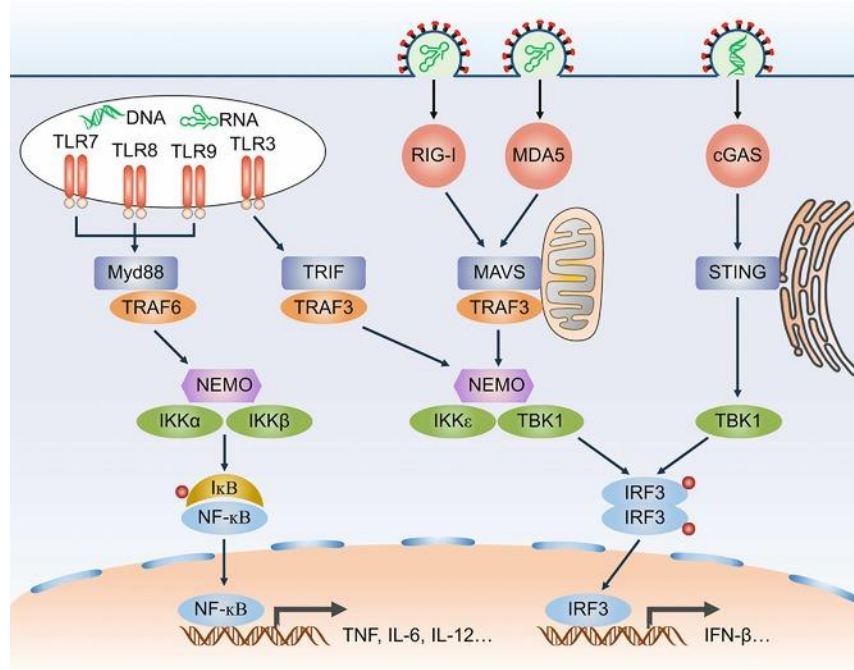


Figure 1.6. Innate immune signaling for DNA and RNA virus detection (adapted from Zhou *et al.*¹⁵⁵).

Gasdermin-mediated pyroptosis provides a defensive mechanism for the host to combat pathogen infection. Upon the cleavage by caspase family proteases or bacterial effector proteins, the N-terminus domain of gasdermins will be released, oligomerize and form pore structures on cell membrane to induce lytic cell death^{156–158}. The release of pro-inflammatory factors will then trigger the systematic innate immune response against infection. Zhang *et al.* demonstrated that granzyme B produced by effector T cells can directly cleave GSDME to allow the pore formation on tumor cells, which makes a significant contribution to T cell-mediated cell death. Liu *et al.* also noticed that GSDME on tumor cells is required for effective CAR-T cell therapy¹⁵⁹. Likewise, granzyme A-triggered GSDMB cleavage contributes to target cell death by cytotoxic T cells¹⁶⁰. Wang *et al.* developed a biorthogonal system and unveiled that induction of GSDME cleavage improved the responsiveness of anti-PD-1 treatment on syngeneic breast cancer model which usually responds poorly to immunotherapeutic agents. The anti-tumor activity of some chemo- and targeted therapies were achieved in part by the initiation of pyroptotic cell death^{161,162}.

1.2 4-1BB, a potent accelerator of anti-tumor immunity

1.2.1 Molecular foundation of 4-1BB as a stimulatory immune signaling receptor

4-1BB (also termed CD137, TNFRSF9 or ILA) is a transmembrane glycoprotein belonging to the tumor necrosis factor receptor superfamily (TNFRSF). 4-1BB was first identified as a potent co-stimulatory receptor on activated T lymphocytes¹⁶³. Later, more studies unveiled that the inducible expression of 4-1BB is also present on other immune cells including monocytes¹⁶⁴, DCs¹⁶⁵, B cells¹⁶⁴, and NK cells¹⁶⁶, *etc.* The expression of 4-1BB could also be detected on adipocytes¹⁶⁷, vascular endothelial cells¹⁶⁸, skeleton muscle cells¹⁶⁹ and malignant cells¹⁷⁰.

While undetectable in resting condition, 4-1BB can be rapidly induced on T cells as well as other types of immune cell following activation. Laderach *et al.* noticed that the expression of 4-1BB on antigen-specific CD8⁺ T cells increased after *in vitro* stimulation by anti-CD3 but decreased rapidly after reaching peak level¹⁷¹. Another study by Kim *et al.* also showed a quick decrease of 4-1BB after the transient expression following T cell stimulation¹⁷², and more importantly, identified that the transcriptional activation of 4-1BB was achieved by nuclear factor κ B (NF- κ B) and activating protein-1 (AP-1) upon TCR stimulation¹⁷². The transcription of TNFRSF9 is also affected by the DNA methylation status of the promoter region¹⁷³.

4-1BB ligand (4-1BBL, TNFSF9) has been identified as the functional ligand expressed on professional APCs^{174,175}. 4-1BBL forms three-bladed propeller-shaped homotrimer through intermolecular hydrophobic interface and recruit three 4-1BB monomers¹⁷⁶. The complex of 4-1BB-4-1BBL showed structural similarity with other TNFRSFs^{177,178}. Upon the engagement with trimerized 4-1BBL, the cross-linked monomeric 4-1BB recruits trimerized TNFR-Associated-Factor (TRAF) adaptor protein to its TRAF binding motif located at cytosolic tail ₂₃₄TTQEE₂₃₈ and ₂₄₆PEEEEE₂₅₀ (Fig 1.7A)^{179,180}. Madireddi *et al.* reported that Galectin 9 stabilizes the 4-1BB aggregates on cell membrane and facilitates 4-1BB signal amplification¹⁸¹. It has been reported that TRAF trimer can be assembled by homotrimerized TRAF1/2 or TRAF1:(TRAF2)₂ heterotrimer. Afterwards, each one of the TRAF2 molecule within the trimer can use its C-end zinc-RING finger domain to dimerize with a TRAF2 within the adjacent TRAF trimer, resulting in the growth of hexagonal signal network (Fig 1.7B). Right after ligand-mediated crosslinking, the signature K63 polyubiquitination signal can be observed on TRAF2 in 4-1BB signalosome. It is possible but not completely sure that TRAF2 is ubiquitinated by cIAP1/2 which are physically

interact with TRAF2¹⁸². Subsequently, the downstream effectors including transforming growth factor beta-activated kinase (TAK)-1 and TAK binding proteins (TAB)-1, 2 and 3 will be recruited to K63 polyubiquitin chain on TRAFs. TAK1 will transduce signals to turn on the pathways such as canonical and non-canonical NF- κ B pathways¹⁸³, p38 mitogen-activated protein kinase (MAPK) pathway¹⁸⁴ and ERK pathway¹⁸⁵. Conversely, deubiquitinating enzymes A20 and CYLD are also remove the K63-linked ubiquitination, therefore shutting down the 4-1BB signal transduction¹⁸⁶. 4-1BB can also be crosslinked and activated by monoclonal antibodies (mAb). Forero *et al.* observed that upon the ligation with some antibodies, 4-1BB can be internalized and initiate the TRAFs-dependent signaling from endosomal vesical¹⁸⁷. Still, there lacks molecular investigation discussing whether the internalization of 4-1BB is universal or limited to certain antibodies or ligands. It should be noted that disulfide bond-mediated dimerization of 4-1BB has also been observed and proposed as a signal amplifier¹⁸⁸. Li *et al.* comprehensively evaluated the pattern of 4-1BB/4-1BBL binding and realized that one trimerized 4-1BBL can interact with two dimerized 4-1BB and exclude the binding of another 4-1BB molecule (monomer or dimer), which was proposed as a mechanism prohibiting the uncontrolled aggregation and activation of 4-1BB (termed “limited-crosslinking”)¹⁸⁹.

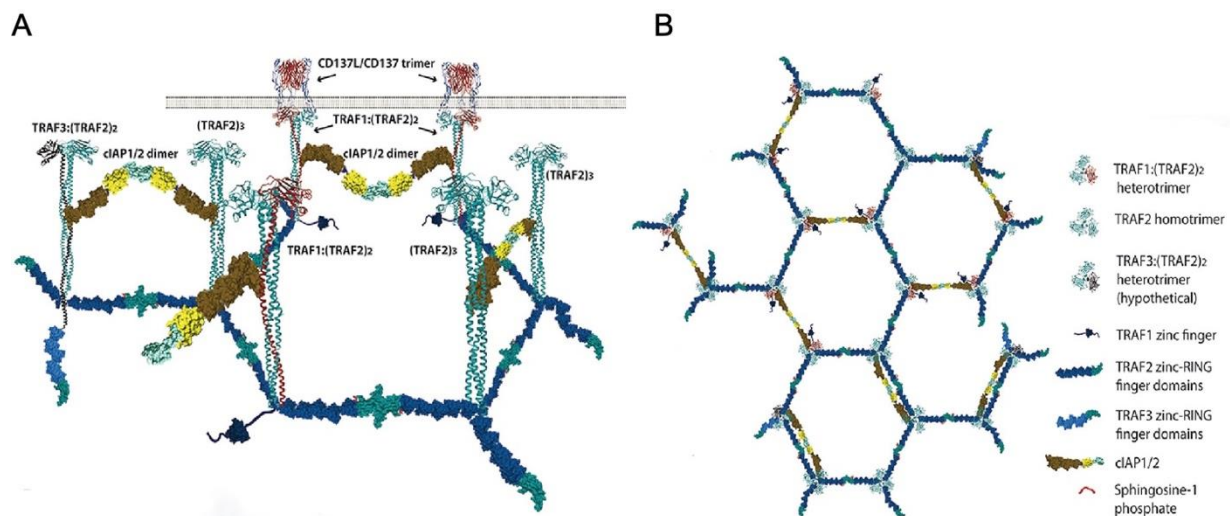


Figure 1.7. The molecular insights into the 4-1BB signalosome assembly. (A) the side view of 4-1BB downstream signal components in the presence of 4-1BBL engagement. (B) The top view of 4-1BB signal network after 4-1BBL-mediated clustering (modified from Zapata *et al.* ¹⁹⁰).

The activation of 4-1BB lead to a variety of molecular events that are all supportive to T cell survival and functions. Signaling through 4-1BB drives the production of Th1-type (interleukin (IL)-2, IFN γ ^{191–194}), Th2-type (IL-6, IL-13^{195,196}) cytokines or tumor necrosis factor (TNF)^{197,198}, *etc.*, on various cell types. 4-1BB co-stimulation fuels the survival of CD8⁺ T lymphocytes by inducing antiapoptotic genes like Bcl-X_L and Bfl-1¹⁹⁹ and prevent the activation-induced cell death (AICD)^{200,201}. Cross-linking of 4-1BB also induce the expression of Cyclin D2 and E to permit the G1 phase entry and G1/S transition²⁰². Lee *et al.* showed 4-1BB activation potentiate the proliferation of CD8⁺ T cells by activating the TCF1/ β -catenin axis via the PI3K/AKT/ERK pathway²⁰³. 4-1BB signal potentiates CD8⁺ T cell proliferation through reprogramming glucose and FA metabolism as well²⁰⁴. It has also been observed that antibody-mediated stimulation of 4-1BB led to mitochondria enlargement and function enhancement^{205,206}. A recent work showed superior T cell activation by *in cis* over *trans* 4-1BB co-stimulation²⁰⁷. More intriguingly, the *in cis* 4-1BB co-signaling resulted in critically significantly altered profile of gene expression especially in cell cycle control and DNA damage repair compared to *in trans*, leading to the assumption that 4-1BB works better in the context of TCR-centralized immune synapse²⁰⁷.

Through alternative mRNA splicing or shedding from membrane, soluble form 4-1BB can be generated and detected in circulate^{208–210}. Significant elevation of serum s4-1BB level was detected in rheumatoid arthritis patients in comparison to healthy donors^{211,212}. Later studies observed the abnormality of s4-BB in patients with leukemia²¹³ or immune disorders including multiple sclerosis²¹⁴, type I diabetes²¹⁵, hepatitis C virus-induced liver cirrhosis²¹⁶, *etc.* s4-1BB is also involved in cancer immunotherapy. Glez-Vaz *et al.* showed increase of blood s4-1BB level upon 4-1BB co-stimulation in mice and human system²¹⁷. Zhang *et al.* showed that high s4-1BB level in serum as a biomarker is correlated with prolonged survival in advanced hepatocellular carcinoma²¹⁸. Trimerized s4-1BB can also outcompete membrane-bound form to elicit stronger 4-1BBL reverse signaling and led to systematic lupus in mice²¹⁹.

1.2.2 The biological significance of 4-1BB in cancers and non-cancer diseases

The physiological essentiality of 4-1BB as an immune stimulator has been well documented since the discovery of it. Kwon *et al.* first generated a mouse model with systematic deletion of 4-1BB. Although the displayed normal development and hormonal immunity appeared to be normal, the T cell immunity was significantly diminished in 4-1BB^{−/−} mice²²⁰. In addition to the

anti-tumor activity of 4-1BB mAb *in vivo*^{221,222}, the tumor-suppressive role of 4-1BB was proved by Ju *et al.* showing that 4-1BB^{+/+} mice survive longer against xenografted melanoma versus the 4-1BB^{-/-} littermate²²³. Clinically, several loss-of-function mutations of 4-1BB have been reported to be correlated with defected T cell and B cell immunity and enhance the susceptibility to Epstein-Barr virus (EBV)-associated lymphoma^{224,225}. Several studies showed that 4-1BB expression defines the tumor infiltrated and antigen reactive CTLs^{226–228}. Single-cell transcriptomic analysis of tumor-infiltrating T cells characterized a group of *TNFRSF9*^{high} activated T_{reg} cells whose frequency is correlated with poorer survival of non-small-cell lung cancer (NSCLC) patients²²⁹. This cell signature was also observed by Freeman *et al.* who showed superior 4-1BB expression in intratumoral over peripheral T_{reg} cells on multiple mouse syngeneic models²³⁰. Depletion of 4-1BB-expressing T_{reg} cells by the IgG2a rather than IgG1 isotype 4-1BB antibody exhibited strong CTL-mediated tumor rejection^{230,231}. 4-1BB also plays key roles protecting hosts against bacterial, fungal and viral infections^{232–236}. Repeated activation of 4-1BB signal by agonistic antibodies resulted in granuloma development in TDLNs of mice owing to the macrophages recruitment²³⁷. The unexpected activation of 4-1BB signaling on was found to accelerate pathogenesis or induce severe adverse effects upon the systematic administration of therapeutic antibodies. Dubrot *et al.* reported the increased CD8⁺ T cell accumulation in liver which was associated with elevated transaminase²³⁸. As indicated by the study of Bartkowiak *et al.*, the activation of liver-resident myeloid cells via 4-1BB pathway triggers the production of IL-27, which is associated with liver-infiltrating CD8⁺ T cell activity and causes severe hepatitis²³⁹. Jiang and colleagues also found that 4-1BB can promote the differentiation and tumoral infiltration of monocytes/macrophages by upregulating *Fra1* and facilitates the bone metastasis of breast cancer²⁴⁰. 4-1BB⁺ B cells secrete pro-inflammatory cytokines such as TNF α and IL-6 upon engagement with 4-1BBL-expressing cells and led to multiple sclerosis¹⁹⁶. The upregulation of 4-1BB can also be found on adipocytes upon obesity-related factors and results in adipose inflammation¹⁶⁷. Conversely, deficiency of 4-1BB protects mice against obesity-induced inflammation²⁴¹. 4-1BB is involved in cardiovascular diseases as well. According to a study by Olofsson *et al.*, the expression of 4-1BB on vascular endothelial cells contributes to the development of atherosclerosis¹⁶⁸. In summary, the biological behaviors and functions of 4-1BB are rather complicated and likely to be tissue- and cell lineage-dependent, and the profound understanding of their differentiated regulation would help resolve the dilemma of how to precisely target 4-1BB on tumor-reactive T cells.

1.2.3 4-1BB in clinical cancer immunotherapy

The potent T cell stimulation effect of 4-1BB made it a promising choice for cancer immunotherapy. The anti-tumor potential of 4-1BB has been appreciated since 1997 when Melero *et al.* reported the first proof-of-concept study showing that activation of 4-1BB by mAbs (1D8) led to profound tumor suppression for both high- and low-immunogenic mouse tumor models, and both CD4⁺ and CD8⁺ T cells were required for the anti-tumor activity²²¹. After that, accumulating preclinical results support the anti-tumor potential of 4-1BB agonism for diverse types of cancers. 4-1BB activation could also synergize with PD-1/PD-L1 blockade antibody on tumor models that are poorly responsive towards PD-1/PD-L1 monotherapy^{206,242–244}.

The first open-label clinical trial of 4-1BB was launched in 2005 evaluating Urelumab (BMS-663513, fully human IgG4 mAb) for treating advanced solid tumors (NCT00309023). Despite the encouraging signs of single agent efficacy including three cases of partial response and four cases of stable disease, the study was stalled due to the life-threatening hepatotoxicity (maximum tolerable dose is as low as 0.1 mg/kg per 3 weeks²⁴⁵). Utomilumab (PF-05082566, humanized IgG1 mAb) is another 4-1BB agonistic antibody that is under clinical investigations. Unlike Urelumab which binds to the CRD1 region of 4-1BB, Utomilumab binds to CDR3 and partially competes against 4-1BBL²⁴⁶. While Utomilumab is better tolerated compared to Urelumab, it showed moderate clinical effect as a monotherapy (ORR 3.8% for solid tumor and 13.3% for Merkel cell carcinoma²⁴⁷), presumably due to its relatively lower 4-1BB activation magnitude²⁴⁶. The active and completed clinical trials (registered on ClinicalTrials.gov) using Urelumab or Utomilumab in combination with other targets were summarized in Table 1.1 and 1.2.

Table 1.1. The summary of clinical trials involving Urelumab in combination with other regimens.

NCT #	Drugs	Conditions	Phase
NCT01775631	Urelumab + Rituximab	B-cell non-Hodgkin lymphoma	I
NCT03792724	Urelumab + Nivolumab	Solid tumors	I/II
NCT02110082	Urelumab + Cetuximab	Colorectal cancer/Head and neck cancer	I
NCT02845323	Urelumab + Nivolumab	Urothelial cancer/Bladder cancer	II
NCT02253992	Urelumab + Nivolumab	Solid Tumors / B-cell non-Hodgkin lymphoma	I/II
NCT02252263	Urelumab + Elotuzumab	Multiple myeloma	I
NCT02534506	Urelumab + Nivolumab	Solid tumors	I
NCT03431948	Urelumab + Radiation therapy	Solid tumors	I
NCT02451982	Cyclophosphamide + GVAX + Urelumab + Nivolumab	Pancreatic cancer	II

Table 1.2. The summary of clinical trials involving Utomilumab in combination with other regimens.

NCT #	Drugs	Conditions	Phase
NCT03258008	Utomilumab + ISA101b	Oropharyngeal cancer	II
NCT03318900	T-cell infusion + Aldesleukin + Utomilumab	Ovarian cancer	II
NCT03704298	Axicabtagene Ciloleucel + Utomilumab	Large B-cell lymphoma	I
NCT03440567	Avelumab + Utomilumab + Rituximab + Ifosfamide + Carboplatin + Etoposide	Large B-cell lymphoma / Mantle cell lymphoma	I
NCT03414658	Trastuzumab + Vinorelbine + Avelumab + Utomilumab	HER2 ⁺ breast cancer	I
NCT03364348	Ado-trastuzumab Emtansine + Utomilumab	HER2 ⁺ breast cancer	I
NCT03290937	Irinotecan + Cetuximab + Utomilumab	Colorectal cancer	I
NCT03217747	PF-04518600 + Utomilumab + avelumab	Colorectal cancer	I/II
NCT02554812	Utomilumab + Avelumab	Solid tumors	II
NCT03971409	Utomilumab + Avelumab	Triple-negative breast cancer	II
NCT05059522	Avelumab + CMP 001 + Utomilumab	Solid tumors	III

Other approaches have been designed to utilize 4-1BB for tumor control. For instance, 4-1BB activation enhanced the *ex vivo* expansion and cytotoxicity of patients-derived CD8⁺ TILs which opened a novel avenue to optimize TIL-based adoptive cell transfer (ACT) therapy^{227,248}. A unique perspective of 4-1BB regarding the pharmaceutical value is the incorporation of 4-1BB signal (cytosolic) domain into the chimeric antigen receptor (CAR). The clinically utilized CAR-T regimens against CD19 positive B cell malignancies are based on the “28BBz” design which includes the tandemly fused CD28 costimulatory domain, 4-1BB costimulatory domain and CD3ζ activation domain. Mechanistically, the 4-1BB segment improves the persistence and cytotoxicity of CAR-T cells by driving both canonical and non-canonical NF-κB pathways^{249,250}. Nevertheless, the robust CAR tonic signaling (the signal in the absence of antigen) transduced from 4-1BB domain may result in T cell apoptosis due to enhanced CAR expression out of a positive feedback loop when using gammaretroviral long terminal repeat promoter, which can be addressed by vector optimization²⁵¹. The signaling domain of 4-1BB is also used to engineer other receptors. Oda *et al.* developed an immunomodulatory fusion protein by replacing the intracellular tail of Fas (Tnfrsf6) with 4-1BB costimulatory domain (Fas-4-1BB)²⁵². T cells engineered to express Fas-4-1BB exhibited improved proliferation and cytotoxicity in ACT therapy against leukemia and ovarian cancer^{252,253}.

1.3 Protein ubiquitination

1.3.1 The process and functions of protein ubiquitination

Ubiquitination (equivalent to ubiquitylation) is one of the most frequent and extensively characterized post-translational regulatory mechanism on proteins. Ubiquitin (Ub) is a 76 amino acid post-translational protein modifier originally identified in 1975 and later found to exist universally in eukaryotes and displays high interspecies sequence conservation^{254,255}. As is a prevalent, dynamic, multifunctional posttranslational modifications, protein ubiquitination is involved in virtually all aspects of physiological processes. Eukaryotic protein ubiquitination, by which single or multiple Ub molecules are covalently attached to the target locus on substrates, is accomplished through an ATP-dependent reaction catalyzed by E1 (activation), E2 (conjugation) and E3 (ligation) enzymes sequentially (Fig 1.8)²⁵⁶. Ub is initially activated by E1 enzyme in an ATP-dependent manner and results in the formation of a thioester bond between its active-site

cysteine and the C-terminal glycine residue of ubiquitin. The active ubiquitin is then loaded onto E2 through a transesterification reaction. E3 ligases then engage Ub-loaded E2 and transfer the Ub molecule from E2 to the protein substrate through the formation of an isopeptide bond between the ϵ -amine group of a lysine (Lys, K) residue in the protein substrate and the C-terminal glycine residue of ubiquitin. To date, the most profound collection of Ub enzymes includes 8 E1 ubiquitin activating enzymes, 41 E2 ubiquitin conjugating enzymes, 634 E3 ubiquitin ligases²⁵⁷. Depending on the representative structural character, E3 ligases are categorized in RING (really interesting new gene) type, HECT (homologous to E6AP C terminus) type, and RBR (RING-in-between-RING) type²⁵⁸. Some E3 ligases exist as complexes with different subunits serving substrate recognition, E2 binding, scaffolding functions, individually (such as Cullin-RING complex²⁵⁹). Substrates can be modified by monomeric ubiquitin molecule at one site (monoubiquitination) or multiple sites (multi-monoubiquitination). More frequently seen is the polyubiquitination of substrate proteins out of multiple cycles of E1-E2-E3 reactions. Depending on locus where the intermolecular link between Ub is formed, the poly-Ub chain can be categorized into M1 (conjugated on the α -amino group of the N-terminal methionine), K6, K11, K27, K29, K33, K48 and K63 (conjugated on the ϵ -amino group of one of the seven Lys residues) linkage types. The monoubiquitination or poly-Ub chains can be removed by a group of proteases known as deubiquitinases (DUB). Ubiquitination and deubiquitination systems coordinatively keep protein stability and function under precise regulation.

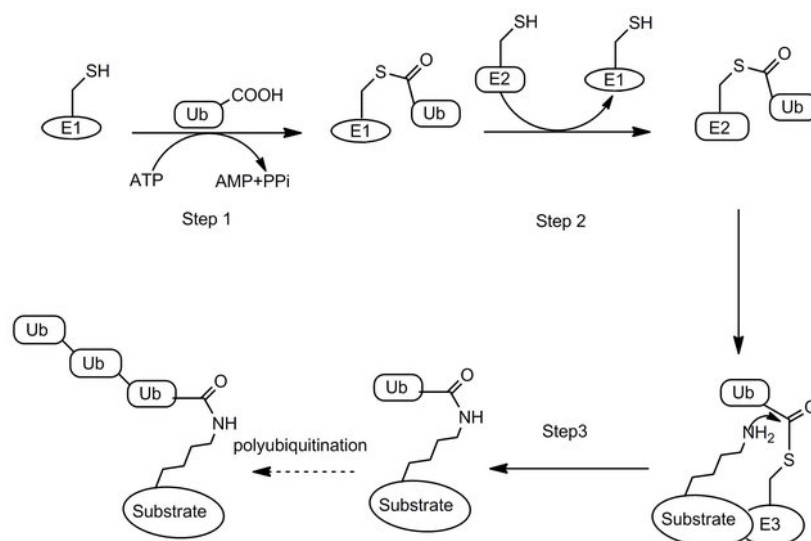


Figure 1.8. The conjugation process of protein ubiquitination (adapted from Jiang *et al.*²⁶⁰).

The term “ubiquitin code” was used to describe the complicated molecular functions of protein ubiquitination²⁶¹. K48-linked polyubiquitination, which is the most frequently occurred linkage-type (> 60%)²⁶², is accepted as a molecular signal to highlight the proteins that need to be eradicated in 26S proteasome. As the second frequent kind of Ub linkage, K63-linked poly-Ub chain accounts for around 30% of human protein ubiquitination. It is generally known that K63-ubiquitination serves critical functions in signal transduction, and one of the best characterized examples is TRAF family adaptor proteins which do not have enzymatic activity and must rely on K63 polyubiquitin chain to recruit the downstream signal mediators²⁶³. studies and their pivotal roles in triggering protein degradation and signal complex assembly, respectively, have been well characterized. The biological functions other ubiquitin linkage types, which have been underappreciated for many years, has been realized as key function mediators in a wide span of molecular events²⁶⁴. The other linkage types are not as abundant and do not seem to have conserved biological functions²⁶⁵. Despite the homogeneous chains which are frequently established, diverse linkage types may occur to the same ubiquitination site, resulting the formation of branched poly-Ub chain (10-20% of all ubiquitination cases as estimated²⁶²). Nowadays, the biological importance of branched Ub chains is being increasingly valued^{266,267}.

1.3.2 Impact of ubiquitination in anti-tumor immunity

Protein ubiquitination plays essential roles in maintaining protein homeostasis. Ubiquitination signaling plays extremely important roles in innate and adaptive immune responses²⁶⁸⁻²⁷⁰. Many studies so far have highlighted the involvement of ubiquitin system especially key E3 enzymes in cancer immunity^{271,272}. Many immune activators and suppressors are known to be regulated by ubiquitination, which underlines the rationale to co-target this process for the refinement of immunotherapy. We have mentioned the dependence of K63-linked ubiquitin of TRAFs for TNFRSF signaling upon receptor clustering^{261,264,273}. In the following paragraph, I will present a few additional examples explaining how protein ubiquitination, specifically E3s and DUBs, affect anti-tumor immunity by modulating key proteins. Notably, many functional screens identified E3 ligases/DUBs as significant mediators of immunotherapy without unveiling the detailed mechanisms. Here I only discuss some candidates which has clear targets identified through biochemical assays.

MHC-I molecule is known to be downregulated by ERAD E3 ligases such as TMEM129 and TRC8^{274,275}. Likewise, MHC-II can be ubiquitinated by membrane-associated RING-CH (MARCH)1/8 which control its surface abundance^{276–278}. MARCH1 also mediates the ubiquitination of CD86 that binds to CD28 to elicit second signal for T cell activation^{279,280}. Berg *et al.* noticed that CD28 also undergoes polyubiquitination and internalization along with CTLA-4 upregulation during T cell anergy²⁸¹. The intracellular abundance of PD-1 and PD-L1, the best-characterized pair of co-inhibitory ligand/receptor, are both dynamically regulated by UPS. Specifically, FBXO38 and KLHL22 were confirmed to target surface (mature) and cytosolic (immature) PD-1 protein, respectively, for proteasomal degradation^{282,283}. The modulation of PD-L1 by ubiquitination is more extensively investigated and a large variety of E3 ligases (*e.g.*, SPOP²⁸⁴, β -TrCP²⁸⁵, FBXO22²⁸⁶, ARIH1²⁸⁷, TRAF6²⁸⁸) and DUBs (*e.g.*, CSN5²⁸⁹, USP22²⁹⁰, USP8²⁸⁸) involved has been reported so far. Genetic or pharmacologic manipulation of them altered anti-tumor response or PD-1/PD-L1 blockade efficacy *in vivo*. Abnormal expression of these E3s/DUBs are associated with heterogeneous clinical outcome in clinical cancer immunotherapy.

As mentioned, IFN γ response determines tumor susceptibility to immune attack. From a genome-wide CRISPR/Cas9 screen, ubiquitin ligase STUD1 was found necessary for anti-PD-1 effect by destabilizing tumor IRNGR1 and JAK1²⁹¹. A recent work characterized that loss-of-function mutation of FBXW7 confers refractoriness to PD-1 blockade in melanoma patient by inactivating RNA sensing and IFN γ signaling despite the lack of detailed mechanism characterization²⁹². Wang *et al.* identified E3 ligase COP1 from *in vivo* genome-wide functional screening as a tumor-intrinsic mediator of immunotherapy resistance in TNBC. Mechanistically, COP1 degrades CCAAT/Enhancer-binding protein beta (C/EBP β) which serves as a transcription factor driving the expression of M2 macrophages recruitment chemokines²⁹³. Stabilization of central T_{reg} differentiation factor FoxP3 by USP7 underscores the immune-suppressive capacity by T_{reg}²⁹⁴.

1.3.3 Protein ubiquitination as a target for cancer immunotherapy

Considering the fundamental impact of protein ubiquitination in anti-tumor immune response, the combination with UPS modulation gave rise to an innovative strategy to optimize the current immunotherapy. Unfortunately, limited number of E3 ligases can be pharmacologically

targeted with small molecule inhibitors to date. I hereby will introduce some works describing how immunotherapy can be improved by UPS intervention.

Targeting IAP family E3 ligases (cIAP1, cIAP2, and X-linked IAP) with small molecule inhibitors as anti-cancer regimen have been well-documented²⁹⁵, and many studies have started to use it for in combinational immunotherapy. Chesi *et al.* reported the clinical efficacy of IAP inhibitor LCL161 against multiple myeloma and the effect was mediated by cancer-autonomous and APC-related immune-stimulatory mechanisms²⁹⁶. Later, Roehle *et al.* demonstrated that treatment of LCL161 induced T cell-dependent, phagocytic macrophages-mediated eradication of MHC-I negative tumors²⁹⁷. IAP antagonism was also found to restore co-stimulatory signaling in T cells²⁹⁸. Another extensively focused E3 ligase is MDM2 which degrades tumor suppressor p53 and is frequently amplified in tumors²⁹⁹. As indicated by Fang *et al.*, APG-115, a MDM2 antagonist/p53 activator, synergize with PD-1 blockade in syngeneic models on *Tp53^{WT}* host³⁰⁰. Accordingly, they designed a clinical trial using APG-115 in combination with anti-PD-1 for solid tumor resistant to immuno-oncologic drugs³⁰¹. A recently published study showed that ARG-115-induced MDM2 accumulation by uncoupling of p53-MDM2 interaction unleashed anti-tumor T cell activity by sustains STAT5 stability, which is independent of p53 status³⁰². Another MDM2 inhibitor AMG-232, which showed the potential to sensitize tumors to immune attack *in vivo*³⁰³, has entered clinical trials for advanced development (NCT03787602).

Selective protein degradation by proteolysis-targeting chimera (PROTAC) provides a novel approach to target “undruggable” proteins by harnessing cell-intrinsic proteolysis machinery³⁰⁴. Wang *et al.* designed a small molecular degrader of PD-L1 which is effective *in vivo*³⁰⁵. Cotton *et al.* reported an antibody-based PROTACs (AbTACs) strategy by which cell surface PD-L1 and membrane-bound E3 ligase RNF43 were crosslinked by a bivalent antibody, thereby induce internalization and lysosomal degradation of PD-L1³⁰⁶.

Ubiquitination also guides the design of CAR for T cell therapy. Li *et al.* noticed that CAR undergoes polyubiquitination and degradation following antigen-mediated CAR-T activation. By deleting all cytoplasmic Lys residues on CAR that can potentially trigger UPS-mediated proteolysis, the CAR^{KR}-T cells elicit increased cytotoxicity and longevity *in vivo* due to the stabilization of CAR³⁰⁷.

1.4 Protein *N*-glycosylation

1.4.1 Overview of *N*-linked glycosylation

Glycosylation is defined as the association of a carbohydrate moiety to predominantly proteins but also lipid or nucleic acid substrates^{308–310}. Protein glycosylation is involved in a broad range of cellular processes including protein folding^{311,312}, transportation³¹³, signal transduction³¹⁴, *etc.* It has been claimed that over 50% of human proteins are modified by glycosylation³¹⁵. Depending on the acceptor atom used for sugar conjugation, the protein glycosylation can be divided into two types: *N*-linked and *O*-linked. For *N*-linked glycosylation, oligosaccharide chains are attached by an amide bond to asparagine (Asn, N) residues located in a consensus sequence asparagine-X-serine/threonine (N-X-S/T, where X can be any amino acid except proline). For *O*-linked glycosylation, sugar molecules are conjugated to the oxygen atom in the active hydroxy group which is often seen in S/T residues. While *N*-glycans are usually large in size and predominantly found on membrane or secretory proteins, *O*-linked glycosylation is more challenging to study since the superior complexity of size, modified sites and underlying functions. In the next sections, I will compactly introduce the biosynthesis and potential immunotherapeutic implications of *N*-glycosylation.

1.4.2 The biosynthesis of *N*-glycoproteins

Protein *N*-glycosylation is an enzyme-mediated, multi-step reaction cascade initiated in endoplasmic reticulum (ER) and completed in Golgi apparatus³¹⁶. This process can be divided into four steps: the assembly of a lipid-lined oligosaccharide (LLO) as the core glycan precursor, the *en bloc* transfer of the *N*-glycan precursors to the target sites by oligosaccharyltransferase (OST) in the luminal side of the ER; the early glycan processing in ER and the advanced glycan modification in Golgi apparatus. The general process and representative enzymes of mammalian protein *N*-glycosylation are summarized in Fig 1.9.

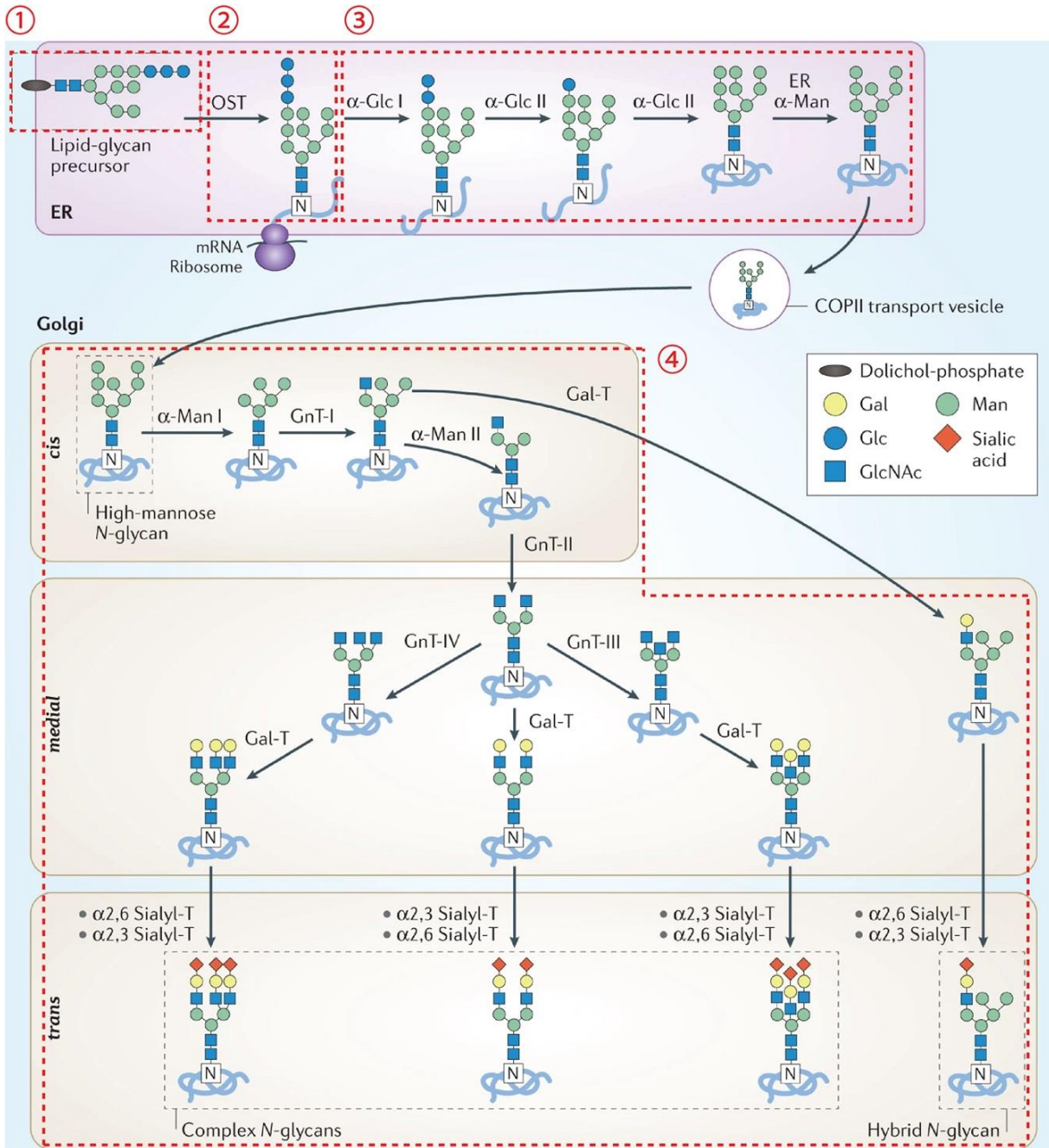


Figure 1.9. A simplified pictorial summary of mammalian protein N-glycosylation process. The figure was adapted from Reily *et al.*³¹⁷. The four steps mentioned above are outlined and marked.

LLO precursor is generated through adding sugar molecules to dolichol phosphate (Dol-P) by a series of glycosyltransferases (encoded by *ALG* family genes)-triggered reactions. The glycan synthesis takes place initially on the cytoplasmic site of ER and is translocated to ER lumen by protein RFT1 homolog (encoded by *RFT1*)-mediated flipping step³¹⁶.

The transfer of 14-sugar (Glc₃Man₉GlcNAc₂) block from LLO precursor to the substrate Asn residues is achieved by OST complex. There are two distinct isoforms of mammalian OST complex containing either STT3A or STT3B catalytic subunit. It was proposed that the STT3A OST isoform is associated with ER membrane-bound ribosomes and co-translationally glycosylates the N-terminus acceptor sites on the nascent polypeptide chains, whereas STT3B isoform can promote post-translationally glycosylation close to C-terminus that are skipped by STT3A-OST³¹⁸. OST scans the nascent polypeptide, recognizes predominantly N-X-S/T sequon but also some rarely occurred non-canonical locus^{319,320}. Structural analysis of OST-substrate complex explained the conformational rigidity of proline makes it unacceptable for on the X position³²¹.

The early modification steps involve the trimming of three glucose (Glc) and one mannose (Man) to yield Man₈GlcNAc₂. This process is achieved by α -glucosidases I/II (α -Glc I/II) and ER α -mannosidase I (ER α -man, MAN1B1) as indicated in Fig 1.9 Still, the incomplete enzyme-mediated saccharide removal may lead to Glc retention when exiting ER. The glycan moieties at this point are termed high mannose type.

The structure formed in ER will be transported through Cop-II coated vesicles to *cis* Golgi where the vast complexity and heterogeneity of glycan structures are created. In *cis* Golgi compartment, α -(1, 2)-mannosidases IA/B (MAN1A1/MAN1B1) acts by trimming four mannose residues from high mannose type glycan to give Man₅GlcNAc₂ which is a key intermediate for further glycan assembly. N-acetylglucosaminyltransferase (GnT-I or MGAT1) will add a GlcNAc residue Man₅GlcNAc and now the glycoproteins can either enter *medial* Golgi directly to become hybrid form or undergo sequential processing by α -mannosidase II and GnT-II to join the pathway of complex glycan establishment. Various architectures of complex glycans are formed in *medial* Golgi via the catalyzation of GnT-III or IV. Additional enzymes including galactosyltransferase, fucosyltransferase and sialyltransferases assist the terminal maturation of carbohydrate chain.

1.4.3 Targeting protein *N*-glycosylation for cancer immunotherapy

Aberrant *N*-glycome has emerged as a novel cancer hallmark as well as a target for cancer treatment^{322,323}. Many key membrane receptors are modified by *N*-glycosylation³²⁴. Sun *et al.* showed that human PD-1 relies on *N*-glycans to maintain its stability and interaction with PD-L1³²⁵. They developed a glycan-targeting antibody STM418 that induced advantageous *in vivo* tumor rejection over nivolumab and pembrolizumab³²⁵. *N*-linked glycans of PD-1 are frequently core fucosylated as identified by mass spectrometry studies^{325,326}. Antagonism of α -(1,6)-fucosyltransferase (FUT8) abolished PD-1 expression and reinforced the anti-tumor immune response^{326,327}. PD-L1 is another immune checkpoint that heavily relies on *N*-glycosylation to elicit its immunological function. Like PD-1, PD-L1 also requires glycosylation for its stabilization and ligand binding^{285,328}. Antibody STM108 that selectively recognizes induces the lysosomal degradation of fully but not partially *N*-glycosylated PD-L1³²⁸. BMS1166, a small molecule inhibitor blocking the PD-1/PD-L1 binding on the cell surface, abrogates the intracellular production of PD-L1 by disrupting the *N*-glycosylation process³²⁹. AMP-activated protein kinase (AMPK)-mediated phosphorylation hampered PD-L1 glycosylation and led to its ER retention and proteasomal degradation³³⁰. It was shown recently that administration of D-mannose induced AMPK-dependent PD-L1 deglycosylation and synergize with radiation therapy on TNBC model *in vivo*³³¹. Shi and colleagues integrated previously published clinical studies, functional screens, and omics databases and identified alpha-mannosidase 2 (MAN2A) as a regulator of T-cell dysfunction by controlling *N*-glycan maturation of PD-L1 in the Golgi apparatus³³². Swainsonine, a potent inhibitor of MAN2A1, synergized with PD-L1 blockade in syngeneic cancer models that responded poorly to monotherapy³³². Glycosylation inhibitors were found to restore anti-tumor immunity by affecting other receptors. Membrane expression and immune-suppressive effect of B7-H3 could be rendered by FUT8 inhibition³³³. Similarly, pharmacological antagonism of *N*-glycosylation with NGI-1 induced B7-H4 proteolysis and synergized with PD-L1 blockade *in vivo*³³⁴. Removal of branched *N*-glycan by MAN1 antagonist kifunensine (Kif) improved the high mannose glycan-dependent immune recognition globally on colorectal cancer cells³³⁵. In another study, Kif treatment was found to inhibit the terminal addition of poly-LacNac by β -(1, 3)-*N*-acetylglucosaminyltransferase (encoded by *B3GNT2*) and restore the T cell-mediated cytotoxicity by stabilizing over 10 pairs of stimulatory ligand-receptor binding³³⁶.

N-glycosylation reprogramming has also been applied to rewire CAR-T therapy. As is known, failure of CAR-T therapy occurs frequently in solid tumors, and one of the underlying mechanisms is PD-1-induced CAR-T-cell exhaustion³³⁷. Shi *et al.* deleted one *N*-glycan on PD-1 on CAR-T cells by introducing a point mutation on the N74 codon using a base-editing strategy, thereby dampening the surface PD-1 expression and enhancing CAR-T-cell proliferation and cytokine production. Xenograft models subjected to PD-L1 N74-edited CAR-T cells had delayed tumor development and improved overall survival³³⁸. The aberrant glycosylation presented on tumor surface also confers CAR-T therapy resistance. Genetically or pharmacologically ablation of MGAT5 enhances the CAR-T efficacy against many syngeneic cancer models³³⁹. Other studies also tried to reengineer CAR-T cells to either specifically target glycol antigen or strengthen sugar-mediated adhesion with malignant cell^{340,341}.

CHAPTER 2. IDENTIFICATION OF FBXL20 AS AN E3 UBIQUITIN LIGASE THAT FACILITATES THE PROTOSOMAL DEGRADATION OF 4-1BB

2.1 Summary

4-1BB is a significant immune-stimulatory receptor that delivers signals to sustain T cell viability and activity. The strategy to eliminate cancers by agonistically targeting 4-1BB has been under pre-clinical and clinical investigations for over two decades. As a protein expressed following stimulation, 4-1BB is controlled precisely on both transcription and translation levels to maintain its abundance. While the transcriptional activation mechanism of 4-1BB has been well interpreted; however, it remains unclear how 4-1BB is regulated on the protein level. In this work, we presented experimental evidence establishing that mature 4-1BB is heavily polyubiquitinated and subjected to the ubiquitin-proteasomal system (UPS) for degradation. By performing proximity-labeling (PL) screening coupled with biochemical assays, we identified that F-Box/LRR-Repeat Protein 20 (FBXL20) acts as the E3 ubiquitin ligase that triggers the polyubiquitination of 4-1BB at the intracellular Lys residues. Our data shed light on 4-1BB regulation on the protein level by unmasking, for the first time, a post-translational mechanism governing 4-1BB abundance in cells. FBXL20 might potentially be utilized as a predictor of 4-1BB function in TME and the outcome of ICB or ACT therapies for cancers.

2.2 Results

2.2.1 Tumoral 4-1BB expression is associated with optimal antitumor immunity

4-1BB along with other TNFRSF family receptors are generally accepted as an immune stimulatory molecule boosting anti-tumor immune response^{342,343}. To study the impact of TNFRSFs on cancer prognosis, we examined the correlation between tumor *TNFRSF* mRNA levels and the overall survival (OS) or disease-free survival (RFS) of high-TMB cancer types selected from Wang *et al.*³⁴⁴. As shown in Fig 2.1, most of the examined TNFRSF receptors are positively correlated with prolonged OS of skin cutaneous melanoma (SKCM) dataset. Among them, however, only 4-1BB along with *TNFRSF1B* (encoding TNFR2) can predict an improved RFS of SKCM patients.

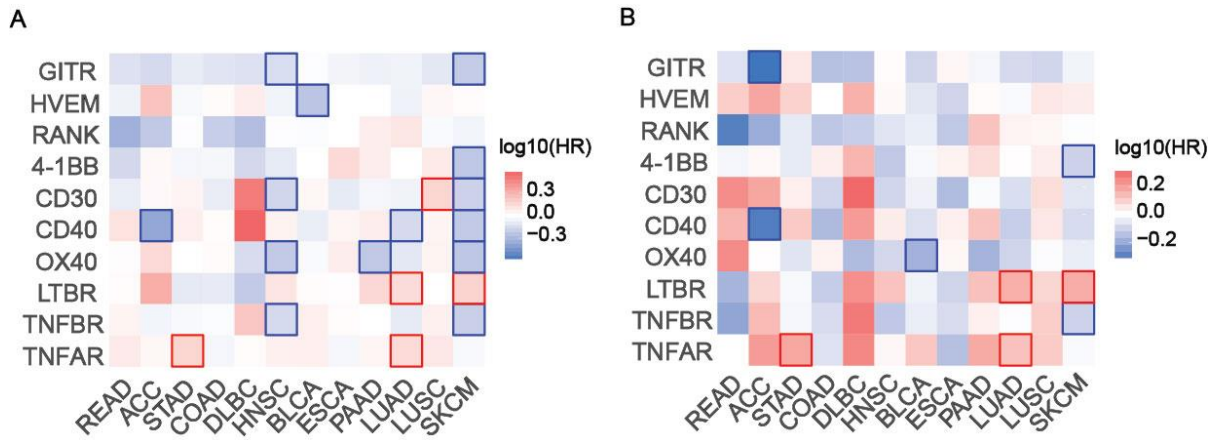


Figure 2.1. The correlation between the *TNFRSF* transcription and OS (A) or RFS (B) of high-TMB TCGA cancers. The figure was generated by GEPIA2. Bold outline, $p < 0.05$ (Log-rank analysis); HR, hazards ratio. A lower HR indicates positive correlation of gene expression and patients' survival.

Next, we set out to assess whether 4-1BB contributes to the clinical benefits of particularly immune checkpoint therapy in cancer. As uncovered by Tumor Immune Dysfunction and Exclusion (TIDE) platform³⁴⁵, melanoma patients with higher 4-1BB expression are more likely to respond to immune checkpoint therapy (Fig 2.2), which agrees with the previous finding that high 4-1BB expression on both tumor-infiltrating and circulating CTLs defines better prognosis of cancer patients^{228,346,347}.

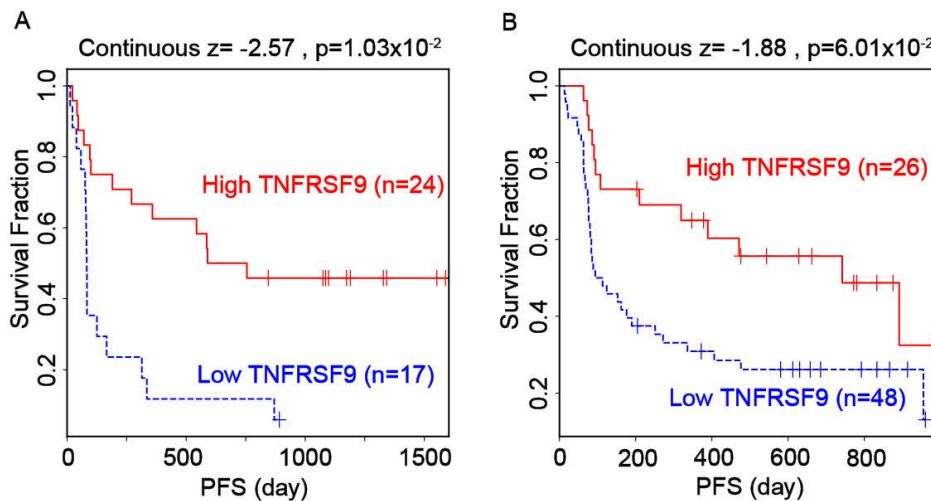


Figure 2.2. The Kaplan-Meier survival plots showing the correlation between *TNFRSF9* expression and ICB outcomes of melanoma patients (A, dataset PRJEB23709³⁴⁸, $n = 41$; B, dataset phs000452.v3.p1³⁴⁹, $n = 74$). The figures were acquired from TIDE. The p values were calculated by Log-rank analysis.

Another robust algorithm we exploited was Tumor Immune Estimation Resource (TIMER2.0)³⁵⁰, which can be used for studying the impact of gene expression on tumor immune infiltration. We found that *TNFRSF9* mRNA level is associated with augmented tumoral infiltration of anti-tumor immune cells such as CD4⁺ T cells, CD8⁺ T cells, NK cells, DCs and M1-like macrophages. On the other hand, 4-1BB is negatively correlated with the abundance of immune-suppressive cell types including MDSC and M2-like macrophages (Fig 2.3). Together, these findings cooperatively supported that 4-1BB restrained tumor progression by establishing a highly inflamed TIME.

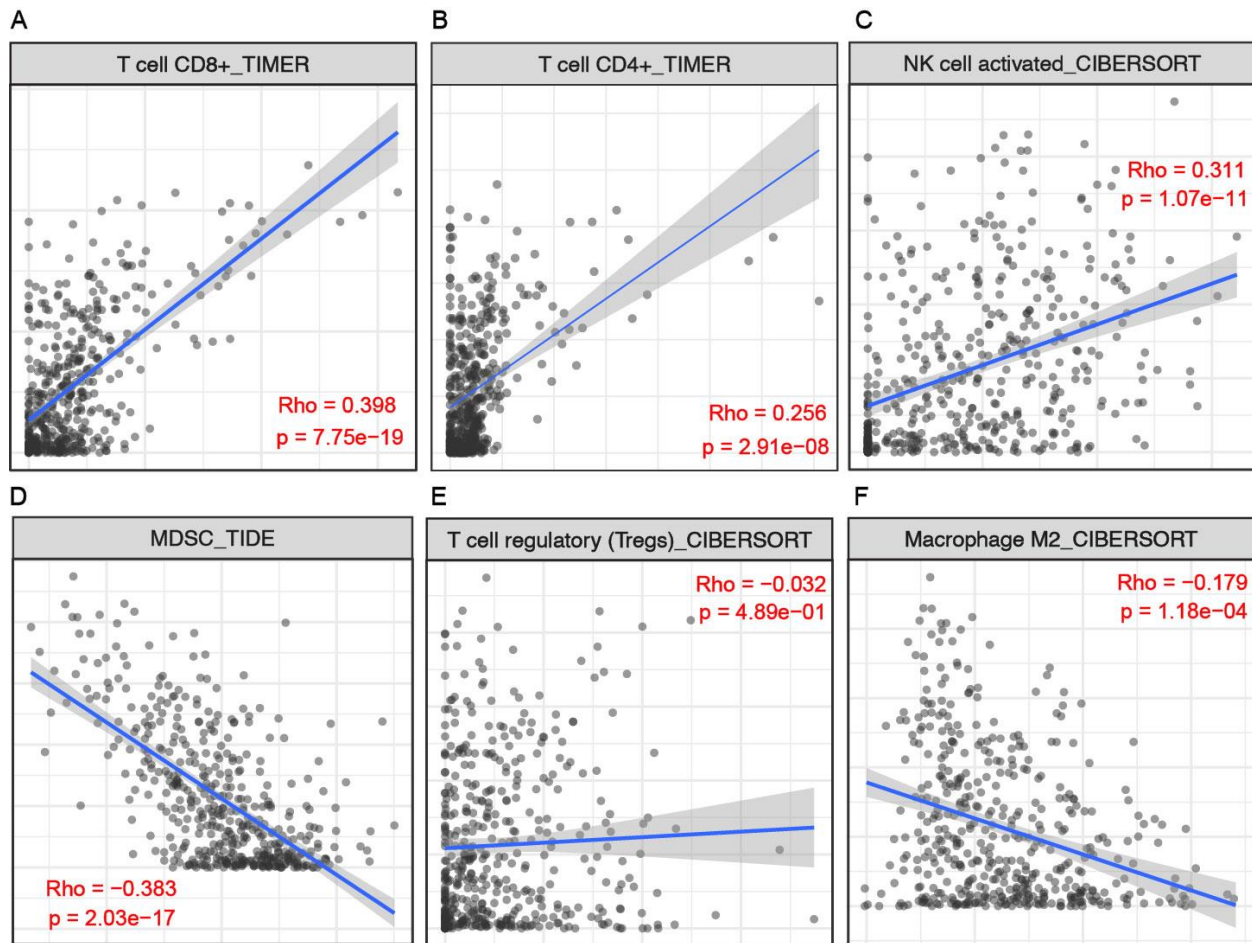


Figure 2.3. High level of *TNFRSF9* transcript is associated with an inflamed cancer immune microenvironment. (A-F) The correlation between *TNFRSF9* expression with the infiltration level of CD8⁺ T cell (A), CD4⁺ T cell (B), NK cells (C), MDSC (D), T_{reg} cells (E) and M2 macrophages (F) in TCGA-SKCM dataset (n = 471) unveiled by TIMER2.0. The x and y axis represents infiltration level and relative *TNFRSF9* expression, respectively. The p values were calculated by Spearman's correlation analysis.

2.2.2 4-1BB has four acceptor sites for polyubiquitination

Considering the essentiality of 4-1BB in the TIME, we aimed to decipher the regulation of 4-1BB primarily on protein level where attention has never been focused yet. Ubiquitination, one of the most frequently occurred post-translational modifications on proteins, is well-characterized as a signal of target degradation through the 26S proteasome^{261,351}. We learned from previous proteomics data that 4-1BB can be ubiquitinated on its intracellular domains^{352,353}. Inspired by those findings, we conducted immunoprecipitation and mass spectrometry studies to verify the formation of Poly-Ub smear on 4-1BB. As shown in Fig S1, polyubiquitination of both human and murine 4-1BB can be detected in cultured cell lines. Liquid chromatography-tandem mass spectrometry (LC-MS/MS) analysis on immunoprecipitated human 4-1BB from HEK293T cells unveiled di-glycine modified Lys residues on all four intracellular Lys sites, namely K214, K218, K219 and K225 (designated as 4-K motif), as acceptors of ubiquitin (Fig 2.4). Through the combination of published data and our present results, we came to the benchmark that 4-1BB is modified by poly-Ub.

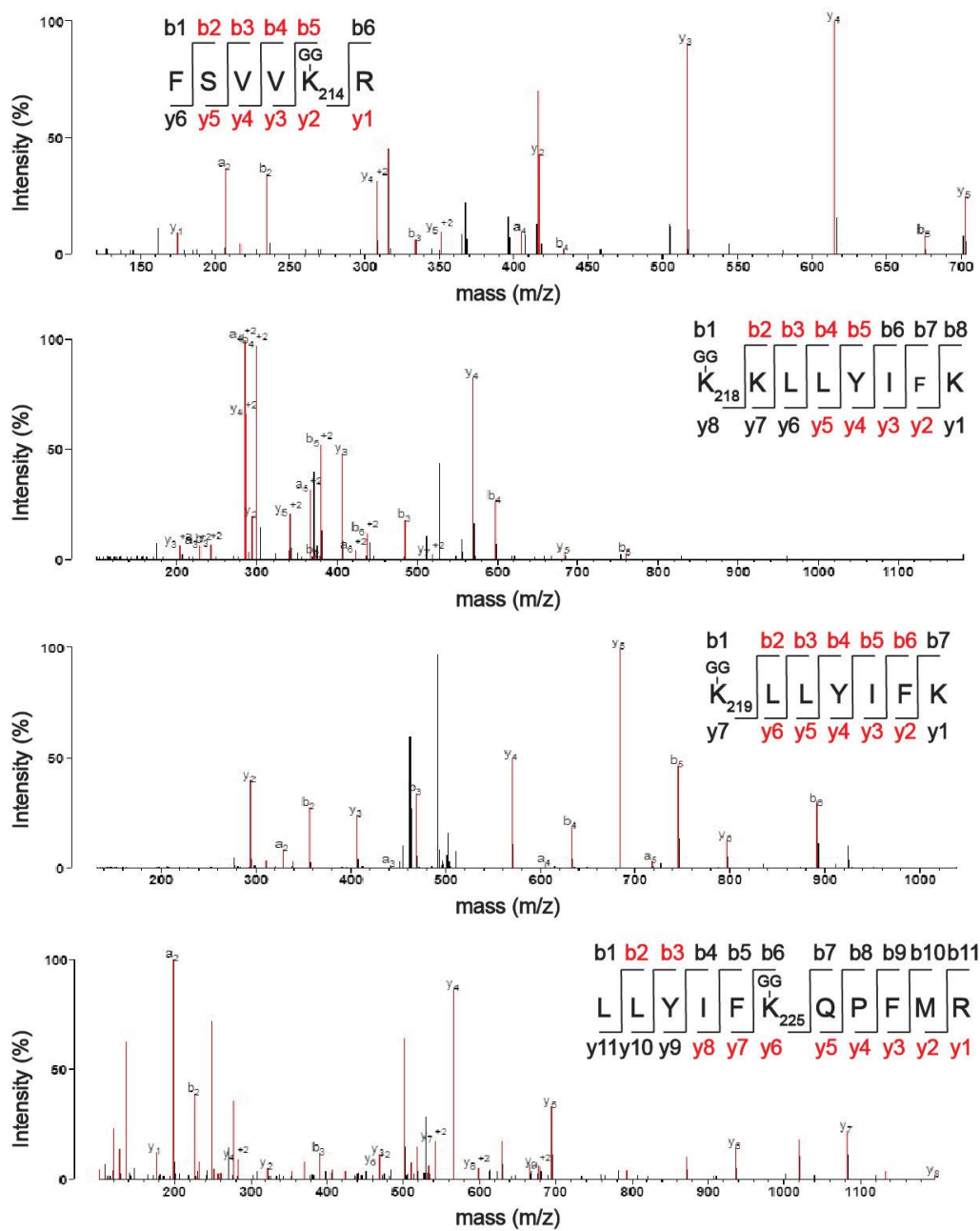


Figure 2.4. The tandem mass spectrum of a human 4-1BB fragment with ubiquitinated K214, K218, K219 and K225 locus. The recognized y and b ions were highlighted in red.

We also examined the 4-1BB amino acid sequences and noticed that the 4-K motif is evolutionarily conserved among a panel of mammalian species (Fig 2.5 A and S2), indicating that this region could be responsible to some critical biological functions. Next, we aimed to elucidate the biological importance of this modification in detail. As expected, mutation of the four Lys residues to arginine (K214R/K218R/K219R/K225R, or 4KR) results in greatly rendered polyubiquitination of 4-1BB compared to wild-type (WT) (Fig 2.5 B).

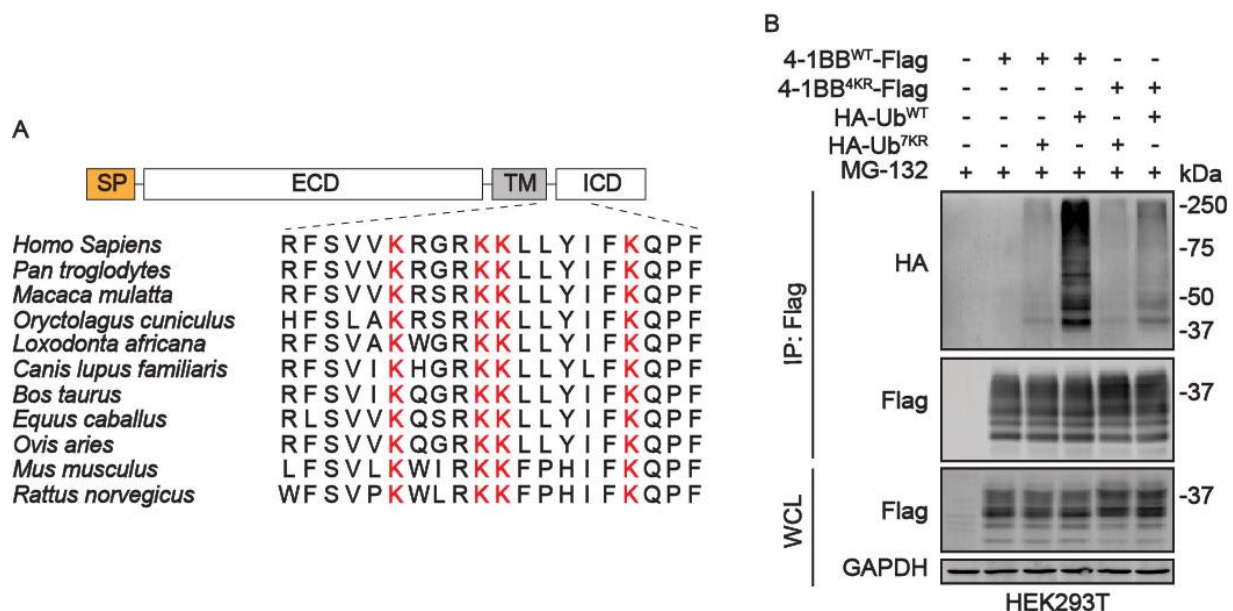


Figure 2.5. human 4-1BB is polyubiquitinated on four Lys residues. (A) Amino acid sequence alignment of mammalian 4-1BB on its ubiquitinated region located in the intracellular domain. (B) *In vivo* ubiquitination assay comparing the ubiquitination of 4-1BB WT and 4KR. The indicated plasmids were co-transfected to HEK293T cells followed by *in vivo* ubiquitination assay. SP, signal peptide; ECD, extracellular domain; TM, transmembrane domain; ICD, intracellular domain; IP, immunoprecipitant; WCL, whole cell lysate.

2.2.3 4-1BB is degraded through UPS

Through biochemical and proteomics study, we managed to identify the ubiquitination sites of human 4-1BB. As protein degradation is the most frequent outcome of ubiquitination, we asked whether 4-1BB follows the same mode of regulation. We conducted cycloheximide (CHX)-chase assay on HEK293T cells and found that 4-1BB 4KR exerts markedly augmented stability versus the WT (Fig 2.6), which suggested that 4-K motif contributes to 4-1BB stability.

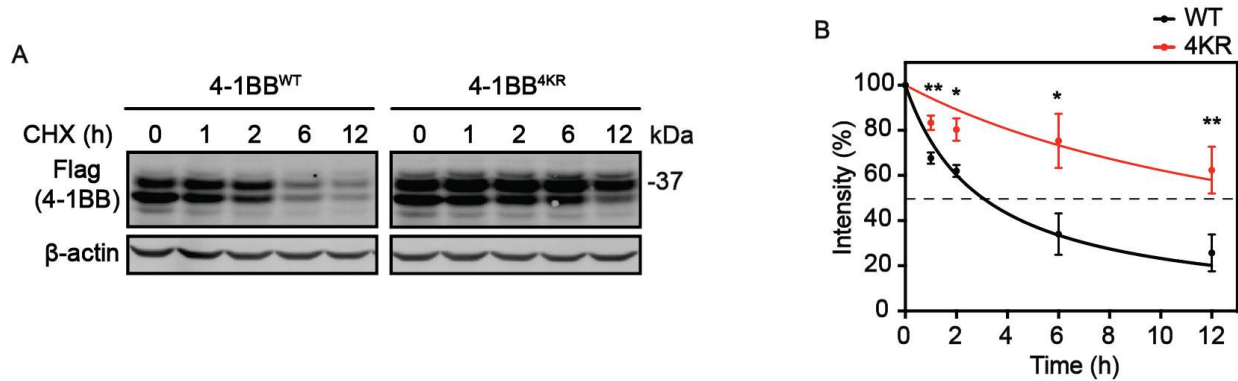


Figure 2.6. The comparison of turnover between 4-1BB WT and 4KR. (A) Representative immunoblotting (IB) results of CHX-chase assay comparing degradation of 4-1BB WT and 4KR. (B) The quantitative results of the remaining 4-1BB at each time point. 50% degradation was indicated by the dashed line. Monoexponential decay curve was used for data exhibition. Results represent mean \pm SD. * $p < 0.05$; ** $p < 0.01$ (two-tailed student's t -test).

To characterize whether 4K ubiquitination governs 4-1BB stability in T lymphocytes, we stably overexpressed WT or 4KR mutant of 4-1BB in parallel on Jurkat cell line (4-1BB negative, Fig 2.7 A, B) which is friendly to lentivirus-based gene manipulation. The lentivirus vector with spleen focus-forming virus (SFFV) promoter was chosen because it drives robust gene expression in Jurkat cells³⁵⁴. To make sure the differential expression of 4-1BB WT and 4KR are not caused by unequal lentivirus transduction, an EGFP coding segment was fused downstream of 4-1BB coding region with a T2A self-cleavage peptide as a reporter to monitor transduction efficiency. As displayed in Fig 2.7 B and C, 4-1BB 4KR mutant exhibited substantially elevated membrane level as against WT, supporting the delayed turn-over and increased accumulation of 4KR than WT. These results cooperatively confirmed that 4-1BB degradation is dictated by ubiquitination on its 4-K motif.

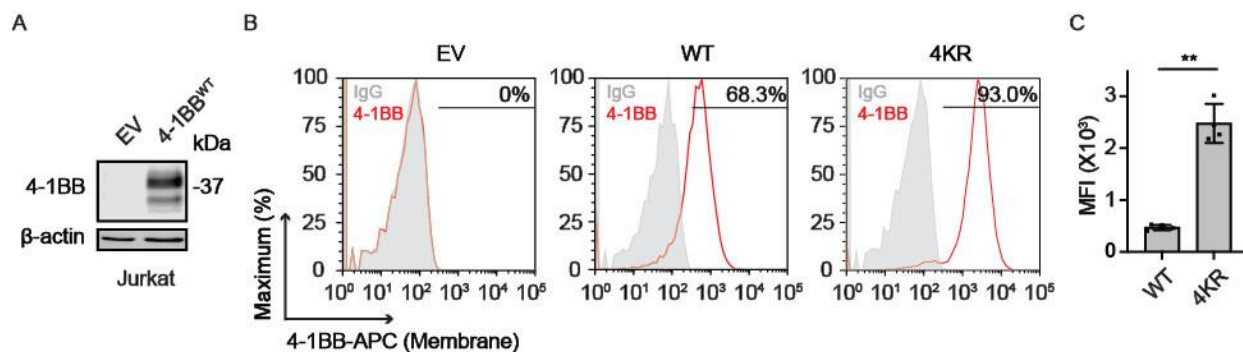


Figure 2.7. The membrane expression of 4-1BB WT and 4KR. (A) IB analysis of 4-1BB expression on parental and lentivirus-transduced Jurkat cells. (B) Flow cytometry analysis comparing membrane level of 4-1BB WT and 4KR. Jurkat cells were transduced with lentivirus encoding 4-1BB WT or 4KR followed by flow cytometry detection. (C) Quantification of membrane 4-1BB WT and 4KR level in (A) ($n = 4$). Results represent mean \pm SD. ** $p < 0.01$ (two-tailed student's t -test); MFI, mean fluorescence intensity.

Proteasome inhibition causes the accumulation of proteins which are meant to be degraded via UPS. Upon the treatment of proteasome inhibitor MG-132, the protein level of 4-1BB could be rapidly augmented in Hodgkin lymphoma cell line HDLM-2 and NSCLC cell line H1975 in six hours (Fig 2.8 A and C). However, qRT-PCR results showed that mRNA levels of *TNRSF9* in the two cell lines were not upregulated (Fig 2.8 B and D), suggesting that 4-1BB is very likely to be degraded through UPS mechanism. We also established several cell lines that harbored lentivirus-driven 4-1BB expression. As shown in Fig 2.8 E and F, ectopically expressed 4-1BB, like the endogenous one, can be upregulated upon proteasome inhibitor, further underpinning that the effect of MG-132 was achieved post-translationally.

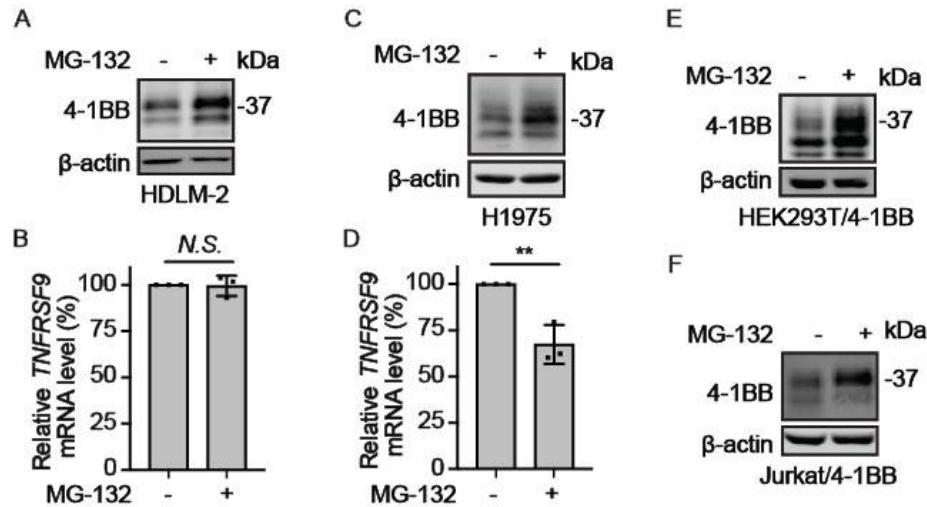


Figure 2.8. The protein level of 4-1BB upon the treatment with MG-132. (A - D) Proteasome inhibition by MG-132 treatment led to 4-1BB protein accumulation by not mRNA upregulation in HDLM-2 (A, B) and H1975 (C, D). (E, F) Proteasome inhibition by MG-132 treatment led to upregulation of ectopically expressed 4-1BB ectopically in HEK293T (E) and Jurkat cells (F). Results represent mean \pm SD. N.S. $p > 0.05$; ** $p < 0.01$ (two-tailed student's t -test).

As anticipated, degradation of 4-1BB was greatly retarded with the presence of MG-132 in CHX-chase assay (Fig 2.9). However, the administration of MG-132 could not completely recapitulate the stability of 4-1BB 4KR, suggesting additional ubiquitination-dependent mechanisms that promote 4-1BB degradation. As shown in Fig S3, 4-1BB is also accumulated under autosomal/lysosomal inhibition by chloroquine (CQ) or ammonium chloride (NH_4Cl). Pretreatment of CQ also stabilizes 4-1BB to an even higher extent than MG-132. Impressively, 4-1BB 4KR protein displayed minor elevation in comparison to 4-1BB WT, indicating the involvement of ubiquitination-dependent autophagic degradation for the regulation of 4-1BB.

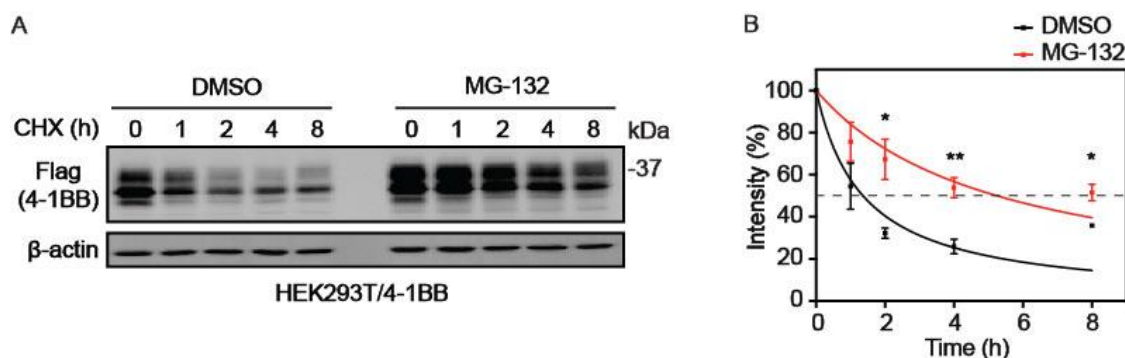


Figure 2.9. The turn-over of 4-1BB is determined by ubiquitination. (A) CHX-chase assay comparing the degradation of 4-1BB with or without proteasome inhibition. HEK293T/4-1BB cells were pre-treated with DMSO or 10 μ M MG-132 for 2 h, then incubated with CHX (100 μ M) for indicated periods of time. (B) The quantification of IB results in (A) ($n = 3$). 50% degradation was indicated by the dashed line. Monoexponential decay curve was used for data exhibition. Results represent mean \pm SD. ** $p < 0.01$ (two-tailed student's t -test).

Since polyubiquitin chains can be utilized by some proteins as scaffolds for the assembly of signaling complexes³⁵¹, we compared the potential of 4-1BB WT and 4KR to drive the activation of NF- κ B which is known to be the major transcription factor that 4-BB signals through. We established HEK293T/NF- κ B reporter cell line and noticed that transient transfection of 4-1BB 4KR elicited stronger NF- κ B activity in comparison to WT (Fig 2.10), suggesting that the polyubiquitin chain is unlikely to contribute to 4-1BB signaling. According to our previous experience from CHX-chase assay, expression of 4-1BB WT and 4KR are very similar 24 h after transient transfection in HEK293T cells, suggesting the high reporter activity from 4KR was unlikely the result of stability-caused protein accumulation. More likely are the other alterations of 4KR (such as subcellular distribution or transportation) that led to the reporter activity change. These data collectively confirm that the abundance and biological functions of 4-1BB are negatively regulated by the UPS-mediated proteolysis.

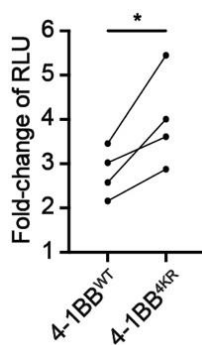


Figure 2.10. Luciferase assay comparing the amplification of NF- κ B activity by 4-1BB WT and 4KR. Plasmids were transfected to HEK293T/NF- κ B reporter cell line and harvested to analyze the NF- κ B reporter activity by measuring bioluminescence (n = 4). Data acquired from the same set of experiment were paired. * $p < 0.05$ (two-tailed, paired student's t -test); RLU, relative light unit.

2.2.4 Ubiquitination-mediated proteolysis of 4-1BB depends on its *N*-glycosylation status

We then comparatively evaluated the expression pattern of 4-1BB WT and 4KR from whole cell lysate by IB. It met our expectation that 4KR had increased band intensity than WT due to its slow turnover; however, the different bands of 4-1BB showed unidentical ratio change. As demonstrated in Fig 2.11 A, the higher membrane expression of 4-1BB 4KR mutant is associated only with the increased high molecular weight (high-MW) band on IB, giving rise to the speculation that high-MW band of 4-1BB represents the membrane-resident form, and is more sensitive to UPS-mediated degradation. Supplementarily, we have long been noticing that 4-1BB exhibit multiple IB bands regardless of expression source, therefore, we aimed to characterize the differences of those 4-1BB bands which might help us have a better understanding with respect to the feature and behaviors of this protein. 4-1BB is a heavily glycosylated protein with two putative *N*-glycosylation sites (N138 and N149 for humans, as shown in Fig 2.11 B) as predicted on basis of the consensus N-X-S/T motif which is the canonical receptor of *N*-glycan. After introduction with N-to-Q mutation to these two residues, the *N*-glycosylation level of 4-1BB was dramatically abolished as indicated by the band shift towards lower molecular weight on SDS-PAGE. We supplementarily performed an enzymatic digestion assay using peptide *N*-glycosidase F (PNGase F) which is a bacteria-derived enzyme selectively cleaving *N*-linked glycans from the substrates^{355,356}. As shown by Fig 2.11 C and S2, PNGase F treatment led to the vanishing of both high- and medium-MW bands of 4-1BB WT, indicating that high- and medium-MW bands represent 4-1BB at distinct *N*-glycoforms. There are no additional *N*-linked glycosylation sites

except N138 and N149 since 4-1BB N138Q/N149Q (designated as 2NQ) no longer respond to PNGase F treatment.

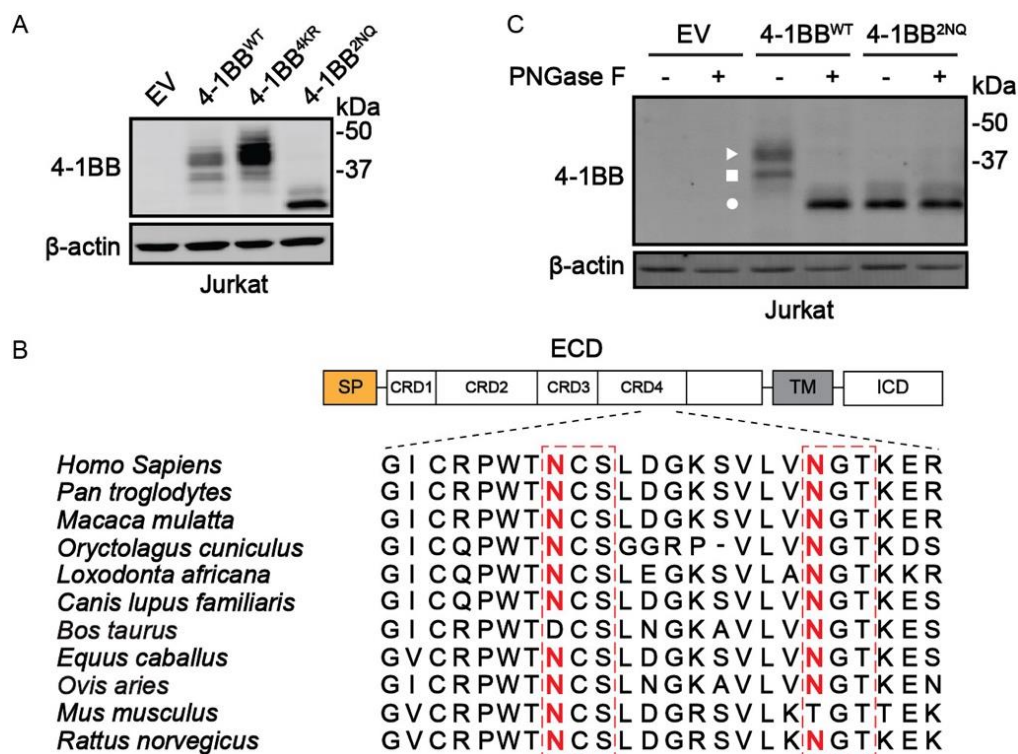


Figure 2.11. Highly-glycosylated 4-1BB is more susceptible to ubiquitination-mediated degradation. (A) IB analysis of 4-1BB WT, 4KR and 2NQ from Jurkat cells transduced with indicating lentivirus. (B) IB analysis of PNGase F digestion of lysate from Jurkat cells stably expressing 4-1BB WT and 2NQ mutant. The 4-1BB mutants were lentivirally expressed on Jurkat cells. (C) Amino acid sequence alignment of mammalian 4-1BB on its *N*-glycosylation region at extracellular domain. EV, empty vector; Triangle, high-MW band (mature form) of 4-1BB; Square, medium-MW band (immature form) of 4-1BB; Circle, low-MW band (*N*-glycan-abolished form) of 4-1BB. SP, signal peptide; ECD, extracellular domain; CRD, cysteine-rich domain; TM, transmembrane domain; ICD, intracellular domain.

N-glycosylation, which has been confirmed to exist on 4-1BB, is a multistep reaction taking place in the ER and Golgi apparatus by a series of enzymes. Pharmacologically arresting 4-1BB translocation by brefeldin A (BFA, an ER-to-Golgi transportation blocker³⁵⁷) treatment causes the decrease of only high-MW bands and accumulation of medium-MW band in a time-dependent manner (Fig 2.12 A), indicating that the two bands represent distinct forms 4-1BB at pre- and post-Golgi compartments. Interestingly, the decreased abundance ratio of high/mid MW band was found to be associated with diminished membrane 4-1BB localization after BFA treatment (Fig 2.12 B). Short-time BFA treatment led to a significant decrease of high-MW 4-1BB WT rather

than 4KR (Fig 2.12 C), which is consistent with our previous hypothesis that high-MW 4-1BB is sensitive to ubiquitination-triggered clearance. Considering protein *N*-glycosylation is achieved by sequential enzymatic reactions taking place in ER and Golgi, we presumed that medium-MW is referred to as partially *N*-glycosylated 4-1BB which is generated in ER, whereas high-MW band is the mature 4-1BB that has passed the entire *N*-glycosylation pathway. We also exploited the cell membrane proteome labeling with sulfo-NHS-SS-biotin, a cell-impermeable reagent that can biotinylate primary amine groups on proteins. As demonstrated in Fig 2.12 D, the biotinylated fraction of 4-1BB was constituted mainly by the high-MW form. A little amount of medium-MW form can also be enriched but the abundance was much lower, relatively. Altogether, we proposed that the high-MW bands which represent fully *N*-glycosylated 4-1BB are committed to cell surface, while the medium-MW ones confer the ER-resident, partially *N*-glycosylated form. The rapid degradation of mature 4-1BB, which underwent the entire *N*-glycosylation process, was mediated by the polyubiquitination on the intracellular domain in cytosol.

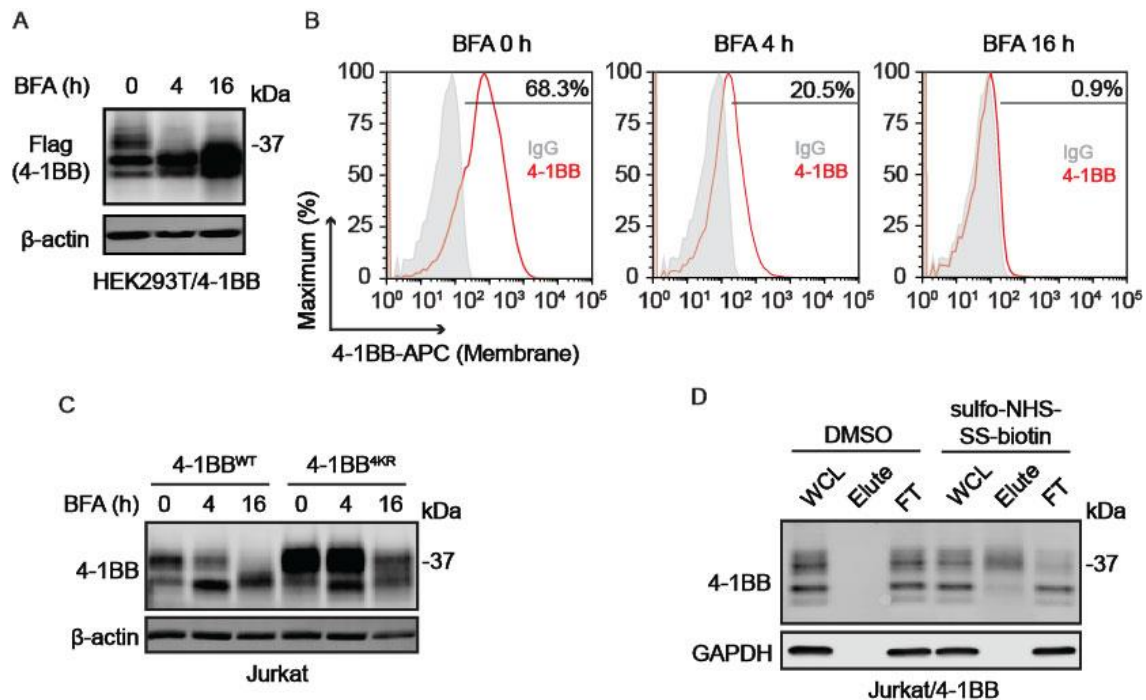


Figure 2.12. Highly-glycosylated 4-1BB represents the membrane-localized form. (A) Impact of BFA treatment to 4-1BB WT on HEK293T/4-1BB cells analyzed by IB (B) FACS assessment of membrane 4-1BB level of HEK293T/4-1BB cells following 1 μ M BFA treatment identical to (A). (C) Jurkat cells were transduced with lentivirus encoding 4-1BB WT or 4KR, then incubated with 1 μ M BFA for IB analysis. (D) Enrichment of membrane-associated 4-1BB by sulfo-NHS-SS-biotin labeling. WCL, whole cell lysate; FT, flow-through.

2.2.5 Profiling the interacting partners of 4-1BB by PL coupled with proteomics analysis

The protein PTMs are under the regulations by “writers” and “erasers” to maintain dynamic control and require certain “readers” proteins to elicit the downstream functions. E3 ligase is known as the key component to promote target ubiquitination and allow proteolysis to take place predominantly but not exclusively through the proteasomal pathway^{358,359}. The protein-protein interaction landscape of 4-1BB has never been reported before. As so, we planned to carry out proteomics-based approaches to systematically profile the protein interaction landscape of 4-1BB, and from which identify potential 4-1BB-specific E3 enzymes. Affinity pull-down combined with mass spectrometry analysis has been broadly used to map the protein-protein interaction; however, it has a major caveat which is weak or transient interactions can hardly be captured during sample preparation. PL as an alternative strategy overcomes the limitations of traditional approaches and has been applied in an ample quantity of studies. Natural or engineered peroxidases (*e.g.*, APEX2, HRP) / biotin ligases (*e.g.*, BioID, TurboID, *etc.*) were genetically fused with the protein of interest (POI) to allow the proximal interacting proteins to be biotinylated with biotin or biotin derivatives as substrate³⁶⁰. Considering the transient nature of E3 ligase-substrate interaction, which made it challenging to capture E3 enzymes via affinity pulldown, we conducted PL which is an ideal approach to map the weak or transient interacting partners of a given POI³⁶⁰. Besides, several reports have shown that PL can be leveraged to identify either E3 ligases/deubiquitinating enzymes of given substrates^{361,362} or the interaction partners of immune receptors^{363,364}, which further justified the feasibility of our research strategy.

To set up the PL assay, BioID2 (an optimized promiscuous biotin ligase with smaller size and superior labeling efficiency³⁶⁵) was fused to the cytoplasmic end of human 4-1BB with a hemagglutinin (HA) tag (4-1BB-BioID2-HA) and was stably expressed in HEK293FT cell line. The C-terminus of 4-1BB and N-terminus of BioID2 are both flexible as illustrated in Fig 2.13 A, suggesting that the overall structure would unlikely be disrupted with an additional GGGGS linker in between. Although it has been suggested that a longer linker may help capture more interacting partners³⁶⁵, we had only one GGGGS linker incorporated for protein fusion in wish to minimize the false-positive biotinylation. We chose the C-end for BioID2 fusion for two reasons. First, the addition of BioID2 to the extracellular domain may affect the transportation of the whole protein; second, the intracellular domain of membrane protein is more likely to possess sophisticated functions in the presence of interaction partners. The labeling process is briefly described in Fig

2.13 B. The proximal labeling efficiency was validated by streptavidin blotting before the mass spectrometry sample collection (Fig 2.13 C). Cells expressing the BioID2-HA construct were utilized to exclude the proteins that were randomly tagged by biotin in cells.

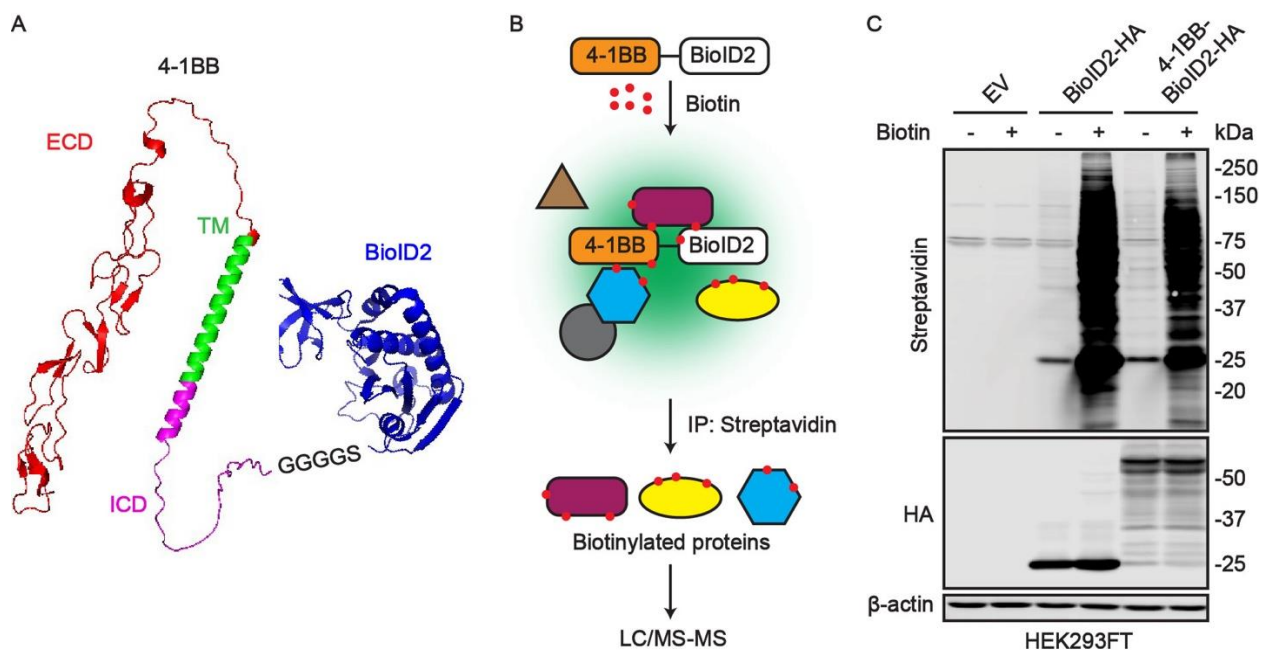


Figure 2.13. The assay setup of 4-1BB PL. (A) The estimated structure of 4-1BB-BioID2 fusion protein. The structure of human 4-1BB is predicted by Alpha-fold, while BioID2 was taken from PDB# 2EAY. (B) The flow diagram of the cellular biotinylation process. (C) Validation of target biotinylation in BioID cell lines by streptavidin blotting. Lysates of biotin-treated cells were subjected to IB and visualized with dye-conjugated streptavidin. ECD, extracellular domain; TM, transmembrane domain; ICD, intracellular domain; N, N-terminus; C, C-terminus; EV, empty vector.

The labeling assay was performed in triplicate. The efficient protein biotinylation was confirmed before MS analysis (Fig 12.4 A). The reproducibility of sample preparation and MS analysis was satisfactory as illustrated in Fig 12.4B. We applied stringent data filtration criteria and only proteins with unique peptides recognized in all three biological replicates were considered as meaningful hits. As expected, 4-1BB was significantly enriched in 4-1BB-BioID2 group with a fold change (FC) > 8 according to label-free quantification (LFQ) (Fig 12.4 C, table), indicating that the labeling process was performed successfully. Consequently, a total of 362 enriched in 4-1BB-BioID2 group, of which 264 hits were considered significant (FC value > 2, adjusted p value < 0.01). We also performed GO analysis for the 264 hits (Fig S4 - 6).

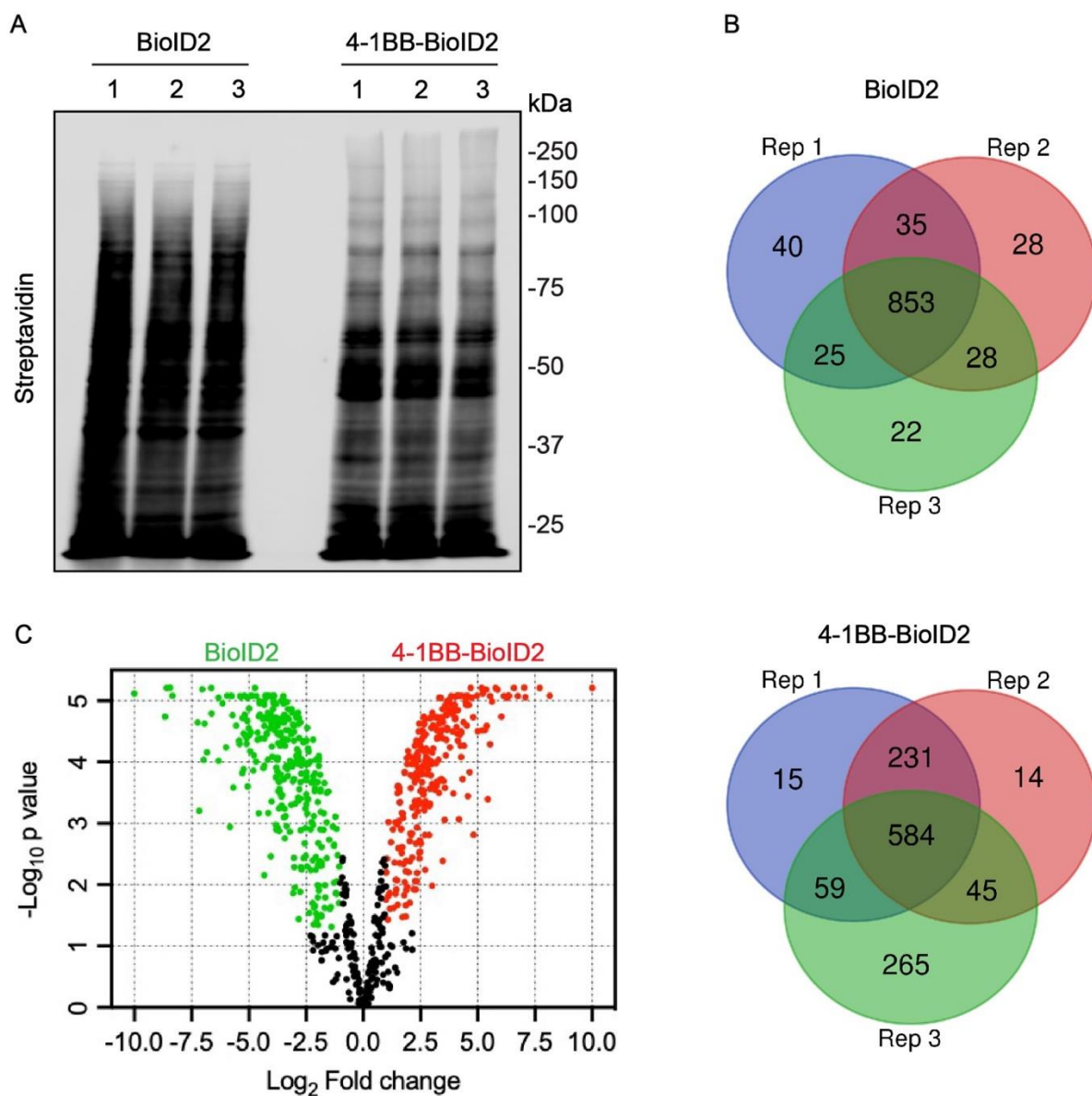


Figure 2.14. The sample preparation for PL assay and label-free quantification of MS results. (A) The streptavidin blotting result of the triplicated pull-down samples. (B) Venn plot showing the reproducibility of BioID pull-down and mass spectrometry profiling. (C) Volcano plot illustrating the differentially enriched biotinylated proteins in BioID2 group versus 4-1BB-BioID2 group. Three replicated sets of samples were included for LFQ. Significant hits ($FC > 2$, $p < 0.01$) were highlighted (BioID2 group by blue dots, and 4-1BB-BioID2 group by red dots).

2.2.6 Identification and validation of FBXL20 acts as the E3 ligase promoting 4-1BB ubiquitination and degradation

We next searched for E3 ubiquitin ligase from the 264 candidates against a collection of 634 human E3 ligases²⁵⁷. Notably, F-box/LRR-repeat protein 20 (FBXL20) was the only E3 ligase that could be identified from all three replicates of 4-1BB- BioID2 samples but not the BioID2 samples (FC = 2.36, $p = 4.43\text{E-}05$), suggesting FBXL20 serves as a 4-1BB interacting protein with high reliability. An E2 enzyme, UBE2J1, was also enriched in 4-1BB group (FC = 3.33, $p = 8.65\text{E-}06$).

FBXL20, also known as SCRAPPER, was originally identified from the central nervous system³⁶⁶. Sequence analysis confirmed SCRAPPER as a member of the F-box family E3 ligase according to its F-box domain on N-terminus. F-box proteins function as the substrate recognition subunit and cooperate with S phase kinase-associated protein 1 (SKP1) and Cullin1 (CUL1) to form SCF complexes (a subtype of Cullin-RING complex) that have the intact E3 ligase activity^{259,367}. The SCF E3 ligase complex mediates the degradation of a wide range of proteins. Among over 70 members of F-box family proteins, the substrate specificity and biological importance of FBXL20 are less clarified. Our preliminary results from PL screening prompted us to dissect whether 4-1BB expression is regulated through FBXL20-mediated polyubiquitination. As demonstrated in Fig 2.15 A, the interaction of 4-1BB and FBXL20 was confirmed by co-immunoprecipitation (co-IP) assay. As expected, overexpression of FBXL20 led to a decrease of 4-1BB (Fig 2.15 B). On the contrary, knockdown of FBXL20 by two distinct siRNAs resulted in the accumulation of total cellular 4-1BB (Fig 2.15 C, D). Overexpression of FBXL20 promoted the polyubiquitination level of 4-1BB in cells. We also established an F-box domain-deleted version of FBXL20 (FBXL20^{dF}), which fails to interact with SKP1 and CUL1 to assemble SCF E3 ligase complex. As illustrated in Fig 2.15 E, the loss-of-function mutant FBXL20^{dF} was unable to ubiquitinate 4-1BB in HEK293T cells.

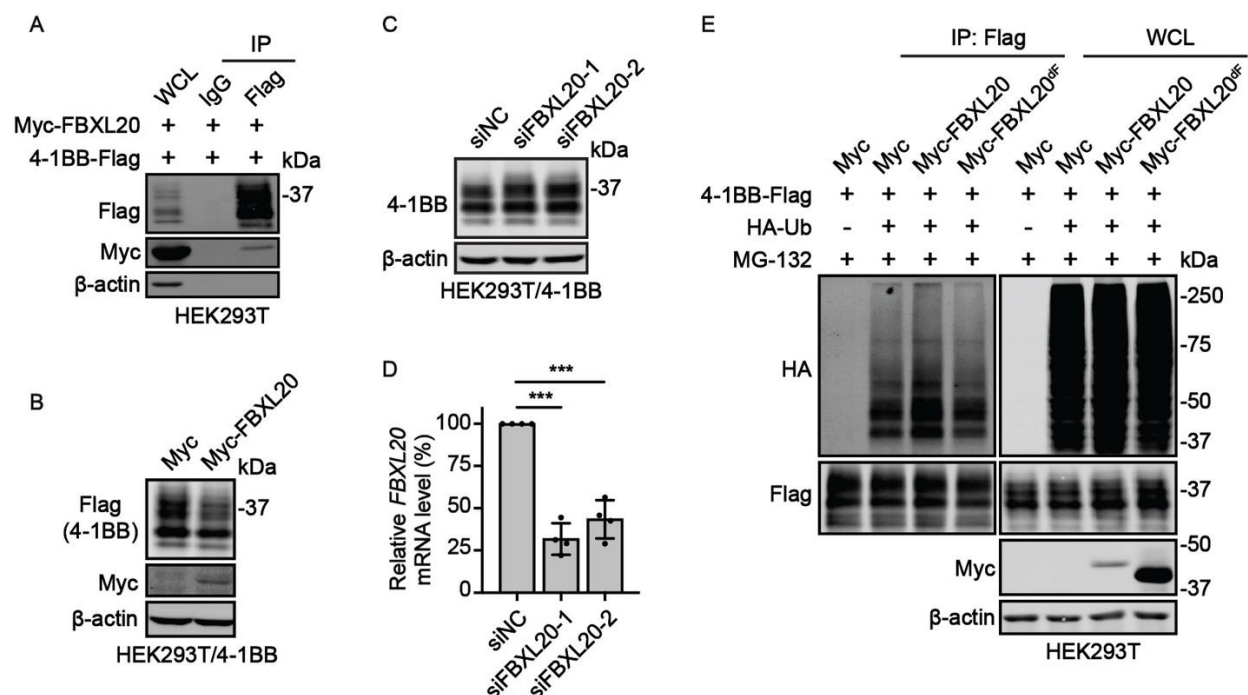


Figure 2.15. FBXL20 promotes the polyubiquitination and degradation of 4-1BB. (A) Co-IP confirmation of 4-1BB-FBXL20 interaction. HEK293T cells were co-transfected with 4-1BB-Flag and Myc-FBXL20 plasmids followed by anti-Flag immunoprecipitation. (B) IB results of 4-1BB protein level change on HEK293T/4-1BB cell line upon transfection of empty vector or Myc-FBXL20 plasmid. (C) IB result showing 4-1BB protein level change on HEK293T/4-1BB cell line upon the transfection of non-targeting or FBXL20-targeting siRNA. (D) Validation of FBXL20 knockdown by measuring mRNA level through qRT-PCR (n = 4). Results represent mean \pm SD. (E) Assessment of FBXL20-promoted polyubiquitination of 4-1BB. Myc-FBXL20 and HA-Ub plasmids were co-transfected to HEK293T/4-1BB cell line followed by *in vivo* ubiquitination assay. *** $p < 0.001$ (two-tailed student's *t*-test); EV, empty vector; siNC, non-targeting siRNA; IP, immunoprecipitant; WCL, whole cell lysate.

We then took advantage of bioinformatics platforms to study the impact of FBXL20 on cancer immunotherapy. As unveiled by TCGA datasets, FBXL20 expression was inversely correlated with the overall survival of individuals harboring stomach carcinoma (STAD) and ovarian serous cystadenocarcinoma (OV) (Fig 2.16 A and B). More importantly, high FBXL20 expression is associated with less satisfactory clinical outcomes of ICB therapy in two independent cohorts (Fig 2.16 C and D) as assessed by TIDE algorithm. These data suggested that FBXL20 may serve critical roles in anti-tumor immunity, and this is possibly related to its regulatory function on 4-1BB.

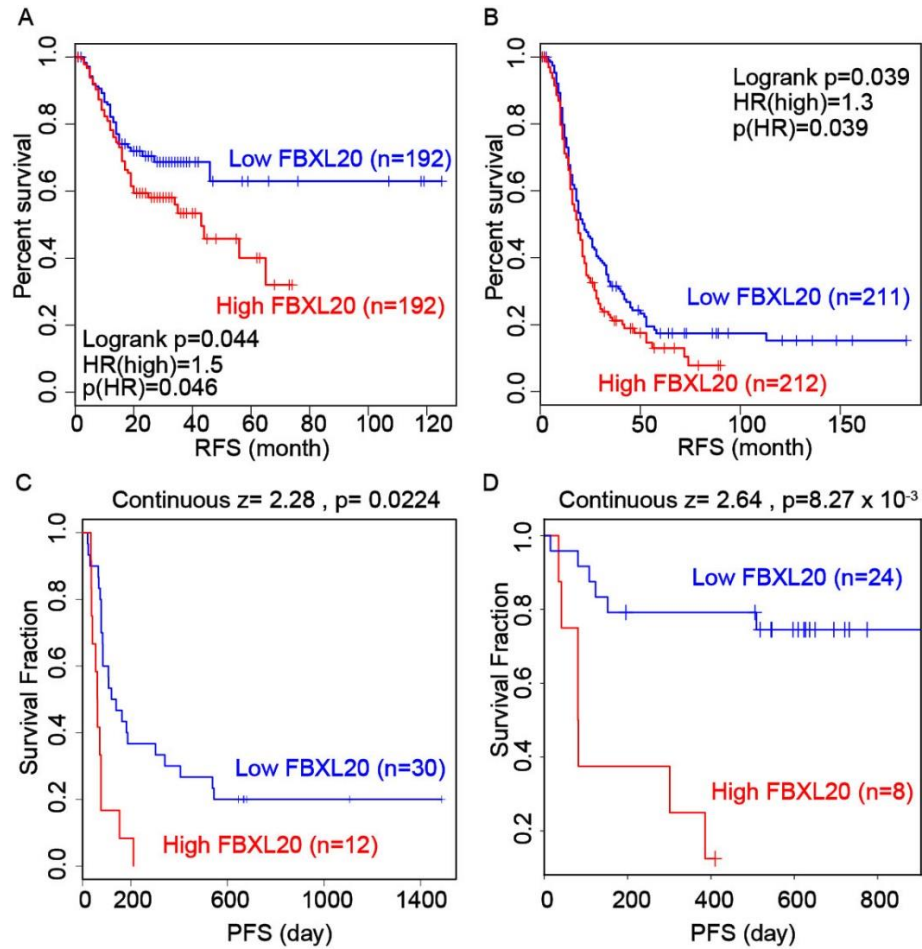


Figure 2.16. Impact of FBXL20 in cancer development and ICB treatment outcome. (A, B) Kaplan-Meier survival curves showing the inverse correlation of FBXL20 transcripts with the disease-free survival of patients in TCGA-STAD (A) and TCGA-OV (B) datasets. (C, D) Kaplan-Meier survival curves showing the inverse correlation of FBXL20 transcripts and ICB outcomes in two cohorts of melanoma patients (C, dataset phs000452.v2.p1³⁶⁸, n = 42; D, dataset PRJEB23709³⁴⁸, n = 32). The figures were acquired on GEPIA2 and TIDE. Significance values were calculated by log-rank analysis.

2.3 Discussion

In this section, we reported that 4-1BB undergoes the polyubiquitination for the subsequent degradation through the proteasomal system. Through PL profiling and molecular studies, FBXL20 was identified as an E3 ligase that promotes poly-Ub chain conjugation on 4-1BB at the four intracellular loci (K214, K218, K219, and K225). Clinically, FBXL20 predicts a favorable response to ICB in melanoma patients.

As the first broadly applied immunotherapeutic targets, PD-1 undergoes ubiquitination for degradation, and different E3 proteins act on PD-1 at distinct stages during glycosylation process. While FBXO38 was identified by Meng *et al.* as the E3 ligase destabilizing membrane-associated PD-1²⁸², KLHL22 alternatively targets the partially glycosylated PD-1 before it reaches Golgi apparatus²⁸³. The functional participation of ubiquitination in regards of 4-1BB signaling pathway has been discussed in a few studies. The regulation of TNFRSF signal transduction by E3 enzymes and DUBs has been well demonstrated using 4-1BB as an example^{186,187}. In our research, we demonstrated that FBXL20-promoted ubiquitination is involved in the modulation of 4-1BB by directing its proteolysis. According to Guo *et al.*, the E3 ligase NEDD4 negatively regulates the expression of GITR and therefore dampens T cell-mediated cytotoxic effect³⁶⁹. Another highlighted finding in our study is that we noticed the unidentical pattern of proteasomal degradation of 4-1BB at distinct glycoforms. The interplay between glycosylation and ubiquitination has been reported on many proteins. Previous studies reported that *N*-glycosylation of immune receptors can directly or indirectly impede E3 ligase engagement and therefore sustain their stability^{285,334}. Conversely, some E3 ligase functions by specifically recognizing *N*-glycosylated degron on substrates³⁷⁰. We hypothesized that *N*-glycosylation affects 4-1BB stability possibly through regulating its spatial distribution instead of E3 ligase recruitment for two reasons: first, the post-Golgi fraction of 4-1BB is more sensitive to UPS-mediated degradation than the pre-Golgi fraction. It has been reported that FBXL20 encompasses a C-terminal isoprenylated CAAX membrane sorting signal^{366,371}, which allows it to engage the surface 4-1BB and promote degradation; second, the intracellular domain (ICD) and the extracellular *N*-glycosylation motifs of 4-1BB are separated into distinct subcellular compartments by the plasma membrane. Given that the ubiquitination of 4-1BB occurs on the ICD, it is very likely that FBXL20 recognizes the ICD-localized degron regardless of the *N*-glycosylation status on the extracellular domain. Nevertheless, the crosstalk between these two modifications on 4-1BB should and will be further explored in depth.

One question that arose was how FBXL20 recognizes 4-1BB. FBXLs are a subgroup of F-box proteins which are distinguished by their C-end leucine-rich repeat (LRR) domains. FBXLs use their LRR domain to recognize specific short motifs (also known as degrons) of substrates and promote the polyubiquitination³⁷². In the research by Xiao *et al.*, FBXL20 drives ubiquitination-dependent degradation of Vsp34, and key degron of Vsp34 was identified to be the phosphorylated

T159 residue³⁷¹. Recently, Manne *et al.* described that proapoptotic proteins PUMA and BAX are both degraded by FBXL20-induced K48-linked polyubiquitination, and this process is licensed by Akt-mediated phosphorylation of substrates³⁷³. FBXL20 also interacts and ubiquitinates PR55 α which has multiple known phosphorylation sites³⁷⁴. It remains to be characterized when and where is 4-1BB degraded by FBXL20 under the physiological situations, and whether it requires additional stimuli (*e.g.*, PTM like phosphorylation) for the FBXL20 engagement to occur. Additionally, or PL assay was done on HEK293T cell line and obtained FBXL20 as the only potential E3 ligase for 4-1BB. More E3 ligase candidates might be identified if we repeat this assay on other cell lines or most ideally *in vivo* like the strategy exploited by Feng *et al.*³⁷⁵. Some of the known 4-1BB interaction proteins (*e.g.*, TRAF2) were not identified presumably because the fusion with BioID2 prohibited their engagement to the cytosolic tail of 4-1BB, and this obviously is another drawback of PL. In close, each methods have their pros and cons and must be combined to illustrate the comprehensive interactome of the POI. It was not our primary goal but still attractive to see that the expression of FBXL20 by transient transfection was robustly enhanced when the F-box domain (Ala22-Ile68) was deleted (Fig 2.15 E). Manne *et al.* reported the FBXO31-mediated UPS-degradation of FBXL20 but did not identify the specific ubiquitinated Lys sites³⁷³. Our observation suggested a potential mechanism relying on the F-box region to guide FBXL20 stability.

In conclusion, we unmasked that 4-1BB is a polyubiquitinated TNFRSF protein that undergoes UPS-mediated degradation. FBXL20 was found to serves as an E3 ligase to ubiquitinate and destabilize 4-1BB. Bioinformatics analysis on basis of public data also indicated that FBXL20 can predict the unsatisfactory clinical outcome of checkpoint inhibitors.

CHAPTER 3. THE FUNCTIONAL CHARACTERIZATION OF N-GLYCOSYLATION IN THE REGULATION OF 4-1BB

3.1 Summary

Leveraging the adaptive immunity against tumors represents a revolutionary category of cancer therapy. 4-1BB is a well-characterized costimulatory immune receptor existing on activated T cells and mediating their proliferation and cytotoxicity under infectious diseases and cancers. Despite the accumulating interest in implementing 4-1BB as a therapeutic target for immune-related disorders, less is known about the pattern of its intracellular behaviors and regulations. It has been previously demonstrated that 4-1BB is heavily modified by *N*-glycosylation; however, the biological importance of this modification remains inexplicit. Through biochemical, biophysical, and cell-biological approaches, we systematically evaluated the impact of *N*-glycosylation on the ligand interaction, stability, and subcellular residency of 4-1BB. We hereby highlighted that *N*-glycan functions by preventing the oligomerization of 4-1BB, thus permitting its membrane transportation and fast turn-over. Without *N*-glycosylation, 4-1BB could be aberrantly accumulated intracellularly and fail to be sufficiently inserted in the membrane. The *N*-glycosylation-guided intracellular processing of 4-1BB serves as the potential mechanism explicitly modulating the “on” and “off” of 4-1BB through the control of protein abundance. Our study will further solidify the understanding of the biological properties of 4-1BB and facilitate the clinical practice against this promising therapeutic target.

3.2 Results

3.2.1 Identification of *N*-glycosylation sites on human 4-1BB

N-glycosylation occurs predominantly on canonical N-X-S/T motifs on substrates^{376–378}. Through the examination and alignment of the amino acid sequence of mammalian 4-1BB proteins, we speculated that extracellular domain-localized N-X-S/T motifs that could potentially be *N*-glycosylated, namely N138 and N149 (based on human sequence, shown in Fig 2.11B). To verify the *N*-glycosylation status of native 4-1BB, we established HEK293T cell lines stably overexpressing WT or N138Q/N149Q (2NQ) mutation and treated the cell lysates with PNGase F

to study the enzymatic deglycosylation effect. As illustrated by the IB result in Fig 2.11 C, WT protein showed an increased mobility shift after PNGase F digestion. On the contrary, the 2NQ mutation protein no longer responded to the enzyme treatment, indicating that human 4-1BB only possesses these two *N*-glycosylation sites. We also performed glycomics analysis to profile the various *N*-glycan species on 4-1BB. The HEK293T cells-expressed human 4-1BB protein that has intact *N*-glycosylation was used for glycan profiling. Strikingly, over 30 types of *N*-linked glycans derived from the two modified sites can be identified by matrix-assisted laser desorption/ionization coupled with time-of-flight mass spectrometry (MALDI-TOF) (Fig S7, Table S1), thus demonstrating the extensive heterogeneity of *N*-linked sugar modification on 4-1BB. The majority of 4-1BB-derived carbohydrates belong to the complex type with core fucosylation. To sum up, human 4-1BB protein is *N*-glycosylated on two N-X-S/T motifs exclusively and appears as a diverse pool of glycoforms. In the subsequent sections, we will discuss the biological function of 4-1BB *N*-glycosylation from several aspects.

3.2.2 *N*-glycosylation of human 4-1BB has minimal contribution to its engagement with 4-1BBL

One commonly seen function of protein *N*-glycan moieties is to mediate the protein-protein interaction. It has been reported that the ligand binding affinity of several immune receptors such as PD-L1 and inducible co-stimulator (ICOS) is determined by their *N*-glycosylation status^{285,379}. As unveiled by the structural biology works, 4-1BB interacts with 4-1BBL through CRD2 and CRD3^{188,189}, which are distant from the two *N*-glycosylation sites located within CRD4, leading to the assumption that the engagement to 4-1BBL of 4-1BB is independent to its *N*-glycan moieties. To test this hypothesis, we performed both plate-based ligand binding assay and Octet-based bio-layer interferometry (BLI) assay to quantitatively compare the binding affinity and kinetics of 4-1BBL to 4-1BB with intact or ablated *N*-glycosylation. The purified 4-1BB (extracellular domain) protein was subjected to PNGase F for deglycosylation and the product was confirmed by Coomassie blue staining (Fig 3.1 A). As unveiled by ligand binding assay, the interaction of 4-1BB with its ligand was not affected by *N*-glycosylation (Fig 3.1 B). Octet assay results in Fig 3.1 C also confirmed that the K_D values between untreated and enzyme-treated 4-1BB protein have a marginal difference (10 nM versus 11 nM). Collectively, we drew the conclusion that *N*-linked glycan is not strictly required for 4-1BB to interact with 4-1BBL.

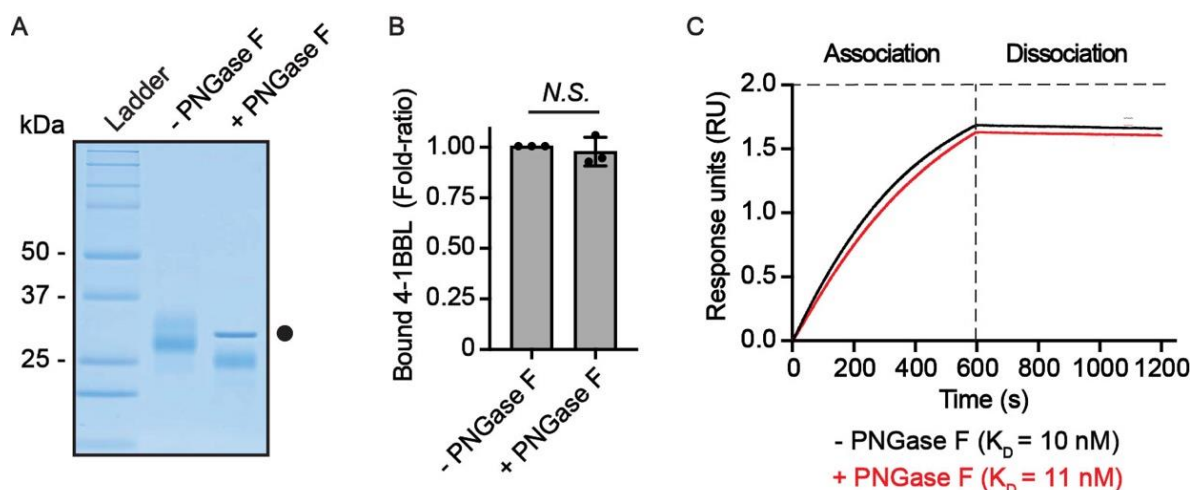


Figure 3.1. The impact of *N*-glycosylation to 4-1BB/4-1BBL interaction. (A) The validation of PNGase F-mediated 4-1BB deglycosylation. (B) The relative level of bound 4-1BBL to PNGase F-treated and untreated 4-1BB protein ($n = 3$). (C) Octet analysis calculating the binding affinity of glycosylated (black) and deglycosylated 4-1BB (red) to 4-1BBL along with the K_D values. *N.S.*, $p > 0.05$ (two-tailed student's *t*-test); Black dot, PNGase F band.

3.2.3 *N*-glycosylation contributes to 4-1BB transportation towards cell membrane

N-glycosylation is required for the membrane trafficking of many membrane proteins. To evaluate the impact of *N*-glycans on 4-1BB membrane expression, we established a panel of 4-1BB mutants with single or double mutation of its glycosylated Asn sites (N138 and N149) and compared their total and membrane levels on Jurkat cells by executing flow cytometry and IB assays. As demonstrated in Fig 3.1 A and B, the single mutation of N138Q, but not N149Q, led to a notable decrease of membrane 4-1BB level. Dual mutation of the two sites (designated as 2NQ) further mitigated 4-1BB membrane expression compared to N138Q alone. We also confirmed that the MFI differences were not caused by variation of lentivirus transduction (Fig S8). Intriguingly, according to IB in Fig 3.1 C, the single or double N-to-Q mutation led to an increase of overall 4-1BB expression. Also, the N138Q mutation caused more molecular weight loss than N149Q, indicating that N138 was used to form a larger glycan architecture, which potentially harbors more impactful functions. We also confirmed that the antibody we utilized for flow cytometry staining (clone 4B4-1) does not distinguish glycosylated non-glycosylated 4-1BB in respect of binding (Fig S9), thus ensuring that the decreased membrane levels of glycosylation-deficient mutants were caused by the alteration of the protein itself. Hence, we proposed that *N*-glycosylation plays a role in transporting 4-1BB onto the cell membrane.

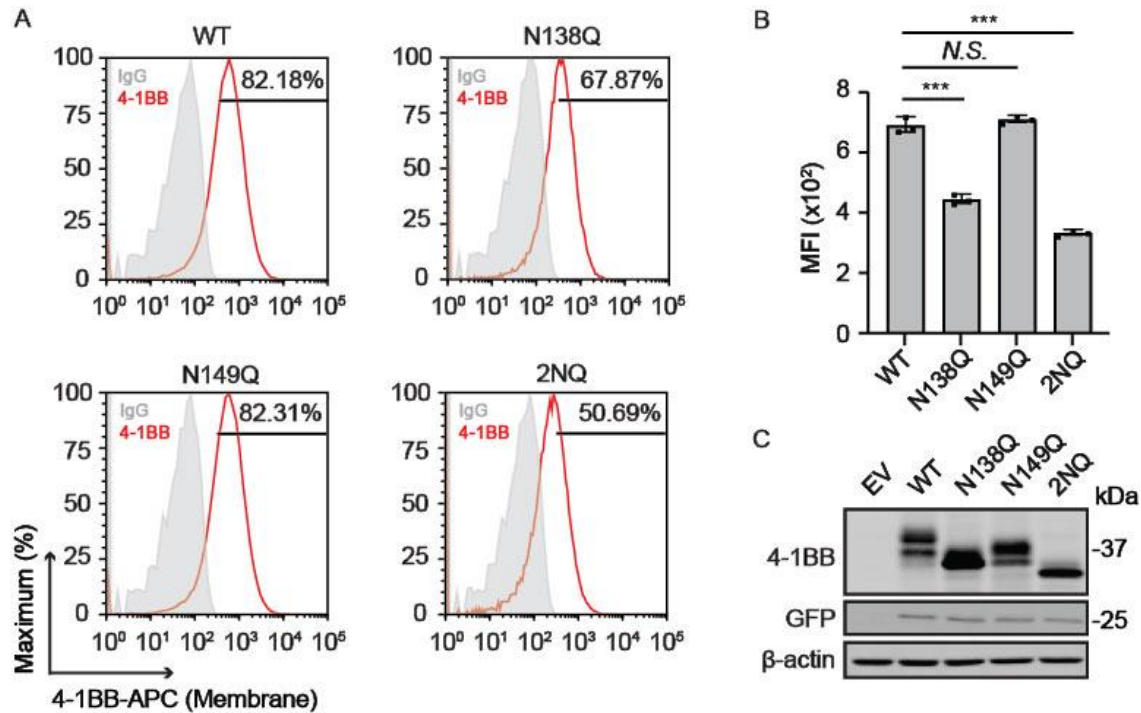


Figure 3.2. The cell surface level of 4-1BB is determined by *N*-glycosylation. (A) Jurkat cells were transduced with lentivirus encoding 4-1BB WT and glycosylation-deficient mutant including N138Q, N149Q and 2NQ, respectively. The membrane levels of 4-1BB in each group were compared by flow cytometry. The percentages of positive events were included in the plots. (B) The quantitative results of membrane 4-1BB level in each group in (A) ($n = 3$). (C) The IB analysis of total 4-1BB from cells in (A). Results represent mean \pm SD. One-way analysis of variance (ANOVA) was applied for statistical analysis in (B). *N.S.*, $p > 0.05$; ***, $p < 0.001$; MFI, mean fluorescence intensity.

3.2.4 4-1BB is destabilized by *N*-glycosylation

Another well-characterized role of *N*-glycosylation is to regulate the stability of modified substrates³⁸⁰. Accordingly, we were interested to learn whether 4-1BB protein turn-over is determined by *N*-linked glycans. As illustrated in the CHX-chase assay in Fig 3.3, 4-1BB is markedly stabilized when lacking the *N*-glycosylation sites. which is the opposite of many reported glycosylated immune receptors³²⁴. Specifically, N138 seems to elicit a more profound impact augmenting 4-1BB stability compared to N149.

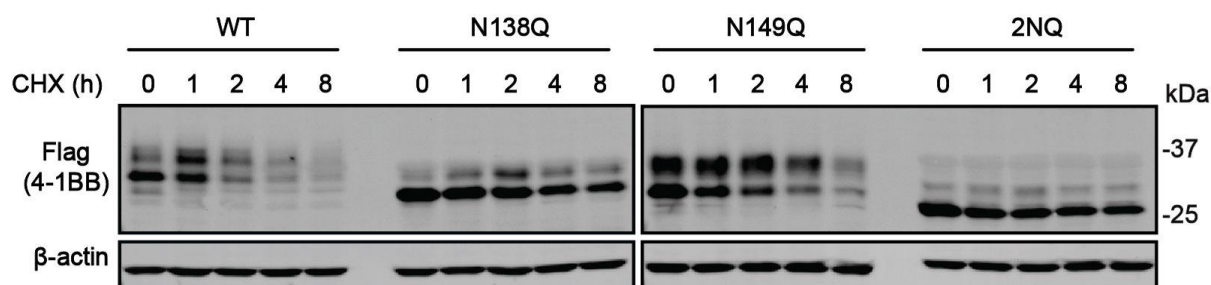


Figure 3.3. *N*-glycans stabilize 4-1BB. Indicated 4-1BB plasmids were transfected to HEK293T for CHX-chase assay (0-8 h).

Realizing the protein stabilization by *N*-glycans, we then sought to explain how the alteration occurred. Unlike the 4-1BB WT, which was markedly upregulated upon proteasome antagonism, only mild accumulation was observed on 4-1BB 2NQ upon MG-132 treatment (Fig 3.4 A), suggesting that UPS-mediated degradation of 4-1BB was influenced by *N*-glycosylation. As demonstrated in Fig 3.4 B, the 2NQ mutation of 4-1BB showed a decreased level of polyubiquitination compared to WT, which matched with our assumption. At this point, we concluded that *N*-glycosylation facilitates the rapid degradation of 4-1BB through the ubiquitin-proteasome pathway. According to our data in Chapter 2, 4-1BB can be ubiquitinated on its intracellular domain (K214, K218, K219 and K225), which guides its proteasomal degradation. Some E3 ubiquitin ligases are known to ubiquitinate the glycosylated substrates by recognizing the *N*-glycan moieties³⁷⁰; however, no reports have shown transmembrane E3 ligases that recognize extracellular *N*-glycan degon of substrates and conjugate ubiquitin molecules on the cytosolic sites. As such, we investigated the potential mechanisms to explain the vastly increased stability of non-*N*-glycosylated 4-1BB.

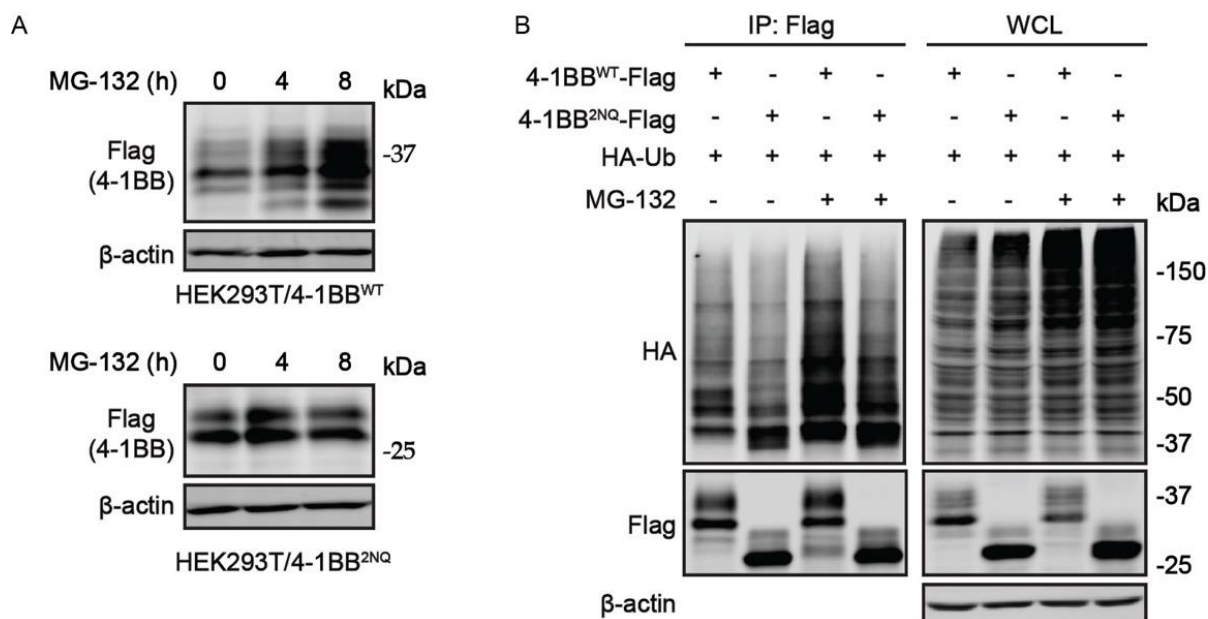


Figure 3.4. The increased stability of 4-1BB 2NQ was accompanied by decreased polyubiquitination and proteasomal degradation. (A) IB analysis of MG-132 effect on 4-1BB WT and 2NQ. HEK293T/4-1BB WT and HEK293T/4-1BB 2NQ cells were treated by 10 μ M MG-132 for 0, 4 and 8 h followed by IB assay. (B) Comparison of polyubiquitination level between WT and 2NQ 4-1BB. 4-1BB-Flag and HA-Ub plasmids were co-transfected to HEK293T cells followed by *in vivo* ubiquitination assay 48 h after transfection. IP, immunoprecipitant. WCL, whole cell lysate.

3.2.5 *N*-glycosylation-deficient 4-1BB is more intensively multimerized

Protein-protein interaction of oligomerization could be regulated by *N*-glycosylation^{381,382}. By performing non-reducing SDS-PAGE, we noticed substantially enhanced covalent 4-1BB oligomerization was formed by 2NQ but not WT (Fig 3.5 A). The ectodomain of 4-1BB is composed of four CRDs which are the hallmark structures of the TNFRSF receptor family³⁸³. As illustrated by previous structural investigations^{188,189}, 20 out of 21 cysteine residues in the extracellular domain are used to form intramolecular disulfide bonds, allowing C121 to be the only unpaired cysteine can possibly be used to create an intermolecular disulfide bond to stabilize 4-1BB dimers^{188,189}. As displayed in Fig 3.5 B, the oligomerization of 4-1BB 2NQ was largely diminished when a C-to-A mutation was introduced to C121. We also saw that BFA treatment could also enforce 4-1BB multimerization gradually in a time-dependent manner (Fig S10), suggesting the formation of 4-1BB multimer exist in ER.

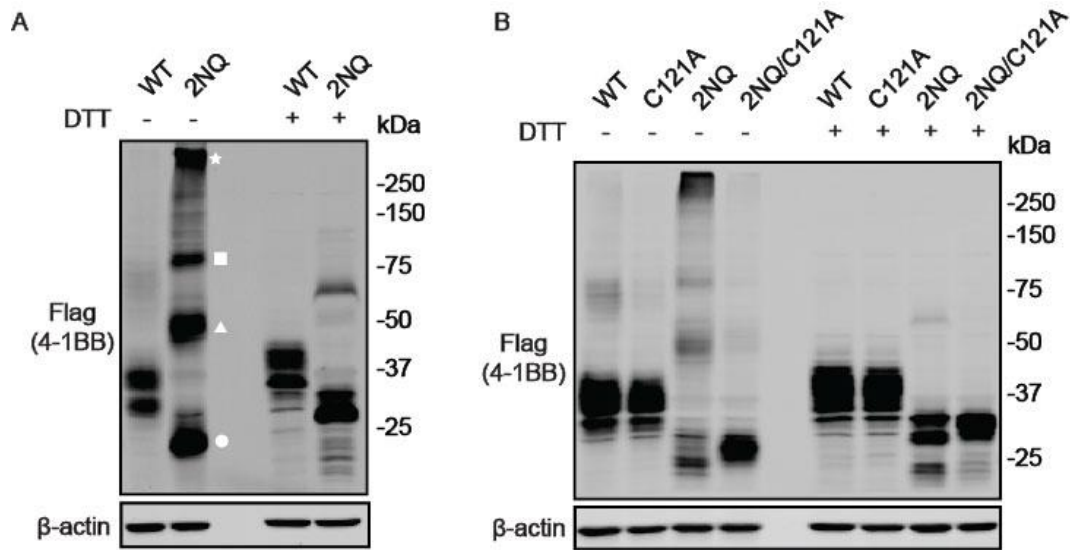


Figure 3.5. Unglycosylated 4-1BB form covalent multimer through C121 residue. (A) Plasmids were transfected to HEK293T cells before sample harvesting. Non-reducing SDS-PAGE uncovered the formation of dimerized, trimerized and oligomerized 4-1BB 2NQ. The major bands exist in the presence of DTT (lane 4 and 5) were considered monomers. The white circle, triangle, square and star represent monomerized, dimerized, trimerized and oligomerized form of 4-1BB 2NQ. (B) 4-1BB 2NQ failed to form multimer when lacking the key cysteine residue C121 (lane 3 v.s. 4). Sample preparation process was identical to (A).

We then aimed to explain the influence of glycans to C121 by performing structurally analysis. Fortunately, a recently published work successfully obtained the 4-1BB structure possessing both N138 and N149-linked sugar moiety³⁸⁴. As indicated in Fig 3.6, similar orientation was shared by the sulfite atom of C121 with N138 but not N149-linked glycan, which might explain why N138 plays a more decisive role in regulating the property (stability and localization) of 4-1BB.

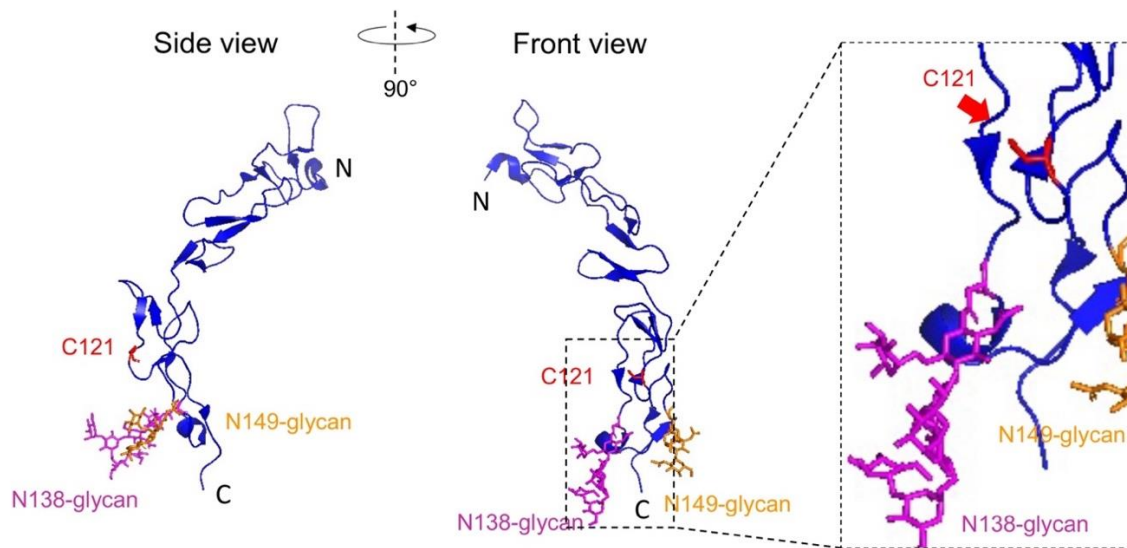


Figure 3.6. Topological analysis showing the relative position and orientation of C121 residue N138-linked carbohydrate of human 4-1BB. The protein structure was obtained from PDB #7D4B and modified using PyMOL 2.5. Blue, 4-1BB ectodomain; Magentas, N138-linked glycan; Orange, N149-linked glycan; Red, C121 residue.

As we expected, the slow turn-over of 4-1BB 2NQ was also rescued by the C121A mutation (Fig 3.7), suggesting that *N*-linked carbohydrate is not a stringent prerequisite of 4-1BB membrane transportation as long as the C121-mediated multimerization remains absent.

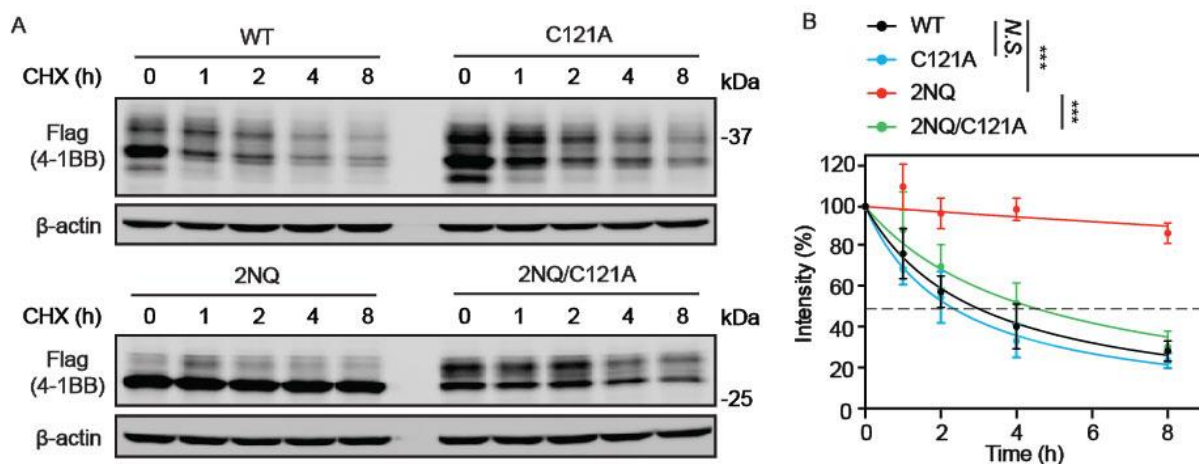


Figure 3.7. Oligomerization is coupled with augmented stability of non-*N*-glycosylated 4-1BB. (A) HEK293T cells were transfected with Flag-tagged 4-1BB WT, C121A, 2NQ and 2NQ/C121A followed by CHX-chase assay to compare their stability. (B) The quantification of the remaining 4-1BB at each time points ($n = 3$). The percentage values of band intensity were normalized to time 0 h. 50% degradation was indicated by the dashed line. Results represent mean \pm SD. One-way ANOVA was performed to compare the percentage values on 8 h point. Monoexponential decay curve was used for data exhibition. *N.S.*, $p > 0.05$; ***, $p < 0.001$.

To further inspect whether the turn-over of 4-1BB is associated with membrane transportation, we compared the surface level of 4-1BB 2NQ with that of 4-1BB 2NQ/C121A. As shown in Fig 3.8 A and B, in the absence of the C121-mediated disulfide bond, *N*-glycosylation-deficient 4-1BB exhibited comparable expression to WT, which is much higher than 2NQ. The lentivirus transduction load was confirmed identical across all groups (performed as Fig S8) before MFI calculation. The overall expression of 4-1BB 2NQ and 2NQ/C121A are similar, despite the altered ratio of the two bands (Fig 3.8 C). In addition, we generated the ECD truncation of 4-1BB WT and mutants and compared their secretion in cell culture medium. As demonstrated in Fig S11, 4-1BB^{ECD} 2NQ showed minimal secretion which could be rescued by depleting the S-S bridge by C121. Collectively, we proposed the model whereby *N*-glycosylation of 4-1BB hinders the C121-mediated aggregation, hence allowing 4-1BB to be correctly delivered via the secretory pathway to the cell membrane, from which it undergoes ubiquitination-triggered degradation.

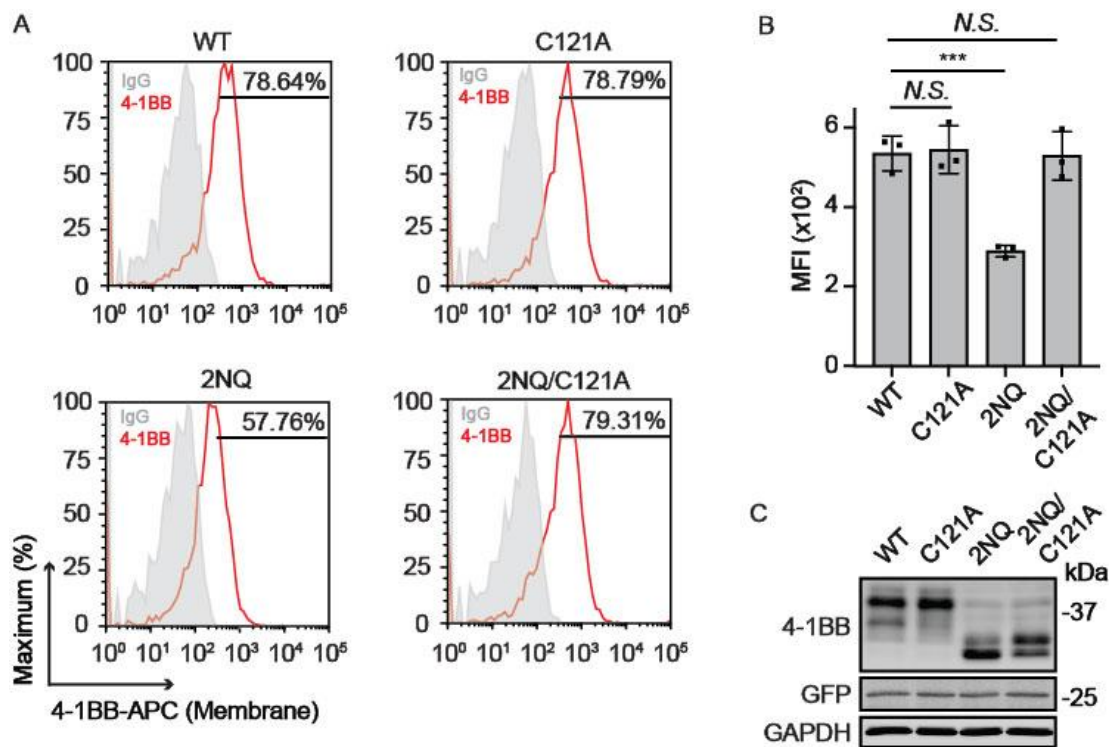


Figure 3.8. C121-mediated multimerization governs the localization of non-*N*-glycosylated 4-1BB. (A) Jurkat cells were transduced with lentivirus encoding 4-1BB WT, C121A, 2NQ and 2NQ/C121A, respectively. The membrane levels of 4-1BB in each group were compared by FACS. The percentages of positive events were included in the plots. (B) The quantitative results of membrane 4-1BB level in each group in (A) ($n = 3$). (C) The IB analysis of total 4-1BB from each group of cells in (A). Results represent mean \pm SD. *N.S.*, $p > 0.05$; ***, $p < 0.001$ (one-way ANOVA); MFI, mean fluorescence intensity.

3.2.6 A modified form of 4-1BB 2NQ is membrane-localized and sensitive to UPS-degradation

Since the loss of *N*-glycans could not completely block the membrane expression of 4-1BB, we set out to characterize which fraction of 4-1BB 2NQ represents the surface-bound form. By performing membrane proteome enrichment assay displayed in Fig 3.9 A, we surprisingly saw that the membrane-localized 4-1BB is mainly constituted by the additional band of 4-1BB 2NQ (Fig 3.8 C). The estimated MW of flag-tagged 4-1BB 2NQ is 26.3 kDa which is likely the major band which migrates faster. We hereby hypothesized that the upper band is generated by another type of modification which licensed 4-1BB 2NQ to travel through secretory pathway to cell membrane. In Fig 3.9 B, the membrane form of 4-1BB 2NQ responded to MG-132 treatment, which matches our previous discovery that membrane-localized form of 4-1BB is subjected to UPS-mediated degradation. Likewise, the elevated membrane expression and degradation rate of 4-1BB 2NQ/C121A over 2NQ was also accompanied by the accumulated upper band. On the other hand, CQ led to a substantive accumulation of 4-1BB WT but not 2NQ (both bands, Fig 3.9B), suggesting the autophagic degradation work on 4-1BB by a distinct mode. These findings collectively suggested the even more complicated crosstalk among PTMs on 4-1BB.

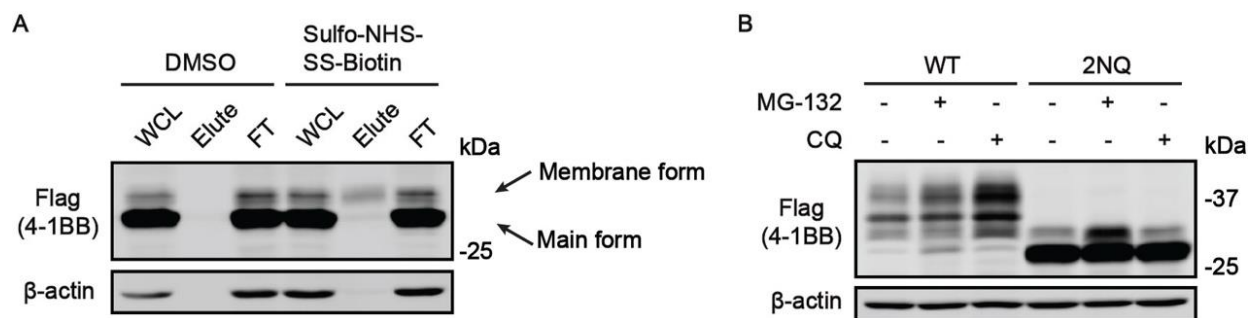


Figure 3.9. A subset of 4-1BB 2NQ is membrane-bound and proteasomally degraded. (A) Enrichment of membrane-associated 4-1BB 2NQ by sulfo-NHS-SS-biotin labeling strategy. The membrane proteome of Jurkat/4-1BB cells was labeled, enriched, and analyzed by IB. (B) The IB result of 4-1BB from HEK293T/4-1BB 2NQ cells treated with 50 μ M CQ or 10 μ M MG-132 for 8 h. WCL, whole cell lysate. FT, flow-through.

3.3 Discussion

Glycosylation refers to the conjugation of carbohydrate chains to predominantly protein substrates, but also lipids³¹⁰ and even nucleic acids³⁰⁸. *N*-linked glycosylation is a frequently

occurring, post-translational modification of proteins in the context of immune receptors. Its enormous complexity makes the site-specific dissection and manipulation of protein *N*-glycosylation extremely challenging³⁸⁵. The predicted molecular weight of human 4-1BB (with C-terminus Flag tag) without signal peptide is about 26.3 kDa, which is far lower than the molecular weights of two major bands observed on SDS-PAGE (approximately 32 and 40 kDa), thus suggesting significant structural, and potentially functional, contributions of *N*-linked glycans to 4-1BB.

Our study is the first report focusing on the biological value of *N*-glycosylation to the immune activation receptor 4-1BB. Specifically, human 4-1BB undergoes *N*-glycosylation on N138 and N149 for its maturation and membrane localization, and the glycan moieties indeed caused the molecular weight increase compared to the theoretical value. Mechanistically, once the *N*-linked oligosaccharide chains are no longer conjugated to 4-1BB, the under-glycosylated protein will alternatively use its free cysteine residue, C121, to form disulfide bond-mediated dimers and oligomers, which become considerably more stable than monomers and consequently cannot be appropriately trafficked towards the cell membrane. Similarly, other TNFRSF members such as CD40 or GITR can appear disulfide bond-stabilized dimer, suggesting the diverse oligomeric states of these receptors to be dissected^{386,387}. Given that *N*-glycosylation serves as a quality control step in protein synthesis and folding, and abnormal glycan structures can mark the protein for ER-associated degradation (ERAD), we asked why the *N*-glycosylation-deficient 4-1BB was neither eradicated by ERAD nor became less stable. Since ERAD is initiated by the recognition of abnormally glycosylated protein³⁸⁸, we reasoned that the *N*-glycosylation-deficient 4-1BB does not contain the structural signature that triggers ERAD. Still, we cannot reject the possibility that *N*-glycosylated 4-1BB undergoes abnormal glycosylation and is consequently disposed through ERAD mechanism. In addition to prior publications, which only reported the dimerized form of 4-1BB, we observed the existence of DTT-sensitive trimers and oligomers as well (especially for 2NQ), suggesting there might be additional free cysteine residues exposed owing to the conformational change caused by the abnormality of 4-1BB *N*-glycosylation. Another possible explanation is that some other proteins may serve as a hub to covalently tether multiple monomeric 4-1BB together which appeared as oligomer-like bands on DTT-free SDS-PAGE. The disappearance of oligomerization after mutation of one cysteine residue was also reported on Tau protein³⁸⁹. Nonetheless, our original dissection of 4-1BB 2NQ dimerization was based on the

previous literature; however, we could not exclude the possibility that the dimer band we observed was heterodimerized protein instead of 4-1BB homodimer. Without the capability of high yield membrane protein purification, we may need to rely on mass spectrometry to identify the composition of the dimer and even oligomer bands. One intriguing finding, which we were not able to outline yet, is that there are two distinct bands of 4-1BB 2NQ exhibited on SDS-PAGE. The major band which migrated faster is likely to be the Flag-tagged 4-1BB 2NQ protein, therefore, we presumed that the upper band (membrane form) refers to some type of modification that creates a molecular weight increase. The intensity ratio between the upper and lower band was significantly increased when the C121A mutation was included (Fig 3.7 and 3.8), indicating this specific modification is directly influenced by the thiol group on C121. Nonetheless, in-depth investigations should be carried out to characterize the difference between these two species, as well as the molecular mechanisms by which they are generated in cells.

In closing, we described a novel mechanism by which the organization and localization of 4-1BB are directed by *N*-linked glycan. Our findings manifested the correlation between the *N*-glycosylation status and membrane expression of the promising immunotherapy target 4-1BB. The individual *N*-glycosylation landscape could be harnessed as an indicator to predict the clinical efficacy of 4-1BB agonism therapy.

CHAPTER 4. CONCLUSIONS AND FUTURE DIRECTIONS

4.1 Conclusions

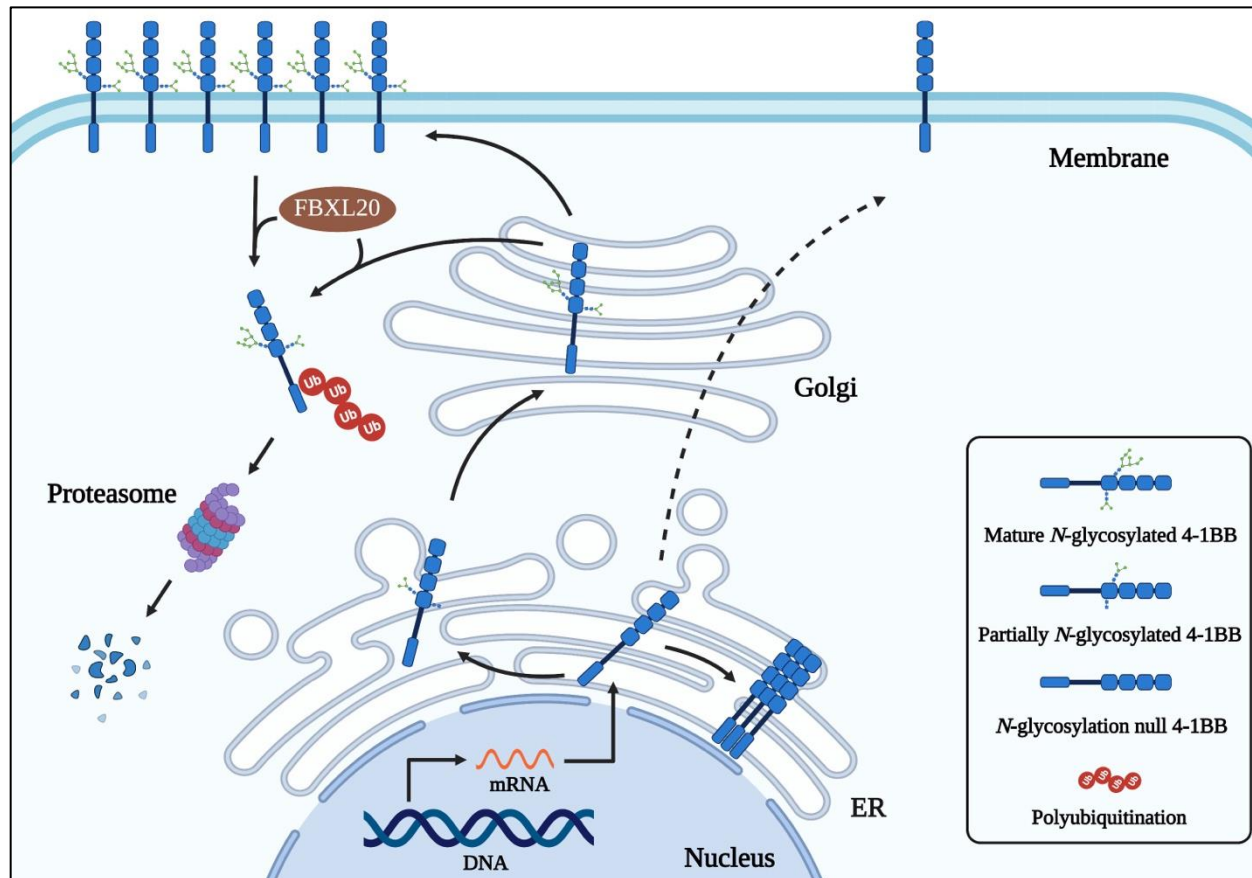


Figure 4.1. A graphic summary of the observations in this study. The figure was created on BioRender.

This present study focused on the molecular regulation of 4-1BB by PTMs. The two major findings (as illustrated in Fig 4.1) include:

1) Mature 4-1BB undergoes FBXL20-mediated polyubiquitination for degradation. 4-1BB is a heavily *N*-glycosylated protein which can be detected as multiple *N*-glycoforms in cells. The fully *N*-glycosylated (mature) 4-1BB can be ubiquitinated by the E3 ligase FBXL20 and degraded through ubiquitin-proteasome machinery. The ubiquitination sites of 4-1BB locates near the junction of transmembrane and cytoplasmic domain.

2) *N*-glycosylation facilitates membrane transportation of 4-1BB. The membrane-associated 4-1BB predominantly consists of the mature form which undergoes quick turnover as well. C121 residue of 4-1BB is masked by *N*-linked sugar moiety naturally. For partially *N*-glycosylated 4-1BB, however, C121 is exposed and used to form intermolecular disulfide bond which promotes 4-1BB multimerization. Unlike the native, monomeric one, the multimerized 4-1BB is intracellular retained and resistant to proteasomal degradation.

4.2 Questions to be answered

It was fortunate for me to be able to test some hypotheses with respect to 4-1BB post-translational regulation. Despite that, some hypotheses and concerns were regrettably unsolved. In this section I will summarize the questions (some of them have been covered in previous sections) raised from the current data and hopefully can be answered in the future.

Question 1: What other E3 ligases can act on 4-1BB? In the first part of this study, FBXL20 was identified through PL as one E3 ligase that promotes 4-1BB ubiquitination. Nevertheless, knockdown and overexpression of FBXL20 resulted in a significant but limited change of 4-1BB expression which suggests additional enzymes regulating 4-1BB abundance. Now high throughput approaches such as CRISPR screen with Ub library are available which can potentially be used to study the degradation of 4-1BB and other immune receptors^{390,391}.

Question 2: Is 4-1BB degraded divergently upon stimulation compared to resting status? The abundance and activity of immune receptors are tightly regulated to maintain the threshold of action. It has been shown that 4-1BB is increasingly transcribed upon antibody-mediated co-stimulation, which theoretically requires additional mechanisms to rapidly remove the extra 4-1BB protein.

Question 3: What is the molecular basis of covalent 4-1BB oligomerization? The results in part 2 clearly showed the presence of covalently formed 4-1BB oligomer; however, the handful number of structural analyses up to date can hardly explain the formation of homomultimer of 4-1BB as only one free cysteine residue is exposed. A proteomic investigation using purified, unglycosylated and oligomerized 4-1BB protein can be very helpful to answer whether 4-1BB monomers are tethered by some other proteins to make it appear like oligomers.

Question 4: What underlines the upper band on 4-1BB 2NQ (upper band in short)? We learned from part 2 that first, the upper band represent the membrane-bound, MG-132-sensitive

fraction of 4-1BB 2NQ; second, mutation of C121 on 4-1BB 2NQ led to increased abundance of the upper band. These messages suggested that the *N*-glycans are not strictly necessary for 4-1BB membrane transportation. Indeed, the upper band may confer a decisive mechanism governing 4-1BB localization regardless of glycosylation status.

4.3 Future directions

The existence of target protein and the functional molecular pathway are the foundation of drug therapy. Without the positive expression of the target, drugs will not be able to work efficaciously (which is defined as target-missing resistance by some scholars). The understanding of 4-1BB processing, transportation and degradation will potentially support the drug development for different purposes. For example, the systematic toxicity of ipilimumab is associated with drug-induced CTLA-4 degradation which led to the loss of checkpoint function. It has been shown that the suboptimal balance of efficacy and safety profile of CTLA-4 therapy can be improved by the pH-insensitive antibodies which enables CTLA-4 endosomal recycling³⁹². ONC-392, an antibody designed to block and preserve cell surface CTLA-4 simultaneously, has entered clinic for assessment (NCT04140526). As introduced before, 4-1BB serves versatile roles on different cell types. For instance, signal activation antibodies may strengthen the anti-tumor activity of CTLs and NK cells; On the contrary, antibodies which guide the internalization and degradation of 4-1BB might be employed in patients who display abundant 4-1BB⁺ T_{reg} cells in TME.

The severe liver damage largely halted the development of 4-1BB therapy. Urelumab and Utomilumab as two extremes have both been proved impractical for clinical practice especially as single agent. Accumulating evidence has outlined that 4-1BB agonist-induced hepatotoxicity is caused by activation of liver-resident immune cells^{238,239}. A growing collection of 4-1BB-targeting strategies are being tested aiming to achieve both effectiveness and safety profile (Table 4.1). It has been proposed by Qi *et al.* that weak agonistic antibodies which rely on FcγRIIB-mediated crosslinking to elicit maximized agonistic activity may confer minimal toxicity since FcγRIIB does not induce antibody dependent cellular cytotoxicity (ADCC)³⁹³. Accordingly, many antibodies have been developed and some of which are under early clinical investigations now^{393–397}. Some studies presented safe pro-antibodies (probodyes) that are locally activated by tumor-associated proteases³⁹⁸, hypoxia³⁹⁹, and elevated extracellular ATP⁴⁰⁰. Multi-specific antibodies (or peptides) which activate 4-1BB in the presence of one or several other cancer-associated molecules (*e.g.*,

HER2, PD-L1, *etc.*) may bypass liver toxicity by enhancing tumor local accumulation of drug^{197,401–409}. In the meantime, protein engineering focusing on 4-1BBL which is the natural agonist of 4-1BB signaling has also achieved amazing successes and some has entered the clinical investigation stage. These attempts usually involve the genetic fusion of 4-1BBL to an mAb targeting TME-associated molecules such as CD19⁴¹⁰, FAP⁴¹¹, fibronectin⁴¹², *etc.*

Table 4.1. Some representative studies aiming to overcome 4-1BB-related liver toxicity.

Name	Type	Mechanism	References
LVGN6051	Fc-optimized antibody	FcγR-dependent	Qi <i>et al.</i> ³⁹³ ; Fu <i>et al.</i> ³⁹⁴
AGEN2373	Fc-optimized antibody	FcγR-dependent	Tolcher <i>et al.</i> ³⁹⁵
ATOR1017	Fc-optimized antibody	FcγR-dependent	Ullenhag <i>et al.</i> ³⁹⁶
CTX-471	Fc-optimized antibody	FcγR-dependent	Eskiocak <i>et al.</i> ³⁹⁷
Anti-CD137 Pb-Tx	Probody	Activated by tumor-associated proteases	Etxeberria <i>et al.</i> ³⁹⁸
SW _{REDOXa} 4-1BB	Probody	Activated by tumor-associated hypoxia	Zhao <i>et al.</i> ³⁹⁹
STA551	Probody	Activated by tumor-associated ATP	Kamata-Sakurai <i>et al.</i> ⁴⁰⁰
PRS343	Multi-specific antibody	4-1BB x HER2	Hinner <i>et al.</i> ⁴⁰¹
PRS344	Multi-specific antibody	4-1BB x PD-L1	Peper-Gabriel <i>et al.</i> ⁴⁰²
GEN1046	Multi-specific antibody	4-1BB x PD-L1	Garralda <i>et al.</i> ⁴⁰³
GEN1042	Multi-specific antibody	4-1BB x CD40	Johnson <i>et al.</i> ⁴⁰⁴
702 TJ-CD4B	Multi-specific antibody	4-1BB x Claudin18.2	Jiang <i>et al.</i> ⁴⁰⁵
4-1BB ^{N/C} EGFR	Multi-specific antibody	4-1BB x EGFR	Compte <i>et al.</i> ¹⁹⁷ ; Compte <i>et al.</i> ⁴⁰⁶
MP0310	Multi-specific antibody	4-1BB x FAP	Link <i>et al.</i> ⁴⁰⁷
NM21-1480	Multi-specific antibody	4-1BB x PD-L1 x HSA	Snell <i>et al.</i> ⁴⁰⁸
BT7480	Multi-specific peptide	4-1BB x Nectin 4	Hurov <i>et al.</i> ⁴⁰⁹
RG6076	Fusion protein	4-1BBL-anti-CD19	Herter <i>et al.</i> ⁴¹⁰
RG7826	Fusion protein	4-1BBL-anti-FAP	Claus <i>et al.</i> ⁴¹¹
F8-4-1BBL	Fusion protein	4-1BBL-anti-EDA of fibronectin	Mock <i>et al.</i> ⁴¹²

Immune receptors are membrane proteins; however, they may serve comprehensive functions in distinct subcellular compartments. It has been proposed that nucleus resident PD-L1 act as a transcription co-factor that drives the expression of pro-inflammatory and antigen-presentation genes^{413,414}. So far there is no report showing any TNFR-independent function of 4-1BB. We identified several components of the nuclear pore complex (*e.g.*, NDC1, NUP155) or nucleus membrane proteins (*e.g.*, LEMD3, LRRC59) by 4-1BB PL, which suggest potential roles played by 4-1BB in the perinuclear region. As for the glycosylation study in Chapter 3, we have not been able to explain the formation of “4-1BB oligomer” with existing knowledge. Native-PAGE examination of purified protein may help answer whether 4-1BB itself can form oligomer, and proteomics study can help identify whether there are additional proteins complex with 4-1BB to generate heterooligomer.

Given that glycosylation is fundamental to various biological processes, it is unsurprising to see efforts focusing on targeting protein glycosylation for therapeutic purposes. Instrumental and computational advances have been made for profiling and sequencing of *N*-glycan⁴¹⁵⁻⁴¹⁷. Systematic disruption of protein glycosylation may induce unacceptable side effects. Targeted glycan modification, however, could preserve the pharmacological effect with minimized adverse effects. Works have demonstrated the concept of selective glycan-editing using antibody-glycosidase conjugate but are limited to cultured cell lines⁴¹⁸⁻⁴²⁰. As protein design and evolution are being widely exploited in academia and industry for generating eligible tools to solve biological problem⁴²¹, we may expect more precise targeting of tissue-specific glycosylation in the future.

Immunotherapy has been validated as a vital component in clinical oncology. With the lessons we learned from the past decade from both benchside and bedside, many new questions have arisen and needs to be focused on the next stage. Chen *et al.* summarized the ten critical challenges we encountered after over ten years’ practice of immunotherapy clinically⁴²²:

1. Development of pre-clinical models that translate to human immunity.
2. Determining the dominant drivers of cancer immunity.
3. Understanding organ-specific tumor immune contexture.
4. Understanding the molecular and cellular drivers of primary versus secondary immune escape
5. Elucidating the benefit of endogenous versus synthetic immunity.

6. Effective and efficient assessment of cancer immunotherapy combinations in early-phase clinical studies.
7. Full characterization of the impact of steroids and immune suppression on cancer immunotherapy and autoimmune toxicities.
8. Maximizing personalized approaches through composite biomarkers.
9. Developing improved regulatory endpoints for cancer immunotherapy.
10. Optimizing long-term survival with multi-agent cancer immunotherapy combination regimens.

The challenges listed above, which covers perspectives ranging from optimizing pre-clinical research models to personalized drug development, need to be carefully answered to more cancer immunology and immunotherapy forward to the next era. Advanced genomics, proteomics and imaging approaches will assist both the laboratory research and clinical diagnostics. It might remain unrealistic to anticipate immunotherapy as the “cure” for cancer therapy in the coming years, yet the expansion and utilization of the knowledge of immuno-oncology will allow more patients to experience a refined anti-tumor immunity which to a large extent is indispensable to cancer treatment.

CHAPTER 5. MATERIALS AND METHODS

5.1 Instruments and materials

5.1.1 Instruments

The instruments (self-owned and shared) used in this dissertation can be found in table 5.1.

Table 5.1. The list of equipment (parental and self-established) used in this study.

Name	Vendor	Catalog #
Milli-Q Direct Water Purification System	Millipore	ZR0Q008WW
MSC-Advantage™ Class II Biological Safety Cabinet	Thermo Scientific	51028226
Forma™ Steri-Cycle™ i60 CO2 Incubator	Thermo Scientific	50145522
Primovert Microscope	Zeiss	491206-0001-000
Attune NxT Flow Cytometer	Thermo Scientific	A29001
LSE 49 Liter Incubator	Corning	CLS6750
NanoDrop One	Thermo Scientific	ND-ONE-W
Locator™ Plus Rack and Box System	Thermo Scientific	CY509109
Tube Revolver Rotator	Thermo Scientific	88881001
Model 120 Sonic Dismembrator	Fisherbrand	FB120110
Cimarec+™ Hotplate	Thermo Scientific	SP88857100
Digital Dry Baths/Block Heater	Thermo Scientific	88870001
Compact Digital Dry Bath/Block Heater	Thermo Scientific	88871004
Vari Mix Platform Rocker	Thermo Scientific	M79735
Legend Micro 21 Centrifuge	Thermo Scientific	75002437
Legend Micro 21R Centrifuge	Thermo Scientific	75002445
Sorvall ST16R Centrifuge	Thermo Scientific	75004381
MySpin 6 minicentrifuge	Thermo Scientific	75004061
MUPID-EXU Submarine electrophoresis system	Takara Bio	AD140
LP vortex mixer	Thermo Scientific	88880017
LED illuminator	Gel company	TLB-01
Imagel	Gel company	GDR-500
Heratherm™ Compact Microbiological Incubator	Thermo Scientific	50125590

Table 5.1 Continued

Odyssey CLx imaging system	Li-COR	
Precision Balance AMF104	Fisherbrand	S94790B
Precision Balance AMF602	Fisherbrand	S94791C
Precision General Purpose Baths GP-10	Fisherbrand	TSGP10
Isotemp™ general purpose deluxe water bath GPD-2S	Fisherbrand	FSGPD2S
PowerPac Basic Power Supply	Bio-Rad	1645050
Mini-PROTEAN Tetra System	Bio-Rad	1658001FC
Synergy LX Multi-mode reader	Bio-Tek	SLXASI
T100 Thermal Cycler	Bio-Rad	1861096
CFX Connect Real-time PCR Detection System	Bio-Rad	1855201
Octet RED384 system	Forte Bio (Now Sartorius)	OCTET RED384

5.1.2 Cell lines

The cell lines used in this dissertation can be found in table 5.2.

Table 5.2. The list of cell lines (parental and self-established) used in this study.

Cell line	Description	Origin
HEK293T	Human embryonic kidney cells	Takara Bio
HEK293FT	Human embryonic kidney cells	Thermo Scientific
Jurkat (E6-1)	T lymphocytes	ATCC
HEK293T/4-1BB WT	HEK293T stably expresses human 4-1BB (WT)	In house
HEK293T/4-1BB 2NQ	HEK293T stably expresses human 4-1BB (N138Q/N149Q)	In house
HEK293FT/BioID2	HEK293FT stably expresses BioID2-HA	In house
HEK293FT/4-1BB-BioID2	HEK293FT stably expresses 4-1BB-BioID2-HA	In house

5.1.3 Chemical reagents

The chemicals (including those used for cell-based experiments) used in this dissertation can be found in table 5.3.

Table 5.3. The list of chemical reagents used in this study.

Name	Vendor	Catalog #
2-Mercaptoethanol	Fisher Scientific	BP176-100
2-Propanol	Fisher Scientific	A415-4
Absolute Ethanol	Fisher Scientific	BP2818-4
Acetic Acid, Glacial	Fisher Scientific	BP1185-500
Acrylamide (30%)	National Diagnostic	50-899-90118
Agarose	Fisher Scientific	BP1356-500
Ammonium Persulfate	Fisher Scientific	BP179-100
Ampicillin Sodium Salt	Fisher Scientific	BP1760-5
Aprotinin	Sigma Aldrich	A1153-10MG
Bio-Glo luciferase substrate	Promega	G7940
Brefeldin A	Cayman Chemical	11861
Brilliant Blue G-250	Fisher Scientific	B392-5
Bromophenol Blue	Fisher Scientific	A1420703
Buffer PB Binding buffer	Qiagen	19066
Buffer PE Wash buffer	Qiagen	19065
Buffer QG Solubilization buffer	Qiagen	19063
Chloroform	Fisher Scientific	C298-500
Chloroquine Diphosphate	ACROS Organics	455240250
Cycloheximide	ACROS Organics	357420010
D (+) Biotin	Alfa Aesar	A1420703
Dimethyl Sulfoxide	Sigma Aldrich	D8418-500mL
Dithiothreitol	Fisher Scientific	BP172-25
Ethylenediaminetetraacetic Acid, Disodium Salt	Fisher Scientific	BP120-500
GelGreen® Nucleic Acid Gel Stain	Biotium	41005
Glycerol	Affymetrix	16374 500mL
Glycine	Fisher Scientific	G45-212
HEPES	Fisher Scientific	BP310-100
Immobilon®-FL Membrane	Millipore	IPFL00010
Leupeptin	Sigma Aldrich	L2884-10MG
Lipofectamine RNAiMAX transfection reagent	Invitrogen	13778075

Table 5.3 Continued

Lithium Chloride	Fisher Scientific	L121-100
Methanol	Fisher Scientific	A412-20
MG-132	Selleckchem	S2619
Nonidet™ P40 Substitute	Affymetrix	19628-500ML
Passive lysis buffer (5 x)	Promega	E1941
PBS (10 x)	Bioland Scientific	PBS01-03
Pepstatin A	Sigma Aldrich	P5318-5MG
PMSF	Sigma Aldrich	78830-5G
Polybrene	Santa Cruz	sc-134220
Ponceau S	Alfa Aesar	AAJ60744
PR-619	ApexBIO	A8212
Puromycin	Invivogen	ant-pr-1
Sodium Chloride	Fisher Scientific	S271-1
Sodium Deoxycholate	Alfa Aesar	J6228814
Sodium Dodecyl Sulfate	Fisher Scientific	BP8200500
Sodium Fluoride	Fisher Scientific	S299-100
Sodium Hydroxide	Fisher Scientific	S318-1
Sodium Vanadate	Fisher Scientific	S454-50
Sulfo-NHS-SS-Biotin	APEXBIO	A8005
TEMED	Fisher Scientific	BP150-20
Tris Base	Fisher Scientific	BP152-10
Triton X-100	Fisher Scientific	BP151-500
TRIzol reagent	Invitrogen	15596026
Tween-20	Fisher Scientific	20605 500ML
Urea	Fisher Scientific	BP169 500
X-treme GENE HP DNA transfection reagent	Roche	06 366 236 001

5.1.4 Biological reagents

The biological reagents including antibodies, enzymes, recombinant proteins and cell culture materials, *etc.*, are listed in table 5.4.

Table 5.4. The list of biological reagents used in this study.

Name	Vendor	Catalog #
Human 4-1BB protein (6 x His tagged)	Acro Biosystems	41B-H52Hc
Anti-Flag tag	Sigma Aldrich	F1804
Anti-Flag tag agarose	Sigma Aldrich	A2220
Anti-Flag tag	CST	2368S
Anti-HA tag	CST	3724S
Anti-Myc tag	CST	2278S
Anti-4-1BB	CST	34594S
Anti-His	CST	12698S
Anti- β -actin	Santa Cruz	sc-47778
Anti-GAPDH	CST	5174
Anti-GFP	Santa Cruz	sc-9996
Anti-LC3A/B	CST	12741
Anti-human CD137, APC	BD	561702
IRDye® 800 streptavidin	Li-Cor	926-32230
IRDye® 800CW Goat anti-Rabbit IgG	Li-Cor	926-32211
IRDye® 680RD Goat anti-Mouse IgG	Li-Cor	926-68070
KpnI-HF	NEB	R3142S
NheI-HF	NEB	R3131S
NotI-HF	NEB	R3189S
HindIII-HF	NEB	R3104S
XbaI	NEB	R0145S
XhoI-HF	NEB	R0146S
DpnI	NEB	R0176S
Phusion® High-Fidelity DNA Polymerase	NEB	M0530S
Quick ligation kit	NEB	M2200S
NEBuilder® HiFi DNA Assembly Master Mix	NEB	E2621S
PNGase F	NEB	P0704S
Rapid PNGase F	NEB	P0710S
High-Capacity Streptavidin Agarose	Thermo Scientific	20357

Table 5.4 Continued

3 x Flag peptide	APExBIO	A6001
Quick ligation kit	NEB	M2200S
LB agar	RPI	L24030-100.0
LB broth	Fisher Scientific	BP1426-500
2XYT broth	RPI	X15600-100.0
Bovine serum albumin	Fisher Scientific	BP1605-100
Dry powder milk	RPI	M17200-500.0
TrypLE Express Enzyme (1 x)	Gibco	12604021
DMEM (high glucose, pyruvate)	Gibco	11995065
RPMI 1640	Cytiva	SH30255.01
Opti-MEM	Gibco	31985070
X-treme GENE HP DNA transfection reagent	Roche	06 366 236 001
Lipofectamine RNAiMAX	Invitrogen	13778030
Fetal bovine serum	Corning	35010CV
Penicillin-Streptomycin (10,000 U/ml)	Gibco	15140122
HEPES (1M)	Gibco	15630080
Sodium Pyruvate (100 mM)	Gibco	11360070
L-glutamine (100 mM)	Gibco	25030081
Dry powder milk	RPI	M17200-500.0
SsoAdvanced Universal SYBR Green Supermix	Bio-Rad	1725272
O'GeneRuler 1 kb DNA Ladder	Thermo Scientific	SM1163
O'GeneRuler 1 kb DNA Ladder	Thermo Scientific	SM1153

5.1.5 Kits

All commercial kits used in this study are listed in table 5.5.

Table 5.5. The list of kits used in this study.

Name	Vendor	Catalog #
BCA protein assay kit	Thermo Scientific	23225
QIAprep Spin Miniprep Kit	Qiagen	27106
HiSpeed Plasmid Midi Kit	Qiagen	12643
iScript cDNA Synthesis Kit	Bio-Rad	1708890
Zenoquick Competent E. Coli Transformation Kit	GenDEPOT	Z6001-001

5.1.6 Buffer preparation

Radio-Immunoprecipitation Assay (RIPA) cell lysis buffer. 50 mM Tris-HCl (pH 7.5), 150 mM NaCl, 1% (v/v) NP-40, 0.1% (w/v) SDS, 1 mM EDTA, 0.5% (w/v) Sodium Deoxycholate, 1 µg/mL pepstatin A, 2 µg/mL aprotinin, 2 µg/mL leupeptin and 1 mM PMSF.

NP-40 lysis buffer. 50 mM Tris-HCl (pH 7.5), 150 mM NaCl, 0.5% (v/v) NP-40, 1 mM EDTA, 1 µg/mL Pepstatin A, 2 µg/mL Aprotinin, 2 µg/mL leupeptin and 1 mM PMSF.

6 x Laemmli sample buffer. 375 mM Tris-HCl, 9% (w/v) SDS, 50% (v/v) Glycerol, 0.03% (w/v) Bromophenol blue.

10 x TBS. 200 mM Tris, 1.5 M NaCl.

10 x Running buffer. 250 mM Tris, 1.92 mM Glycine, 1% (w/v) SDS.

10 x Transfer buffer. 250 mM Tris, 1.92 mM Glycine.

Ponceau S staining buffer. 0.1% (w/v) Ponceau S, 5% acetic acid.

Blocking buffer. 5% (w/v) skim milk in TBST.

Antibody dilution buffer. 3% (w/v) BSA in TBST.

Coomassie blue staining buffer. 0.25% (w/v) G-250, 50% (v/v) ddH₂O, 40% (v/v) MeOH, 10% (v/v) acetic acid.

Coomassie blue destaining buffer. 60% (v/v) ddH₂O, 30% (v/v) MeOH, 10% (v/v) acetic acid.

BioID lysis buffer 1. 50 mM Tris-HCl (pH 7.4), 500 mM NaCl, 0.4% SDS, 5 mM EDTA, 1 mM DTT.

BioID lysis buffer 2. 50 mM Tris-HCl (pH 7.4).

BioID wash buffer 1. 2% (w/v) SDS.

BioID wash buffer 2. 50 mM HEPES (pH 7.5), 0.1% (w/v) Sodium Deoxycholate, 1% (v/v) Triton X-100, 500 mM NaCl, 1 mM EDTA.

BioID wash buffer 3. 10 mM Tris-HCl (pH 8.0), 250 mM LiCl, 0.5% (v/v) NP-40, 0.5% (w/v) Sodium Deoxycholate, 1 mM EDTA.

BioID wash buffer 4. 50 mM Tris-HCl (pH 7.4), 50 mM NaCl.

FACS wash buffer. 0.5% BSA, 2 mM EDTA in PBS.

5.1.7 Oligonucleotides

All DNA and siRNA (sequence not provided) oligoes used in my study were purchased from Integrated DNA Technologies. The oligonucleotide sequences are displayed in Table 5.6.

Table 5.6. The list of DNA oligoes used in this study.

Molecular cloning	
Name	Sequence 5'-3'
4-1BB_KpnI_F	CGGGGTACCATGGGAAACAGCTGTTACAACATAGTAG
4-1BB_Flag_NotI_R	TTTTCCTTTTGCGGCCGCTCACTTATCGTCGTCATCCTTGTAATCC AGTTCACATCCTCCTTCTTCTTCTTCTGG
4-1BB_NheI_F	CTACTAGCTAGCATGGGAAACAGCTGTTACAACATAGTAGCC
4-1BB_ECD_His6_XhoI_R	CGGCTCGAGTCAGTGGTGATGGTGATGATGCTGCGGAGAGTGTC CTGG
hCD137_K225R_mut_F	GTATATATTCAGACAACCATTATGAGAC
hCD137_K225R_mut_R	AGGAGTTTCTTTCTGCCC
hCD137_K219R_mut_F	GGGCAGAAAGAGACTCCTGTATATATTC
hCD137_K219R_mut_R	CGTTTAACAACAGAGAAACG
hCD137_K214R_mut_F_2	GTTTCTCTGTTGTTAGACGGGGCAGAAAGAG
hCD137_K214R_mut_R_2	CTCTTTCTGCCCCGTCTAACAACAGAGAAAC

Table 5.6 Continued

hCD137_K218 R_mut_F_2	GTTGTTAGACGGGGCAGAAGGAGACTCCTGTATATATTC
4- 1BB_N138Q_mut_F	ACCCTGGACACAGTGTTCTTTGG
4- 1BB_N138Q_mu t_R	CGACAGATGCCACGTTTC
4- 1BB_N149Q_mu t_F	TGTGCTTGTGCAAGGGACGAAGG
4- 1BB_N149Q_mu t_R	GACTTTCCATCCAAAGAAC
h4- 1BB_C121A_VF	AGACTGTGCGTTTGGGACATTTAACG
h4- 1BB_C121A_IR	GTCCCAAACGCACAGTCTTTACAACC
h4-1BB_myc_IR	GGGGGAGGGAGAGGGTCACAGATCCTCTTCAGAGATGAGTTTC TGCTCCAGTTCACATCCTCCTTCTTCTTCTTC
EGFP EcoRI R	CCGGAATTCTTACTTGTACAGCTCGTCCATGC
pHR2.1_VF	CAAGTAAGAATTCGGGGCTTATCGATAATCAACCTCTGGATTAC
pHR2.1_VR	CCATGGTGGCGGTACCGGCTGTCCACCTGCCTTGCTC
myc-T2A_VR	CTGCCCTCTCCACTGCCAGATCCTCTTCAGAGATGAGTTTC
T2A_F	GGCAGTGGAGAGGGCAGAG
pHR2_h4- 1BB_IF	AGGCAGGTGGACAGCATGGGAAACAGCTGTTACAACATAGTAG
pHR2_h4- 1BB_VR	AACAGCTGTTTCCCATGCTGTCCACCTGCCTTGCTC
m4-1BB_NheI_F	CCCCCGCTAGCATGGGAAACAACCTGTTACAACGTG
m4-1BB_NotI_R	CCCCCGCGGCCGCTCACTTATCGTCGTCATCCTTGTAATCCAGC TCATAGCCTCCTCCTC
FBXL20_KpnI_F	GGGGTACCAGGAGGGACGTGAACGGAG
FBXL20_XhoI_ R	CCGCTCGAGTCATAGGATGATGCAGCATCTGCAG
FBXL20_dF- box_HiFi_R	CAAATAGGTCTTCATCACTATTTGAGAACATCTCAAACC
FBXL20_dF- box_HiFi_F	TAGTGATGAAGACCTATTTGATTTCCAGAGGGATATTG
BioID2_KpnI_F3	CCGGTACCGCCACCATGGGCTTCAAGAACCTGATCTGGCTGAA GG
pGIPZ_BioID2_ R	GCCCATGGTGGCGGTACCGGCCTCTAGTAGAGTCGGTGTCTTC

Table 5.6 Continued

HA_R_XbaI	GCTCTAGACTATGCGTAATCCGGTACATCGTAAGG
pGIPZ_HA_F	GATTACGCATAGTCTAGAGCAAGTAGCGGCCGCAAATTCC
Vector(B)_GGG GS_R	GGAGGCGGTGGATCTTTCAAGAACCTGATCTGGCTGAAGG
4- 1BB_GGGGS_R	AGATCCACCGCCTCCCAGTTCACATCCTCCTTCTTCTTCTG G
Vector_4-1BB_F	ATGGTGGCAAGCTTGGGCCCCAAGCTTGGGTCTCCCTATAGTGA G
4- 1BB_HindIII_F2	GGGCCCAAGCTTGCCACCATGGGAAACAGCTGTTACAACATAG TAG
qRT-PCR	
Name	Sequence 5'-3'
hACTB_F_2	AGAGCTACGAGCTGCCTGAC
hACTB_R_2	AGGAAGGAAGGCTGGAAGAG
hCD137_F	CGCTCCGTTTCTCTGTTGTTA
hCD137_R	GCTACAGCCATCTTCCTCTTG
hFBXL20_F	TAGCCAGGTGAAGCATTGAG
hFBXL20_R	AGAGGGTGCTTCTTCTTGGA

5.1.8 Software

The software used in this dissertation can be found in table 5.7.

Table 5.7. The list of software used in this study.

Name	Developer
Office 365	Microsoft
Illustrator 2022	Adobe
Image Studio 5.2	Li-Cor
SnapGene 6.0	SnapGene
Prism 9	GraphPad
Attune™ NxT software	Invitrogen
PyMOL 2.5	Schrodinger

5.2 Experimental procedures

5.2.1 Cell culture

HEK293T, HEK293FT, H1975, B16F10 cells were maintained in DMEM medium supplemented with 10% FBS and 1 x Pen-Strep. Jurkat cells were maintained in RPMI 1640 medium with 10% FBS, 1 x Pen-Strep, 2 mM L-glutamine, 10 mM HEPES, 1 mM sodium pyruvate. HDLM-2 cells were maintained in RPMI 1640 medium with 20% FBS, 1 x Pen-Strep. All cells were kept in humidified incubators with 5% CO₂ at 37 °C.

5.2.2 Molecular cloning

Recombinant DNA constructs were established for gene expression and phenotype studies. The process of molecular cloning involves several steps which will be described in the following paragraphs.

Polymerase Chain Reaction (PCR). The addition of new restriction enzyme sites or epitope tags to inserted DNA fragments were achieved by PCR.

Set up the reaction mixture on ice following the table below:

Component	25 µl reaction	50 µl reaction	Final concentration
Nuclease-free water	16.75 µl	32.5 µl	
5 x HF or GC buffer	5 µl	10 µl	1 x
10 mM dNTPs	0.5 µl	1 µl	200 µM
10 µM Forward Primer	1.25 µl	2.5 µl	0.5 µM
10 µM Reverse Primer	1.25 µl	2.5 µl	0.5 µM
Template DNA (0-10 ng/µl)	1 µl	1 µl	0-10 ng
Phusion polymerase	0.25 µl	0.5 µl	1.0 unit/50 µl PCR

Note: GC buffer works better for the amplification of vector (> 10 kbp).

Mix the reaction mixture thoroughly and spin down on a minicentrifuge. Set up the thermo cycles on a PCR machine:

Step	Temperature	Time
Initial denaturation	98 °C	30 s
25-35 cycles	98 °C	10 s
	T _m	30 s
	72 °C	30 s / kb
Final extension	72 °C	2 min
Hold	4 °C	

The PCR product can be immediately subjected to the downstream applications or stored at -20 °C.

DNA electrophoresis. To make agarose gels for DNA electrophoresis, mix agarose with TAE buffer at a concentration of 0.5-1% in a glass flask. Cover the flask with plastic wrap and poke a few holes for air release. Boil the mixture using microwave oven for about 1 min until the mixture is clear. Leave the liquified gel for a few minutes for chilling down, then add DNA dye and mix well by shaking. Pour the gel in the cassette and allow at least 30 min for solidification, then pull out the comb gently and place the gel (with the tray) in the electrophoresis tank filled with TAE buffer. To prepare the samples, mix 5 volumes of DNA solution with 1 volume of loading dye (6 x), then carefully load the samples in the gel wells.

DNA purification from PCR reaction. Add 5 volumes of PB buffer to PCR product, mix well by agitation, then transfer the mixture into a QIAquick column. Spin down the column at 10,000 x g for 1 min, discard the flow through, then wash the column with 700 µl PE buffer. Spin down the column at 10,000 x g for 1 min, discard the flow through, then spin again at 15,000 x g for 1 min to remove the residue buffer. Place the column on a microcentrifuge tube and add 20 µl ddH₂O and let the column stand for 1 min. Centrifuge at 20,000 x g for 1 min to elute DNA. the DNA concentration was measured using NanoDrop.

DNA recovery from agarose gels. After DNA electrophoresis, place the agarose gel under the UV imager and excise the DNA band with a clean blade. Weigh the gel slice in a microcentrifuge tube and add 3 volumes of QG buffer to 1 volume of gel (add 300 µl buffer to 100 mg gel slice). For DNA fragments < 600 bp or > 6 kb, add 1 volume of isopropanol to increase the recovery yield. Incubate the mixture at 50 °C for about 10 min until gels are completely dissolved. Transfer the mixture to a QIAquick column. Spin down the column at 5,000 x g for 1 min, discard

the flow through, then wash the column with 700 μ L PE buffer. Spin down the column at 15,000 x g for 1 min, discard the flow through, then spin again at 20,000 x g for 1 min to remove the residue buffer. Place the column on a microcentrifuge tube and add 20 μ L ddH₂O and let the column stand for 1 min. Centrifuge at 20,000 x g for 1 min to elute DNA. the DNA concentration was measured using NanoDrop spectrophotometer.

Restriction enzyme digestion. Mix 1 μ L enzyme A, 1 μ L enzyme B, 2 μ L 10 x Cut Smart buffer, 16 μ L DNA (containing 1 μ g DNA and fill the rest with ddH₂O). Incubate the mixture at 37 °C for 1 h. (Note: some enzymes may have different optimal temperatures. Refer to the manufactures' recommendations to set up the digestion reaction). Mix 5 volumes of digestion product with 1 volume of loading dye (6 x), then perform agarose gel electrophoresis followed by DNA recovery (as described above).

DNA ligation. A 1:5 molar ratio was applied to ligate a linearized empty vector (1) with a short insert fragment (5). The ligation reaction was usually done with 50 ng vector DNA, and the mass of insert DNA can be calculated by NEBioCalculator (<https://nebiocalculator.neb.com/#!/ligation>). Mix the vector DNA, insert DNA, 0.5 μ L Quick ligase and 5 μ L 2 x Quick ligation buffer at a total volume of 10 μ L in a microcentrifuge tube. Let the mixture stand at room temperature overnight for sufficient ligation.

HiFi assembly. HiFi assembly was applied when there was no proper choice of restriction enzyme, or when > 3 DNA fragments were to be assembled. Briefly, blunt end vector and insert DNA fragments were acquired by PCR reaction. To achieve high recombination yield, a 20 bp overlap region between fragments with a > 48 °C T_m should be created though PCR primer design. Mix 50 ng vector DNA and 3 folds (molar ratio) of insert DNA fragments, then fill the volume to 5 μ L with ddH₂O. Add 5 μ L 2 x Master Mix and incubate the mixture at 50 °C for 1 h. To assemble 1 vector with 2 insert DNA fragments, apply 1:3:3 molar ratio. Place the assembly product in 4 °C.

Point mutation using Q5[®] Site-Directed Mutagenesis Kit. Some of the point mutation plasmids were constructed by the Q5[®] Site-Directed Mutagenesis Kit. The mutagenesis primers were designed by the online tool NEBaseChanger (<https://nebasechanger.neb.com/>).

Point mutation by a kit-free site-directed mutagenesis method. Another quick and efficient approach to achieve the point mutation is through homologous recombination.

Bacterial transformation. Take aliquoted DH5 α competent cells out of -80 °C freezer and thaw on ice. Mix 1-10 μ L DNA product into 25 μ L of competent cells and mix thoroughly by flicking

the tube. Place the DNA/competent cell mixture on ice for 30 min. The required amount of DNA depends on the quality of the competent cells. Place the mixture in a 42°C water bath for 45 s to allow transformation, then put back on ice immediately for chilling down. Add 1 ml plain LB broth medium to the transformation mixture and grow the bacteria in a 37°C shaking incubator for 1 h. Pellet the cells by centrifugation at 1,000 x g for 2 min, pour the medium out and leave ~100 µl. Resuspend the cells by pipetting and transfer to LB agar plates (containing appropriate antibiotic) for streaking (by pipette tip or glass beads). Incubate the plate for 12-16 h.

Plasmid purification. Pick at least two E. Coli colonies (large, round, isolated colonies are better) from overnight-cultured agar plates and culture in 4 ml LB broth (containing appropriate antibiotic) for 20-24 h in a 37°C shaking incubator. Pellet cells at 10,000 x g for 1 min and discard the medium.

The extraction of plasmid DNA was achieved by using QIAprep Spin Miniprep Kit. The plasmid constructions were confirmed by Sanger sequencing (Purdue Genomics core facility or Genewiz) or diagnostic enzyme digestion before use. The plasmids used for this study (purchased and in house-generated) are summarized in table 5.8.

Table 5.8. The list of plasmids used in this study.

Name	Origin
pcDNA3	In house
pcDNA3-myc	In house
pcDNA3-HA-Ub WT	In house
pcDNA3-HA-Ub 7KR	In house
pMD18-T-h4-1BB ORF	Sino Biologics # HG10041-M
pcDNA3-h4-1BB WT-Flag	In house
pcDNA3-h4-1BB 4KR-Flag	In house
pcDNA3-h4-1BB N138Q-Flag	In house
pcDNA3-h4-1BB N149Q-Flag	In house
pcDNA3-h4-1BB N138/149Q-Flag	In house
pcDNA3-h4-1BB C121A-Flag	In house
pcDNA3-h4-1BB C121A/N138Q/N149Q-Flag	In house
pcDNA3.1-m4-1BB-Flag	GeneScript #OMu18167
pCDH-CMV-MCS-Puro	System Biosciences # CD510B-1

Table 5.8 Continued

pCDH-CMV-h4-1BB WT-Flag	In house
pCDH-CMV-h4-1BB 4KR-Flag	In house
pCDH-CMV-h4-1BB 2NQ-Flag	In house
PX458	Addgene #48138
pHR-SFFV	Addgene #79121
pHR-SFFV-EGFP	In house
pHR-SFFV-h4-1BB WT-T2A-EGFP	In house
pHR-SFFV-h4-1BB 4KR-T2A-EGFP	In house
pHR-SFFV-h4-1BB N138Q-T2A-EGFP	In house
pHR-SFFV-h4-1BB N149Q-T2A-EGFP	In house
pHR-SFFV-h4-1BB N138/149Q-T2A-EGFP	In house
pHR-SFFV-h4-1BB C121A-T2A-EGFP	In house
pHR-SFFV-h4-1BB C121A/N138Q/N149Q-T2A-EGFP	In house
pcDNA3-4-1BB WT ECD-6xHis	In house
pcDNA3-4-1BB C121A ECD-6xHis	In house
pcDNA3-4-1BB N138Q/N149Q ECD-6xHis	In house
pcDNA3-4-1BB C121A/N138Q/N149Q ECD-6xHis	In house
pcDNA3.1-MCS-BioID2-HA	Addgene #74224
pGIPZ-TurboGFP	In house
pGIPZ-BioID2-HA	In house
pGIPZ-h4-1BB-BioID2-HA	In house
pLenti6.3/V5-FBXL20	DNASU #HsCD00942792
pcDNA3-myc-FBXL20	In house
pcDNA3-myc-FBXL20 dF-box	In house
pGreenFire1-NFkB-EF1-Neo	System Biosciences #TR012PA-N
pGreenFire1-NFkB-EF1-Puro	In house

5.2.3 Transfection

Plant HEK293T cells in 6-well plate and let them reach 50-70% confluency which achieves optimal transfection efficiency. To perform transfection, add 1 μ g plasmid to 200 μ l Opti-MEM medium in a low-binding microcentrifuge tube and mix well by brief vortex. Add 2.5 μ l XtremeGENE HP DNA Transfection Reagent (TR) to the plasmid mixture and vortex briefly. Keep

the mixture standing at room temperature for 10 min to allow the formation of DNA-complex. Meanwhile, replace the culture medium of HEK293T with 2.3 mL pre-warmed Opti-MEM. Add the transfection mixture to HEK293T dropwise, gently swirl the plate, then incubate cells at 37 °C, 5% CO₂ for 6 h. Replace Opti-MEM with 3 mL fresh culture medium. The transfection can also be done overnight. Harvest the cell/protein/RNA samples 24 or 48 h after transfection depending on the protein expression level.

5.2.4 Lentivirus packaging & Stabling cell line establishment

Lentivirus packaging. The lentivirus is packaged by the second-generation lentiviral systems composed of pMD2.G, psPAX2 and desired transfer vector. The packaging was done using HEK293T cells line which was designed for high yield lentivirus production. 1 µg lentivirus transfer plasmid, 0.5 µg pMD2.G and 0.75 µg psPAX2 were co-transfected to HEK293T cells. Maintain the cells for 48 h and harvest the supernatant which contains lentivirus particles. Centrifuge the supernatant at 2,000 x g for 10 min to remove the cell debris to get the clarified lentivirus samples which can be either directly used for transduction or stored at 4 °C (less than 1 week) or -80°C (long-term) for future use.

Transduction. Grow cells in 10 cm dish (adherent cells) or T25 flask (suspension cells) at appropriate density (~10% for adherent cells and 0.5 x 10⁶/ml for suspension cells). Replace the old medium by fresh complete medium with lentivirus sample. 0.8 µg/ml polybrene was added to enhance transduction efficiency (except Jurkat cells). Incubate the cells with lentivirus for 24 h, then with fresh complete medium for another 24 h, then start antibiotics selection (for 1 week) if necessary.

5.2.5 Immunoblotting assay

The relative abundance of a given protein in the bulk cell lysate was determined by immunoblotting (IB), which is broadly used, semi-quantitative method.

Sample preparation. The cell samples were prewashed with ice-cold PBS and harvested in ice-cold RIPA buffer for 30 min. The sample was sonicated to enhance protein extraction efficiency. Afterwards, the cell lysates were clarified by centrifugation at 20,000 x g for 15 min. The clear supernatant was transferred to new tubes and the protein concentrations were quantified

with BCA kit. By mixing cell lysate with calculated volume of 6 x and 1 x Laemmli sample buffer, samples in the same set were normalized (usually 1-2 mg/ml) for sample loading. The samples can be kept in 4 °C for less than 2 days and -20 °C for long-term storage.

Gel casting. Sodium dodecyl sulfate polyacrylamide gel electrophoresis (SDS-PAGE) gels were hand-casted for electrophoresis. First, prepare clean inner and outer glasses and assemble gel casting cassettes. Then, prepare the resolving gel mixture (for 2 gels):

Component	Volume	
	8%	10%
30% Polyacrylamide	4 ml	5 ml
1.5 M Tris-HCl (pH 8.8)	3.75 ml	3.75 ml
ddH ₂ O	6.95 ml	6.95 ml
10% SDS	150 µl	150 µl
TEMED	7.5 µl	7.5 µl
10% APS	150 µl	150 µl

Mix the resolving gel solution thoroughly and immediately pour ~7 ml of it into each glass cassette (0.1 cm thickness). Overlay the resolving gel with 1 ml isopropanol. Allow 30-60 min for the resolving gel to solidify. Then pour the isopropanol off and wash the top of resolving gel with ddH₂O, then dry the area above the resolving gel using filter paper. Prepare the stacking gel mixture (for two gels):

Component	Volume
30% Polyacrylamide	0.8 ml
0.5 M Tris-HCl (pH 6.8)	1.5 ml
ddH ₂ O	3.6 ml
10% SDS	60 µl
TEMED	6 µl
10% APS	60 µl

Mix the stacking gel solution thoroughly and immediately pour it above the resolving gel layer to the top edge of the inner glass. Insert the comb into the stacking gel and allow 30 min for polymerization. The gels can be wrapped by wet paper towel (with comb) and stored in 4 °C for up to two weeks.

Electrophoresis. Remove the combs carefully from stacking gels and rinse the wells with ddH₂O. Place the gels in electrophoresis tank and add enough running buffer. A total of 20-30 µg protein samples were loaded on gels and set the voltage to 80 V initially to allow sample electrophoresis. When the entire samples enter the stacking gel, increase the voltage to 120 V and keep running. When samples enter the resolving gel (the protein size marker bands start to separate), increase the voltage to 180 V and keep the sample running until the bromo phenol blue bands are ~1 cm to the bottom of the gels.

Transferring. Wash the gels in fresh transfer buffer for a few minutes. Meanwhile, prepare the PVDF membranes by incubating them in methanol for 15 s, H₂O for 5 s, and then fresh transfer buffer. Assemble the transfer sandwich (sponge-filter paper-gel-membrane-filter paper-sponge) and place the cassette in transfer tank filled with transfer buffer at 4 °C. Transfer at 250 mA for 1.5-3 h depending on the sizes of target proteins. After transfer, incubate the membrane in Ponsceus staining buffer for a few seconds to make sure the transfer was done at high quality. Rinse the Ponsceus stain with fresh transfer buffer for a few minutes until the membrane is colorless. Rinse again with TBST.

Blocking. Place the membranes in blocking buffer and incubate on a shaker for 30 min.

Antibody incubation. Incubate the blocked membranes with primary antibodies diluted in antibody dilution buffer. Incubate the blot at 4 °C overnight with end-to-end shaking. One the next day, remove the primary antibody and wash the blot 3 times for 10 min with enough volume of TBST. Subsequently, add the secondary antibody diluted in blocking buffer for 1 h at room temperature with end-to-end shaking. Wash the blots 3 times for 10 min with enough volume of TBST.

Visualization and analysis. Place the blot on the Odyssey imager and acquire the blot images with Image Studio software. The absolute band intensities were also acquired in Image Studio.

5.2.6 Coomassie blue staining.

To directly visualize protein on polyacrylamide gels, the protein samples were prepared and separated as described above. The gels were then washed by ddH₂O quickly and by destaining buffer for 10 min. Subsequently, add enough staining buffer that can submerge the gels and stain at room temperature with slow shaking for 1 h. The staining buffer was then collected for future

use. Gels were washed initially by destaining buffer 3 times for 10 min, and then overnight with shaking (until the background is clear). The buffer used for the 3 quick washes can be heated (but not boiled) which enhances the wash efficiency. Before imaging, discard the destaining buffer and wash the gel multiple times by ddH₂O. place the gels on the scanner for image acquisition.

5.2.7 Immunoprecipitation

The physical interactions between proteins were determined by performing immunoprecipitation assay.

Sample preparation. Cells were pre-washed by PBS and lysed in NP-40 lysis buffer on ice for 30 min. The sample clarification and quantification were described in the “immunoblotting” section. Totally 0.5-1 mg protein was incubated with antibody-conjugated beads overnight on a rotor placed in 4 °C refrigerator. Take 10% sample and boil with Laemmli buffer to get whole cell lysate (WCL) samples.

Elution. Afterwards, the samples were centrifugated at 2000 x g for 2 min and supernatant was discarded. 1 mL fresh, ice-cold NP-40 buffer was used for washing the beads. The washing step was repeated for four times. After the last wash, leave approximately 100 µl buffer with the beads and add 20 µl 6 x Laemmli buffer (with 2-ME), mix thoroughly by vortexing and place the sample on 95 °C heat plate for 10 min to elute the bead-bond proteins (IP samples). The IP samples and WCL samples were loaded together on the SDS-PAGE gels according to the experiment set up. The following procedures for analysis are identical to the standard immunoblotting protocol.

5.2.8 *In vivo* ubiquitination assay

The *in vivo* ubiquitination assay was exploited to evaluate the poly-ubiquitination level of proteins in live cells. The cells were treated with 20 µM MG-132 for 6 h, then lysed in NP-40 buffer with extensive sonication. 1% of SDS was added to the cell lysate and incubate on 95 °C heat plate for 10 min to dissociate non-specifically binding proteins. Afterwards, add 9-fold fresh NP-40 buffer to the lysate to reach 0.1% SDS at the end, which is usually adaptive to affinity-pulldown. The following steps were identical to the section of “Immunoprecipitation”.

5.2.9 Cycloheximide (CHX) chase assay

The CHX-chase assay was performed to compare the stability of: 1) proteins harboring different mutants, 2) the same protein in the presence of different drug treatment. On day 1, cells were split and cultured in 12- or 24-well plates overnight to allow attachment. On day 2, add 100 μ M CHX to each well and harvest cell samples on indicated time points. The cell pellets were stored in a -80 °C freezer temporarily until all samples were obtained. If the protein of interest is not expressed endogenously, alternatively perform transient transfection of the corresponding plasmids on day 1 and split cells to multi-well plates when transfection was completed (6 h is usually sufficient). If the experiment was for comparing protein degradation under MG-132 or CQ treatments, the reagents should be added 2 hours prior to the starting of CHX treatment. DMSO should also be added simultaneously to the control groups. The following protein extraction and IB analysis were executed as described in the section of “Immunoblotting”. The relative intensities values were normalized against β -actin at the corresponding time points, and 0 h was considered 100%. The experiment should be done in at least triplicate to get quantitative results.

5.2.10 PNGase F digestion

The *N*-linked glycosylation of 4-1BB is analyzed by glycosidase treatment. 4-1BB-expressing cells were lysed in NP-40 buffer and subjected to PNGase F following the protocol provided by the manufacturer. For assays involving ligand binding, the protein was digested by PNGase F following non-reducing protocol. The enzymatic digestion results were analyzed by IB or Coomassie blue staining as described above.

5.2.11 Membrane protein labeling and enrichment

To label membrane-bound proteins, cells were washed twice with ice-cold PBS. Cells were incubated with 1 mg/mL sulfo-NHS-SS-biotin (freshly prepared) for 30 min at 4 °C. The extra biotinylation reagent was quenched by adding 100 mM glycine in PBS, and total protein was extracted in RIPA buffer with vigorous sonication (until no visible clump remains). The biotinylated protein was isolated with high-capacity streptavidin agarose overnight at 4 °C and eluted by sample buffer with 2-ME. All samples were analyzed by IB.

5.2.12 RNA extraction and qRT-PCR

RNA extraction. Total cellular RNA was extracted using Trizol reagent following the guidance. All following steps were executed with RNase-free equipment. Cell samples were pellet and lysed in 0.5 mL Trizol reagent. 0.1 mL chloroform was added to the clear lysate and vortex rigorously for 15 s to allow sufficient RNA solubilization. Incubate the mixture for 3 min at room temperature, then centrifuge for 15 min at $12,000 \times g$ at 4°C . Carefully transfer the aqueous phase to a new tube and add 0.25 mL isopropanol to precipitate the RNA. After 15 min incubation, centrifuge for 10 min at $12,000 \times g$ at 4°C . carefully discard the supernatant and wash the precipitate with 75% ethanol. After 5 min centrifugation at $7500 \times g$ at 4°C , discard the ethanol and dry the RNA precipitate completely. Resuspend the RNA in appropriate volume of ddH₂O and measure the concentration on NanoDrop.

cDNA synthesis and qRT-PCR. The relative levels of transcripts were quantified by qRT-PCR. cDNA was synthesized using 1 μg total cellular RNA with iScript cDNA Synthesis Kit following the manufacturers' instruction. qRT-PCR was performed with SsoAdvanced Universal SYBR Green Supermix on a CFX96 real-time PCR system. The relative gene expression was normalized to human β -actin and calculated by $\Delta\Delta\text{Cq}$ method. The primer specificity was validated by the single peak on melting curve.

5.2.13 Determination of 4-1BB/4-1BBL binding affinity

The K_D value of 4-1BB/4-1BBL interaction was determined by Octet Biolayer interferometry (BLI) using the Octet RED384 system. Briefly, the native and deglycosylated 6 x His-tagged 4-1BB proteins (prepared as the “5.2.10 PNGase F digestion” section) were loaded on the Octet NTA biosensor at a concentration of 200 nM. The association step was performed by submerging the sensors in a single concentration of 4-1BBL (50 mM) in the kinetic buffer. Dissociation was performed and monitored in fresh kinetic buffer. Data were analyzed with Octet Analysis HT software (Sartorius). The K_D value was calculated based on a 1:1 binding ratio.

5.2.14 Detection of cell surface 4-1BB

All following steps were executed on ice or at 4°C . Cells after drug treatment or lentivirus transduction were washed with FACS wash buffer twice. 10^6 cells were incubated with antibody

diluted in 100 μ l FACS wash buffer for 30 min on a rotator. After incubation, cells were washed with 1 mL FACS wash buffer three times and loaded on flow cytometer for analysis. Data analysis was performed on Attune NxT software.

5.2.15 Mass spectrometry

For the LC-MS/MS detection of ubiquitinated 4-1BB peptides, Flag-tagged 4-1BB (expressed in HEK293T) was purified using anti-Flag M2 affinity resin and eluted using 3 x Flag peptide (100 μ M/ml in 1 x PBS). Cells were pre-incubated with 20 μ M MG-132 for 4 h for enrichment of ubiquitinated protein. The immunoprecipitated protein was resolved and collected from SDS-PAGE. To employ BioID assay, we first established HEK293FT cell lines stably expressing pGIPZ-h4-1BB-BioID2-HA or pGIPZ-BioID2-HA constructs. Cells were treated by 50 μ M D (+) biotin for 24 h to biotinylate the promiscuous interactors of 4-1BB. After three washes with ice-cold PBS, cells were pelleted and stored at -80 °C for protein enrichment later. Samples were prepared in triplicate. The isolation of biotinylated protein was conducted as described in Kim *et al.*³⁶⁵. Biotinylated protein was precipitated by high-capacity streptavidin agarose. 5% of resin was used for validating the protein biotinylation, and the rest of the protein-bound beads were suspended in 50 mM NH_4HCO_3 and stored at -80 °C.

Gels or beads samples were shipped to Proteomics and Mass Spectrometry facility at University of Georgia and analyzed by Dr. Chau-Wen Chou. The following stepwise procedures were summarized based on Dr. Chou's description. The gels were minced and rinsed with 50% acetonitrile/20 mM ammonium bicarbonate (pH 7.5) twice. The gel pieces were dehydrated with acetonitrile and dried out on SpeedVac. Protein was on-gel digested by 0.01 mg/mL trypsin in 20 mM NH_4HCO_3 . The trypsinized peptides were extracted twice from gel with 50% acetonitrile/0.1% formic acid and dried. On-bead digestion was performed by directly adding trypsin to the beads suspended in 50 mM NH_4HCO_3 . The LC-MS/MS analyses were performed using a LTQ Orbitrap Elite Mass Spectrometer coupled with a Proxeon Easy NanoLC system. The data-dependent acquisition (DDA) method was used to acquire MS data. A survey MS scan was obtained first, and then the top 8 ions in the MS scan were selected for following CID MS/MS analysis. Both MS and MS/MS scans were acquired by Orbitrap at the resolutions of 120,000 and 15,000, respectively. Data were gained using Xcalibur software (version 2.2, Thermo Fisher Scientific). Protein identification and modification characterization were performed using Thermo Proteome

Discoverer (version 1.4) with Mascot (Matrix Science) and Uniprot human protein database (protein count: 78,120, Proteome ID: UP000005640). The spectra of possible modified peptides were further inspected to verify the accuracy of the assignments.

The raw data were processed by MaxQuant (v2.0.3.0) and searched against UniProt human protein database. The false discovery rate was set to 0.01. Fold change along with *p* values of all identified proteins were analyzed and visualized using LFQ-Analyst platform (<https://bioinformatics.erc.monash.edu/apps/LFQ-Analyst/>)⁴²³.

5.2.16 Glycomics

The identity and relative quantity of *N*-glycans derived from human 4-1BB was analyzed with the support of National Center for Biomedical Glycomics (Complex carbohydrate research center) at University of Georgia (led by Dr. Parastoo Azadi). The procedure of glycomics analysis was based on Shajahan *et al.*⁴²⁴.

5.2.17 In-silico analysis

The tools and corresponding websites for *in-silico* analysis are listed in Table 5.9.

Table 5.9. The summary of all tools used for *in-silico* analysis in this study.

Name	Link	Purpose
Uniprot	uniprot.org	Protein sequences
PDB	rcsb.org	Protein structure
Alpha-fold	alphafold.ebi.ac.uk	Protein structure
GEPIA2	gepia2.cancer-pku.cn/#index	Cancer survival analysis
TIMER2.0	timer.cistrome.org	Tumor immune infiltration analysis
TIDE	tide.dfci.harvard.edu/login	Immunotherapy outcome analysis
LFQ-Analyst	bioinformatics.erc.monash.edu/apps/LFQ-Analyst/	Label-free quantification of LC-MS data
Meatascape	metascape.org/gp/index.html#/main/step1	GO/KEGG analysis

5.2.18 Statistics

All figures were generated by Illustrator and Prism unless specified. Statistical analysis was performed on Prism. Two-tailed student's *t*-test or one-way ANOVA were used for significance evaluation and $p < 0.05$ was considered statistically significant. All quantitative experimental results were presented as mean \pm SD calculated from at least three replicates.

APPENDIX A. SUPPLEMENTARY FIGURES

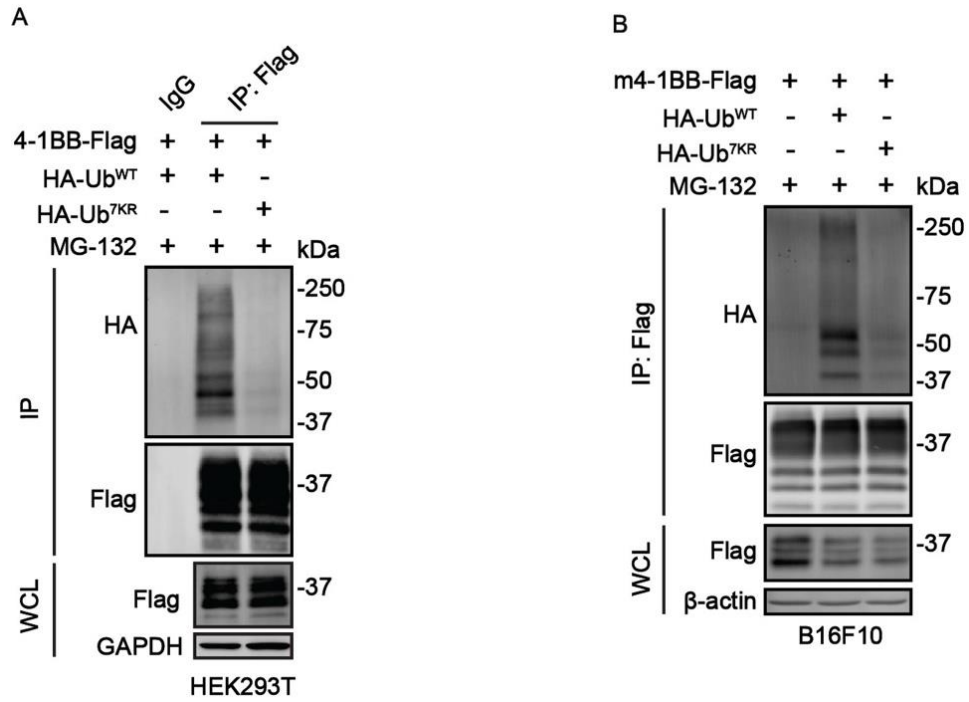


Figure S1. 4-1BB is polyubiquitinated in cultured cell lines. Human (HEK293T, panel A) and mouse (B16F10, panel B) cell lines were transfected by the indicated plasmids followed by *in vivo* ubiquitination assay. IP, immunoprecipitant. WCL, whole cell lysate.

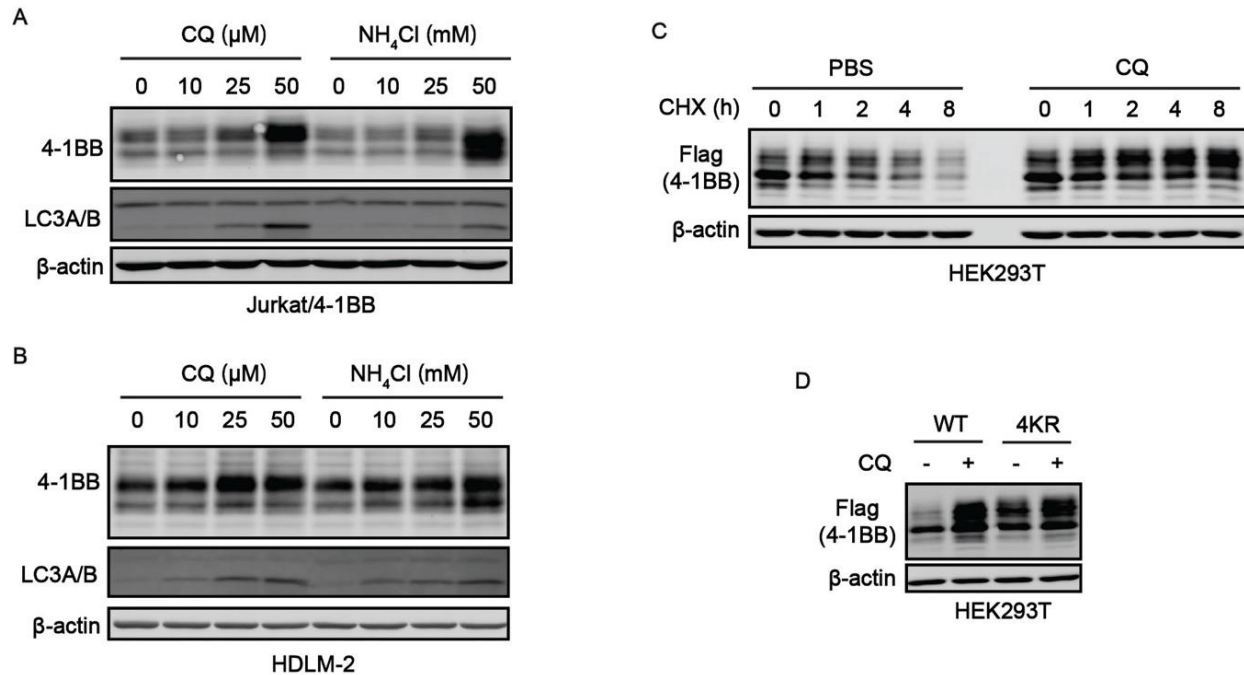


Figure S3. Human 4-1BB is degraded through autophagic pathway. (A, B) Immunoblotting (IB) analysis of 4-1BB alteration upon autophagy inhibition. Jurkat/4-1BB (A) and HDLM-2 (B) cells were treated with CQ or NH_4Cl at indicated concentration overnight. (C) CHX-chase assay comparing the degradation of 4-1BB with or without autophagy inhibition. HEK293T/4-1BB cells were pre-treated with DMSO or 50 μ M CQ for 2 h, then incubated with CHX (100 μ M) for indicated periods of time. (D) Effect of CQ treatment to 4-1BB WT and 4KR. 50 μ M CQ was added to HEK293T cells 24 h post-transfection.

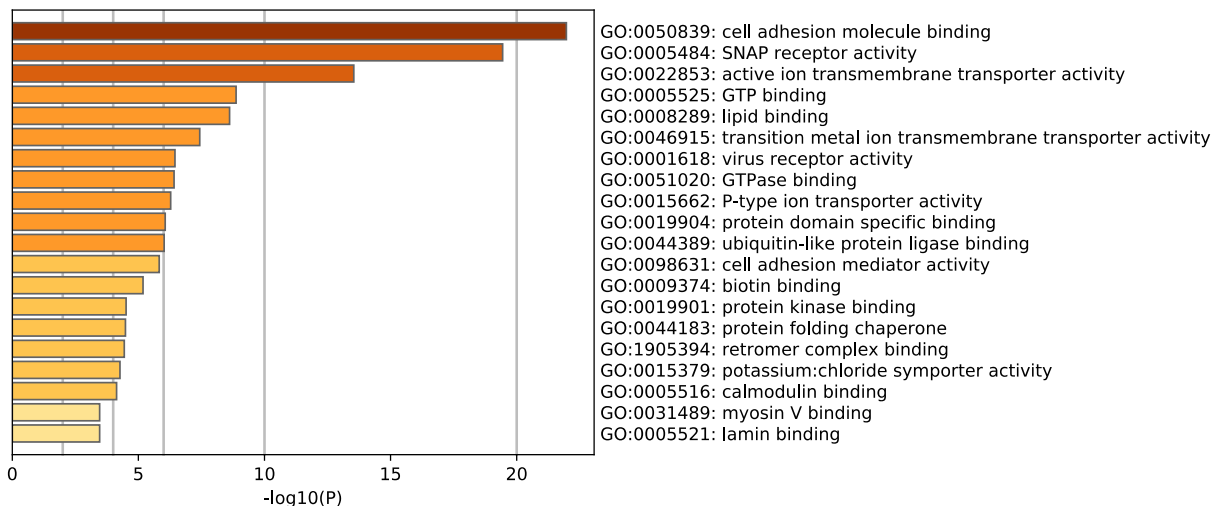


Figure S4. GO (molecular function) analysis of proteins significantly enriched in 4-1BB-BioID2 group. The figure was generated on Metascape.

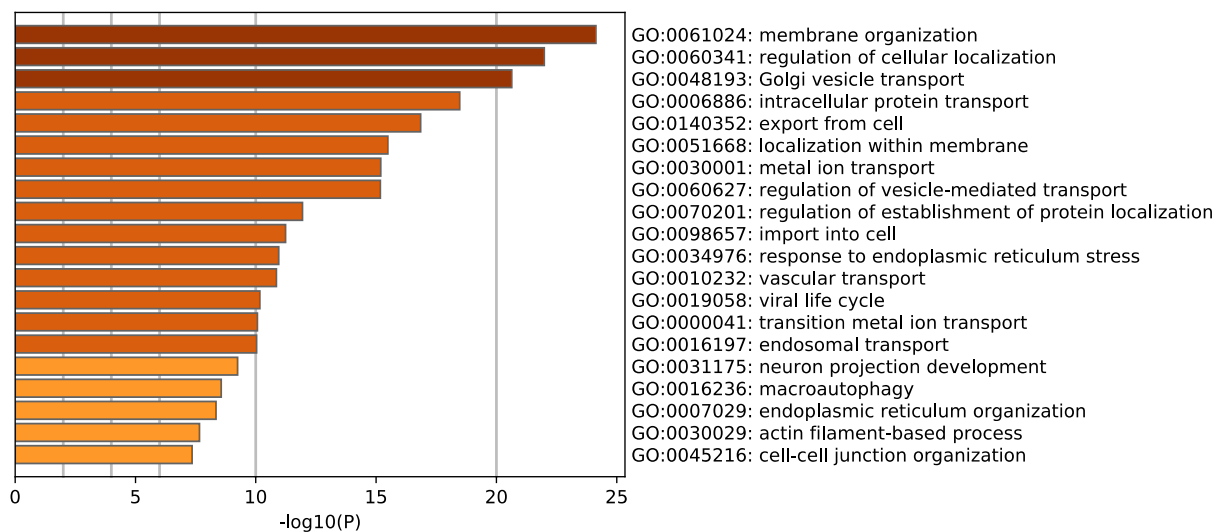


Figure S5. GO (biological process) analysis of proteins significantly enriched in 4-1BB-BioID2 group. The figure was generated on Metascape.

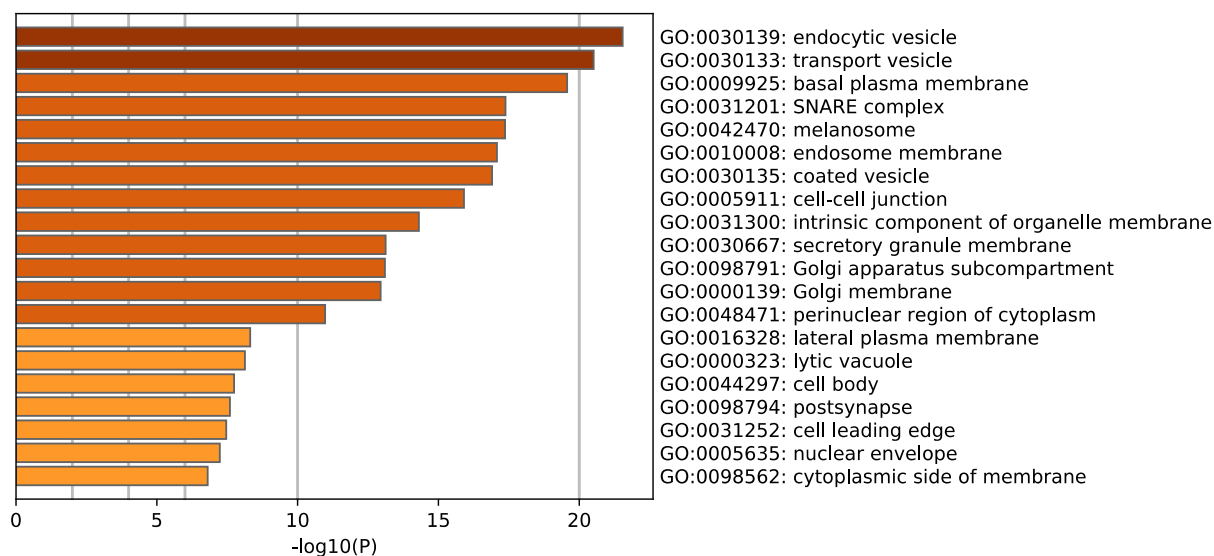


Figure S6. GO (cellular compartment) analysis of proteins significantly enriched in 4-1BB-BioID2 group. The figure was generated on Metascape.

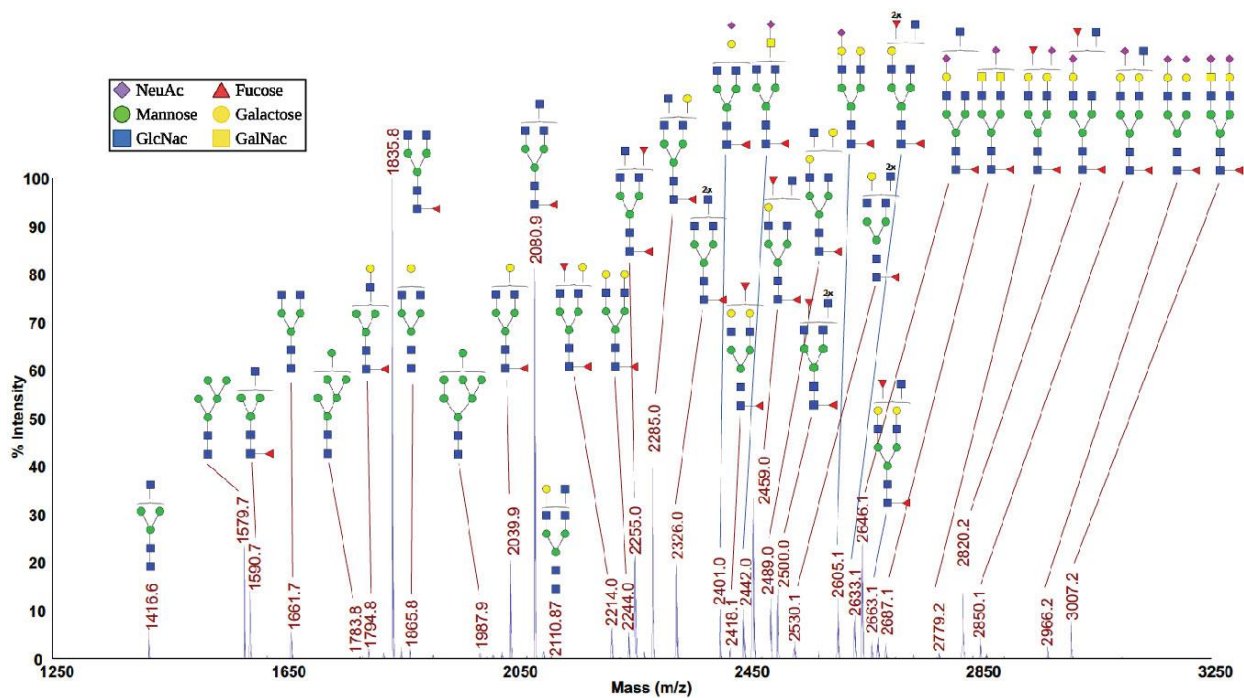


Figure S7. *N*-glycan species derived from 4-1BB. The glycans were released from 4-1BB^{ECD} protein by PNGase F treatment followed by MALDI-MS analysis.

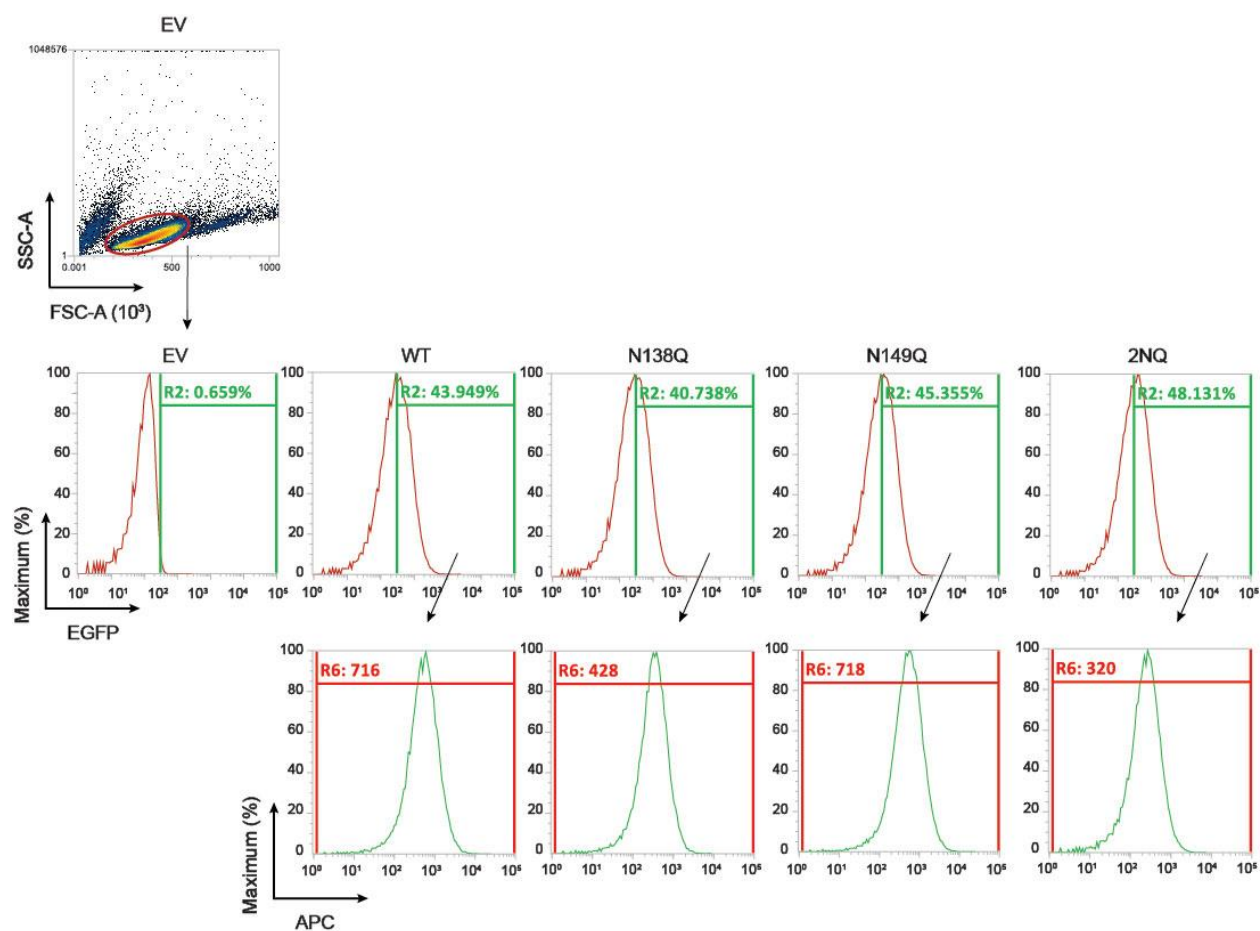


Figure S8. The gating strategy of 4-1BB MFI analysis. Jurkat cells transduced with EV lentivirus were considered as EGFP negative control. MFI values of EGFP⁺ population were used for statistical analysis.

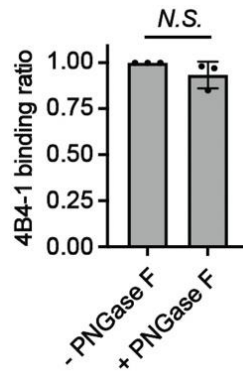


Figure S9. 4B4-1 antibody does not distinguish glycosylated and deglycosylated 4-1BB. Same amount of plate-bound native and PNGase F-treated human 4-1BB protein was incubated with 4B4-1 at the concentration used for flow cytometry staining. HRP-conjugated anti-mouse secondary antibody was used for measuring bound 4B4-1. *N.S.*, $p > 0.05$ (two-tailed student's *t*-test).

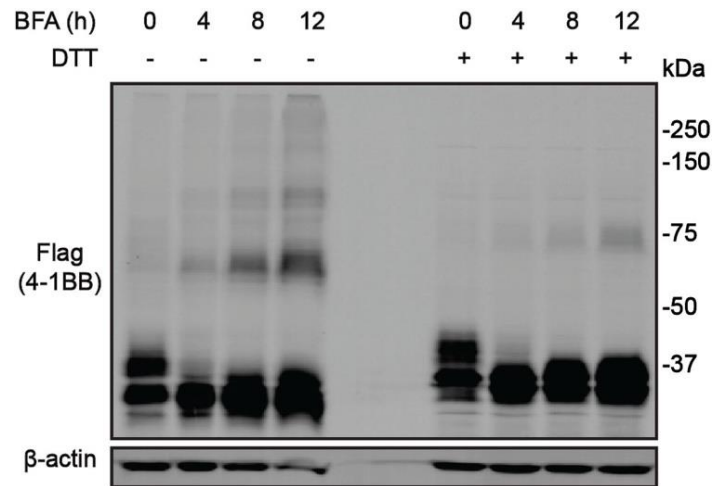


Figure S10. BFA treatment enforces 4-1BB oligomerization in cells. HEK293T/4-1BB WT cells were treated by 1 μ M BFA for 0-12 h. Protein oligomerization was analyzed by SDS-PAGE (with or without DTT).

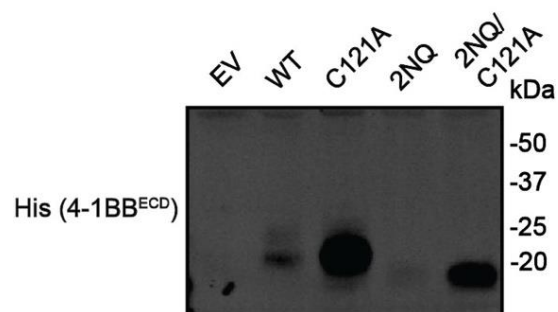


Figure S11. Secretion of 4-1BB ECD truncates with indicated mutations. HEK293T cells were transfected with EV or pcDNA3-4-1BB ECD plasmids (WT or mutants). Medium was collected for IB analysis against 4-1BB. the transfection load was not normalized.

APPENDIX B. SUPPLEMENTARY TABLES

Table S1. The relative percentage of permethylated *N*-linked glycans released from human 4-1BB. The masses of corresponding glycans are presented as $[M+Na^+]$ values. The structural determination of the *N*-glycans is based on the molecular weight, composition analysis via MALDI-MS derived data and follows the principles of the *N*-glycan biosynthesis pathway.

Multiple possible structures might be assigned to one MALDI-MS peak.

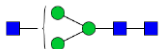
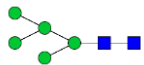

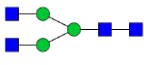
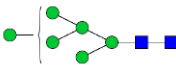


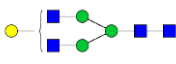
No.	Mass (m/z)	Percentage (%)	Possible structures	Glycan class
1	1416.6	1.22%		Hybrid
2	1579.7	4.91%		High mannose
3	1590.7	2.92%		Hybrid [fucosylated]
4	1661.7	1.18%		Complex
5	1783.8	0.21%		High mannose
6	1794.8	0.43%		Complex [fucosylated]
7	1835.8	20.91%		Complex [fucosylated]
8	1865.8	0.42%		Complex

Table S1 Continued

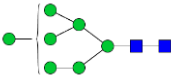
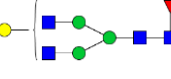
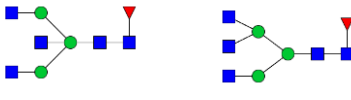

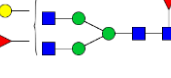
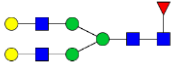

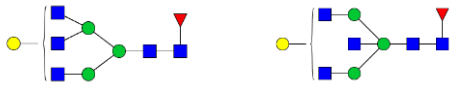

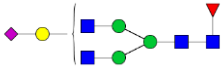
9	1987.9	0.23%		High mannose
10	2039.9	4.26%		Complex [fucosylated]
11	2080.9	16.96%		Complex [fucosylated]/ bisecting GlcNAc
12	2110.9	0.09%		Complex/ bisecting GlcNAc possible
13	2214.0	1.30%		Complex [fucosylated]
14	2244.0	1.17%		Complex [fucosylated]
15	2255.0	4.03%		Complex [fucosylated]/ bisecting GlcNAc
16	2285.0	8.26%		Complex [fucosylated]/ bisecting GlcNAc
17	2326.0	3.64%		Complex [fucosylated]/ bisecting GlcNAc
18	2401.0	1.83%		Complex [fucosylated, sialylated]

Table S1 Continued





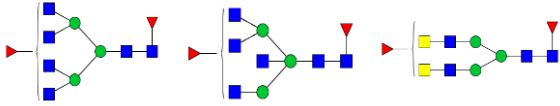
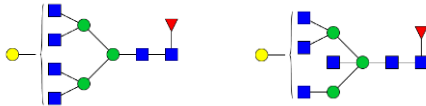
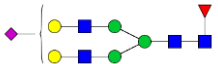
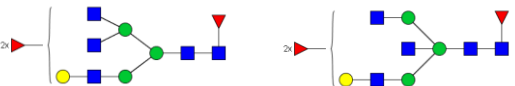

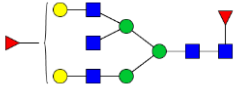
19	2418.1	0.43%		Complex [fucosylated]
20	2442.0	1.70%		Complex [fucosylated, sialylated]
21	2459.0	6.04%		Complex [fucosylated]/ bisecting GlcNAc
22	2489.0	2.15%		Complex [fucosylated]/ bisecting GlcNAc
23	2500.0	2.38%		Complex [fucosylated]/ bisecting GlcNAc
24	2530.1	0.44%		Complex [fucosylated]/ bisecting GlcNAc
25	2605.1	2.02%		Complex [fucosylated, sialylated]
26	2633.1	1.36%		Complex [fucosylated]/ bisecting GlcNAc
27	2646.1	3.90%		Complex [fucosylated, sialylated] / bisecting
28	2663.1	0.45%		Complex [fucosylated]

Table S1 Continued

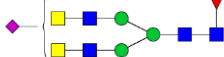
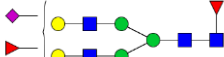
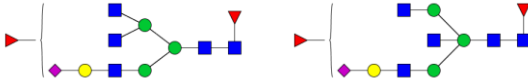



29	2687.1	0.65%		Complex [fucosylated, sialylated]
30	2779.2	0.18%		Complex [fucosylated, sialylated]
31	2820.2	2.71%		Complex [fucosylated, sialylated] / bisecting
32	2850.1	0.51%		Complex [fucosylated, sialylated] / bisecting
33	2966.2	0.24%		Complex [fucosylated, sialylated]
34	3007.2	0.88%		Complex [fucosylated, sialylated]

Table S2. The quantification results acquired from LFQ-Analyst. The log₂ fold change value and *p*_{adj} value are both presented as 4-1BB-BioID2 : BioID2.

Gene Name	Protein IDs	log ₂ fold change	<i>p</i> _{adj}
AATF	Q9NY61	-3.46	1.72E-05
ACACA	Q13085	1.72	0.0335
ACBD3	Q9H3P7	4.24	3.58E-05
ACIN1	Q9UKV3	-3.72	8.59E-05
ACSL3	O95573	4.29	3.31E-05
ADAR	P55265	-4.32	2.57E-05
ADD3	Q9UEY8	1.8	0.000149
ADNP	Q9H2P0	-3.93	9.94E-06
AGPAT6	Q86UL3	3.06	6.00E-05
AGTPBP1	Q9UPW5	-2.82	0.0361
AKAP1	Q92667	-5.78	8.33E-06

Table S2 Continued

AKAP12	Q02952	3.49	2.24E-05
AP3D1	O14617	-2.22	0.0198
ARCN1	P48444	2.33	4.44E-05
ARF3	P61204	3.18	2.82E-05
ARF5	P84085	2.84	6.54E-05
ARFIP1	P53367	2.71	0.00571
ARFIP2	P53365	2.3	0.000108
ARHGAP1	Q07960	2.35	0.00642
ARID1B	Q8NFD5	-3.48	9.97E-06
ARL6IP5	O75915	4.28	8.32E-05
ATAD3A	Q9NVI7	2.38	0.000636
ATP11C	Q8NB49	2.45	0.00299
ATP13A1	Q9HD20	2.62	0.000115
ATP13A3	Q9H7F0	1	0.0174
ATP1A1	P05023	2.65	1.82E-05
ATP2B1	P20020	4.18	0.000856
ATP2B4	P23634	3.41	0.000189
ATP2C1	P98194	7.08	8.78E-06
ATP7A	Q04656	4.3	8.33E-06
ATRX	P46100	-2.71	0.000113
ATXN2L	Q8WWM7	-6.32	9.55E-05
ATXN3	P54252	-2.81	4.04E-05
AUP1	Q9Y679	4.11	8.35E-06
BASP1	P80723	2.15	0.00359
BAZ1B	Q9UIG0	-5.39	8.35E-06
BCAP31	P51572	1.69	0.00246
BCLAF1	Q9NYF8	-5.94	8.33E-06
BET1	O15155	3.56	0.000875
BICD2	Q8TD16	-2.48	0.000147
BMS1	Q14692	-3.73	2.53E-05
BPTF	Q12830	-1.83	0.00427
BRD2	P25440	-2.39	6.68E-05
BSG	P35613	6.15	8.37E-06

Table S2 Continued

BYSL	Q13895	-3.4	0.000121
C17orf85	Q53F19	-3.44	0.000575
C19orf43	Q9BQ61	-4	0.000439
C1orf21	Q9H246	3.94	1.69E-05
C1orf43	Q9BWL3	2.13	0.00145
C2CD5	Q86YS7	1.41	0.014
CALD1	Q05682	-3.07	0.000206
CAMLG	P49069	2.49	5.29E-05
CANX	P27824	4.7	6.16E-06
CAPZB	P47756	-2.01	0.0335
CBX3	Q13185	-3.36	0.0011
CBX5	P45973	-4.86	8.33E-06
CC2D1A	Q6P1N0	-1.16	0.00883
CCAR1	Q8IX12	-2.56	0.00211
CCAR2	Q8N163	-3.8	0.00126
CCDC137	Q6PK04	-3.81	1.90E-05
CCDC47	Q96A33	5.63	1.03E-05
CCDC8	Q9H0W5	3.65	1.72E-05
CCNT1	O60563	-3.28	1.36E-05
CCT2	P78371	-1.97	0.0454
CCT3	P49368	2.57	0.000213
CCT4	P50991	1.65	0.00121
CCT5	P48643	-2.48	4.44E-05
CCT6A	P40227	-1.88	0.000301
CCT8	P50990	-2.82	6.90E-05
CD2AP	Q9Y5K6	-3.01	0.00511
CD2BP2	O95400	-5.19	1.92E-05
CD44	P16070	3.71	1.39E-05
CDC42BPA	Q5VT25	1.01	0.0063
CDC42EP1	Q00587	4.55	1.16E-05
CDC5L	Q99459	-3.57	9.94E-06
CDC73	Q6P1J9	-2.06	0.0294
CDCA2	Q69YH5	-3.42	5.37E-05

Table S2 Continued

CDK13	Q14004	-3.71	0.000298
CDKAL1	Q5VV42	2.7	9.57E-05
CEBPZ	Q03701	-2.2	0.00105
CEP170	Q5SW79	-2.84	0.000425
CFDP1	Q9UEE9	-3.34	1.05E-05
CGN	Q9P2M7	-5.22	0.00013
CHAMP1	Q96JM3	-5.17	8.37E-06
CHD4	Q14839	-1.46	0.0248
CHERP	Q8IWX8	-5	3.68E-05
CHORDC1	Q9UHD1	-1.94	0.000115
CISD2	Q8N5K1	4.48	8.78E-06
CKAP4	Q07065	4.58	0.000361
CKAP5	Q14008	-2.73	0.00129
CLCC1	Q96S66	2.99	1.81E-05
CLGN	O14967	5.28	6.61E-06
CLINT1	Q14677	1.21	0.00202
CNKSRR3	Q6P9H4	3.4	1.88E-05
CNN3	Q15417	-2.45	0.00503
CNNM3	Q8NE01	2.72	0.000436
CNP	P09543	2.1	0.00154
COIL	P38432	-4.9	8.33E-06
CORO1C	Q9ULV4	-2.32	9.84E-05
CPD	O75976	7.71	6.16E-06
CSDE1	O75534	-4.91	3.26E-05
CSNK1G3	Q9Y6M4	3.29	9.26E-05
CTPS1	P17812	-4.26	8.96E-06
CTTN	Q14247	-1.73	0.00126
CXADR	P78310	6.35	8.33E-06
CXorf56	Q9H5V9	-2.21	0.004
CYB5R3	P00387	2.26	0.000211
DCAF7	P61962	-1.92	0.00429
DCBLD2	Q96PD2	2.68	0.000529
DCUN1D4	Q92564	1.51	0.0211

Table S2 Continued

DDHD1	Q8NEL9	-1.82	0.00242
DDOST	P39656	1.87	0.00407
DDRGK1	Q96HY6	2.26	0.000752
DDX21	Q9NR30	-1.12	0.0033
DDX3X	O00571	-1.27	0.00222
DDX42	Q86XP3	-4.14	8.33E-06
DDX46	Q7L014	-2.71	0.000154
DDX55	Q8NHQ9	-3.64	0.000316
DDX56	Q9NY93	2.98	2.77E-05
DENND4A	Q7Z401	2.03	0.0197
DHRS7	Q9Y394	3.25	1.85E-05
DHX15	O43143	-1.98	0.000448
DHX29	Q7Z478	-2.2	4.29E-05
DIDO1	Q9BTC0	-2.11	0.000265
DNAJB1	P25685	-4.03	2.00E-05
DNTTIP2	Q5QJE6	-3.37	1.87E-05
DSG2	Q14126	2.07	0.000163
DVL3	Q92997	1.58	0.000305
EBNA1BP2	Q99848	-4.78	7.76E-05
ECE1	P42892	2.77	0.00011
EDC4	Q6P2E9	-4.73	6.16E-06
EEF1B2	P24534	-2.17	0.0441
EEF1D	P29692	-2.49	0.00049
EEF1G	P26641	-2.51	0.00335
EIF3C	Q99613	-3.92	2.37E-05
EIF3D	O15371	-1.06	0.0198
EIF4B	P23588	-2.16	0.00076
EIF4G1	Q04637	-5.01	2.82E-05
EIF4G2	P78344	-2.2	0.000171
EIF4G3	O43432	-4.36	1.87E-05
EMD	P50402	3.22	3.04E-05
EPB41	P11171	1.5	0.00032
EPB41L1	Q9H4G0	2.65	0.00029

Table S2 Continued

EPB41L2	O43491	2.63	6.56E-05
EPB41L3	Q9Y2J2	2.35	4.64E-05
EPB41L4B	Q9H329	2.03	0.00413
EPB41L5	Q9HCM4	3.03	0.000102
EPHA2	P29317	3.21	0.000243
EPHA7	Q15375	1.92	0.0109
EPN2	O95208	1.59	0.00444
ERCC5	P28715	-3.7	0.000207
ERH	P84090	-2.16	0.0238
ESF1	Q9H501	-2.93	1.82E-05
ESYT1	Q9BSJ8	1.58	0.000264
ESYT2	A0FGR8	1.98	0.00626
EXOSC10	Q01780	-2.79	0.000276
EXOSC9	Q06265	-2.84	8.71E-05
FAF2	Q96CS3	1.89	0.0122
FAM129B	Q96TA1	2.3	0.00211
FAM177A1	Q8N128	2.65	2.38E-05
FAM208A	Q9UK61	-3.13	1.42E-05
FAM21C	Q9Y4E1	-2.3	0.00125
FAM92A1	A1XBS5	2.49	0.00289
FASN	P49327	-1.33	0.00112
FBXL20	Q96IG2	2.59	3.17E-05
FERMT2	Q96AC1	2.52	0.000461
FIP1L1	Q6UN15	-2.81	1.92E-05
FKBP8	Q14318	2.25	0.000436
FLNA	P21333	-3.92	8.35E-06
FLVCR1	Q9Y5Y0	3.8	5.73E-05
FRS2	Q8WU20	2.82	9.55E-05
FTSJ3	Q8IY81	-4.54	1.01E-05
FUBP1	Q96AE4	-3.02	0.000188
FUBP3	Q96I24	-3.67	0.00132
FUS	P35637	-2.89	6.16E-05
G3BP1	Q13283	-5.34	8.78E-06

Table S2 Continued

GART	P22102	-1.85	0.000279
GATAD2A	Q86YP4	-1.97	9.12E-05
GATAD2B	Q8WXI9	-4.08	2.82E-05
GCFC2	P16383	-1.41	0.0229
GEMIN5	Q8TEQ6	-2.99	0.0111
GIGYF2	Q6Y7W6	-1.89	0.00413
GLUD1	P00367	3.37	3.31E-05
GNL2	Q13823	-3.1	0.000108
GOLGA4	Q13439	4.48	1.02E-05
GOLGA5	Q8TBA6	2.42	0.000426
GOPC	Q9HD26	6.75	8.35E-06
GORASP2	Q9H8Y8	6.35	8.33E-06
GOSR1	O95249	3.87	1.16E-05
GPATCH4	Q5T3I0	-3.55	2.24E-05
GPKOW	Q92917	-4.32	4.13E-05
GTF2I	P78347	-4.15	0.00068
GTF3C4	Q9UKN8	-2.47	0.000194
GTF3C5	Q9Y5Q8	-3.66	0.000274
H2AFV	Q71UI9	-3.72	4.88E-05
HACD3	Q9P035	2.25	5.37E-05
HAT1	O14929	-5.1	5.05E-05
HCFC1	P51610	-8.34	8.33E-06
HDAC2	Q92769	-2.84	0.000377
HDGFRP2	Q7Z4V5	-3.1	0.000119
HDLBP	Q00341	-2.85	1.56E-05
HGS	O14964	2.54	0.000283
HIST1H4A	P62805	-2.75	0.000395
HIST2H2AA3	Q6FI13	-1.82	0.00487
HLA-A	P04439	3.97	1.42E-05
HM13	Q8TCT9	4.57	8.33E-06
HMOX2	P30519	5.22	7.61E-06
HNRNPA1	P09651	-2.49	0.000109
HNRNPA2B1	P22626	-2.27	0.000214

Table S2 Continued

HNRNPA3	P51991	-1.72	0.000682
HNRNPC	P07910	-1.87	0.00486
HNRNPD	Q14103	-2.52	0.000195
HNRNPF	P52597	-2.42	5.99E-05
HNRNPK	P61978	-1.49	0.00184
HNRNPL	P14866	-2.07	0.00351
HNRNPM	P52272	-2.92	1.90E-05
HSP90AB1	P08238	-1.04	0.00505
HSP90AB2P	Q58FF8	-3.03	4.44E-05
HSP90B1	P14625	1.96	6.54E-05
HSPD1	P10809	4.18	8.33E-06
HSPE1	P61604	3.66	2.77E-05
IGF2BP1	Q9NZI8	-3.48	1.12E-05
IGF2R	P11717	2.41	5.09E-05
IK	Q13123	-4.18	1.56E-05
ILF3	Q12906	-2.52	0.000569
ILKAP	Q9H0C8	-3.63	5.35E-05
INTS12	Q96CB8	-2.29	0.00579
IST1	P53990	-1.59	0.000958
ITGB1	P05556	6.04	1.82E-05
JPH1	Q9HDC5	3.02	6.98E-05
JUP	P14923	2.21	0.0118
KDM3B	Q7LBC6	-3.56	0.000508
KHDRBS1	Q07666	-1.96	0.0021
KHSRP	Q92945	-4.37	2.00E-05
KIAA0319L	Q8IZA0	3.02	1.82E-05
KIAA1324L	A8MWY0	3.32	0.000316
KMT2A	Q03164	-3.81	1.13E-05
KNOP1	Q1ED39	-4.02	2.38E-05
KRI1	Q8N9T8	-3.38	1.94E-05
L3MBTL3	Q96JM7	-5.06	8.96E-06
LAMTOR1	Q6IAA8	1.53	0.000243
LARP1	Q6PKG0	-4.04	0.00345

Table S2 Continued

LAS1L	Q9Y4W2	-3.89	8.33E-06
LBR	Q14739	2.73	3.53E-05
LEMD3	Q9Y2U8	1.5	0.000249
LIMA1	Q9UHB6	-5.75	8.37E-06
LIN54	Q6MZP7	-3.38	3.01E-05
LLGL1	Q15334	3.01	0.000225
LNP	Q9C0E8	3.23	4.15E-05
LRRC59	Q96AG4	2.67	2.38E-05
LSR	Q86X29	2.28	0.000482
LYN	P07948	5.54	5.09E-05
MAP1B	P46821	-3.75	0.000142
MAP4	P27816	-8.66	1.82E-05
MAP7D3	Q8IWC1	-3.97	1.96E-05
MARCKS	P29966	2.71	0.000121
MARCKSL1	P49006	3.46	4.04E-05
MARK2	Q7KZI7	2.31	0.000153
MARVELD2	Q8N4S9	2.08	0.000266
MATR3	P43243	-5.28	0.000151
MBOAT7	Q96N66	4.81	1.85E-05
MCCC1	Q96RQ3	1.91	8.65E-05
MCCC2	Q9HCC0	-1.94	0.0104
MCM4	P33991	-2.41	0.000108
MDC1	Q14676	-3.95	8.33E-06
MED1	Q15648	-3.58	0.000366
MFAP1	P55081	-3.14	1.37E-05
MFAP3	P55082	2.89	0.000522
MGA	Q8IWI9	-3.99	5.57E-05
MKI67	P46013	-6.64	6.16E-06
MMGT1	Q8N4V1	4.38	2.24E-05
MOSPD2	Q8NHP6	2.08	8.32E-05
MPHOSPH10	O00566	-2.36	0.0288
MPP6	Q9NZW5	2.22	0.000179
MPP7	Q5T2T1	2.75	0.000104

Table S2 Continued

MRE11A	P49959	-3.49	8.37E-06
MRPL12	P52815	2.29	0.012
MRPS28	Q9Y2Q9	1.42	0.00824
MTA1	Q13330	-3.85	8.59E-05
MTA2	O94776	-2.48	0.000174
MTAP	Q13126	-3.43	0.00175
MT-CO2	P00403	3.22	0.000209
MXRA7	P84157	2.88	0.00155
MYBBP1A	Q9BQG0	-3.53	4.44E-05
NAP1L1	P55209	-4.94	6.66E-05
NASP	P49321	-4.21	3.34E-05
NAT10	Q9H0A0	-7.04	6.53E-06
NCAPH	Q15003	-3.43	1.72E-05
NCL	P19338	-10	7.61E-06
NDC1	Q9BTX1	3.61	7.80E-05
NELFA	Q9H3P2	-2.26	0.000946
NHSL2	Q5HYW2	2.55	0.000147
NIFK	Q9BYG3	-5.18	1.68E-05
NOC2L	Q9Y3T9	-3.15	0.000498
NOC3L	Q8WTT2	-3.39	0.000761
NOL10	Q9BSC4	-2	0.0102
NOL11	Q9H8H0	-3.8	0.000123
NOL6	Q9H6R4	-6.82	6.90E-05
NOL8	Q76FK4	-3.77	2.23E-05
NOL9	Q5SY16	-2.08	0.00571
NOLC1	Q14978	-6.94	2.37E-05
NONO	Q15233	-4.05	8.35E-06
NOP14	P78316	-4.99	1.34E-05
NOP2	P46087	-3.6	0.00016
NOP58	Q9Y2X3	-1.28	0.00232
NOTCH2	Q04721	3.03	1.56E-05
NPM1	P06748	-3.02	3.22E-05
NPM3	O75607	-4.28	8.33E-06

Table S2 Continued

NSFL1C	Q9UNZ2	-5.41	5.05E-05
NUDC	Q9Y266	-3.82	1.90E-05
NUDT21	O43809	-3.86	3.06E-05
NUFIP2	Q7Z417	-3.86	2.82E-05
NUMB	P49757	1.53	0.00253
NUP153	P49790	-2.08	9.19E-05
NUP155	O75694	1.45	0.0119
NUP214	P35658	-8.59	6.16E-06
NUP50	Q9UKX7	-4.36	0.000125
ORC2	Q13416	-2.93	9.84E-05
ORC3	Q9UBD5	-2.49	0.000334
OSBPL8	Q9BZF1	1.73	0.000688
PAICS	P22234	-2.1	0.000205
PAK4	O96013	1.48	0.00844
PALD1	Q9ULE6	1.86	0.0215
PALM	O75781	3.18	0.000105
PALM2	Q8IXS6	4.07	2.67E-05
PARP1	P09874	-1.28	0.00925
PC	P11498	2.26	0.000173
PCBP1	Q15365	-1.52	0.000301
PCBP2	Q15366	-1.94	7.94E-05
PCCA	P05165	2.13	0.000108
PCF11	O94913	-2.42	0.000404
PCNP	Q8WW12	-4.21	3.53E-05
PDIA3	P30101	3.66	3.01E-05
PDLIM1	O00151	-1.99	0.000212
PDXDC1	Q6P996	4.65	0.000147
PES1	O00541	-4.32	1.02E-05
PGRMC1	O00264	2.27	0.00871
PHACTR4	Q8IZ21	1.3	0.00125
PHF3	Q92576	-4.26	1.85E-05
PHF8	Q9UPP1	4.41	5.35E-05
PIAS1	O75925	-3.19	0.000102

Table S2 Continued

PICALM	Q13492	1.41	0.000958
PKP4	Q99569	2	8.04E-05
PLEKHA8	Q96JA3	1.86	0.0328
PLRG1	O43660	-5.22	3.42E-05
POLDIP3	Q9BY77	-2.97	0.000478
PPM1G	O15355	-4.32	1.17E-05
PPT1	P50897	3.8	1.56E-05
PRAF2	O60831	2.94	0.000105
PRCC	Q92733	-4.07	1.82E-05
PRDX3	P30048	2.97	0.000108
PREB	Q9HCU5	3.77	9.55E-06
PRKAR2A	P13861	-1.69	0.00022
PRPF3	O43395	-3.75	9.19E-05
PRPF4	O43172	-4.32	0.00699
PRPF40A	O75400	-4.17	9.19E-05
PRRC2A	P48634	-3.31	4.32E-05
PRRC2C	Q9Y520	-4.23	8.35E-06
PSIP1	O75475	-3.47	0.000189
PSMC2	P35998	-2.03	0.0379
PSMD4	P55036	-3.02	0.00361
PSME3	P61289	-1.84	0.0308
PSPC1	Q8WXF1	-4.69	9.84E-05
PTK7	Q13308	2.74	6.00E-05
PTPN1	P18031	4.5	1.16E-05
PTPN13	Q12923	1.11	0.000946
PTPN2	P17706	4.1	8.33E-06
PUM1	Q14671	-3.56	2.00E-05
PVRL2	Q92692	5.45	0.000402
PVRL3	Q9NQS3	2.58	3.04E-05
RAB11A	P62491	2.91	0.000478
RAB11FIP1	Q6WKZ4	1.38	0.00432
RAB11FIP2	Q7L804	2.33	7.76E-05
RAB13	P51153	2.34	0.000188

Table S2 Continued

RAB1A	P62820	2.74	8.11E-05
RAB23	Q9ULC3	4.35	0.000188
RAB27A	P51159	4.01	2.00E-05
RAB3GAP2	Q9H2M9	-2.76	0.013
RAB6A	P20340	4.04	1.94E-05
RAB7A	P51149	2.21	9.83E-05
RAB9A	P51151	2.47	0.00189
RABL3	Q5HYI8	3.46	1.37E-05
RALA	P11233	6.58	6.16E-06
RALB	P11234	3.17	1.85E-05
RANBP2	P49792	-6.15	1.10E-05
RANGAP1	P46060	-1.94	0.0123
RAP1B	P61224	1.65	0.00125
RASAL2	Q9UJF2	1.34	0.0237
RBBP4	Q09028	-2.53	0.00119
RBBP6	Q7Z6E9	-5.2	8.33E-06
RBBP7	Q16576	-4.32	0.000115
RBM10	P98175	-4.16	2.00E-05
RBM17	Q96I25	-5.1	4.10E-05
RBM25	P49756	-8.44	6.10E-06
RBM26	Q5T8P6	-2.79	8.24E-05
RBM27	Q9P2N5	-5.07	2.15E-05
RBM39	Q14498	-2.22	0.000211
RBM4	Q9BWF3	-3.11	1.56E-05
REEP4	Q9H6H4	3.31	0.000206
REEP5	Q00765	4.74	8.96E-06
RELL1	Q8IUW5	3.64	4.37E-05
RFC4	P35249	-2.87	7.59E-05
RFTN1	Q14699	1.71	0.00246
RICTOR	Q6R327	1.79	0.0148
RIF1	Q5UIP0	-3.98	8.17E-05
RNF169	Q8NCN4	-1.67	0.0102
RNF2	Q99496	-2.61	0.00368

Table S2 Continued

RNF219	Q5W0B1	-2.75	2.24E-05
ROR2	Q01974	3.91	3.18E-05
RPA1	P27694	-2.66	9.23E-05
RPL10A	P62906	1.17	0.0244
RPL13	P26373	2.15	0.000108
RPL13A	P40429	2.34	0.0087
RPL14	P50914	-1.85	0.000646
RPL24	P83731	-1.6	0.000316
RPL27A	P46776	2.4	0.000125
RPN1	P04843	-2.64	4.55E-05
RPRD2	Q5VT52	-3.68	2.00E-05
RPS8	P62241	1.08	0.0369
RRBP1	Q9P2E9	2.63	0.000337
RRP1B	Q14684	-3.21	0.00136
RTN4	Q9NQC3	1.04	0.00376
RUVBL1	Q9Y265	-6	5.73E-05
RUVBL2	Q9Y230	-4.52	1.68E-05
SAFB	Q15424	-5.2	3.58E-05
SAFB2	Q14151	-3.68	0.000573
SAP30BP	Q9UHR5	-2.45	2.77E-05
SAR1A	Q9NR31	2.74	0.000112
SARS	P49591	-1.39	0.0487
SART1	O43290	-6.33	8.92E-06
SCAMP1	O15126	5.18	6.16E-06
SCFD1	Q8WVM8	2.32	0.000187
SEC22B	O75396	4.53	2.53E-05
SEC24B	O95487	2.54	5.89E-05
SEC63	Q9UGP8	1.77	0.00455
SERBP1	Q8NC51	-2.83	2.38E-05
SETD2	Q9BYW2	-3.91	1.11E-05
SF1	Q15637	-3.65	0.000206
SF3A1	Q15459	-3.82	0.00105
SF3A2	Q15428	-3.46	2.27E-05

Table S2 Continued

SF3A3	Q12874	-4.19	8.35E-06
SF3B1	O75533	-6.97	9.26E-05
SF3B2	Q13435	-5.72	1.72E-05
SF3B3	Q15393	-2.12	0.000298
SFPQ	P23246	-5.56	2.53E-05
SLC12A2	P55011	4.82	0.00152
SLC12A4	Q9UP95	2.49	0.000124
SLC12A7	Q9Y666	3.6	1.17E-05
SLC16A1	P53985	3.71	1.42E-05
SLC1A5	Q15758	5.79	6.16E-06
SLC20A1	Q8WUM9	1.61	0.000449
SLC20A2	Q08357	2.46	0.00372
SLC29A1	Q99808	2.66	3.75E-05
SLC30A1	Q9Y6M5	5.39	2.58E-05
SLC30A5	Q8TAD4	1.74	0.000813
SLC30A6	Q6NXT4	4.14	1.42E-05
SLC30A7	Q8NEW0	3.35	2.28E-05
SLC38A1	Q9H2H9	5	3.15E-05
SLC38A2	Q96QD8	3.11	0.000276
SLC38A3	Q99624	2.76	0.000158
SLC39A14	Q15043	1.68	0.00303
SLC3A2	P08195	10	6.16E-06
SLC4A4	Q9Y6R1	2.56	0.000157
SLC4A7	Q9Y6M7	5.2	3.04E-05
SLC6A15	Q9H2J7	4.46	8.35E-06
SLC6A6	P31641	2.84	0.000132
SLC7A11	Q9UPY5	4.14	4.44E-05
SLC7A5	Q01650	5.54	8.35E-06
SLC9A1	P19634	3.94	0.000322
SLITRK5	O94991	3.61	1.68E-05
SMARCA5	O60264	-1.87	0.000161
SMCHD1	A6NHR9	-3.51	1.92E-05
SMPD2	O60906	3.57	0.000263

Table S2 Continued

SNAP23	O00161	7.04	6.10E-06
SNAP29	O95721	1.1	0.0152
SNAP47	Q5SQN1	3.48	0.00406
SNRNP200	O75643	-3.54	0.000345
SNRPD3	P62318	-3.06	0.0137
SNW1	Q13573	-7.24	2.27E-05
SNX3	O60493	4.97	8.33E-06
SOAT1	P35610	2.07	0.00144
SON	P18583	-4.04	1.63E-05
SPCS2	Q15005	4.1	3.40E-05
SRPR	P08240	1.92	0.000108
SRPRB	Q9Y5M8	2.4	0.000167
SSB	P05455	-3.82	0.000178
STAG2	Q8N3U4	-2.88	7.93E-05
STAM	Q92783	6.29	8.96E-06
STAM2	O75886	2.95	0.000164
STAT3	P40763	-2.69	0.00565
STAU2	Q9NUL3	-2.11	0.000153
STBD1	O95210	3.25	4.01E-05
STEAP3	Q658P3	5.37	6.61E-06
STIM1	Q13586	1.81	0.000145
STIP1	P31948	-2.93	7.98E-05
STMN1	P16949	-1.59	0.00366
STRAP	Q9Y3F4	-3.73	3.52E-05
STRN	O43815	-4.56	1.79E-05
STRN3	Q13033	-3.25	2.00E-05
STT3A	P46977	-4.67	8.35E-06
STT3B	Q8TCJ2	1.82	0.0091
STX12	Q86Y82	2.35	0.000509
STX3	Q13277	1.6	0.00046
STX4	Q12846	2.67	0.00061
STX5	Q13190	3.64	1.69E-05
STX7	O15400	3.05	2.51E-05

Table S2 Continued

STXBP3	O00186	2.32	9.07E-05
SUB1	P53999	-3.74	0.00117
SUGP2	Q8IX01	-5.27	1.92E-05
SUPT16H	Q9Y5B9	-3.26	3.02E-05
SVIL	O95425	-2.87	0.000107
SYAP1	Q96A49	1	0.00628
SYTL4	Q96C24	2.03	0.00195
TAF15	Q92804	-3.35	1.84E-05
TAF6	P49848	-3.41	1.92E-05
TAF9	Q16594	-4.97	3.58E-05
TARDBP	Q13148	-1.94	9.02E-05
TCERG1	O14776	-4.2	8.37E-06
TCOF1	Q13428	-5.05	0.000248
TCP1	P17987	-1.17	0.00122
TEX264	Q9Y6I9	3.15	0.000279
TFRC	P02786	2.69	0.00155
THRAP3	Q9Y2W1	-5.83	0.00113
TJP1	Q07157	-2.61	4.76E-05
TJP2	Q9UDY2	-1.22	0.00078
TLDC1	Q6P9B6	2.45	2.37E-05
TMED8	Q6PL24	2.7	2.01E-05
TMEM109	Q9BVC6	5.32	3.01E-05
TMEM214	Q6NUQ4	4	1.17E-05
TMEM237	Q96Q45	4.63	1.17E-05
TMEM87A	Q8NBN3	1.15	0.0137
TMOD3	Q9NYL9	-3.15	3.53E-05
TMPO	P42166	-4.5	4.15E-05
TMPO.1	P42167	2.39	8.78E-05
TMX1	Q9H3N1	5.87	6.61E-06
TNFRSF9	Q07011	8.14	8.33E-06
TNKS1BP1	Q9C0C2	-1.15	0.014
TOP2A	P11388	-3.62	3.31E-05
TOR1AIP1	Q5JTV8	3.39	8.92E-06

Table S2 Continued

TOR1AIP2	Q8NFAQ8	3.01	0.0104
TOX4	O94842	-2.72	0.00512
TP53	P04637	-5.68	0.000259
TP53I11	O14683	1.69	0.00068
TPD52L2	O43399	2.56	4.25E-05
TPX2	Q9ULW0	-4.81	0.000137
TRIM28	Q13263	-3.61	3.65E-05
TRIM33	Q9UPN9	-1.68	0.0238
TRPM4	Q8TD43	2.94	9.55E-05
U2AF2	P26368	-2.86	9.67E-05
U2SURP	O15042	-7.17	0.000624
UBAP2L	Q14157	-6.63	1.62E-05
UBC	P0CG48	1.56	0.000911
UBE2J1	Q9Y385	3.33	8.96E-06
UBTF	P17480	-3.32	0.000129
UBXN4	Q92575	4.02	8.67E-06
UGT8	Q16880	2.39	6.88E-05
USP6NL	Q92738	2.43	3.17E-05
UTP14A	Q9BVJ6	-4.63	4.29E-05
UTP3	Q9NQZ2	-3.2	9.47E-05
VAMP3	Q15836	3.45	2.99E-05
VAMP7	P51809	2.81	0.000113
VAMP8	Q9BV40	4.27	3.15E-05
VANGL1	Q8TAA9	3.47	2.00E-05
VANGL2	Q9ULK5	2.14	0.000551
VAPA	Q9P0L0	3.67	1.02E-05
VAPB	O95292	3.85	8.35E-06
VCP	P55072	-3.07	2.45E-05
VIM	P08670	-5.42	4.44E-05
VKORC1L1	Q8N0U8	2.91	0.000271
VPS51	Q9UID3	1.48	0.00103
VRK2	Q86Y07	2.87	9.26E-05

Table S2 Continued

WAPAL	Q7Z5K2	-3.3	0.000169
WBP11	Q9Y2W2	-3.36	0.000115
WDR20	Q8TBZ3	2.92	1.94E-05
WDR33	Q9C0J8	-3.44	4.21E-05
WDR70	Q9NW82	-3.03	2.57E-05
WDR75	Q8IWA0	-3.94	1.36E-05
WIZ	O95785	-1.99	0.0161
WVOX	Q9NZC7	2.35	0.00116
XAB2	Q9HCS7	-2.74	0.000211
XRCC5	P13010	-1.2	0.0137
XRCC6	P12956	-1.83	0.0328
XRN2	Q9H0D6	-2.11	0.0221
YES1	P07947	4.26	5.35E-05
YIPF3	Q9GZM5	2.51	0.000296
YKT6	O15498	3.51	0.000204
YLPM1	P49750	-1.98	0.00487
YTHDF2	Q9Y5A9	-2.46	0.000392
ZC3H11A	O75152	-4.53	1.11E-05
ZC3H14	Q6PJT7	-4.56	0.000682
ZC3H18	Q86VM9	-4.62	3.31E-05
ZC3HAV1	Q7Z2W4	1.86	0.006
ZDHHC5	Q9C0B5	3.3	2.37E-05
ZFPL1	O95159	2.52	0.00212
ZMYND8	Q9ULU4	-2.45	0.000693
ZNF318	Q5VUA4	-1.87	0.00125
ZNF638	Q14966	-3.89	1.11E-05
ZNF687	Q8N1G0	-3.46	0.000791
ZNF830	Q96NB3	-1.65	0.016
ABCE1	P61221	0.206	0.434
ACLY	P53396	-1.97	0.0961
ACTB	P60709	-0.16	0.574
ADD1	P35611	0.722	0.0123
AGFG1	P52594	0.669	0.0689

Table S2 Continued

AGPAT9	Q53EU6	2.14	0.114
AHCTF1	Q8WYP5	-0.744	0.0121
AHNAK	Q09666	0.697	0.0458
ALDH18A1	P54886	-0.377	0.243
ANKLE2	Q86XL3	0.537	0.0355
ANXA2	P07355	0.599	0.179
APBB1	O00213	-0.268	0.307
ARF6	P62330	1.17	0.447
ARFGAP1	Q8N6T3	-0.562	0.0571
ARFGAP2	Q8N6H7	0.932	0.0303
ATP2A2	P16615	0.816	0.0121
ATP5A1	P25705	-0.124	0.548
BCCIP	Q9P287	-0.631	0.569
CAMSAP1	Q5T5Y3	-1.74	0.0874
CDK12	Q9NYV4	-0.726	0.346
CFL1	P23528	-0.164	0.58
CHMP2B	Q9UQN3	0.12	0.852
CHMP4B	Q9H444	-0.499	0.0894
CSNK1A1	P48729	0.118	0.548
CTNND1	O60716	0.628	0.0214
DDX17	Q92841	-0.52	0.0429
DDX18	Q9NVP1	0.845	0.00429
DDX39B	Q13838	0.0547	0.79
DDX5	P17844	0.282	0.558
DHX9	Q08211	-0.911	0.00407
DLG1	Q12959	0.966	0.15
DVL2	O14641	0.964	0.00489
EARS2	Q5JPH6	0.877	0.0336
EDF1	O60869	-0.668	0.11
EEF1A1	P68104	-0.918	0.00757
EEF2	P13639	-0.754	0.0564
EHBP1	Q8NDI1	0.79	0.00862
EIF3A	Q14152	-2.22	0.07

Table S2 Continued

EIF4A1	P60842	0.407	0.176
EIF4A3	P38919	0.815	0.185
EIF5A	P63241	-0.735	0.0666
EIF5B	O60841	-1.34	0.0865
ELAVL1	Q15717	-0.257	0.274
ENO1	P06733	0.0296	0.912
EPS15L1	Q9UBC2	0.101	0.664
ERBB2IP	Q96RT1	0.78	0.00625
FAM126A	Q9BYI3	1.09	0.413
FANCF	Q9NPI8	-0.568	0.734
FBL	P22087	-0.0825	0.729
GLO1	Q04760	-0.2	0.854
GNB2L1	P63244	-1.82	0.17
HIST1H1C	P16403	0.405	0.252
HIST1H2BB	P33778	0.227	0.518
HIST1H2BL	Q99880	0.568	0.211
HIST1H3A	P68431	-0.565	0.15
HN1	Q9UK76	-2.19	0.0838
HN1L	Q9H910	-0.711	0.0865
HNRNPH1	P31943	0.875	0.292
HNRNPU	Q00839	-0.648	0.0583
HSP90AA1	P07900	-2.19	0.117
HSPA1A	P0DMV8	-0.765	0.0153
HSPA5	P11021	0.728	0.0374
HSPA8	P11142	-0.788	0.0559
HSPA9	P38646	0.523	0.165
ITGA2	P17301	0.727	0.102
KCNB2	Q92953	1.77	0.0869
KIAA0196	Q12768	-0.738	0.0465
KIDINS220	Q9ULH0	0.552	0.429
KIF23	Q02241	-1.63	0.119
LDHA	P00338	-1.12	0.288
LDHB	P07195	-0.308	0.425

Table S2 Continued

LMAN1	P49257	0.0496	0.93
LRSAM1	Q6UWE0	0.773	0.0166
LYPLA2	O95372	2.13	0.0619
MCM2	P49736	0.844	0.0606
MLLT4	P55196	0.364	0.183
MTDH	Q86UE4	0.994	0.0107
NACA	E9PAV3	-0.531	0.0399
NKRF	O15226	-1.22	0.11
NSRP1	Q9H0G5	-1.67	0.0665
NUP98	P52948	-0.405	0.13
OCLN	Q16625	0.345	0.693
PCMT1	P22061	-0.361	0.215
PDE8A	O60658	0.708	0.0878
PEAK1	Q9H792	0.762	0.0526
PHB	P35232	0.41	0.321
PIP5K1A	Q99755	1.48	0.269
PKM	P14618	-0.723	0.0864
PPP1CC	P36873	0.332	0.209
PRDX1	Q06830	0.121	0.66
PRDX6	P30041	-0.509	0.207
PRPF8	Q6P2Q9	-0.436	0.255
PTBP1	P26599	-0.893	0.0142
PTDSS1	P48651	0.679	0.0687
RAB10	P61026	0.222	0.87
RAB29	O14966	1.19	0.0963
RAB8A	P61006	1.15	0.485
RAI14	Q9P0K7	0.648	0.0134
RAN	P62826	0.486	0.0394
RBSN	Q9H1K0	-0.204	0.383
RPL10	P27635	0.172	0.48
RPL11	P62913	0.282	0.21
RPL12	P30050	0.354	0.477
RPL15	P61313	0.702	0.0115

Table S2 Continued

RPL17	P18621	0.114	0.704
RPL18	Q07020	-2.3	0.0672
RPL18A	Q02543	0.502	0.0338
RPL21	P46778	-0.131	0.531
RPL23	P62829	-0.0251	0.914
RPL28	P46779	1.07	0.137
RPL3	P39023	-0.529	0.105
RPL34	P49207	-0.194	0.769
RPL36	Q9Y3U8	1.4	0.224
RPL4	P36578	-1.15	0.0688
RPL5	P46777	-0.19	0.394
RPL6	Q02878	0.365	0.347
RPL7A	P62424	-0.998	0.00941
RPL8	P62917	0.106	0.701
RPL9	P32969	-0.0747	0.854
RPS11	P62280	-0.183	0.358
RPS14	P62263	-0.382	0.135
RPS15A	P62244	-0.151	0.514
RPS16	P62249	1.09	0.262
RPS20	P60866	-0.42	0.0644
RPS23	P62266	-1.31	0.383
RPS27	P42677	0.197	0.454
RPS3	P23396	0.223	0.276
RPS4X	P62701	0.398	0.128
RPS6	P62753	0.177	0.573
RSL1D1	O76021	0.603	0.353
SCAMP3	O14828	1.87	0.11
SCRIB	Q14160	0.921	0.00382
SEC16A	O15027	0.547	0.0663
SEP7	Q16181	0.019	0.924
SF3B6	Q9Y3B4	-1.59	0.111
SH3GL1	Q99961	-0.879	0.0202
SLC25A3	Q00325	0.843	0.0513

Table S2 Continued

SLC25A5	P05141	-0.327	0.162
SLC25A6	P12236	0.193	0.387
SLK	Q9H2G2	-0.676	0.0423
SNX1	Q13596	0.657	0.0431
SNX9	Q9Y5X1	-0.818	0.0116
SPAG1	Q07617	0.785	0.103
SPECC1	Q5M775	-0.395	0.312
SPG20	Q8N0X7	-1.19	0.347
SPTBN1	Q01082	1.26	0.102
SRP14	P37108	-1.07	0.157
SRP54	P61011	-0.147	0.495
SRP68	Q9UHB9	-0.617	0.0328
STOML1	Q9UBI4	0.873	0.394
STUB1	Q9UNE7	-1.42	0.104
TAGLN2	P37802	-0.719	0.0879
TRAP1	Q12931	0.902	0.0109
TRIP11	Q15643	0.375	0.207
TUBA1B	P68363	-0.77	0.0137
TUBB	P07437	-0.903	0.00366
TUBB4B	P68371	-0.773	0.00991
TUFM	P49411	0.364	0.106
UBA1	P22314	0.558	0.265
UBE2M	P61081	-1.8	0.125
VDAC2	P45880	0.256	0.254

REFERENCES

1. Coley, W. B. Contribution to the knowledge of sarcoma. *Annals of Surgery* **14**, (1891).
2. Burnet, M. Cancer: a biological approach. III. Viruses associated with neoplastic conditions. *British Medical Journal* **1**, (1957).
3. Chen, D. S. & Mellman, I. Oncology meets immunology: The cancer-immunity cycle. *Immunity* vol. 39 (2013).
4. Shankaran, V. *et al.* IFN γ and lymphocytes prevent primary tumour development and shape tumour immunogenicity. *Nature* **410**, (2001).
5. Ikeda, H., Old, L. J. & Schreiber, R. D. The roles of IFN γ in protection against tumor development and cancer immunoediting. *Cytokine and Growth Factor Reviews* vol. 13 (2002).
6. Schreiber, R. D., Old, L. J. & Smyth, M. J. Cancer immunoediting: Integrating immunity's roles in cancer suppression and promotion. *Science* vol. 331 (2011).
7. Rosenthal, R. *et al.* Neoantigen-directed immune escape in lung cancer evolution. *Nature* **567**, (2019).
8. Martin, T. D. *et al.* The adaptive immune system is a major driver of selection for tumor suppressor gene inactivation. *Science* (1979) **373**, (2021).
9. Purroy, N. & Wu, C. J. Coevolution of leukemia and host immune cells in chronic lymphocytic leukemia. *Cold Spring Harbor Perspectives in Medicine* **7**, (2017).
10. Brunet, J.-F. *et al.* A new member of the immunoglobulin superfamily-CTLA-4. *Nature* **328**, 267–270 (1987).
11. Krummel, M. F. & Allison, J. P. CD28 and CTLA-4 have opposing effects on the response of T cells to stimulation. *Journal of Experimental Medicine* **182**, 459–465 (1995).
12. Leach, D. R., Krummel, M. F. & Allison, J. P. Enhancement of antitumor immunity by CTLA-4 blockade. *Science* (1979) **271**, (1996).
13. Qureshi, O. S. *et al.* Trans-endocytosis of CD80 and CD86: A molecular basis for the cell-extrinsic function of CTLA-4. *Science* (1979) **332**, (2011).
14. Hodi, F. S. *et al.* Improved survival with ipilimumab in patients with metastatic melanoma. *New England Journal of Medicine* **363**, 711–723 (2010).

15. Robert, C. *et al.* Ipilimumab plus Dacarbazine for previously untreated metastatic melanoma. *New England Journal of Medicine* **364**, 2517–2526 (2011).
16. Schadendorf, D. *et al.* Pooled analysis of long-term survival data from phase II and phase III trials of ipilimumab in unresectable or metastatic melanoma. *Journal of Clinical Oncology* **33**, (2015).
17. Ishida, Y., Agata, Y., Shibahara, K. & Honjo, T. Induced expression of PD-1, a novel member of the immunoglobulin gene superfamily, upon programmed cell death. *EMBO Journal* **11**, (1992).
18. Freeman, G. J. *et al.* Engagement of the PD-1 immunoinhibitory receptor by a novel B7 family member leads to negative regulation of lymphocyte activation. *Journal of Experimental Medicine* **192**, (2000).
19. Latchman, Y. *et al.* PD-L2 is a second ligand for PD-1 and inhibits T cell activation. *Nature Immunology* **2**, (2001).
20. Dong, H. *et al.* Tumor-associated B7-H1 promotes T-cell apoptosis: A potential mechanism of immune evasion. *Nature Medicine* **8**, (2002).
21. Topalian, S. L. *et al.* Safety, Activity, and Immune Correlates of Anti-PD-1 Antibody in Cancer. *New England Journal of Medicine* **366**, (2012).
22. Brahmer, J. R. *et al.* Safety and Activity of Anti-PD-L1 Antibody in Patients with Advanced Cancer. *New England Journal of Medicine* **366**, (2012).
23. Larkin, J. *et al.* Combined Nivolumab and Ipilimumab or Monotherapy in Untreated Melanoma. *New England Journal of Medicine* **373**, (2015).
24. Upadhaya, S., Neftelinov, S. T., Hodge, J. & Campbell, J. Challenges and opportunities in the PD1/PDL1 inhibitor clinical trial landscape. *Nature Reviews Drug Discovery* (2022) doi:10.1038/d41573-022-00030-4.
25. Wei, S. C. *et al.* Distinct cellular mechanisms underlie anti-CTLA-4 and anti-PD-1 checkpoint blockade. *Cell* **170**, (2017).
26. Mpekris, F. *et al.* Combining microenvironment normalization strategies to improve cancer immunotherapy. *Proceedings of the National Academy of Sciences* **117**, 3728–3737 (2020).
27. Triebel, F. *et al.* LAG-3, a novel lymphocyte activation gene closely related to CD4. *Journal of Experimental Medicine* **171**, 1393–1405 (1990).

28. Wang, J. *et al.* Fibrinogen-like Protein 1 Is a Major Immune Inhibitory Ligand of LAG-3. *Cell* **176**, (2019).
29. Maruhashi, T. *et al.* Binding of LAG-3 to stable peptide-MHC class II limits T cell function and suppresses autoimmunity and anti-cancer immunity. *Immunity* (2022) doi:10.1016/j.immuni.2022.03.013.
30. Tawbi, H. A. *et al.* Relatlimab and Nivolumab versus Nivolumab in Untreated Advanced Melanoma. *New England Journal of Medicine* **386**, 24–34 (2022).
31. Eshhar, Z., Waks, T., Gross, G. & Schindler, D. G. Specific activation and targeting of cytotoxic lymphocytes through chimeric single chains consisting of antibody-binding domains and the gamma or zeta subunits of the immunoglobulin and T-cell receptors. *Proceedings of the National Academy of Sciences* **90**, 720–724 (1993).
32. Singh, A. K. & McGuirk, J. P. CAR T cells: continuation in a revolution of immunotherapy. *The Lancet Oncology* **21**, e168–e178 (2020).
33. Kochenderfer, J. N. *et al.* Eradication of B-lineage cells and regression of lymphoma in a patient treated with autologous T cells genetically engineered to recognize CD19. *Blood* **116**, (2010).
34. Porter, D. L., Levine, B. L., Kalos, M., Bagg, A. & June, C. H. Chimeric Antigen Receptor–Modified T Cells in Chronic Lymphoid Leukemia. *New England Journal of Medicine* **365**, (2011).
35. Grupp, S. A. *et al.* Chimeric Antigen Receptor–Modified T Cells for Acute Lymphoid Leukemia. *New England Journal of Medicine* **368**, (2013).
36. Maude, S. L. *et al.* Chimeric Antigen Receptor T Cells for Sustained Remissions in Leukemia. *New England Journal of Medicine* **371**, (2014).
37. Neelapu, S. S. *et al.* Axicabtagene Ciloleucel CAR T-Cell Therapy in Refractory Large B-Cell Lymphoma. *New England Journal of Medicine* **377**, (2017).
38. Schuster, S. J. *et al.* Tisagenlecleucel in Adult Relapsed or Refractory Diffuse Large B-Cell Lymphoma. *New England Journal of Medicine* **380**, (2019).
39. Munshi, N. C. *et al.* Idecabtagene Vicleucel in relapsed and refractory multiple myeloma. *New England Journal of Medicine* **384**, (2021).
40. Melenhorst, J. J. *et al.* Decade-Long Remissions of Leukemia Sustained By the Persistence of Activated CD4+ CAR T-Cells. *Blood* **138**, (2021).

41. Newick, K., O'Brien, S., Moon, E. & Albelda, S. M. CAR T cell therapy for solid tumors. *Annual Review of Medicine* **68**, (2017).
42. Hou, A. J., Chen, L. C. & Chen, Y. Y. Navigating CAR-T cells through the solid-tumour microenvironment. *Nature Reviews Drug Discovery* vol. 20 (2021).
43. Yarchoan, M., Hopkins, A. & Jaffee, E. M. Tumor Mutational Burden and Response Rate to PD-1 Inhibition. *New England Journal of Medicine* **377**, (2017).
44. Le, D. T. *et al.* PD-1 Blockade in Tumors with Mismatch-Repair Deficiency. *New England Journal of Medicine* **372**, (2015).
45. Le, D. T. *et al.* Mismatch repair deficiency predicts response of solid tumors to PD-1 blockade. *Science (1979)* **357**, (2017).
46. Routy, B. *et al.* Gut microbiome influences efficacy of PD-1-based immunotherapy against epithelial tumors. *Science (1979)* **359**, (2018).
47. Davar, D. *et al.* Fecal microbiota transplant overcomes resistance to anti-PD-1 therapy in melanoma patients. *Science (1979)* **371**, (2021).
48. Wang, W. *et al.* CD8⁺ T cells regulate tumour ferroptosis during cancer immunotherapy. *Nature* **569**, (2019).
49. Helmink, B. A. *et al.* B cells and tertiary lymphoid structures promote immunotherapy response. *Nature* **577**, (2020).
50. Meylan, M. *et al.* Tertiary lymphoid structures generate and propagate anti-tumor antibody-producing plasma cells in renal cell cancer. *Immunity* (2022) doi:10.1016/j.immuni.2022.02.001.
51. Sharma, P., Hu-Lieskovan, S., Wargo, J. A. & Ribas, A. Primary, Adaptive, and Acquired Resistance to Cancer Immunotherapy. *Cell* vol. 168 (2017).
52. Weichselbaum, R. R., Liang, H., Deng, L. & Fu, Y. X. Radiotherapy and immunotherapy: A beneficial liaison? *Nature Reviews Clinical Oncology* vol. 14 (2017).
53. Blass, E. & Ott, P. A. Advances in the development of personalized neoantigen-based therapeutic cancer vaccines. *Nature Reviews Clinical Oncology* vol. 18 (2021).
54. Galluzzi, L., Buqué, A., Kepp, O., Zitvogel, L. & Kroemer, G. Immunogenic cell death in cancer and infectious disease. *Nature Reviews Immunology* vol. 17 (2017).
55. Kalaora, S. *et al.* Immunoproteasome expression is associated with better prognosis and response to checkpoint therapies in melanoma. *Nature Communications* **11**, (2020).

56. Yamamoto, K. *et al.* Autophagy promotes immune evasion of pancreatic cancer by degrading MHC-I. *Nature* **581**, (2020).
57. Ling, A. *et al.* TAP1 down-regulation elicits immune escape and poor prognosis in colorectal cancer. *OncoImmunology* **6**, (2017).
58. Sultan, M. *et al.* Epigenetic silencing of TAP1 in Aldefluor+ breast cancer stem cells contributes to their enhanced Immune evasion. *Stem Cells* **36**, (2018).
59. Sade-Feldman, M. *et al.* Resistance to checkpoint blockade therapy through inactivation of antigen presentation. *Nature Communications* **8**, (2017).
60. Alspach, E., Lussier, D. M. & Schreiber, R. D. Interferon γ and its important roles in promoting and inhibiting spontaneous and therapeutic cancer immunity. *Cold Spring Harbor Perspectives in Biology* **11**, (2019).
61. Gocher, A. M., Workman, C. J. & Vignali, D. A. A. Interferon- γ : teammate or opponent in the tumour microenvironment? *Nature Reviews Immunology* (2021) doi:10.1038/s41577-021-00566-3.
62. Gao, J. *et al.* Loss of IFN- γ Pathway Genes in Tumor Cells as a Mechanism of Resistance to Anti-CTLA-4 Therapy. *Cell* **167**, (2016).
63. Zaretsky, J. M. *et al.* Mutations Associated with Acquired Resistance to PD-1 Blockade in Melanoma. *New England Journal of Medicine* **375**, (2016).
64. Shin, D. S. *et al.* Primary resistance to PD-1 blockade mediated by JAK1/2 mutations. *Cancer Discovery* **7**, (2017).
65. Torrejon, D. Y. *et al.* Overcoming genetically based resistance mechanisms to PD-1 blockade. *Cancer Discovery* **10**, (2020).
66. Ayers, M. *et al.* IFN- γ -related mRNA profile predicts clinical response to PD-1 blockade. *Journal of Clinical Investigation* **127**, (2017).
67. Patel, S. J. *et al.* Identification of essential genes for cancer immunotherapy. *Nature* **548**, (2017).
68. Manguso, R. T. *et al.* In vivo CRISPR screening identifies Ptpn2 as a cancer immunotherapy target. *Nature* **547**, (2017).
69. Katkeviciute, E. *et al.* Protein tyrosine phosphatase nonreceptor type 2 controls colorectal cancer development. *Journal of Clinical Investigation* **131**, (2021).

70. Zhou, Y. *et al.* Activation of NF- κ B and p300/CBP potentiates cancer chemoimmunotherapy through induction of MHC-I antigen presentation. *Proceedings of the National Academy of Sciences* **118**, e2025840118 (2021).
71. Wang, G. *et al.* Crispr-gemm pooled mutagenic screening identifies kmt2d as a major modulator of immune checkpoint blockade. *Cancer Discovery* **10**, (2020).
72. Burr, M. L. *et al.* An Evolutionarily Conserved Function of Polycomb Silences the MHC Class I Antigen Presentation Pathway and Enables Immune Evasion in Cancer. *Cancer Cell* **36**, (2019).
73. Zhou, L., Mudianto, T., Ma, X., Riley, R. & Uppaluri, R. Targeting EZH2 enhances antigen presentation, antitumor immunity, and Circumvents anti-PD-1 resistance in head and neck cancer. *Clinical Cancer Research* **26**, 290–300 (2020).
74. Li, G. *et al.* LIMIT is an immunogenic lncRNA in cancer immunity and immunotherapy. *Nature Cell Biology* **23**, (2021).
75. Chabanon, R. M. *et al.* Targeting the DNA damage response in immuno-oncology: developments and opportunities. *Nature Reviews Cancer* vol. 21 (2021).
76. Samstein, R. M. *et al.* Mutations in BRCA1 and BRCA2 differentially affect the tumor microenvironment and response to checkpoint blockade immunotherapy. *Nature Cancer* **1**, (2020).
77. Zhang, M. *et al.* RNA editing derived epitopes function as cancer antigens to elicit immune responses. *Nature Communications* **9**, (2018).
78. Bowling, E. A. *et al.* Spliceosome-targeted therapies trigger an antiviral immune response in triple-negative breast cancer. *Cell* **184**, (2021).
79. Lu, S. X. *et al.* Pharmacologic modulation of RNA splicing enhances anti-tumor immunity. *Cell* **184**, (2021).
80. Harrington, K., Freeman, D. J., Kelly, B., Harper, J. & Soria, J. C. Optimizing oncolytic virotherapy in cancer treatment. *Nature Reviews Drug Discovery* vol. 18 (2019).
81. Smith, C. C. *et al.* Endogenous retroviral signatures predict immunotherapy response in clear cell renal cell carcinoma. *Journal of Clinical Investigation* **128**, (2018).
82. Alspach, E. *et al.* MHC-II neoantigens shape tumour immunity and response to immunotherapy. *Nature* **574**, (2019).

83. Oh, D. Y. & Fong, L. Cytotoxic CD4⁺ T cells in cancer: Expanding the immune effector toolbox. *Immunity* **54**, 2701–2711 (2021).
84. Jhunjhunwala, S., Hammer, C. & Delamarre, L. Antigen presentation in cancer: insights into tumour immunogenicity and immune evasion. *Nature Reviews Cancer* vol. 21 (2021).
85. Nagarsheth, N., Wicha, M. S. & Zou, W. Chemokines in the cancer microenvironment and their relevance in cancer immunotherapy. *Nature Reviews Immunology* vol. 17 (2017).
86. Proper, D. J. & Balkwill, F. R. Harnessing cytokines and chemokines for cancer therapy. *Nature Reviews Clinical Oncology* (2022) doi:10.1038/s41571-021-00588-9.
87. Peng, D. *et al.* Epigenetic silencing of TH1-type chemokines shapes tumour immunity and immunotherapy. *Nature* **527**, (2015).
88. Nagarsheth, N. *et al.* PRC2 epigenetically silences Th1-type chemokines to suppress effector T-cell trafficking in colon cancer. *Cancer Research* **76**, 275–282 (2016).
89. Mikucki, M. E. *et al.* Non-redundant requirement for CXCR3 signalling during tumoricidal T-cell trafficking across tumour vascular checkpoints. *Nature Communications* **6**, (2015).
90. Chow, M. T. *et al.* Intratumoral Activity of the CXCR3 Chemokine System Is Required for the Efficacy of Anti-PD-1 Therapy. *Immunity* **50**, (2019).
91. House, I. G. *et al.* Macrophage-derived CXCL9 and CXCL10 are required for antitumor immune responses following immune checkpoint blockade. *Clinical Cancer Research* **26**, (2020).
92. Barreira Da Silva, R. *et al.* Dipeptidylpeptidase 4 inhibition enhances lymphocyte trafficking, improving both naturally occurring tumor immunity and immunotherapy. *Nature Immunology* **16**, (2015).
93. Dangaj, D. *et al.* Cooperation between Constitutive and Inducible Chemokines Enables T Cell Engraftment and Immune Attack in Solid Tumors. *Cancer Cell* **35**, (2019).
94. Hollinger, S. & Hepler, J. R. Cellular regulation of RGS proteins: Modulators and integrators of G protein signaling. *Pharmacological Reviews* vol. 54 (2002).
95. Huang, D. *et al.* Targeting regulator of G protein signaling 1 in tumor-specific T cells enhances their trafficking to breast cancer. *Nature Immunology* **22**, (2021).
96. Ugel, S., de Sanctis, F., Mandruzzato, S. & Bronte, V. Tumor-induced myeloid deviation: When myeloid-derived suppressor cells meet tumor-Associated macrophages. *Journal of Clinical Investigation* vol. 125 (2015).

97. Flores-Toro, J. A. *et al.* CCR2 inhibition reduces tumor myeloid cells and unmasks a checkpoint inhibitor effect to slow progression of resistant murine gliomas. *Proc Natl Acad Sci U S A* **117**, (2020).
98. Barreira da Silva, R. *et al.* Loss of the intracellular enzyme QPCTL limits chemokine function and reshapes myeloid infiltration to augment tumor immunity. *Nature Immunology* (2022) doi:10.1038/s41590-022-01153-x.
99. Highfill, S. L. *et al.* Disruption of CXCR2-mediated MDSC tumor trafficking enhances anti-PD1 efficacy. *Science Translational Medicine* **6**, (2014).
100. Marshall, L. A. *et al.* Tumors establish resistance to immunotherapy by regulating Treg recruitment via CCR4. *Journal for ImmunoTherapy of Cancer* **8**, e000764 (2020).
101. Huang, Y. *et al.* Vascular normalizing doses of antiangiogenic treatment reprogram the immunosuppressive tumor microenvironment and enhance immunotherapy. *Proc Natl Acad Sci U S A* **109**, (2012).
102. di Tacchio, M. *et al.* Tumor vessel normalization, immunostimulatory reprogramming, and improved survival in glioblastoma with combined inhibition of PD-1, angiopoietin-2, and VEGF. *Cancer Immunology Research* **7**, (2019).
103. Li, Q. *et al.* Low-dose anti-angiogenic therapy sensitizes breast cancer to PD-1 blockade. *Clinical Cancer Research* **26**, (2020).
104. Schmittnaegel, M. *et al.* Dual angiopoietin-2 and VEGFA inhibition elicits antitumor immunity that is enhanced by PD-1 checkpoint blockade. *Science Translational Medicine* **9**, (2017).
105. Zhang, N. *et al.* DLL1 orchestrates CD8+ T cells to induce long-term vascular normalization and tumor regression. *Proc Natl Acad Sci U S A* **118**, (2021).
106. Sun, Y. *et al.* Blockade of the CD93 pathway normalizes tumor vasculature to facilitate drug delivery and immunotherapy. *Science Translational Medicine* **13**, (2021).
107. Martinet, L. *et al.* Human solid tumors contain high endothelial venules: Association with T- and B-lymphocyte infiltration and favorable prognosis in breast cancer. *Cancer Research* **71**, (2011).
108. Asrir, A. *et al.* Tumor-associated high endothelial venules mediate lymphocyte entry into tumors and predict response to PD-1 plus CTLA-4 combination immunotherapy. *Cancer Cell* (2022) doi:10.1016/j.ccell.2022.01.002.

109. Sun, X. *et al.* Tumour DDR1 promotes collagen fibre alignment to instigate immune exclusion. *Nature* **599**, (2021).
110. Nicolas-Boluda, A. *et al.* Tumor stiffening reversion through collagen crosslinking inhibition improves t cell migration and anti-pd-1 treatment. *Elife* **10**, (2021).
111. Liberti, M. v. & Locasale, J. W. The Warburg Effect: How Does it Benefit Cancer Cells? *Trends in Biochemical Sciences* **41**, 211–218 (2016).
112. Fischer, K. *et al.* Inhibitory effect of tumor cell-derived lactic acid on human T cells. *Blood* **109**, (2007).
113. Brand, A. *et al.* LDHA-associated lactic acid production blunts tumor immunosurveillance by T and NK cells. *Cell Metabolism* **24**, (2016).
114. Watson, M. L. J. *et al.* Metabolic support of tumour-infiltrating regulatory T cells by lactic acid. *Nature* **591**, (2021).
115. Kumagai, S. *et al.* Lactic acid promotes PD-1 expression in regulatory T cells in highly glycolytic tumor microenvironments. *Cancer Cell* (2022) doi:10.1016/j.ccell.2022.01.001.
116. Cascone, T. *et al.* Increased Tumor Glycolysis Characterizes Immune Resistance to Adoptive T Cell Therapy. *Cell Metabolism* **27**, (2018).
117. Li, W. *et al.* Aerobic Glycolysis Controls Myeloid-Derived Suppressor Cells and Tumor Immunity via a Specific CEBPB Isoform in Triple-Negative Breast Cancer. *Cell Metabolism* **28**, (2018).
118. Liu, Y. *et al.* Tumors exploit FTO-mediated regulation of glycolytic metabolism to evade immune surveillance. *Cell Metabolism* **33**, (2021).
119. Renner, K. *et al.* Restricting Glycolysis Preserves T Cell Effector Functions and Augments Checkpoint Therapy. *Cell Reports* **29**, (2019).
120. Hermans, D. *et al.* Lactate dehydrogenase inhibition synergizes with IL-21 to promote CD8+ T cell stemness and antitumor immunity. *Proc Natl Acad Sci U S A* **117**, (2020).
121. Gu, M. *et al.* NF- κ B-inducing kinase maintains T cell metabolic fitness in antitumor immunity. *Nature Immunology* **22**, (2021).
122. Yu, Y. R. *et al.* Disturbed mitochondrial dynamics in CD8+ TILs reinforce T cell exhaustion. *Nature Immunology* **21**, (2020).

123. Labadie, B. W., Bao, R. & Luke, J. J. Reimagining IDO pathway inhibition in cancer immunotherapy via downstream focus on the tryptophan–kynurenine–aryl hydrocarbon axis. *Clinical Cancer Research* vol. 25 (2019).
124. Tang, K., Wu, Y. H., Song, Y. & Yu, B. Indoleamine 2,3-dioxygenase 1 (IDO1) inhibitors in clinical trials for cancer immunotherapy. *Journal of Hematology and Oncology* vol. 14 (2021).
125. Leone, R. D. *et al.* Glutamine blockade induces divergent metabolic programs to overcome tumor immune evasion. *Science (1979)* **366**, (2019).
126. Bian, Y. *et al.* Cancer SLC43A2 alters T cell methionine metabolism and histone methylation. *Nature* **585**, (2020).
127. Ye, L. *et al.* A genome-scale gain-of-function CRISPR screen in CD8 T cells identifies proline metabolism as a means to enhance CAR-T therapy. *Cell Metabolism* (2022) doi:10.1016/j.cmet.2022.02.009.
128. Lim, S. A. *et al.* Lipid signalling enforces functional specialization of Treg cells in tumours. *Nature* **591**, (2021).
129. Zhang, Y. *et al.* Enhancing CD8⁺ T cell fatty acid catabolism within a metabolically challenging tumor microenvironment increases the efficacy of melanoma immunotherapy. *Cancer Cell* **32**, (2017).
130. Liu, X. *et al.* Reprogramming lipid metabolism prevents effector T cell senescence and enhances tumor immunotherapy. *Science Translational Medicine* **13**, (2021).
131. Yang, W. *et al.* Potentiating the antitumour response of CD8⁺ T cells by modulating cholesterol metabolism. *Nature* **531**, (2016).
132. Ma, X. *et al.* Cholesterol induces CD8⁺ T cell exhaustion in the tumor microenvironment. *Cell Metabolism* **30**, (2019).
133. Rameshbabu, S., Labadie, B. W., Argulian, A. & Patnaik, A. Targeting innate immunity in cancer therapy. *Vaccines* vol. 9 (2021).
134. Zitvogel, L., Galluzzi, L., Kepp, O., Smyth, M. J. & Kroemer, G. Type I interferons in anticancer immunity. *Nature Reviews Immunology* vol. 15 (2015).
135. Sun, L., Wu, J., Du, F., Chen, X. & Chen, Z. J. Cyclic GMP-AMP synthase is a cytosolic DNA sensor that activates the type I interferon pathway. *Science (1979)* **339**, (2013).

136. Wang, H. *et al.* cGAS is essential for the antitumor effect of immune checkpoint blockade. *Proc Natl Acad Sci U S A* **114**, (2017).
137. Demaria, O. *et al.* STING activation of tumor endothelial cells initiates spontaneous and therapeutic antitumor immunity. *Proc Natl Acad Sci U S A* **112**, (2015).
138. Chin, E. N. *et al.* Antitumor activity of a systemic STING-activating non-nucleotide cGAMP mimetic. *Science (1979)* **369**, (2020).
139. Pan, B. S. *et al.* An orally available non-nucleotide STING agonist with antitumor activity. *Science (1979)* **369**, (2020).
140. Li, S. *et al.* Prolonged activation of innate immune pathways by a polyvalent STING agonist. *Nature Biomedical Engineering* **5**, (2021).
141. Ramanjulu, J. M. *et al.* Design of amidobenzimidazole STING receptor agonists with systemic activity. *Nature* **564**, (2018).
142. Lv, M. *et al.* Manganese is critical for antitumor immune responses via cGAS-STING and improves the efficacy of clinical immunotherapy. *Cell Research* **30**, (2020).
143. Rehwinkel, J. & Gack, M. U. RIG-I-like receptors: their regulation and roles in RNA sensing. *Nature Reviews Immunology* vol. 20 (2020).
144. Heidegger, S. *et al.* RIG-I activation is critical for responsiveness to checkpoint blockade. *Science Immunology* **4**, (2019).
145. Such, L. *et al.* Targeting the innate immunoreceptor RIG-I overcomes melanoma-intrinsic resistance to T cell immunotherapy. *Journal of Clinical Investigation* **140**, (2020).
146. Sheng, W. *et al.* LSD1 Ablation Stimulates Anti-tumor Immunity and Enables Checkpoint Blockade. *Cell* **174**, (2018).
147. Zhang, S. M. *et al.* KDM5B promotes immune evasion by recruiting SETDB1 to silence retroelements. *Nature* **598**, (2021).
148. Kawasaki, T. & Kawai, T. Toll-like receptor signaling pathways. *Frontiers in Immunology* vol. 5 (2014).
149. Sun, L. *et al.* Activating a collaborative innate-adaptive immune response to control metastasis. *Cancer Cell* **39**, 1361-1374.e9 (2021).
150. Ribas, A. *et al.* Overcoming PD-1 blockade resistance with CpG-A Toll-like receptor 9 agonist vidutolimod in patients with metastatic melanoma. *Cancer Discovery* **11**, (2021).

151. Sagiv-Barfi, I. *et al.* Eradication of spontaneous malignancy by local immunotherapy. *Science Translational Medicine* **10**, (2018).
152. Michaelis, K. A. *et al.* The TLR7/8 agonist R848 remodels tumor and host responses to promote survival in pancreatic cancer. *Nature Communications* **10**, (2019).
153. Deng, L. *et al.* STING-dependent cytosolic DNA sensing promotes radiation-induced type I interferon-dependent antitumor immunity in immunogenic tumors. *Immunity* **41**, (2014).
154. Pfirschke, C. *et al.* Immunogenic chemotherapy sensitizes tumors to checkpoint blockade therapy. *Immunity* **44**, (2016).
155. Zhou, Y., He, C., Wang, L. & Ge, B. Post-translational regulation of antiviral innate signaling. *European Journal of Immunology* vol. 47 (2017).
156. Shi, J., Gao, W. & Shao, F. Pyroptosis: Gasdermin-Mediated Programmed Necrotic Cell Death. *Trends in Biochemical Sciences* vol. 42 (2017).
157. Deng, W. *et al.* Streptococcal pyrogenic exotoxin B cleaves GSDMA and triggers pyroptosis. *Nature* (2022) doi:10.1038/s41586-021-04384-4.
158. Xia, S. *et al.* Gasdermin D pore structure reveals preferential release of mature interleukin-1. *Nature* **593**, (2021).
159. Zhou, Z. *et al.* Granzyme A from cytotoxic lymphocytes cleaves GSDMB to trigger pyroptosis in target cells. *Science* (1979) **368**, (2020).
160. Liu, Y. *et al.* Gasdermin E-mediated target cell pyroptosis by CAR T cells triggers cytokine release syndrome. *Sci Immunol* **5**, (2020).
161. Wang, Y. *et al.* Chemotherapy drugs induce pyroptosis through caspase-3 cleavage of a gasdermin. *Nature* **547**, (2017).
162. Lu, H. *et al.* Molecular targeted therapies elicit concurrent apoptotic and GSDME-dependent pyroptotic tumor cell death. *Clinical Cancer Research* **24**, (2018).
163. Kwon, B. S. & Weissman, S. M. cDNA sequences of two inducible T-cell genes. *Proc Natl Acad Sci U S A* **86**, (1989).
164. Schwarz, H., Valbracht, J., Tuckwell, J., von Kempis, J. & Lotz, M. ILA the human 4-1BB homologue, is inducible in lymphoid and other cell lineages. *Blood* **85**, (1995).
165. Futagawa, T. *et al.* Expression and function of 4-1BB and 4-1BB ligand on murine dendritic cells. *International Immunology* **14**, (2002).

166. Melero, I., Johnston, J. v., Shufford, W. W., Mittler, R. S. & Chen, L. NK1.1 cells express 4-1BB (CDw137) costimulatory molecule and are required for tumor immunity elicited by anti-4-1BB monoclonal antibodies. *Cellular Immunology* **190**, (1998).
167. Tu, T. H. *et al.* 4-1BB/4-1BBL interaction promotes obesity-induced adipose inflammation by triggering bidirectional inflammatory signaling in adipocytes/macrophages. *Mediators Inflamm* **2012**, 972629 (2012).
168. Olofsson, P. S. *et al.* CD137 is expressed in human atherosclerosis and promotes development of plaque inflammation in hypercholesterolemic mice. *Circulation* **117**, 1292–301 (2008).
169. Le, N. H. *et al.* Blockade of 4-1BB and 4-1BBL interaction reduces obesity-induced skeletal muscle inflammation. *Mediators of Inflammation* **2013**, (2013).
170. Glorieux, C. & Huang, P. Regulation of CD137 expression through K-Ras signaling in pancreatic cancer cells. *Cancer Communications* **39**, (2019).
171. Laderach, D., Movassagh, M., Johnson, A., Mittler, R. S. & Galy, A. 4-1BB co-stimulation enhances human CD8⁺ T cell priming by augmenting the proliferation and survival of effector CD8⁺ T cells. *International Immunology* **14**, (2002).
172. Kim, J. O., Kim, H. W., Baek, K. M. & Kang, C. Y. NF- κ B and AP-1 regulate activation-dependent CD137 (4-1BB) expression in T cells. *FEBS Letters* **541**, (2003).
173. Fröhlich, A. *et al.* Comprehensive analysis of tumor necrosis factor receptor TNFRSF9 (4-1BB) DNA methylation with regard to molecular and clinicopathological features, immune infiltrates, and response prediction to immunotherapy in melanoma. *EBioMedicine* **52**, 102647 (2020).
174. Goodwin, R. G. *et al.* Molecular cloning of a ligand for the inducible T cell gene 4-1BB: a member of an emerging family of cytokines with homology to tumor necrosis factor. *European Journal of Immunology* **23**, (1993).
175. DeBenedette, M. A., Shahinian, A., Mak, T. W. & Watts, T. H. Costimulation of CD28- T lymphocytes by 4-1BB ligand. *J Immunol* **158**, (1997).
176. Won, E.-Y. *et al.* The Structure of the Trimer of Human 4-1BB Ligand Is Unique among Members of the Tumor Necrosis Factor Superfamily. *Journal of Biological Chemistry* **285**, 9202–9210 (2010).

177. Compaaan, D. M. & Hymowitz, S. G. The crystal structure of the costimulatory OX40-OX40L complex. *Structure* **14**, (2006).
178. Chan, S. *et al.* An anti-PD-1–GITR-L bispecific agonist induces GITR clustering-mediated T cell activation for cancer immunotherapy. *Nature Cancer* (2022) doi:10.1038/s43018-022-00334-9.
179. Arch, R. H. & Thompson, C. B. 4-1BB and Ox40 are members of a tumor necrosis factor (TNF)-nerve growth factor receptor subfamily that bind TNF receptor-associated factors and activate nuclear factor κ B. *Molecular and Cellular Biology* **18**, (1998).
180. Jang, I. K., Lee, Z. H., Kim, Y. J., Kim, S. H. & Kwon, B. S. Human 4-1BB (CD137) signals are mediated by TRAF2 and activate nuclear factor- κ B. *Biochemical and Biophysical Research Communications* **242**, (1998).
181. Madireddi, S. *et al.* Galectin-9 controls the therapeutic activity of 4-1BB-targeting antibodies. *Journal of Experimental Medicine* **211**, (2014).
182. Zheng, C., Kabaleeswaran, V., Wang, Y., Cheng, G. & Wu, H. Crystal structures of the TRAF2: cIAP2 and the TRAF1: TRAF2: cIAP2 complexes: Affinity, specificity, and regulation. *Molecular Cell* **38**, (2010).
183. McPherson, A. J., Snell, L. M., Mak, T. W. & Watts, T. H. Opposing roles for TRAF1 in the alternative versus classical NF- κ B pathway in T cells. *Journal of Biological Chemistry* **287**, (2012).
184. Cannons, J. L., Choi, Y. & Watts, T. H. Role of TNF Receptor-Associated Factor 2 and p38 Mitogen-Activated Protein Kinase Activation During 4-1BB-Dependent Immune Response. *The Journal of Immunology* **165**, (2000).
185. Sabbagh, L., Pulle, G., Liu, Y., Tsitsikov, E. N. & Watts, T. H. ERK-Dependent Bim Modulation Downstream of the 4-1BB-TRAF1 Signaling Axis Is a Critical Mediator of CD8 T Cell Survival In Vivo. *The Journal of Immunology* **180**, (2008).
186. Azpilikueta, A. *et al.* Deubiquitinases A20 and CYLD modulate costimulatory signaling via CD137 (4–1BB). *OncoImmunology* **7**, (2018).
187. Martinez-Forero, I. *et al.* T cell costimulation with anti-CD137 monoclonal antibodies is mediated by K63-polyubiquitin-dependent signals from endosomes. *J Immunol* **190**, 6694–706 (2013).

188. Bitra, A., Doukov, T., Croft, M. & Zajonc, D. M. Crystal structures of the human 4-1BB receptor bound to its ligand 4-1BBL reveal covalent receptor dimerization as a potential signaling amplifier. *Journal of Biological Chemistry* **293**, (2018).
189. Li, Y. *et al.* Limited cross-linking of 4-1BB by 4-1BB ligand and the agonist monoclonal antibody Utomilumab. *Cell Reports* **25**, (2018).
190. Zapata, J. M. *et al.* CD137 (4-1BB) signalosome: Complexity is a matter of TRAFs. *Frontiers in Immunology* vol. 9 (2018).
191. Oh, H. S. *et al.* 4-1BB signaling enhances primary and secondary population expansion of CD8⁺ T cells by maximizing autocrine IL-2/IL-2 receptor signaling. *PLoS ONE* **10**, (2015).
192. Barsoumian, H. B., Yolcu, E. S. & Shirwan, H. 4-1BB signaling in conventional T cells drives IL-2 production that overcomes CD4⁺CD25⁺FoxP3⁺ T regulatory cell suppression. *PLoS ONE* **11**, (2016).
193. Wilcox, R. A., Tamada, K., Strome, S. E. & Chen, L. Signaling through NK cell-associated CD137 promotes both helper function for CD8⁺ cytolytic T cells and responsiveness to IL-2 but not cytolytic activity. *The Journal of Immunology* **169**, (2002).
194. Kim, Y. H. *et al.* IFN- γ -indoleamine-2,3 dioxygenase acts as a major suppressive factor in 4-1BB-mediated immune suppression in vivo. *Journal of Leukocyte Biology* **85**, (2009).
195. Shin, S. M. *et al.* 4-1BB triggers IL-13 production from T cells to limit the polarized, Th1-mediated inflammation. *Journal of Leukocyte Biology* **81**, (2007).
196. Wong, H. Y., Prasad, A., Gan, S. U., Chua, J. J. E. & Schwarz, H. Identification of CD137-Expressing B Cells in Multiple Sclerosis Which Secrete IL-6 Upon Engagement by CD137 Ligand. *Front Immunol* **11**, 571964 (2020).
197. Compte, M. *et al.* A tumor-targeted trimeric 4-1BB-agonistic antibody induces potent anti-tumor immunity without systemic toxicity. *Nature Communications* **9**, (2018).
198. Kienzle, G. & von Kempis, J. CD137 (ILA/4-1BB), expressed by primary human monocytes, induces monocyte activation and apoptosis of B lymphocytes. *International Immunology* **12**, (2000).
199. Lee, H.-W. *et al.* 4-1BB Promotes the Survival of CD8⁺ T Lymphocytes by Increasing Expression of Bcl-xL and Bfl-1. *The Journal of Immunology* **169**, 4882–4888 (2002).

200. Hernandez-Chacon, J. A. *et al.* Costimulation through the CD137/4-1BB pathway protects human melanoma tumor-infiltrating lymphocytes from activation-induced cell death and enhances antitumor effector function. *Journal of Immunotherapy* **34**, (2011).
201. Hurtado, J. C., Kim, Y. J. & Kwon, B. S. Signals through 4-1BB are costimulatory to previously activated splenic T cells and inhibit activation-induced cell death. *J Immunol* **158**, (1997).
202. Lee, H. W. *et al.* 4-1BB cross-linking enhances the survival and cell cycle progression of CD4 T lymphocytes. *Cellular Immunology* **223**, (2003).
203. Lee, D. Y. *et al.* 4-1BB Signaling Activates the T Cell Factor 1 Effector/ β -Catenin Pathway with Delayed Kinetics via ERK Signaling and Delayed PI3K/AKT Activation to Promote the Proliferation of CD8⁺ T Cells. *PLoS ONE* **8**, (2013).
204. Choi, B. K. *et al.* 4-1BB signaling activates glucose and fatty acid metabolism to enhance CD8⁺ T cell proliferation. *Cellular and Molecular Immunology* **14**, (2017).
205. Teijeira, A. *et al.* Mitochondrial morphological and functional reprogramming following CD137 (4-1BB) Costimulation. *Cancer Immunology Research* **6**, (2018).
206. Menk, A. v. *et al.* 4-1BB costimulation induces T cell mitochondrial function and biogenesis enabling cancer immunotherapeutic responses. *Journal of Experimental Medicine* **215**, (2018).
207. Otano, I. *et al.* CD137 (4-1BB) costimulation of CD8⁺ T cells is more potent when provided in cis than in trans with respect to CD3-TCR stimulation. *Nature Communications* **12**, 7296 (2021).
208. Setareh, M., Schwarz, H. & Lotz, M. A mRNA variant encoding a soluble form of 4-1BB, a member of the murine NGF/TNF receptor family. *Gene* **164**, (1995).
209. Labiano, S. *et al.* Hypoxia-induced soluble CD137 in malignant cells blocks CD137L-costimulation as an immune escape mechanism. *OncImmunology* **5**, (2016).
210. Seidel, J. *et al.* Role of adam10 and adam17 in regulating cd137 function. *International Journal of Molecular Sciences* **22**, (2021).
211. Michel, J., Langstein, J., Hofstädter, F. & Schwarz, H. A soluble form of CD137 (ILA/4-1BB), a member of the TNF receptor family, is released by activated lymphocytes and is detectable in sera of patients with rheumatoid arthritis. *European Journal of Immunology* **28**, (1998).

212. Jung, H. W., Choi, S. W., Choi, J. I. L. & Kwon, B. S. Serum concentrations of soluble 4-1BB, and 4-1BB ligand correlated with the disease severity in rheumatoid arthritis. *Experimental and Molecular Medicine* **36**, (2004).
213. Furtner, M., Straub, R. H., Krüger, S. & Schwarz, H. Levels of soluble CD137 are enhanced in sera of leukemia and lymphoma patients and are strongly associated with chronic lymphocytic leukemia. *Leukemia* vol. 19 (2005).
214. Sharief, M. K. Heightened intrathecal release of soluble CD137 in patients with multiple sclerosis. *European Journal of Neurology* **9**, (2002).
215. Itoh, A. *et al.* Soluble CD137 Ameliorates Acute Type 1 Diabetes by Inducing T Cell Anergy. *Frontiers in Immunology* **10**, (2019).
216. Weigand, K. *et al.* Soluble CD137 is a novel serum marker of liver cirrhosis in patients with hepatitis C and alcohol-associated disease etiology. *Eur J Immunol* (2021) doi:10.1002/eji.202149488.
217. Glez-Vaz, J. *et al.* Soluble CD137 as a dynamic biomarker to monitor agonist CD137 immunotherapies. *Journal for ImmunoTherapy of Cancer* **10**, e003532 (2022).
218. Zhang, W. *et al.* Serum concentration of CD137 and tumor infiltration by M1 macrophages predict the response to Sintilimab plus Bevacizumab biosimilar in advanced hepatocellular carcinoma patients. *Clinical Cancer Research* OF1–OF10 (2022) doi:10.1158/1078-0432.CCR-21-3972.
219. Shao, Z., Sun, F., Koh, D. R. & Schwarz, H. Characterisation of soluble murine CD137 and its association with systemic lupus. *Molecular Immunology* **45**, (2008).
220. Kwon, B. S. *et al.* Immune responses in 4-1BB (CD137)-deficient mice. *J Immunol* **168**, 5483–90 (2002).
221. Melero, I. *et al.* Monoclonal antibodies against the 4-1BB T-cell activation molecule eradicate established tumors. *Nature Medicine* **3**, (1997).
222. Kim, J. A. *et al.* Divergent effects of 4-1BB antibodies on antitumor immunity and on tumor-reactive T-cell generation. *Cancer Research* **61**, (2001).
223. Ju, S. A. *et al.* Immunity to melanoma mediated by 4-1BB is associated with enhanced activity of tumour-infiltrating lymphocytes. *Immunology and Cell Biology* **83**, (2005).
224. Alosaimi, M. F. *et al.* Immunodeficiency and EBV-induced lymphoproliferation caused by 4-1BB deficiency. *J Allergy Clin Immunol* **144**, 574-583.e5 (2019).

225. Rodriguez, R. *et al.* Concomitant PIK3CD and TNFRSF9 deficiencies cause chronic active Epstein-Barr virus infection of T cells. *Journal of Experimental Medicine* **216**, 2800–2818 (2019).
226. Zacharakis, N. *et al.* Immune recognition of somatic mutations leading to complete durable regression in metastatic breast cancer. *Nature Medicine* **24**, (2018).
227. Harao, M. *et al.* 4-1BB-enhanced expansion of CD8⁺ TIL from triple-negative breast cancer unveils mutation-specific CD8⁺ T cells. *Cancer Immunology Research* **5**, 439–445 (2017).
228. Kim, H. D. *et al.* 4-1BB delineates distinct activation status of exhausted tumor-infiltrating CD8⁺ T cells in hepatocellular carcinoma. *Hepatology* **71**, (2020).
229. Guo, X. *et al.* Global characterization of T cells in non-small-cell lung cancer by single-cell sequencing. *Nature Medicine* **24**, (2018).
230. Freeman, Z. T. *et al.* A conserved intratumoral regulatory T cell signature identifies 4-1BB as a pan-cancer target. *Journal of Clinical Investigation* **130**, (2020).
231. Buchan, S. L. *et al.* Antibodies to Costimulatory Receptor 4-1BB Enhance Anti-tumor Immunity via T Regulatory Cell Depletion and Promotion of CD8 T Cell Effector Function. *Immunity* **49**, (2018).
232. Lee, S. C. *et al.* 4-1BB (CD137) is required for rapid clearance of *Listeria monocytogenes* infection. *Infection and Immunity* **73**, (2005).
233. Bertram, E. M. *et al.* A Switch in Costimulation from CD28 to 4-1BB during Primary versus Secondary CD8 T Cell Response to Influenza In Vivo. *The Journal of Immunology* **172**, (2004).
234. Zhao, Y., Tahiliani, V., Salek-Ardakani, S. & Croft, M. Targeting 4-1BB (CD137) to enhance CD8 T cell responses with poxviruses and viral antigens. *Frontiers in Immunology* **3**, (2012).
235. Tran, V. G., Nguyen, N. N. Z. & Kwon, B. CD137 signaling is critical in fungal clearance during systemic candida albicans infection. *Journal of Fungi* **7**, (2021).
236. Scott Halstead, E., Mueller, Y. M., Altman, J. D. & Katsikis, P. D. In vivo stimulation of CD137 broadens primary antiviral CD8⁺T cell responses. *Nature Immunology* **3**, (2002).
237. Kim, S. H. *et al.* Chronic activation of 4-1BB signaling induces granuloma development in tumor-draining lymph nodes that is detrimental to subsequent CD8⁺ T cell responses. *Cellular and Molecular Immunology* **18**, (2021).

238. Dubrot, J. *et al.* Treatment with anti-CD137 mAbs causes intense accumulations of liver T cells without selective antitumor immunotherapeutic effects in this organ. *Cancer Immunology, Immunotherapy* **59**, (2010).
239. Bartkowiak, T. *et al.* Activation of 4-1BB on liver myeloid cells triggers hepatitis via an interleukin-27-dependent pathway. *Clinical Cancer Research* **24**, 1138–1151 (2018).
240. Jiang, P. *et al.* CD137 promotes bone metastasis of breast cancer by enhancing the migration and osteoclast differentiation of monocytes/macrophages. *Theranostics* **9**, 2950–2966 (2019).
241. Kim, C.-S. *et al.* Deficiency for costimulatory receptor 4-1BB protects against obesity-induced inflammation and metabolic disorders. *Diabetes* **60**, 3159–68 (2011).
242. Woroniecka, K. I. *et al.* 4-1BB agonism averts T_H1 exhaustion and licenses PD-1 blockade in glioblastoma and other intracranial cancers. *Clinical Cancer Research* **26**, (2020).
243. Chen, S. *et al.* Combination of 4-1BB agonist and PD-1 antagonist promotes antitumor effector/memory CD8 T cells in a Poorly Immunogenic Tumor Model. *Cancer Immunology Research* **3**, (2015).
244. Qu, Q. X. *et al.* 4-1BB Agonism Combined With PD-L1 Blockade Increases the Number of Tissue-Resident CD8⁺ T Cells and Facilitates Tumor Abrogation. *Frontiers in Immunology* **11**, (2020).
245. Segal, N. H. *et al.* Results from an integrated safety analysis of urelumab, an agonist anti-CD137 monoclonal antibody. *Clinical Cancer Research* **23**, (2017).
246. Chin, S. M. *et al.* Structure of the 4-1BB/4-1BBL complex and distinct binding and functional properties of utomilumab and urelumab. *Nature Communications* **9**, (2018).
247. Segal, N. H. *et al.* Phase I study of single-agent utomilumab (PF-05082566), a 4-1BB/CD137 agonist, in patients with advanced cancer. *Clinical Cancer Research* **24**, (2018).
248. Sakellariou-Thompson, D. *et al.* 4-1BB agonist focuses CD8⁺ tumor-infiltrating T-cell growth into a distinct repertoire capable of tumor recognition in pancreatic cancer. *Clinical Cancer Research* **23**, 7263–7275 (2017).
249. Li, G. *et al.* 4-1BB enhancement of CAR T function requires NF- κ B and TRAFs. *JCI Insight* **3**, (2018).
250. Philipson, B. I. *et al.* 4-1BB costimulation promotes CAR T cell survival through noncanonical NF- κ B signaling. *Science Signaling* **13**, (2020).

251. Gomes-Silva, D. *et al.* Tonic 4-1BB Costimulation in Chimeric Antigen Receptors Impedes T Cell Survival and Is Vector-Dependent. *Cell Reports* **21**, (2017).
252. Oda, S. K. *et al.* A Fas-4-1BB fusion protein converts a death to a pro-survival signal and enhances T cell therapy. *Journal of Experimental Medicine* **217**, (2020).
253. Anderson, K. G. *et al.* Engineering adoptive T cell therapy to co-opt Fas ligand-mediated death signaling in ovarian cancer enhances therapeutic efficacy. *Journal for ImmunoTherapy of Cancer* **10**, e003959 (2022).
254. Goldstein, G. *et al.* Isolation of a polypeptide that has lymphocyte differentiating properties and is probably represented universally in living cells. *Proc Natl Acad Sci U S A* **72**, (1975).
255. Catic, A. & Ploegh, H. L. Ubiquitin - Conserved protein or selfish gene? *Trends in Biochemical Sciences* **30**, (2005).
256. Hershko, A., Ciechanover, A. & Varshavsky, A. The ubiquitin system. *Nature Medicine* vol. 6 (2000).
257. Liu, L. *et al.* UbiHub: A data hub for the explorers of ubiquitination pathways. *Bioinformatics* **35**, (2019).
258. Buetow, L. & Huang, D. T. Structural insights into the catalysis and regulation of E3 ubiquitin ligases. *Nature Reviews Molecular Cell Biology* vol. 17 (2016).
259. Petroski, M. D. & Deshaies, R. J. Function and regulation of cullin-RING ubiquitin ligases. *Nature Reviews Molecular Cell Biology* vol. 6 (2005).
260. Jiang, Z. Y. *et al.* Insight into the Intermolecular Recognition Mechanism between Keap1 and IKK β Combining Homology Modelling, Protein-Protein Docking, Molecular Dynamics Simulations and Virtual Alanine Mutation. *PLoS ONE* **8**, (2013).
261. Komander, D. & Rape, M. The Ubiquitin Code. *Annual Review of Biochemistry* **81**, 203–229 (2012).
262. Swatek, K. N. *et al.* Insights into ubiquitin chain architecture using Ub-clipping. *Nature* **572**, (2019).
263. Madiraju, C., Novack, J. P., Reed, J. C. & Matsuzawa, S. K63 ubiquitination in immune signaling. *Trends in Immunology* **43**, 148–162 (2022).
264. Akutsu, M., Dikic, I. & Bremm, A. Ubiquitin chain diversity at a glance. *Journal of Cell Science* **129**, (2016).

265. Tracz, M. & Bialek, W. Beyond K48 and K63: non-canonical protein ubiquitination. *Cellular and Molecular Biology Letters* **26**, (2021).
266. French, M. E., Koehler, C. F. & Hunter, T. Emerging functions of branched ubiquitin chains. *Cell Discovery* vol. 7 (2021).
267. Haakonsen, D. L. & Rape, M. Branching out: Improved signaling by heterotypic ubiquitin chains. *Trends in Cell Biology* vol. 29 (2019).
268. Sun, S. C. Deubiquitylation and regulation of the immune response. *Nature Reviews Immunology* vol. 8 (2008).
269. Bhoj, V. G. & Chen, Z. J. Ubiquitylation in innate and adaptive immunity. *Nature* vol. 458 (2009).
270. Hu, H. & Sun, S. C. Ubiquitin signaling in immune responses. *Cell Research* vol. 26 (2016).
271. Fujita, Y., Tinoco, R., Li, Y., Senft, D. & Ronai, Z. A. Ubiquitin Ligases in Cancer Immunotherapy – Balancing Antitumor and Autoimmunity. *Trends in Molecular Medicine* vol. 25 (2019).
272. Zhou, X. & Sun, S. C. Targeting ubiquitin signaling for cancer immunotherapy. *Signal Transduction and Targeted Therapy* vol. 6 (2021).
273. Haglund, K. & Dikic, I. Ubiquitylation and cell signaling. *EMBO J* **24**, 3353–9 (2005).
274. Stagg, H. R. *et al.* The TRC8 E3 ligase ubiquitinates MHC class I molecules before dislocation from the ER. *Journal of Cell Biology* **186**, (2009).
275. van den Boomen, D. J. H. *et al.* TMEM129 is a Derlin-1 associated ERAD E3 ligase essential for virus-induced degradation of MHC-I. *Proc Natl Acad Sci U S A* **111**, (2014).
276. de Gassart, A. *et al.* MHC class II stabilization at the surface of human dendritic cells is the result of maturation-dependent MARCH I down-regulation. *Proc Natl Acad Sci U S A* **105**, (2008).
277. Cho, K. J., Walseng, E., Ishido, S. & Roche, P. A. Ubiquitination by March-I prevents MHC class II recycling and promotes MHC class II turnover in antigen-presenting cells. *Proc Natl Acad Sci U S A* **112**, (2015).
278. Liu, H. *et al.* Ubiquitin ligase MARCH 8 cooperates with CD83 to control surface MHC II expression in thymic epithelium and CD4 T cell selection. *Journal of Experimental Medicine* **213**, 1695–1703 (2016).

279. Baravalle, G. *et al.* Ubiquitination of CD86 Is a Key Mechanism in Regulating Antigen Presentation by Dendritic Cells. *The Journal of Immunology* **187**, (2011).
280. Corcoran, K. *et al.* Ubiquitin-mediated regulation of CD86 protein expression by the ubiquitin ligase membrane-associated RING-CH-1 (MARCH1). *Journal of Biological Chemistry* **286**, (2011).
281. Berg, M. & Zavazava, N. Regulation of CD28 expression on CD8⁺ T cells by CTLA-4. *Journal of Leukocyte Biology* **83**, (2008).
282. Meng, X. *et al.* FBXO38 mediates PD-1 ubiquitination and regulates anti-tumour immunity of T cells. *Nature* **564**, 130–135 (2018).
283. Zhou, X. A. *et al.* KLHL22 maintains PD-1 homeostasis and prevents excessive T cell suppression. *Proc Natl Acad Sci U S A* **117**, 28239–28250 (2020).
284. Zhang, J. *et al.* Cyclin D-CDK4 kinase destabilizes PD-L1 via cullin 3-SPOP to control cancer immune surveillance. *Nature* **553**, (2018).
285. Li, C. W. *et al.* Glycosylation and stabilization of programmed death ligand-1 suppresses T-cell activity. *Nature Communications* **7**, (2016).
286. De, S., Holvey-Bates, E. G., Mahen, K., Willard, B. & Stark, G. R. The ubiquitin E3 ligase FBXO22 degrades PD-L1 and sensitizes cancer cells to DNA damage. *Proc Natl Acad Sci U S A* **118**, (2021).
287. Wu, Y. *et al.* ARIH1 signaling promotes anti-tumor immunity by targeting PD-L1 for proteasomal degradation. *Nature Communications* **12**, (2021).
288. Xiong, W. *et al.* USP8 inhibition reshapes an inflamed tumor microenvironment that potentiates the immunotherapy. *Nature Communications* **13**, 1700 (2022).
289. Lim, S. O. *et al.* Deubiquitination and Stabilization of PD-L1 by CSN5. *Cancer Cell* **30**, (2016).
290. Wang, Y. *et al.* The deubiquitinase USP22 regulates PD-L1 degradation in human cancer cells. *Cell Communication and Signaling* **18**, (2020).
291. Apriamashvili, G. *et al.* Ubiquitin ligase STUB1 destabilizes IFN γ -receptor complex to suppress tumor IFN γ signaling. *Nature Communications* **13**, 1923 (2022).
292. Gstalder, C. *et al.* Inactivation of fbwx7 impairs dsrna sensing and confers resistance to pd-1 blockade. *Cancer Discovery* **10**, (2020).

293. Wang, X. *et al.* In vivo CRISPR screens identify the E3 ligase Cop1 as a modulator of macrophage infiltration and cancer immunotherapy target. *Cell* **184**, (2021).
294. vanLoosdregt, J. *et al.* Stabilization of the transcription factor Foxp3 by the deubiquitinase USP7 increases treg-cell-suppressive capacity. *Immunity* **39**, (2013).
295. LaCasse, E. C. *et al.* IAP-targeted therapies for cancer. *Oncogene* vol. 27 (2008).
296. Chesi, M. *et al.* IAP antagonists induce anti-tumor immunity in multiple myeloma. *Nature Medicine* **22**, (2016).
297. Roehle, K. *et al.* cIAP1/2 antagonism eliminates MHC class I-negative tumors through T cell-dependent reprogramming of mononuclear phagocytes. *Science Translational Medicine* **13**, (2021).
298. Dougan, M. *et al.* IAP inhibitors enhance co-stimulation to promote tumor immunity. *Journal of Experimental Medicine* **207**, (2010).
299. Momand, J. The MDM2 gene amplification database. *Nucleic Acids Research* **26**, 3453–3459 (1998).
300. Fang, D. D. *et al.* MDM2 inhibitor APG-115 synergizes with PD-1 blockade through enhancing antitumor immunity in the tumor microenvironment. *Journal for ImmunoTherapy of Cancer* **7**, (2019).
301. Tolcher, A. W. *et al.* Preliminary results of a phase II study of alrizomadlin (APG-115), a novel, small-molecule MDM2 inhibitor, in combination with pembrolizumab in patients (pts) with unresectable or metastatic melanoma or advanced solid tumors that have failed immuno-oncologic (I-O) drugs. *Journal of Clinical Oncology* **39**, (2021).
302. Zhou, J. *et al.* The ubiquitin ligase MDM2 sustains STAT5 stability to control T cell-mediated antitumor immunity. *Nature Immunology* **22**, (2021).
303. Canon, J. *et al.* The MDM2 inhibitor AMG 232 demonstrates robust antitumor efficacy and potentiates the activity of p53-inducing cytotoxic agents. *Molecular Cancer Therapeutics* **14**, (2015).
304. Lai, A. C. & Crews, C. M. Induced protein degradation: An emerging drug discovery paradigm. *Nature Reviews Drug Discovery* vol. 16 (2017).
305. Wang, Y. *et al.* In vitro and in vivo degradation of programmed cell death ligand 1 (PD-L1) by a proteolysis targeting chimera (PROTAC). *Bioorganic Chemistry* **111**, 104833 (2021).

306. Cotton, A. D., Nguyen, D. P., Gramespacher, J. A., Seiple, I. B. & Wells, J. A. Development of antibody-based PROTACs for the degradation of the cell-surface immune checkpoint protein PD-L1. *J Am Chem Soc* **143**, 593–598 (2021).
307. Li, W. *et al.* Chimeric Antigen Receptor Designed to Prevent Ubiquitination and Downregulation Showed Durable Antitumor Efficacy. *Immunity* **53**, (2020).
308. Flynn, R. A. *et al.* Small RNAs are modified with N-glycans and displayed on the surface of living cells. *Cell* **184**, (2021).
309. Spiro, R. G. Protein glycosylation: Nature, distribution, enzymatic formation, and disease implications of glycopeptide bonds. *Glycobiology* vol. 12 (2002).
310. Bucala, R., Makita, Z., Koschinsky, T., Cerami, A. & Vlassara, H. Lipid advanced glycosylation: Pathway for lipid oxidation in vivo. *Proc Natl Acad Sci U S A* **90**, 6434–6438 (1993).
311. Shental-Bechor, D. & Levy, Y. Effect of glycosylation on protein folding: A close look at thermodynamic stabilization. *Proc Natl Acad Sci U S A* **105**, (2008).
312. Jayaprakash, N. G. & Surolia, A. Role of glycosylation in nucleating protein folding and stability. *Biochemical Journal* vol. 474 (2017).
313. Scheiffele, P. & Füllekrug, J. Glycosylation and protein transport. *Essays in Biochemistry* **36**, (2000).
314. J., B. The Role of Glycosylation in Receptor Signaling. in *Glycosylation* (2012). doi:10.5772/50262.
315. An, H. J., Froehlich, J. W. & Lebrilla, C. B. Determination of glycosylation sites and site-specific heterogeneity in glycoproteins. *Current Opinion in Chemical Biology* vol. 13 (2009).
316. Stanley, P., Taniguchi, N. & Aebi, M. Chapter 9. N-Glycans, Essentials of Glycobiology, 2nd Edition. *Essentials of Glycobiology* (2017).
317. Reily, C., Stewart, T. J., Renfrow, M. B. & Novak, J. Glycosylation in health and disease. *Nature Reviews Nephrology* vol. 15 (2019).
318. Ruiz-Canada, C., Kelleher, D. J. & Gilmore, R. Cotranslational and Posttranslational N-Glycosylation of Polypeptides by Distinct Mammalian OST Isoforms. *Cell* **136**, (2009).
319. Stenflo, J. & Fernlund, P. Amino acid sequence of the heavy chain of bovine protein C. *Journal of Biological Chemistry* **257**, (1982).

320. Baycin-Hizal, D. *et al.* GlycoFish: A database of zebrafish N -linked glycoproteins identified using SPEG method coupled with LC/MS. *Analytical Chemistry* **83**, (2011).
321. Lizak, C., Gerber, S., Numao, S., Aebi, M. & Locher, K. P. X-ray structure of a bacterial oligosaccharyltransferase. *Nature* **474**, (2011).
322. Mereiter, S., Balmaña, M., Campos, D., Gomes, J. & Reis, C. A. Glycosylation in the Era of Cancer-Targeted Therapy: Where Are We Heading? *Cancer Cell* vol. 36 (2019).
323. Pinho, S. S. & Reis, C. A. Glycosylation in cancer: Mechanisms and clinical implications. *Nature Reviews Cancer* vol. 15 (2015).
324. Sun, R., Kim, A. M. J. & Lim, S. O. Glycosylation of immune receptors in cancer. *Cells* vol. 10 (2021).
325. Sun, L. *et al.* Targeting glycosylated PD-1 induces potent antitumor immunity. *Cancer Research* **80**, (2020).
326. Okada, M. *et al.* Blockage of Core Fucosylation Reduces Cell-Surface Expression of PD-1 and Promotes Anti-tumor Immune Responses of T Cells. *Cell Reports* **20**, (2017).
327. Zhang, N. *et al.* Loss of core fucosylation enhances the anticancer activity of cytotoxic T lymphocytes by increasing PD-1 degradation. *European Journal of Immunology* **50**, (2020).
328. Li, C. W. *et al.* Eradication of triple-negative breast cancer cells by targeting glycosylated PD-L1. *Cancer Cell* **33**, (2018).
329. Chen, F. F., Li, Z., Ma, D. & Yu, Q. Small-molecule PD-L1 inhibitor BMS1166 abrogates the function of PD-L1 by blocking its ER export. *OncImmunology* **9**, (2020).
330. Cha, J. H. *et al.* Metformin Promotes Antitumor Immunity via Endoplasmic-Reticulum-Associated Degradation of PD-L1. *Molecular Cell* **71**, (2018).
331. Zhang, R. *et al.* D-mannose facilitates immunotherapy and radiotherapy of triple-negative breast cancer via degradation of PD-L1. *Proceedings of the National Academy of Sciences* **119**, e2114851119 (2022).
332. Shi, S. *et al.* Inhibition of MAN2A1 enhances the immune response to anti-PD-L1 in human tumors. *Clinical Cancer Research* **26**, (2020).
333. Huang, Y. *et al.* FUT8-mediated aberrant N-glycosylation of B7H3 suppresses the immune response in triple-negative breast cancer. *Nature Communications* **12**, (2021).
334. Song, X. *et al.* Pharmacologic suppression of B7-H4 glycosylation restores antitumor immunity in immune-cold breast cancers. *Cancer Discovery* **10**, (2020).

335. Silva, M. C. *et al.* Glycans as immune checkpoints: Removal of branched N-glycans enhances immune recognition preventing cancer progression. *Cancer Immunology Research* **8**, (2020).
336. Joung, J. *et al.* CRISPR activation screen identifies BCL-2 proteins and B3GNT2 as drivers of cancer resistance to T cell-mediated cytotoxicity. *Nature Communications* **13**, 1606 (2022).
337. McGowan, E. *et al.* PD-1 disrupted CAR-T cells in the treatment of solid tumors: Promises and challenges. *Biomedicine and Pharmacotherapy* vol. 121 (2020).
338. Shi, X. *et al.* Targeting glycosylation of PD-1 to enhance CAR-T cell cytotoxicity. *Journal of Hematology and Oncology* **12**, (2019).
339. Greco, B. *et al.* Disrupting N-glycan expression on tumor cells boosts chimeric antigen receptor T cell efficacy against solid malignancies. *Science Translational Medicine* **14**, (2022).
340. Posey, A. D. *et al.* Engineered CAR T Cells Targeting the Cancer-Associated Tn-Glycoform of the Membrane Mucin MUC1 Control Adenocarcinoma. *Immunity* **44**, (2016).
341. Mondal, N., Silva, M., Castano, A. P., Maus, M. v. & Sackstein, R. Glycoengineering of chimeric antigen receptor (CAR) T-cells to enforce E-selectin binding. *Journal of Biological Chemistry* **294**, (2019).
342. Collette, Y., Gilles, A., Pontarotti, P. & Olive, D. A co-evolution perspective of the TNFSF and TNFRSF families in the immune system. *Trends in Immunology* **24**, 387–394 (2003).
343. Croft, M., Benedict, C. A. & Ware, C. F. Clinical targeting of the TNF and TNFR superfamilies. *Nature Reviews Drug Discovery* vol. 12 (2013).
344. Wang, X. & Li, M. Correlate tumor mutation burden with immune signatures in human cancers. *BMC Immunology* **20**, (2019).
345. Jiang, P. *et al.* Signatures of T cell dysfunction and exclusion predict cancer immunotherapy response. *Nature Medicine* **24**, (2018).
346. Li, Y. *et al.* Tumor-infiltrating TNFRSF9+ CD8+ T cells define different subsets of clear cell renal cell carcinoma with prognosis and immunotherapeutic response. *OncoImmunology* **9**, (2020).

347. Zizzari, I. G. *et al.* Circulating CD137+ T cells correlate with improved response to anti-PD1 immunotherapy in patients with cancer. *Clinical Cancer Research* (2022) doi:10.1158/1078-0432.CCR-21-2918.
348. Gide, T. N. *et al.* Distinct immune cell populations define response to anti-PD-1 monotherapy and anti-PD-1/anti-CTLA-4 combined therapy. *Cancer Cell* **35**, 238-255.e6 (2019).
349. Liu, D. *et al.* Integrative molecular and clinical modeling of clinical outcomes to PD1 blockade in patients with metastatic melanoma. *Nature Medicine* **25**, (2019).
350. Li, T. *et al.* TIMER2.0 for analysis of tumor-infiltrating immune cells. *Nucleic Acids Research* **48**, (2020).
351. Haglund, K. & Dikic, I. Ubiquitylation and cell signaling. *EMBO Journal* vol. 24 (2005).
352. Wagner, S. A. *et al.* A Proteome-wide, Quantitative Survey of In Vivo Ubiquitylation Sites Reveals Widespread Regulatory Roles. *Molecular & Cellular Proteomics* **10**, (2011).
353. Povlsen, L. K. *et al.* Systems-wide analysis of ubiquitylation dynamics reveals a key role for PAF15 ubiquitylation in DNA-damage bypass. *Nature Cell Biology* **14**, (2012).
354. Zhang, F. *et al.* Lentiviral vectors containing an enhancer-less ubiquitously acting chromatin opening element (UCOE) provide highly reproducible and stable transgene expression in hematopoietic cells. *Blood* **110**, (2007).
355. Elder, J. H. & Alexander, S. endo-beta-N-acetylglucosaminidase F: endoglycosidase from *Flavobacterium meningosepticum* that cleaves both high-mannose and complex glycoproteins. *Proceedings of the National Academy of Sciences* **79**, 4540–4544 (1982).
356. Plummer, T. H., Elder, J. H., Alexander, S., Phelan, A. W. & Tarentino, A. L. Demonstration of peptide:N-glycosidase F activity in endo-beta-N-acetylglucosaminidase F preparations. *J Biol Chem* **259**, 10700–4 (1984).
357. Klausner, R. D., Donaldson, J. G. & Lippincott-Schwartz, J. Brefeldin A: Insights into the control of membrane traffic and organelle structure. *Journal of Cell Biology* vol. 116 (1992).
358. Ciechanover, A. Proteolysis: From the lysosome to ubiquitin and the proteasome. *Nature Reviews Molecular Cell Biology* vol. 6 (2005).
359. Clague, M. J. & Urbé, S. Ubiquitin: Same molecule, different degradation pathways. *Cell* vol. 143 (2010).

360. Qin, W., Cho, K. F., Cavanagh, P. E. & Ting, A. Y. Deciphering molecular interactions by proximity labeling. *Nature Methods* vol. 18 (2021).
361. Li, Y. *et al.* Preventing abnormal NF- κ B activation and autoimmunity by Otub1-mediated p100 stabilization. *Cell Research* **29**, (2019).
362. Zhang, Y. *et al.* TurboID-based proximity labeling reveals that UBR7 is a regulator of NLR immune receptor-mediated immunity. *Nature Communications* **10**, (2019).
363. Li, T. *et al.* Exploring a Tumor-Intrinsic PD-L1 Signal with Proximity-Dependent Biotin Identification in Lung Cancer Cells. *Biochemistry* **58**, (2019).
364. Liu, Q. *et al.* A proximity-tagging system to identify membrane protein–protein interactions. *Nature Methods* **15**, (2018).
365. Kim, D. I. *et al.* An improved smaller biotin ligase for BioID proximity labeling. *Molecular Biology of the Cell* **27**, (2016).
366. Yao, I. *et al.* SCRAPER-Dependent Ubiquitination of Active Zone Protein RIM1 Regulates Synaptic Vesicle Release. *Cell* **130**, (2007).
367. Kipreos, E. T. & Pagano, M. The F-box protein family. *Genome Biology* vol. 1 (2000).
368. van Allen, E. M. *et al.* Genomic correlates of response to CTLA-4 blockade in metastatic melanoma. *Science (1979)* **350**, 207–211 (2015).
369. Guo, Y., Yang, L., Lei, S., Tan, W. & Long, J. NEDD4 negatively regulates GITR via ubiquitination in immune microenvironment of melanoma. *OncoTargets and Therapy* **12**, (2019).
370. Yoshida, Y., Mizushima, T. & Tanaka, K. Sugar-recognizing ubiquitin ligases: Action mechanisms and physiology. *Frontiers in Physiology* vol. 10 (2019).
371. Xiao, J. *et al.* FBXL20-mediated Vps34 ubiquitination as a p53 controlled checkpoint in regulating autophagy and receptor degradation. *Genes and Development* **29**, (2015).
372. Mason, B. & Laman, H. The FBXL family of F-box proteins: Variations on a theme: The FBXL family of F-box proteins. *Open Biology* vol. 10 (2020).
373. Manne, R. K. *et al.* FBXL20 promotes breast cancer malignancy by inhibiting apoptosis through degradation of PUMA and BAX. *Journal of Biological Chemistry* **297**, (2021).
374. Madduri, L. S. V. *et al.* p53/FBXL20 axis negatively regulates the protein stability of PR55 α , a regulatory subunit of PP2A Ser/Thr phosphatase. *Neoplasia (United States)* **23**, (2021).

375. Feng, W. *et al.* Identifying the cardiac dyad proteome in vivo by a BioID2 knock-in strategy. *Circulation* (2020) doi:10.1161/CIRCULATIONAHA.119.043434.
376. Schwarz, F. & Aebi, M. Mechanisms and principles of N-linked protein glycosylation. *Current Opinion in Structural Biology* vol. 21 (2011).
377. Aebi, M. N-linked protein glycosylation in the ER. *Biochimica et Biophysica Acta - Molecular Cell Research* vol. 1833 (2013).
378. Aebi, M., Bernasconi, R., Clerc, S. & Molinari, M. N-glycan structures: recognition and processing in the ER. *Trends in Biochemical Sciences* vol. 35 (2010).
379. Rujas, E., Cui, H., Sicard, T., Semesi, A. & Julien, J. P. Structural characterization of the ICOS/ICOS-L immune complex reveals high molecular mimicry by therapeutic antibodies. *Nature Communications* **11**, (2020).
380. Helenius, A. & Aebi, M. Intracellular functions of N-linked glycans. *Science* vol. 291 (2001).
381. Darlington, P. J., Kirchhof, M. G., Criado, G., Sondhi, J. & Madrenas, J. Hierarchical Regulation of CTLA-4 Dimer-Based Lattice Formation and Its Biological Relevance for T Cell Inactivation. *The Journal of Immunology* **175**, (2005).
382. Zhuo, Y., Yang, J. Y., Moremen, K. W. & Prestegard, J. H. Glycosylation alters dimerization properties of a cell-surface signaling protein, carcinoembryonic antigen-related cell Adhesion Molecule 1 (CEACAM1). *Journal of Biological Chemistry* **291**, (2016).
383. Kucka, K. & Wajant, H. Receptor Oligomerization and Its Relevance for Signaling by Receptors of the Tumor Necrosis Factor Receptor Superfamily. *Frontiers in Cell and Developmental Biology* vol. 8 (2021).
384. Zhai, T. *et al.* Generation of a safe and efficacious llama single-domain antibody fragment (vHH) targeting the membrane-proximal region of 4-1BB for engineering therapeutic bispecific antibodies for cancer. *Journal for ImmunoTherapy of Cancer* **9**, (2021).
385. de Haas, P., Hendriks, W. J. A. J., Lefeber, D. J. & Cambi, A. Biological and technical challenges in unraveling the role of N-glycans in immune receptor regulation. *Frontiers in Chemistry* vol. 8 (2020).
386. Smulski, C. R. *et al.* Cysteine-rich domain 1 of CD40 mediates receptor self-assembly. *Journal of Biological Chemistry* **288**, (2013).

387. He, C. *et al.* Therapeutic antibody activation of the glucocorticoid-induced TNF receptor by a clustering mechanism. *Science Advances* **8**, (2022).
388. Harada, Y., Ohkawa, Y., Maeda, K. & Taniguchi, N. Glycan quality control in and out of the endoplasmic reticulum of mammalian cells. *FEBS Journal* (2021) doi:10.1111/febs.16185.
389. Chen, H. *et al.* Blocking the Thiol at Cysteine-322 Destabilizes Tau Protein and Prevents Its Oligomer Formation. *ACS Chemical Neuroscience* **9**, (2018).
390. Jia, R. & Bonifacino, J. S. Negative regulation of autophagy by uba6-birc6-mediated ubiquitination of lc3. *Elife* **8**, (2019).
391. Wei, W. *et al.* A20 and RBX1 regulate Brentuximab Vedotin sensitivity in Hodgkin lymphoma models. *Clinical Cancer Research* **26**, (2020).
392. Zhang, Y. *et al.* Hijacking antibody-induced CTLA-4 lysosomal degradation for safer and more effective cancer immunotherapy. *Cell Research* **29**, (2019).
393. Qi, X. *et al.* Optimization of 4-1BB antibody for cancer immunotherapy by balancing agonistic strength with FcγR affinity. *Nature Communications* **10**, (2019).
394. Fu, S. *et al.* Early safety and efficacy from a phase I open-label clinical trial of CD137(4-1BB) agonistic antibody LVGN6051 as monotherapy and in combination with pembrolizumab. *Journal of Clinical Oncology* **39**, (2021).
395. Tolcher, A. W. *et al.* Initial findings of the first-in-human phase I study of AGEN2373, a conditionally active CD137 agonist antibody, in patients (pts) with advanced solid tumors. *Journal of Clinical Oncology* **39**, (2021).
396. Ullenhag, G. J. *et al.* A first-in-human, multicenter, open-label, phase 1 study of ATOR-1017, a 4-1BB antibody, in patients with advanced solid malignancies. *Journal of Clinical Oncology* **39**, (2021).
397. Eskiocak, U. *et al.* Differentiated agonistic antibody targeting CD137 eradicates large tumors without hepatotoxicity. *JCI Insight* **5**, (2020).
398. Ettxeberria, I. *et al.* Antitumor efficacy and reduced toxicity using an anti-CD137 Probody therapeutic. *Proc Natl Acad Sci U S A* **118**, (2021).
399. Zhao, Y. *et al.* Switchable immune modulator for tumor-specific activation of anticancer immunity. *Science Advances* **7**, (2021).

400. Kamata-Sakurai, M. *et al.* Antibody to CD137 activated by extracellular adenosine triphosphate is tumor selective and broadly effective in vivo without systemic immune activation. *Cancer Discovery* **11**, (2021).
401. Hinner, M. J. *et al.* Tumor-localized costimulatory T-cell engagement by the 4-1BB/HER2 bispecific antibody-anticalin fusion PRS-343. *Clinical Cancer Research* **25**, (2019).
402. Peper-Gabriel, J. K. *et al.* The PD-L1/4-1BB bispecific Antibody-Anticalin fusion protein PRS-344/S095012 elicits strong T-cell stimulation in a tumor-localized manner. *Clinical Cancer Research* clincanres.2762.2021 (2022) doi:10.1158/1078-0432.CCR-21-2762.
403. Garralda, E. *et al.* 412 First-in-human phase I/IIa trial to evaluate the safety and initial clinical activity of DuoBody®-PD-L1×4-1BB (GEN1046) in patients with advanced solid tumors. in (2020). doi:10.1136/jitc-2020-sitc2020.0412.
404. Johnson, M. *et al.* 493 First-in-human phase 1/2 trial to evaluate the safety and initial clinical activity of DuoBody®-CD40×4-1BB (GEN1042) in patients with advanced solid tumors. *Journal for ImmunoTherapy of Cancer* **9**, (2021).
405. Jiang, W., Wang, Z., Sheng, Z., Jung, J. & Guo, T. 702 TJ-CD4B (ABL111), a Claudin18.2-targeted 4-1BB tumor engager induces potent tumor-dependent immune response without dose-limiting toxicity in preclinical studies. *Journal for ImmunoTherapy of Cancer* **9**, A730–A730 (2021).
406. Compte, M. *et al.* An Fc-free EGFR-specific 4-1BB-agonistic trimerbody displays broad antitumor activity in humanized murine cancer models without toxicity. *Clinical Cancer Research* **27**, (2021).
407. Link, A. *et al.* Abstract 2273: Selection of first-in-human clinical dose range for the tumor-targeted 4-1BB agonist MP0310 (AMG 506) using a pharmacokinetic/pharmacodynamics modeling approach. in *Immunology 2273–2273* (American Association for Cancer Research, 2020). doi:10.1158/1538-7445.AM2020-2273.
408. Snell, D. *et al.* Abstract 2276: Preclinical development and mechanism of action studies of NM21-1480, a PD-L1/4-1BB/HSA trispecific MATCH3 therapeutic clinical candidate. in (2020). doi:10.1158/1538-7445.am2020-2276.
409. Hurov, K. *et al.* BT7480, a novel fully synthetic Bicycle tumor-targeted immune cell agonistTM (Bicycle TICATM) induces tumor localized CD137 agonism. *Journal for ImmunoTherapy of Cancer* **9**, (2021).

410. Herter, S. *et al.* RG6076 (CD19-4-1BBL): CD19-Targeted 4-1BB Ligand Combination with Glofitamab As an Off-the-Shelf, Enhanced T-Cell Redirection Therapy for B-Cell Malignancies. *Blood* **136**, (2020).
411. Claus, C. *et al.* Tumor-Targeted 4-1BB agonists for combination with T cell bispecific antibodies as off-The-shelf therapy. *Science Translational Medicine* **11**, (2019).
412. Mock, J. *et al.* An engineered 4-1BBL fusion protein with “activity on demand.” *Proc Natl Acad Sci U S A* **117**, (2020).
413. Gao, Y. *et al.* Acetylation-dependent regulation of PD-L1 nuclear translocation dictates the efficacy of anti-PD-1 immunotherapy. *Nature Cell Biology* **22**, (2020).
414. Hou, J. *et al.* PD-L1-mediated gasdermin C expression switches apoptosis to pyroptosis in cancer cells and facilitates tumour necrosis. *Nature Cell Biology* **22**, (2020).
415. Riley, N. M., Hebert, A. S., Westphall, M. S. & Coon, J. J. Capturing site-specific heterogeneity with large-scale N-glycoproteome analysis. *Nature Communications* **10**, (2019).
416. Zeng, W. F., Cao, W. Q., Liu, M. Q., He, S. M. & Yang, P. Y. Precise, fast and comprehensive analysis of intact glycopeptides and modified glycans with pGlyco3. *Nature Methods* **18**, (2021).
417. Shen, J. *et al.* StrucGP: de novo structural sequencing of site-specific N-glycan on glycoproteins using a modularization strategy. *Nature Methods* **18**, (2021).
418. Gray, M. A. *et al.* Targeted glycan degradation potentiates the anticancer immune response in vivo. *Nature Chemical Biology* **16**, (2020).
419. Ge, Y. *et al.* Target protein deglycosylation in living cells by a nanobody-fused split O-GlcNAcase. *Nature Chemical Biology* **17**, (2021).
420. Tang, F. *et al.* Selective N-glycan editing on living cell surfaces to probe glycoconjugate function. *Nature Chemical Biology* **16**, (2020).
421. Packer, M. S. & Liu, D. R. Methods for the directed evolution of proteins. *Nat Rev Genet* **16**, 379–94 (2015).
422. Hegde, P. S. & Chen, D. S. Top 10 Challenges in Cancer Immunotherapy. *Immunity* vol. 52 (2020).
423. Shah, A. D., Goode, R. J. A., Huang, C., Powell, D. R. & Schittenhelm, R. B. LFQ-Analyst: An easy-To-use interactive web platform to analyze and visualize label-free proteomics data

- preprocessed with maxquant. *Journal of Proteome Research* (2019) doi:10.1021/acs.jproteome.9b00496.
424. Shajahan, A., Heiss, C., Ishihara, M. & Azadi, P. Glycomic and glycoproteomic analysis of glycoproteins—a tutorial. *Analytical and Bioanalytical Chemistry* **409**, (2017).

VITA

Ruoxuan Sun was born on July 8th, 1993 in Beijing, P.R. China. He entered the six-year (undergraduate-master) program in the School of Pharmaceutical Sciences at Peking University and in 2011. Upon the completion of undergraduate course study on May 2015, he proceeded the graduate training in the laboratory of Dr. Huihui Zeng in the Department of Chemical Biology and received the degree of Master of Science (M.S.) in May 2017. During the M.S. degree training, Ruoxuan Sun was participated in several research projects and conducted his own study investigating the pharmacological mechanism underlying the anti-tumor effect of etheselen (a potent inhibitor against thioredoxin reductase) on colorectal cancer cells. Then, Ruoxuan Sun actively pursued the advanced scientific training under the supervision of Dr. Seung-Oe Lim at Department of Medicinal Chemistry and Molecular Pharmacology, College of Pharmacy, Purdue University. His research in Dr. Lim's group was focused on the post-translational regulation of cancer immunotherapy targets, primarily 4-1BB. Two research article and one review article have been published on peer reviewed journals by Ruoxuan Sun as the first author. He defended this dissertation on April 19 and was then certified for the degree of Doctor of Philosophy.

PUBLICATIONS

1. Kim, B., Sun, R., Oh, W., Kim, A. M. J., Schwarz, J. R., & Lim, S. O. (2020). Saccharide analog, 2-deoxy-d-glucose enhances 4-1BB-mediated antitumor immunity via PD-L1 deglycosylation. *Molecular Carcinogenesis*, 59(7), 691–700. <https://doi.org/10.1002/mc.23170>
2. Sun, R., Kim, A. M. J., & Lim, S. O. (2021). Glycosylation of immune receptors in cancer. In *Cells (MDPI)*, 10(5), 1110. <https://doi.org/10.3390/cells10051100>
3. Sun, R., Kim, A. M. J., Murray, A. A., & Lim, S. O. (2022). N-glycosylation facilitates 4-1BB membrane localization by avoiding Its multimerization. *Cells (MDPI)*, 11(1), 162. <https://doi.org/10.3390/cells11010162>
4. Sun, R., & Lim, S. O. (2022). FBXL20-mediated ubiquitination triggers the proteasomal degradation of 4-1BB. *FEBS J.* 2022 Feb 3. doi: 10.1111/febs.16383.